Study of Magnetic and Electrical Properties of Spinel Chromites and Ferrites

A Thesis Submitted

By

Ritupan Borah

Roll No: 166121017

In Partial Fulfillment of the Requirements for the Award of the Degree of

Doctor of Philosophy in Physics

Department of Physics

Indian Institute of Technology Guwahati

Guwahati-781039, India

July, 2022

Statement

The work contained in the thesis entitled "**Study of Magnetic and Electrical properties of Spinel Chromites and Ferrites"** has been carried out by me under the supervision of Prof. S. Ravi, Department of Physics, Indian Institute of Technology Guwahati. This work has not been submitted elsewhere for the award of any degree.

July, 2022

Ritupan Borah
Department of Physics
Indian Institute of Technology Guwahati
Guwahati – 781039, India

Certificate

It is certified that the work contained in the thesis entitled **"Study of Magnetic and Electrical properties of Spinel Chromites and Ferrites"** by Mr. Ritupan Borah, a Ph.D. student of the Department of Physics, Indian Institute of Technology Guwahati for the award of the degree of *Doctor of Philosophy* has been carried out under my supervision. This work has not been submitted elsewhere for the award of any degree.

July, 2022

Prof. S. Ravi
Professor, Department of Physics
Indian Institute of Technology Guwahati
Guwahati – 781 039, India

This thesis is dedicated to my parents

Acknowledgements

I would like to acknowledge and give my warmest thanks to my supervisor Prof. S. Ravi who made this work possible. His guidance and advice helped me get through all of the stages of my research. His caring nature and gentle behaviour inspired me to be motivated. Moreover, his valuable insights on numerous technical ideas as well as his vast experience in this sector aided me in resolving issues that developed during the experiments.

I would also like to offer my sincere gratitude to my doctoral committee (DC) members Prof. D. Pal (chairperson), Dr. U. N. Maiti and Prof. V. Manivannan for their thoughtful suggestions and encouragement to comprehend and improve my thesis work from various outlook.

I am very much thankful to present Head of the Department (HoD) of Physics, Prof. A. Perumal and former HoDs of Physics, Prof. S. Ghosh and Prof. Poulose for providing instrument facilities and their cooperation during the tenure of my Ph.D. thesis. I am thankful to all the faculty members and other staff members of the Department of Physics as well.

I am grateful to Prof. G. Pugazhenthi head of the Central Instrumental Facility (CIF), IIT Guwahati, and all the scientific officers and technical staff of CIF, IIT Guwahati, for enabling me to perform the experiments using various sophisticated instruments during my Ph.D. tenure.

I would like to acknowledge my lab-mates Pushpanjali, Debabrata, Shalini, Nibedita and Deepak for their support and maintaining a peaceful environment in the lab. I am appreciative to my seniors Dr. Junmoni Barman and post-doctoral fellow Dr. Vishwajit Manohar Gaikwad for lots of discussions and technical help.

I am grateful to my family members for their encouragement and moral support.

I honestly thank my friends Hirakjyoti and Arabindu for their continuous inspiration and care.

I acknowledge the Department of Science and Technology (DST), Fund for Improvement of S&T Infrastructure (FIST), New Delhi for providing the facilities of Vibrating sample magnetometer, TTRAX III X-ray diffractometer, Physical properties measurements

system. I express my sincere thanks to the Ministry of Human Resource and Development (MHRD) and Indian Institute of Technology Guwahati for providing the financial assistance through institute fellowship during my Ph.D. tenure.

Ritupan Borah

IIT Guwahati

Table of Contents

Abstract

Magnetic materials in solids are a separate discipline of condensed matter physics and take many forms and display several exotic phenomena. In general, the properties of magnetic materials can be altered or manipulated through the application of an external magnetic field. The study of magnetic materials is one of the primary research goals of condensed matter physics due to their applications in modern technology. Chromium-based spinels are a potential class of magnetic materials that exhibit multiferroic, magnetodielectric and magnetostructural coupling, exchange bias, and magnetization reversal etc. The discovery of such multifunctional properties in spinel chromites has opened up the possibilities of potential application in magnetic storage, magnetic switching, sensors, recording media and read-write head, magneto-dielectric devices, spintronics etc. In addition to the spinel chromites, spinel ferrites are also a well-known type of magnetic materials due to their appealing magnetic and dielectric properties. In an attempt to understand and tune the magnetic properties in these directions, our studies are focused on spinel chromites and ferrites.

In normal spinels with the general chemical formula AB_2O_4; the A^{2+} (Co^{2+}, Ni^{2+}, Fe^{2+} etc.) cations occupy the tetrahedral sites, while the B^{3+} (Cr^{3+}, Fe^{3+}, Al^{3+} etc.) cations occupy the octahedral sites. Spinel chromite ACr_2O_4 with magnetic or non-magnetic A site ion is one of the interesting class of magnetic materials due to several applications in light or heat sensitive micromechanical devices, catalytic material or gas sensors. In general, these chromites crystallize in cubic crystal structure with space group $Fd\bar{3}m$. However, Jahn –Teller (JT) active ions such as A = Ni^{2+}, Cu^{2+}, and Fe^{2+} at tetrahedral sites induce a structural transition from cubic to the tetragonal structure. Normal spinel nickel chromite ($NiCr_2O_4$), which crystallizes in tetragonal crystal structure attracts much attention for its rich physical and chemical properties. The magnetic structure of $NiCr_2O_4$ contains two magnetic sublattices at tetrahedral (A) and octahedral (B) sites respectively. Two A sites are grouped into a single sublattice while four B sites are grouped into two sublattices with each sublattice having both longitudinal and transverse components of magnetic moment. It is ferrimagnetic (FIM) in nature with Curie temperature T_C = 70 K. An additional transition occurring at T_N = 31 K is due the antiferromagnetic (AFM) ordering of the transverse components of magnetic moment.

This compound crystallizes in cubic phase at high temperature with space group $Fd\bar{3}m$. When lowering the temperature, the symmetry of the nickel chromite decreases to tetragonal at 320 K driven by the cooperative JT effect associated with the Ni^{2+} cations in the tetrahedral position.

$NiFe_2O_4$ is another interesting spinel and falls under inverse spinel structure. The spinel ferrite exhibit ferrimagnetism (FIM), as a result of anti-parallel alignment of magnetic moments of Fe^{3+} ions at tetrahedral sites and those of Ni^{2+} and Fe^{3+} ions at octahedral sites. The Co substituted $NiFe_2O_4$ has attracted much attention due to its interesting magnetic properties such as high coercivity, moderate saturation magnetization, super paramagnetism (SPM), Verwey transition, etc. Moreover, cobalt substituted nickel ferrites are highly resistive and magnetostrictive. Even though Co substitution is known to play a major role in altering the anisotropy and hence coercivity, the detailed analysis of site occupation of different ions and their influence on structural and magnetic properties are need to be explained.

Although there are many reports available on the magnetic properties of nickel chromite spinel system, systematic study of the effect of magnetic and nonmagnetic ions substitution on spin frustration, magnetocaloric effect, critical behavior and low temperature dielectric and conduction mechanism are still lacking. In addition, a comprehensive study of the effect of cation distribution and ionic states on the basic magnetic properties of the nickel spinel ferrite system is included in this thesis.

Therefore, in the present thesis, we have focused on the following series of mostly bulk samples to study the above objectives.

1) $Ni_{1-x}Mg_xCr_2O_4$ (x = 0 to 0.50)
2) $Ni_{0.85}Mg_{0.15}Cr_2O_4$ nanoparticles
3) $Ni_{1-x}Mn_xCr_2O_4$ (x = 0 to 0.50)
4) $Ni_{1-x}Cd_xCr_2O_4$ (x = 0 to 0.30)
5) $Ni_{1-x}Co_xFe_2O_4$ (x = 0 to 0.50)

The crystallinity and the phase formation of the above-mentioned samples are characterized by recording X-ray diffraction (XRD) patterns. The microstructure and compositional analyses are carried out by using field emission scanning electron microscope

(FESEM) attached with energy dispersive X-ray (EDX) spectrometer. Vibrating sample magnetometer (VSM) and Physical Property Measurement System (PPMS) were used to perform the temperature, time and field variations of magnetization measurements. LCR meter was used to obtain the impedance data in order to study dielectric properties.

This thesis contains six chapters:

1. **Introduction**
2. **Experimental Techniques**
3. **Mg Substituted $NiCr_2O_4$ series**
4. **Mn and Cd substituted $NiCr_2O_4$ series**
5. **Co Substituted $NiFe_2O_4$ series**
6. **Conclusion**

Chapter 1 presents the basics aspect of magnetism and brief discussion on structural, magnetic and dielectric properties of spinel chromite and ferrite compounds. The crystal structure of spinel compounds along with the importance of crystal field and Jahn-Teller (JT) distortion are discussed. Different types magnetic anisotropy and their importance in magnetic properties including exchange bias are discussed. A discussion on impedance spectroscopy and ac conduction mechanism are included in this chapter. Review of past work on $NiCr_2O_4$ and $NiFe_2O_4$ compounds highlighting their structural, magnetic and dielectric properties are reviewed. The main motivation of the present thesis work is given briefly at the end of this chapter.

Chapter 2 is dedicated to details of different experimental techniques used in sample preparation, their characterization and relevant physical measurements. Details of sol-gel and hydrothermal synthesis methods are given along with various equipment used for this. The working principles of various sophisticated instruments such as X – ray diffractometer (XRD), Field emission scanning electron microscope (FESEM), energy dispersive X – ray (EDX) spectrometer, Raman spectrometer, X – ray photoelectron spectrometer (XPS), Vibrating – sample magnetometer (VSM), Quantum Design Physical Property Measurement System (PPMS) and LCR meter are presented in brief along with the details of operational parameters.

Chapter 3 contains the measurement, analysis and discussion of structural and magnetic properties of Mg substituted $NiCr_2O_4$ bulk as well as one nanoparticles sample. Bulk $Ni_{1-x}Mg_xCr_2O_4$(x = 0 - 0.50) samples were synthesized by sol-gel method. The phase purity and crystal structure analysis were carried out by Rietveld refinement of XRD data by using the space group $I4_1/amd$ (tetragonal) for x = 0 and $Fd\bar{3}m$ (cubic) for Mg substituted samples. The structural transformation confirms that some of the JT active Ni^{2+} ions are replaced by Mg^{2+} ions and drives the system into a higher symmetric cubic structure at room temperature. The lattice parameters for the parent compound are found to be $a = b$ = 5.8299 Å, c = 8.4363 Å and they are comparable to earlier reports. The lattice parameters are found to increase with Mg substitution due to the replacement of smaller Ni^{2+} (0.55 Å) ions by Mg^{2+} (0.57 Å) ions. FESEM micrographs of the samples show bipyramidal shape particles with average particle size in the range of 145 to 220 nm. Magnetization measurements in $NiCr_2O_4$ reveals FIM transition at T_C = 70 K followed by a low temperature AFM ordering at T_N = 29 K. With Mg substitution a crossover from FIM to cluster glass like phase for the intermediate doping concentrations x = 0.10, 0.20 & 0.30 and to antiferromagnetic dominant phase for x = 0.40 & 0.50 samples have been observed. The frustration index ($f = \theta/T_C$) and spin disorder are found to be enhanced with Mg substitution. Relaxation of isothermal remanent magnetization (IRM) performed at T = 25 K shows slow and long lasting magnetization decay for these glassy magnetic systems. The relaxation data were analyzed by fitting to the stretched exponential function $M(t) = M_0 + M_{sg}\exp(-(t/\tau)^{1-n})$. Study of EB behavior at T = 5 K shows an increase in H_{EB} from 91 Oe for x = 0 to 747 Oe for x = 0.10 samples. The origin of EB behavior and the enhancement in H_{EB} upon Mg substitution is explained by considering the sublattice model proposed by Tomiyasu and Kagomiya. In addition, we have carried out a detailed analysis of temperature, cooling field and maximum measuring field dependence of H_{EB} in the present system. The training effect of H_{EB} is found to follow typical power-law behavior.

In an attempt to understand the interplay between geometric spin frustration (GMF) and particle size in our present Mg substituted system, we have carried out an in-depth investigation on static and dynamic magnetic properties of 15 atm % Mg substituted $Ni_{0.85}Mg_{0.15}Cr_2O_4$ nanoparticles. Estimated bond angles of the super-exchange networks from Rietveld refinement of XRD data at room temperature indicate the possibilities of collinear spin structure in the system. FESEM and FETEM micrographs reveal strongly agglomerated

nanoparticles with an average particle size of 46 nm. From temperature dependence of magnetization, we have observed a broad ferrimagnetic transition around 76 K followed by a sharp cluster glass like transition around 10 K. The occurrence of cluster glass phase is attributed to the interaction between disordered surface spin and ordered FIM core structure. In contrast to the canted magnetic structure of bulk nickel chromite system, our nanosystem shows tendency towards collinear ferrimagnetism with weak frustration. The reduction in frustration can be attributed to the domination of Ni-O-Cr superexchange interaction over Cr-O-Cr superexchange and Cr-Cr direct exchange interaction. Field dependent $M - T$ measurement, relaxation of thermoremanent magnetization and memory effect support the metastability of our cluster glass system. The peculiar variation of temperature dependent coercivity (H_C) has been explained on the basis of spin freezing characteristic of surface spins and their interactions with core ferrimagnetism. We have observed asymmetric response of magnetic relaxation with respect to change in temperature below the glassy transition temperature. Below T_f, wait-time dependent ageing phenomena is observed.

Chapter 4 contains the study of magnetic and electrical properties of $NiCr_2O_4$ by Mn and Cd substitution at Ni site. Polycrystalline samples of $Ni_{1-x}Mn_xCr_2O_4$ (x = 0.0 – 0.50) were synthesized by using sol-gel method. Room temperature powder X – ray diffraction patterns and Rietveld refinement reveal single phase form with tetragonal ($I4_1/amd$) structure for x = 0 and cubic structure ($Fd\bar{3}m$) in Mn doped samples. Magnetization measurements show ferrimagnetic to paramagnetic (FIM - PM) transition with a decrease in transition temperature (T_C) from T_C = 72 K for x = 0 to T_C = 38 K for x = 0.50 upon Mn substitution. The AFM ordering of $NiCr_2O_4$ at 29 K is found to be suppressed with increase in Mn concentration. The weakening of super-exchange interaction and magnetic frustration is explained on the basis of molecular field theory by fitting of inverse susceptibility data. The M_S value is found to increase from 6.15 emu/g for x = 0 to 10.30 emu/g for x = 0.50 in the series. We have studied the order of magnetic phase transition and magnetocaloric effect by recording a series of isothermal magnetization for x = 0, 0.10 & 0.50 around their respective T_C. The positive slope of Arrott plots (M^2 vs H/M) confirm the second order paramagnetic to ferrimagnetic (PM-FIM) transition in these systems. The value of maximum magnetic entropy changes ($-\Delta S_M^{max}$) for x = 0 is found to be 1.5 ± 0.1 $JKg^{-1}K^{-1}$ at its T_C for an applied field of 9 T and is comparable to the previous report on $NiCr_2O_4$. With Mn substitution, this value increases to 2.9 ± 0.2 JKg^{-}

$^{1}K^{-1}$ for x = 0.50. The relative cooling power (RCP) is found to increase from 26.0 ± 0.2 for x = 0 to 58.2 ± 0.3 for x = 0.50 sample. We have estimated the critical exponents (β, γ & δ) for these samples by using modified Arrott plot analysis and exponents are found to deviate from known theoretical models. The reliability of our calculated critical exponent is further confirmed by the scaling hypothesis. In our present system the observed larger values of β suggested a slower increase in the ordered magnetic moment than mean-field or other classical magnetic systems, which may be due to the significant influence of the canted spin structure in our system. On the other hand, the sharper divergence of initial magnetic susceptibility for x = 0 at T_C as compared to x = 0.50 leads to a smaller value of γ(< 1) for x = 0 sample. Similarly, a smaller value of δ for x = 0 as compared to Mn substituted samples implies a slower saturation due to the presence of competing antiferromagnetic ordering.

We have also studied the Cd substituted $Ni_{1-x}Cd_xCr_2O_4$ (x = 0.0–0.30) samples prepared by the sol-gel method in this Chapter. Rietveld refinement confirms the single phase tetragonal ($I4_1/amd$) for parent (x = 0) and cubic ($Fd\bar{3}m$) crystal structure for Cd substituted samples. The increase in lattice constant with Cd substitution is attributed to the larger ionic size of Cd^{2+} (0.78 Å) as compared to Ni^{2+} (0.55 Å) ion. The results of Rietveld refinements were further utilized in VESTA software to estimate the bond length and bond angles of lattice structures. With Cd substitution, the low temperature AFM transition of the parent compound is found to be completely disappeared and instead we have observed the AFM transition near FIM transition temperature as a result of possible enhancement of canting nature of spin structure. For x = 0.20 & 0.30, we have observed short range cluster glass like phase in the samples. In order to confirm the cluster glass phase, memory effect of ZFC and FC magnetization and relaxation of isothermal remanent magnetization has been investigated for the x = 0.30 sample. Large coercivity is observed for x = 0 & 0.05 samples which can be attributed to the existence of competing long range AFM and FIM interaction. On the other hand, almost linear loop is observed for x = 0.10 – 0.30 samples due to dominant AFM interactions which completely overtakes the FIM interactions. The drastic reduction in M_S from 0.26 μ_B/f. u. for x = 0 to M_S = 0.08 μ_B/f. u. for x = 0.05 with Cd substitution can be attributed to the nonmagnetic nature of Cd and enhancement in canting nature of the spin structure. The estimated values of exchange bias field (H_{EB}) for the Cd substituted samples x = 0.05 & 0.15 are found to be 1653 Oe & 7477

Oe and these values are significantly larger as compared to the parent compound. We have observed both normal and inverse MCE for x = 0.20 sample with a maximum entropy change of $-\Delta S_M = -0.431(3)$ J/kg.K^{-1}. To study the dielectric properties, temperature and frequency dependent dielectric constant (ε') and loss ($tan\ \delta$) have been investigated over a temperature scale from 27 K to 300 K. The increase in dielectric constant with temperature can be attributed to increase in space charge polarization. Complex impedance plane plots (-Z''vs Z': Nyquist plots) have been studied in order to understand the contribution of grains (*G*s) and grain boundaries (*GB*s) in conduction mechanism. An equivalent circuit model comprised of resistance (*R*), capacitance (*C*), constant phase element (*Q*) is proposed to investigate the electrical properties of the materials. The equivalent circuit includes two parallel combinations designated as ($R_{GB}C_{GB}Q_{GB}$)(R_GC_G). The presence of constant phase element in the equivalent circuit represents the deviation of relaxation dynamics from ideal Debye type. The characteristic behavior of ac electrical conductivity (σ_{ac}) with frequency at different temperature is investigated with the help of Jonscher power law (JPL). Our analysis suggests that correlated barrier hopping (CBH) is the predominant conduction mechanism in the present system.

In **Chapter 5** we have discussed the evolution of structural and magnetic properties of $Ni_{1-x}Co_xFe_2O_4$ (x = 0 – 0.50) compounds prepared by the sol-gel technique. The room temperature XRD patterns and typical Rietveld refinement confirm cubic crystal structure with space group $Fd\bar{3}m$ for all the samples. The lattice constant is found to increase from a = 8.3379 Å for x = 0 to a = 8.3584 Å for x = 0.50 compound. Investigation of oxidation state with the help of XPS spectrum suggests that all the three cations possess both 2^+ and 3^+ ionic states in these samples. A sharp rise in thermomagnetic irreversibility below 165 K is attributed to possible metal-insulator transition, which is also known as Verwey transition (T_V) as a result of sharp change in magnetic anisotropy. The value of FIM to PM transition temperature (T_C) is found to decrease from 835 K for x = 0 to 797 K for x = 0.50 compound. An analytical quantum mechanical method was used to estimate the cation distributions in the prepared samples with the help of measured magnetic moment at T = 5 K. The cation distribution analysis revealed the preferential occupation of Co^{2+} and Ni^{2+} ions in octahedral sites and partial occupation in tetrahedral sites, whereas the Fe^{3+} ions have almost equal preference for

both the sublattices. Even though, most of the doped Co ions occupy the octahedral site, considerable distribution of Co^{2+} ions at tetrahedral site is noticed. The drop in T_C with Co substitution can be understood by the weakening of Fe^{3+}-O-Fe^{3+} super-exchange interaction due to the decrease in Fe^{3+} and increase in Co^{2+} ions in the tetrahedral sites. The increase in partial conversion of Fe^{3+} to Fe^{2+} ions in the octahedral sublattices also influence the reduction of T_C in the Co substituted samples. The increase in M_S with Co substitution can be attributed to the higher magnetic moment associated with Co ions as compared to Ni ions. The remnant ratio ($R = M_r/M_s$) at $T = 5$ K is found to increase from 0.2 for $x = 0$ to 0.9 for $x = 0.50$ sample. As Co concentration increases, the Co^{2+} concentration at octahedral sites also increases and it results into large saturation magnetization and magnetic anisotropy in the systems. The obtained value of g from ESR analysis is found to increase with Co^{2+} substitution, indicating the weakening of super-exchange interaction through Fe^{3+} - O - Fe^{3+} networks. The increase in ESR broadening (ΔH_{pp}) with Co substitution reveals the enhancement in magnetocrystalline anisotropy, which is in accordance with magnetization results. The variation in intensity and area of the A_{1g} Raman modes (A_{1g} (1) & A_{1g} (2)) further confirms the cation migration between the octahedral and tetrahedral sites of these compounds with Co substitution.

Chapter 6 is devoted to the overall summary of the important findings in all the series. We have successfully tuned the magnetic properties of nickel chromite and nickel ferrite spinel compound by substituting magnetic and nonmagnetic ions. Exchange bias, frustration, cluster glass and their magnetic dynamics have been studied in both bulk as well as in nanoparticles of Mg substituted nickel chromite system. Entropy, critical behavior, low temperature ac conductivity and impedance spectroscopy have been investigated in Mn and Cd substituted nickel chromite system. Importance of cation distributions and their different ionic states on structural and magnetic properties have been investigated in Co substituted nickel ferrite system. In this chapter, the future scope of the work is also presented.

List of Abbreviations used in this Thesis

FM	Ferromagnetic
AFM	Antiferromagnetic
PM	Paramagnetic
SG	Spin glass
JTD	Jahn-Teller distortion
FIM	Ferrimagnetic
GMF	Geometrical magnetic frustration
RKKY	Ruderman – Kittel – Kasuya – Yosida
DM	Dzyaloshinskii – Moriya
EB	Exchange bias
MCE	Magnetocaloric effect
XRD	X-ray diffraction
FESEM	Field emission scanning electron microscope
FETEM	Field emission transmission electron microscope
EDX	Energy dispersive X-ray
XPS	X – ray photoelectron spectroscopy
VSM	Vibrating sample magnetometer
PPMS	Physical properties measurement system
ESR	Electron spin resonance
BSE	Back-scattered electrons

IRM	Isothermal remanent magnetization
LAS	Law of approach to saturation
CW	Curie –Weiss
G	Grains
GB	Grain boundaries
JPL	Jonscher power law
SPM	Super paramagnetic
ZFC	Zero field cooled
FC	Field cooled
LKDM	Lyons, Kaplan, Dwight and Menyuk

List of Figures

Chapter 1

Chapter 2

Chapter 3

Chapter 4

Chapter 5

List of Tables

Chapter 1

Chapter 3

Chapter 4

Chapter 5

Chapter 1

Introduction

Magnetism in solid material is a vast area under physics that arises from the diverse and complicated inter-atomic interactions that display many exotic phenomena. These materials play a major role in the development of modern civilization from their first application in compass during the Qin dynasty (221-206 BC). Optimization of magnetic properties in these materials towards application in spin-valve and spintronic devices, memory devices, sensors, biotechnology, magnetic refrigeration, medical diagnostics, etc. is the prime goal of researchers at the present time. Depending on the response of the materials against the applied magnetic field, materials are broadly classified as ferromagnetic (FM), antiferromagnetic (AFM), paramagnetic (PM), or nonmagnetic materials. Besides these ordered magnetic states, there are other materials that display peculiar and disordered magnetic phases such as spin glass or spin liquid. [1, 2]. In the past few years, magnetic systems having spin glass (SG) feature has attracted extensive research interest due to their fascinating non-equilibrium spin dynamics and time-dependent phenomena, which are extremely desirable for the deep understanding of complex systems [3-8]. Disorder and frustration are the basic ingredients of a magnetic system that shows SG characteristics.

Chromium-based spinels are an important class of magnetic materials that possess frustrated spin structure and show promising properties such as multiferroic, magnetodielectric and magnetostructural coupling, exchange bias and magnetization reversal, etc. [9-14]. It is interesting to study such frustrated magnetic systems as it is difficult to predict their behavior and can lead to unique state of magnetic phases. Magneto-elastic coupling and spin disorder are the two most important phenomena that can take place in a frustrated magnet. If the frustration is strongly connected to the atomic lattice, magneto-elastic coupling occurs in order to remove the ground state degeneracy [15]. In an attempt to tune the spin frustration and study its effect on various magnetic properties, we have carried out a detailed investigation on

$NiCr_2O_4$ based spinel chromites in both bulk and nanoparticle systems. We have investigated magnetic relaxation, magnetocaloric, critical behaviors, exchange bias, dielectric, and ac conductivity properties to understand the effect of magnetic and nonmagnetic ion substitutions in this spinel chromite system. In addition to the nickel chromite system, a part of my thesis also deals with $NiFe_2O_4$ system. The magnetic structure of the spinel ferrite system is collinear and have a great deal of attraction for decades due to its promising applications in spintronics, magneto-electronics, optoelectronics and biotechnologies etc. [16-19]. Both experimental and theoretical aspects have been investigated in order to explain the effect of magnetic (Mn^{2+}, Co^{2+}) and nonmagnetic (Mg^{2+}, Cd^{2+}) ions substitution on different structural and physical properties in these systems.

1.1 Crystal structure

The general chemical formula for spinel compounds can be expressed as AB_2X_4, where A and B are divalent and trivalent cations respectively (mostly belongs to transition metals) and X is an anion (O, S, Se, Te etc.). Spinel compounds generally crystallize in cubic crystal structure with space group $Fd\bar{3}m$. The atomic positions of A, B and X can be expressed as 8*a* (1/8, 1/8, 1/8), 16*d* (1/2, 1/2, 1/2) and 32*e* (x, x, x) respectively [20, 21]. The cubic crystal structure of spinel compound is shown in Fig. 1.1.

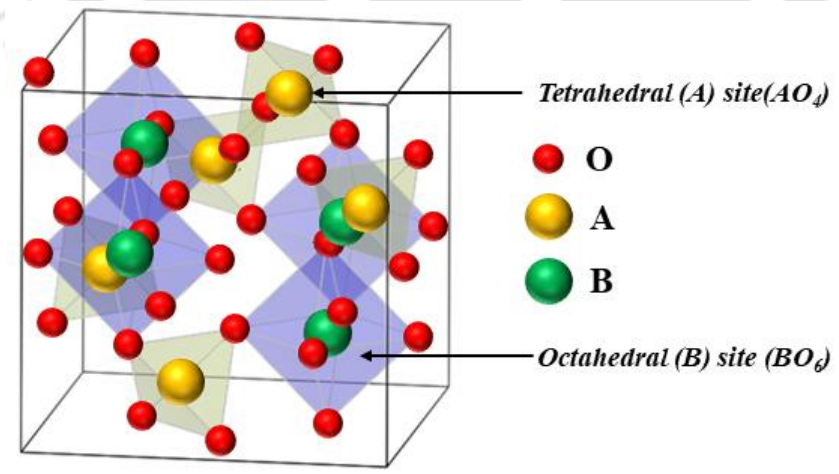

Fig. 1.1: Typical crystal structure of spinel compound.

The ions occupying the tetrahedral and octahedral sites may be magnetic or nonmagnetic in nature. Some of the ions that are generally observed in A site are Zn^{2+}, Cu^{2+},

Co^{2+}, Fe^{2+}, Mn^{2+}, Cd^{2+}, Mg^{2+} etc. and those occupying B sites are Fe^{3+}, Cr^{3+}, Fe^{2+}, Mn^{3+}, V^{3+}, Al^{3+}, Ti^{3+} etc. Depending on the cations distribution on tetrahedral and octahedral sites, spinel compounds are classified as normal, inverse and mixed spinel [22, 23]. If all the 8A cations occupy the tetrahedral sites and all 16 B cations occupy the octahedral sites, then the spinel compound is called normal spinel. $NiCr_2O_4$, $CoCr_2O_4$, and $MnCr_2O_4$ are some examples of normal spinel [22]. On the other hand, if 50 % of the 16 B cations occupy the tetrahedral sites and the other 50% along with all 8A cations occupy the octahedral sites then the resultant structure is called an inverse spinel structure. Some examples of inverse spinel are $NiFe_2O_4$, Fe_3O_4, $MgGa_2O_4$ etc. [23]. In most of the spinels, depending on the synthesis conditions both A and B cations can randomly occupy the tetrahedral or octahedral sites and form mixed spinel [23].

At high temperatures, both $NiCr_2O_4$ and $NiFe_2O_4$ spinels crystallize in cubic crystal structure with space group $Fd\bar{3}m$ [24, 25]. However, in $NiCr_2O_4$, Ni^{2+} ions in the tetrahedral environment undergo splitting of 3*d* orbitals into low lying e_g doublets and higher energy t_{2g} triplets and it is active to Jahn-Teller distortion (JTD) [24]. This distortion in the tetrahedral environment reduces the crystal symmetry from cubic to tetragonal structure at $T = 310$ K [26]. However, such transformation does not occur in $NiFe_2O_4$ as both Ni^{2+} ions in the octahedral and Fe^{3+} ions in the tetrahedral or octahedral environment are inactive to JTD. Some other spinels that exhibit JTD are $CuCr_2O_4$ and $FeCr_2O_4$ [27, 28].

1.2 Crystal field effect

The static electric field produced by the interaction between cations and ligands in a crystal is called a crystal field. The magnetism in the transition elements originated from a partially filled *d* orbital. In general, *d* orbital has five degenerate energy levels and is subdivided into e_g ($d_{x^2-y^2}, d_{z^2}$) and t_{2g} (d_{xy}, d_{yz}, d_{zx}) as shown in Fig. 1.2. The e_g orbitals are aligned along *x*, *y* and *z* axes, but t_{2g} orbitals are oriented in between *x*, *y* and *z* axes. Therefore, when the ligand approaches the *d* orbital in a 3*d* environment, not all parts of the *d* orbital interact directly with the ligand and it results in a non-uniform electrostatic field. Such interaction creates a splitting of *d* orbitals to remove the degeneracy in the energy levels. For example, in an octahedral environment crystal field arises when oxygen with 2*p* orbitals

approaches the *d* orbitals. The 2*p* orbital can be further subdivided into p_x, p_y and p_z oriented along *x*, *y* and *z* directions. Therefore, the e_g orbitals which are also oriented along *x*, *y* and *z* axes will overlap predominantly as compared to those t_{2g} orbitals, that point in between *x*, *y* and *z* axes. As a result, e_g orbitals will experience more electrostatic repulsion as compared to those of t_{2g} orbitals. Consequently, e_g levels lifted up compared to t_{2g} energy levels. However, in a tetrahedral environment, t_{2g} levels are lifted up because of their predominant overlapping with 2*p* orbitals [29]. The splitting of energy levels in the tetrahedral and octahedral environments are shown in Fig. 1.3. The arrangement of electrons in orbitals i.e. high or low spin state depends on competition between crystal field energy of octahedral (Δ_o) or tetrahedral (Δ_t) sublattices and Hund's coupling energy (Δ_H). Therefore, the crystal field directly influences the magnetic moment of a given transition element in the structure. The effective magnetic moment of an ion can be calculated by using the relation $\mu_{eff} = g\sqrt{J(J+1)}\ \mu_B$ (where *J* is the total angular quantum number) [29]. But for most of the transition elements, this theoretical value does not match with the experimental value due to the quenching of orbital magnetic moment. Therefore, the magnetic moment is estimated by using spin only value i.e. $\mu_{eff} = g\sqrt{S(S+1)}\ \mu_B$ (where *S* is the spin quantum number).

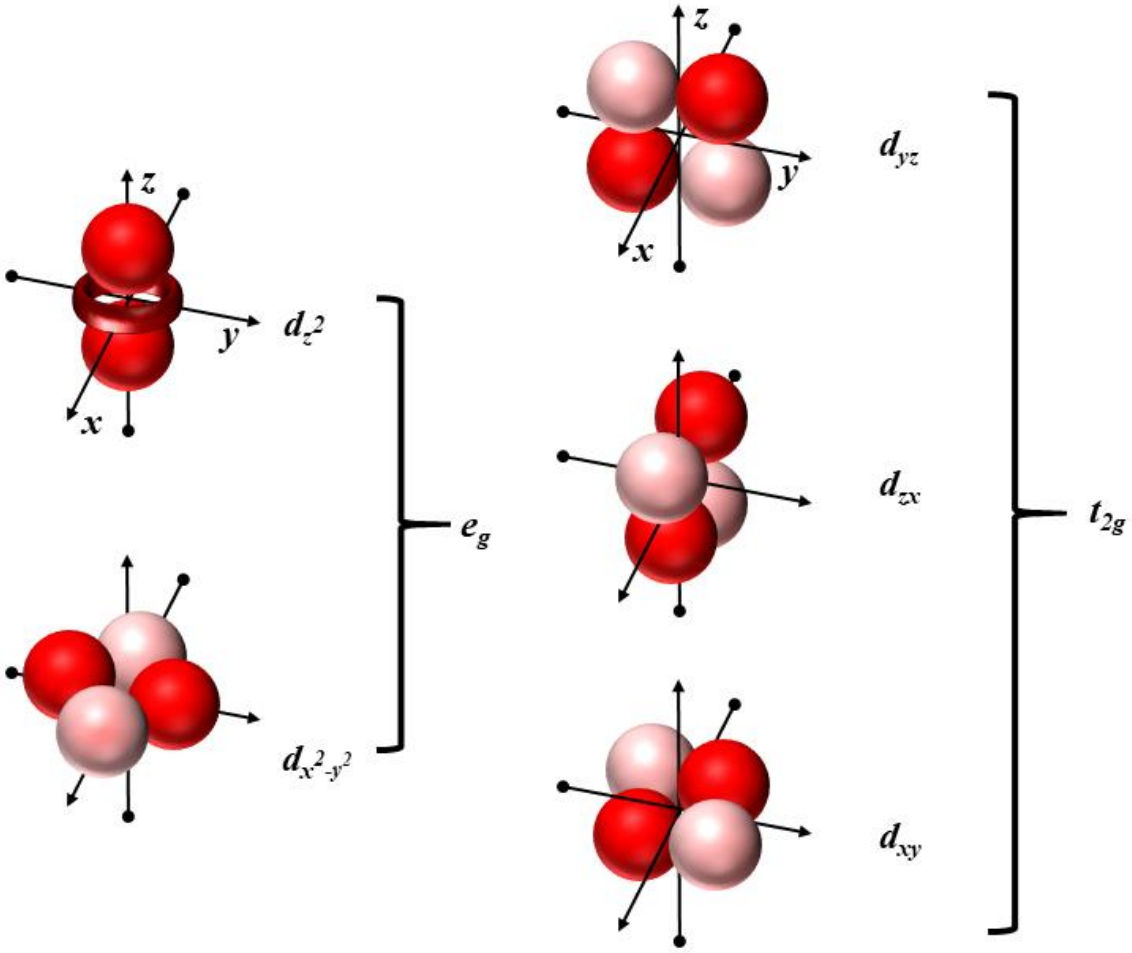

Fig. 1.2: Electronic distribution of 3*d* orbitals.

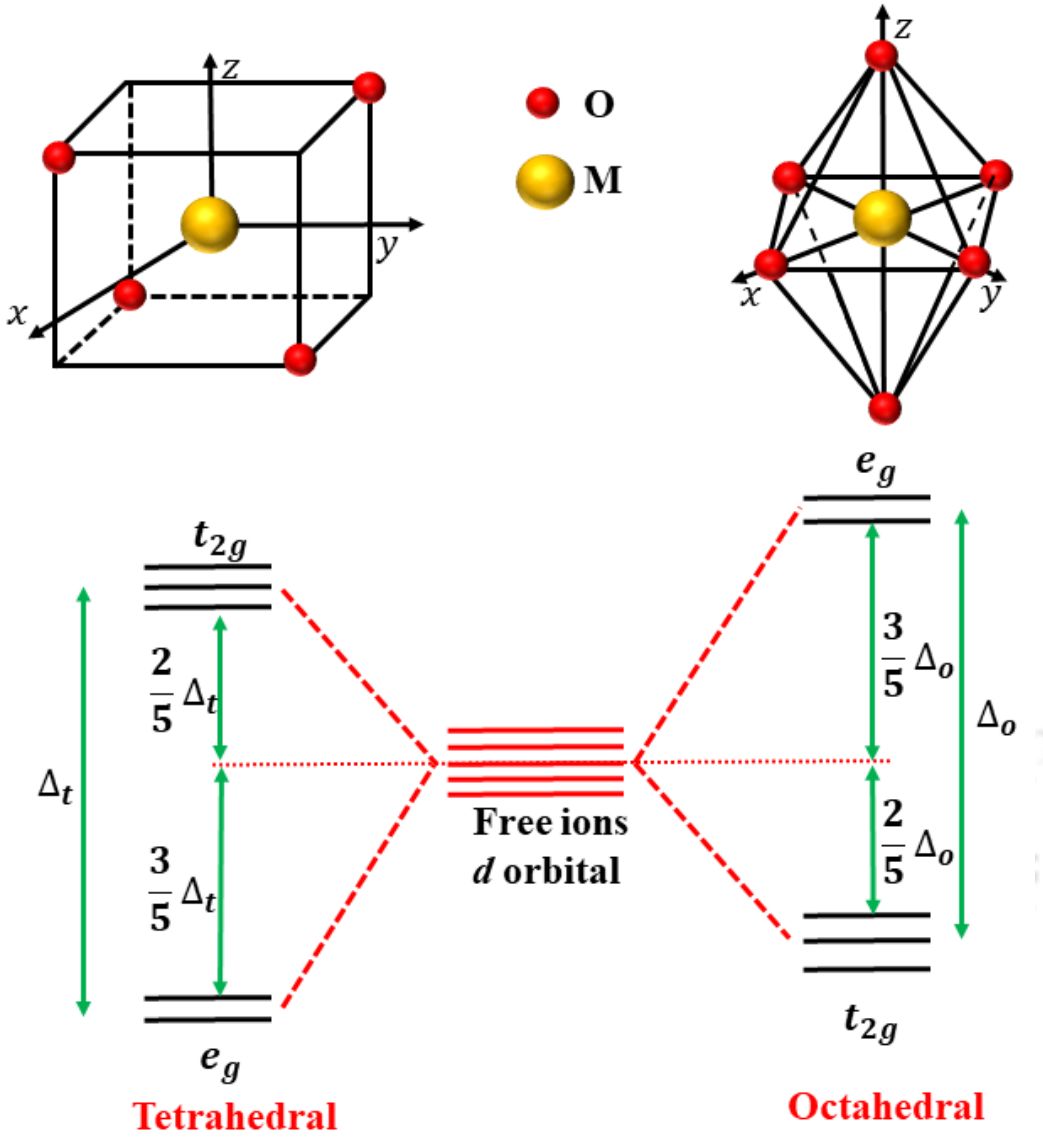

Fig. 1.3: Octahedral and tetrahedral coordination of transition atoms and the energy level diagram in those environments.

1.3 Jahn-Teller distortion (JTD)

In some of the transition elements with a specific ionic state, electrons asymmetrically occupy the degenerate energy levels leading to larger electrostatic energy in the system. In order to reduce the overall energy, the system undergoes a structural distortion (by stretching or compressing) and hence degeneracy of orbitals is lifted up. This distortion is known as Jahn-Teller distortion (JTD) [29]. For example, d^4 configuration in octahedral environments three

electrons occupy the t_{2g} orbitals and fourth electron has the orbital degeneracy in e_g orbitals. In order to remove the degeneracy, the octahedra stretch along Z-axis and this distortion leads to smaller energy of d_{z^2} as compared to $d_{x^2-y^2}$ due to smaller overlapping of d_{z^2} with the adjacent ligand. Therefore, the 4th electron will occupy the d_{z^2} orbitals. However, in some other systems, the energy is reduced by compression of the octahedral. As a result, $d_{x^2-y^2}$ energy level will be lowered and consequently, 4th electron occupies the $d_{x^2-y^2}$ orbital [30]. The schematic diagram of this phenomenon is shown in Fig. 1.4.

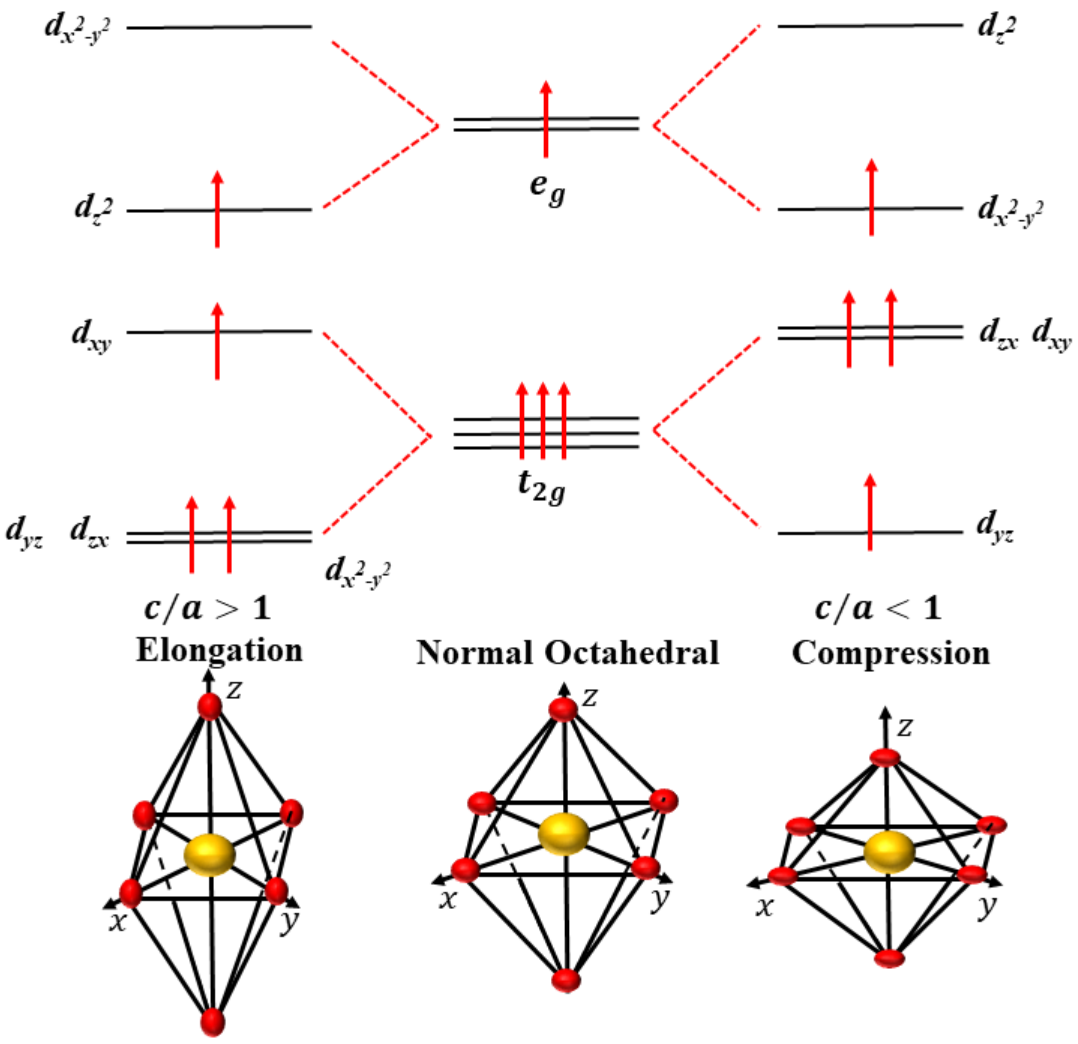

Fig. 1.4: Splitting of t_{2g} and e_g states with d^4 configuration in the octahedral environment due to JTD**.**

In the tetrahedral environment, t_{2g} orbitals lies at higher energy level and JTD distortion is observed for high spin configuration d^3, d^4, d^8, d^9 and low spin configuration d^5, d^6, d^8, d^9. For example, spinel chromites $NiCr_2O_4$, $CuCr_2O_4$ and $FeCr_2O_4$ exhibit JTD and hence cubic to tetragonal crystal structural transition is observed due to the presence of JT active of Ni^{2+}, Cu^{2+} and Fe^{2+} ions in the tetrahedral environment [30-32].

1.4 Magnetic Interactions

The origin of magnetic behavior in magnetic materials generally arises from an intrinsic quantum mechanical property of the electron called spin. It is a perfectly fixed feature of the electron that the magnitude of its intrinsic angular momentum cannot be increased or decreased; all that can be changed is its direction. Solid-state magnetism often exhibits many peculiar and interesting phenomena as a result of diverse and complicated atomic-level interactions. Ferromagnetism (FM), Ferrimagnetism (FIM) and antiferromagnetism (AFM) are the most common form of magnetism in the area of solid state magnetism. In the periodic table, elements belonging to transition metal and rare earth groups mostly influence the area of magnetism due to their unfilled or partially filled *d* or *f* orbital subshell. The leftover un canceled electron spins in their shells give rise to the magnetism in these elements. For example, manganese, cobalt, nickel, gadolinium and dysprosium exhibit ferromagnetism. Interestingly, among all the elements of the periodic table, only chromium forms an antiferromagnetic solid at low temperatures. Details of different types of magnetic materials are discussed later in this chapter.

Magnetic exchange interactions are quantum mechanical effects and they are responsible for FM or AFM interactions between ions in magnetic materials [33]. These interactions are governed by Coulomb interaction and Pauli's exclusion principle and lead to long-range magnetic ordering in a magnetic system. A brief review of different types of exchange interactions that are generally observed in magnetic materials is presented in this section.

Direct exchange interaction: These interactions take place when there is an overlap of electron wave function between two magnetic ions. Since Pauli's exclusion principle keeps electrons with parallel spins away from each other, therefore direct exchange interaction is

generally observed in antiparallel spin configuration. In most of the materials with *d* and *f* orbital magnetic ions, the direct exchange interaction is considered less important due to the insufficient overlapping of the electron wave function.

Super exchange interaction: Super exchange interactions generally take place between two non-neighboring ions through an intermediate anion taking the role of a mediator. According to Kramers' model [34], AFM interaction occurs when cations participating in the exchange interaction have more than half-filled *d* orbital, while cations having less than half-filled *d* orbital leads to FM interaction. However, Slater, Goodenough and Loeb [35, 36] suggest that AFM interaction also occurs among cations having less than half-filled *d* shell.

The superexchange interactions can be understood by taking the example of different types of Mn-O-Mn networks as shown in Fig. 1.5. AFM interaction takes place when core spins of the magnetic cations such as Mn^{2+} ions are antiparallel to each other across the anions O^{2-}. According to Hund's rule, the electrons of Mn^{2+} cations occupy different 3*d* orbitals in order to align parallel to each other. If the spin in the left-most Mn^{2+} ion is in upstate, the neighboring O^{2-} ion share its down spin electron to the left Mn^{2+} ion in order to satisfy the Pauli's exclusion principle. Similarly, the remaining up-spin electron of O^{2-} will be shared to the right side Mn^{2+} ion and for that its electrons should be in down-spin state. This process leads to a AFM interaction between two Mn^{2+} ions via O^{2-} ions as shown in Fig. 1.5 (a).

As shown in Fig. 1.5 (b), FM interaction can take place in Mn^{3+}-O-Mn^{3+} network, if the cation-anion-cation interactions are asymmetric in nature, i.e. covalent bond at one side and ionic at another side. Here, the up spin electron of O^{2-} ion points towards the up spin electron of Mn^{3+} cation (left side) and forms a covalent bond. However, the down spin electron of O^{2-} ion points away from the right-hand side Mn^{3+} cation and hence forms an ionic bond. This results in an overall FM interaction in the network.

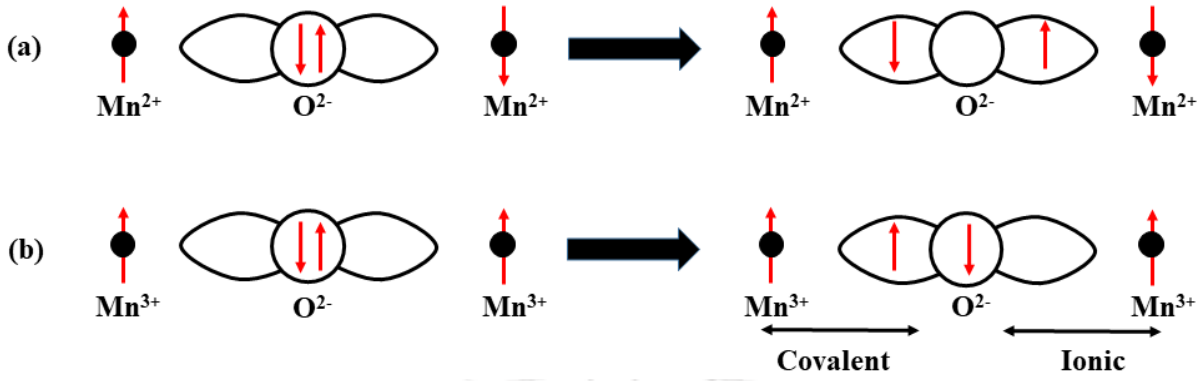

Fig. 1.5: Schematic diagram of (a) AFM and (b) FM superexchange interactions.

In spinel compounds, cations in the tetrahedral (A) sites couple to the cations in the octahedral (B) site via oxygen anion and it is the strongest superexchange interaction in the compound. However, superexchange interaction through A-O-A (J_{AA}) and B-O-B (J_{BB}) networks are also possible but their strength is relatively weak as compared to A-O-B (J_{AB}). In spinel chromite compounds $J_{AB} > J_{BB} > J_{AA}$.

Double exchange interaction: These types of interactions are generally observed in magnetic materials, where the magnetic ions can exist in more than one oxidation state. Similar to superexchange interaction, double exchange interaction is also an indirect exchange interaction. However, here transfer of electrons takes place from one magnetic ion to another magnetic ion via a non-magnetic ion. Fig. 1.6 shows the schematic representation of electron transfer between Mn^{3+} and Mn^{4+} through O^{2-}. Here, O^{2-} gives up its spin-up electron to Mn^{4+} followed by the transfer of a spin-up electron from Mn^{3+} to O^{2-}. This process changes Mn^{4+} to Mn^{3+} ion and at the same time Mn^{3+} to Mn^{4+} ion. According to Zener, in order to satisfy Hund's coupling, the transfer of electrons between these ions can only take place when their respective core electron spins are parallel to each other [37, 38]. Therefore, double exchange interaction always gives rise to ferromagnetism in the system.

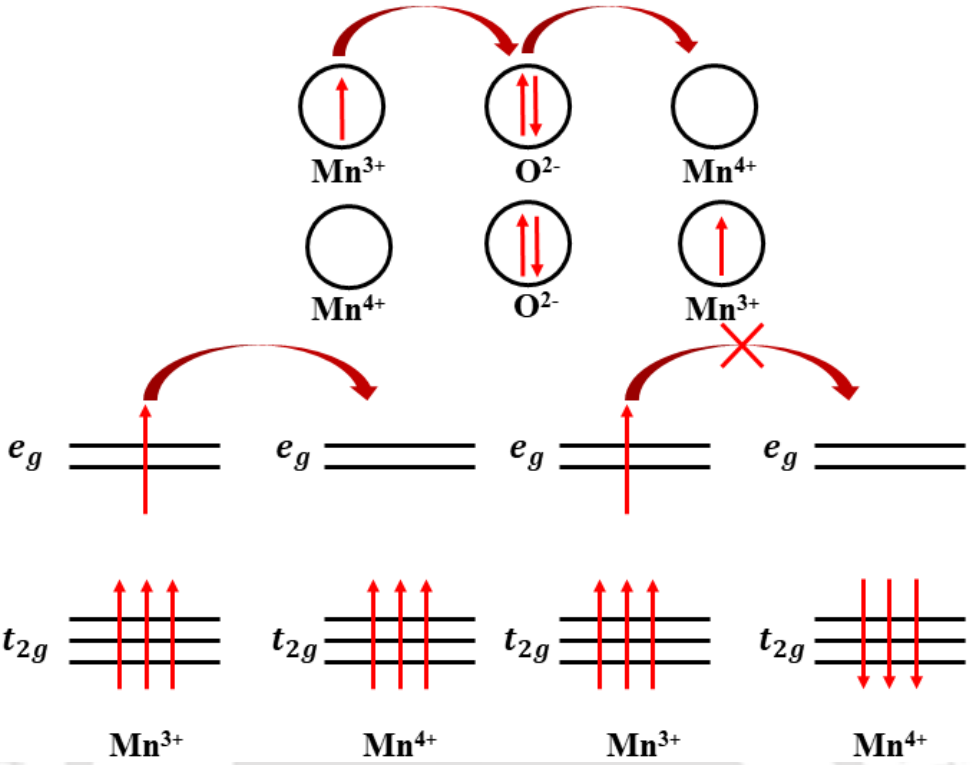

Fig. 1.6: Schematic representation of double exchange interaction between two Mn ions through oxygen ions.

Ruderman–Kittel–Kasuya–Yosida (RKKY) interaction: RKKY interaction takes place in metal with a localized magnetic moment. The exchange interaction between the magnetic ions is mediated by the conduction electron [39]. Depending on the distance between the ions the interaction may be FM or AFM. In this interaction process first, a localized magnetic moment of an ion spin polarizes the mobile electrons and later this polarization couples to the neighboring localized magnetic moment. The strength of RKKY interaction between two magnetic ions is proportional to $\frac{\cos(2k_F r)}{r^3}$, where k_F is the radius of the spherical Fermi surface and r is the distance between the ions [29].

Dzyaloshinskii Moriya (DM) interaction: DM interaction (also known as anisotropic exchange interaction) was originally proposed by Igor Dzyaloshinskii (in 1958) [40] and Toru Moriya (in 1960) [41]. This magnetic exchange interaction leads to canting of the magnetic moment of anti-parallel spin toward each other and hence gives rise to a net magnetic moment. DM interaction is mostly used to explain the magnetic skyrmions phenomena and

magnetoelectric effect in multiferroics materials. The exchange energy in such canted configuration can be written as,

$$H_{DM} = \vec{D}.\left(\overrightarrow{S_1} \times \overrightarrow{S_2}\right) \tag{1.1}$$

where $\overrightarrow{S_1}$ and $\overrightarrow{S_2}$ are the spin of two interacting magnetic ions and $\vec{D}$ represent the DM vector. $\vec{D} = 0$, for an inversion symmetry with respect to the center connecting the two magnetic ions. Generally, this interaction tries to align the two spin at a right angle to each other in a plane perpendicular to $\vec{D}$. DM interaction is mostly observed in AFM materials and gives rise to a small FM component in a direction orthogonal to the spin axis of the antiferromagnet. AFM materials such as Cr_2O_3, $MnCO_3$, $CoCO_3$ etc. exhibit DM interaction [29, 42].

1.5 Magnetic ordering

Both in the classical or quantum world, the energy Hamiltonian is the starting point to understand the underlying physics in a system. The classical Heisenberg Hamiltonian for a solid magnetic system placed in a uniform external filed h, considering only the nearest neighbor interaction can be expressed as [43],

$$H = -J\sum_{\langle xy\rangle} m_x \cdot m_y - h\cdot\sum_{x} m_x \tag{1.2}$$

where x and y indicate the sites in the crystal lattice and $\langle xy\rangle$ represents the nearest neighbor interactions only, m_x and m_y denotes the magnetic moment associated with the spin. The parameter J is associated with spin coupling and its magnitude varies from solid to solid. The second term in the above expression is known as Zeeman energy and it represent the coupling of magnetic moment to an external magnetic field. The transition temperature and nature of interaction depends on the magnitude and sign of J respectively. The larger is the J, the higher T_C or T_N. Considering at a zero external field (h = 0), if J is positive (J > 0) the ground state spin configuration will be parallel to each other and the Hamiltonian describes FM interaction (Fig. 1.7 a). For AFM interaction J is negative (J < 0) and spins are antiparallel to each other (Fig. 1.7 b). In the paramagnetic phase, every spin at any time is equally like to point in any direction due to their thermal fluctuation. Therefore, the paramagnetic phase is “rotationally

invariant". But both for FM and AFM phases, all the spins align along a preferred direction (parallel or antiparallel) therefore rotational symmetry of spin configuration is broken. Similar to FM and AFM, the spin rotation symmetry is also broken for spin glass. The major difference between spin glass and any other ordered magnetic state is that there is no distinct spatial order for spin glass but they are ordered in time (Fig 1.7 c). That is the disorder is quenched or frozen.

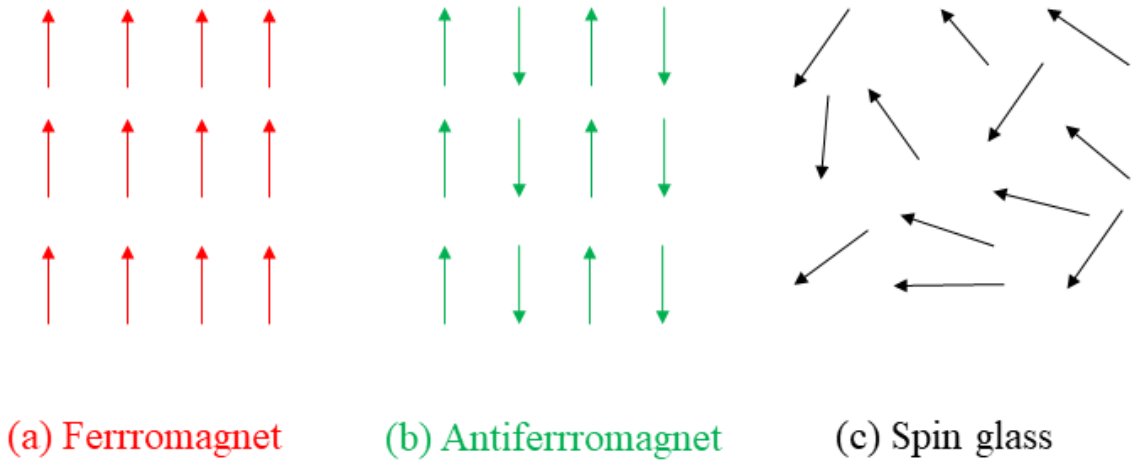

Fig 1.7: Sketches of the ground states spin configuration for (a) ferromagnetic (b) antiferromagnetic and (c) spin glass.

1.5.1 Paramagnetic materials

In PM materials, the time average of magnetic moment associated with the individual spin is zero due to its random orientation in space with time. As a result, the overall magnetization of the material is also zero in the absence of an external field. However, in an external magnetic field, the spins tend to align themselves in the direction of the field and give rise to a small magnetic moment. The degree of spin alignment is proportional to the applied field strength (H) and inversely proportional to temperature (T). According to the classical approach of Langevin's theory, susceptibility (χ) in the PM can be expressed as [29],

$$\chi = \frac{N\mu_0\mu^2}{3k_BT} \tag{1.3}$$

where N is the number of magnetic ions per unit volume with the moment μ. μ_0 is the permeability of free space and k_B is the Boltzmann constant. By considering quantum mechanical analogy, the above expression can also be written as,

$$\chi = \frac{N\mu_0 g^2 \mu_B^2 J(J+1)}{3k_B T} \tag{1.4}$$

where g is the Landé g factor and can be expressed as

$$g = 1 + \frac{J(J+1) + S(S+1) - L(L+1)}{2J(J+1)}$$

Salts of transition elements, salts and oxides of the rare earths, oxygen, aluminum etc. are some examples of paramagnetic substances.

1.5.2 Diamagnetic materials

Similar to PM materials, diamagnetic materials also do not possess any permanent magnetic moment. However, in an external magnetic field, a magnetic moment is induced in the direction opposite to the applied magnetic field. Therefore, these materials exhibit negative susceptibility. Monoatomic rare gas (He, Ne, Ar, etc.), polyatomic gas such as H_2, N_2 and ionic solid like NaCl with closed-shell electrons are some examples of diamagnetic materials.

1.5.3 Ferromagnetic materials

Magnetic materials that exhibit spontaneous magnetization even in the absence of an external magnetic are known as FM materials. Due to the presence of a strong exchange force, the unpaired electron spins try to align themselves in a specific direction and give rise to a net magnetic moment. However, such spontaneous magnetization is restricted to a small region known as the magnetic domain. In polycrystalline materials, due to the random orientation of these magnetic domains the net magnetization is zero in the absence of an external magnetic field. When a FM material is placed in an external magnetic field, all the magnetic domains try to align themselves along the direction of the field and results in large magnetization in the sample. Even after the removal of the external magnetic field, this alignment still tends to survive and gives rise to a magnetic hysteresis loop.

In magnetic materials, ferromagnetism is generally observed below a transition temperature known as Curie temperature (T_C). Above which materials act like a typical paramagnetic behavior and can be described by Curie – Weiss law [44]

$$\chi = \frac{C}{T - T_C} \tag{1.5}$$

Where, C and T_C are Curie constant and Curie temperature, respectively and can be expressed as

$$C = \frac{\mu_0 N g^2 \mu_B^2 J(J+1)}{3k_B} = \frac{\mu_0 N \mu^2}{3k_B}$$

Co, Mn, Ni, Fe, etc. are some common examples of ferromagnetic elements.

1.5.4 Antiferromagnetic materials

In AFM materials, the magnetic moments of ions are antiparallel to each other such that overall magnetization is zero. Similar to FM materials, AFM material also shows its antiferromagnetic nature below a certain temperature known as Neel temperature (T_N) and above which it behaves like a PM material. The behavior of magnetic susceptibility in the PM region can be expressed as [44],

$$\chi = \frac{C}{T + T_N} \tag{1.6}$$

Cr, NiO, CoO etc. are some examples of AFM materials.

1.5.5 Ferrimagnetic materials

FIM materials are the special type of antiferromagnet, where magnetic moments are also antiparallel to each other but the overall magnetization is nonzero due to their different magnitude. For a FIM material with two sublattices A and B, the net magnetic moment can be expressed as $M = M_A - M_B$. Here, M_A and M_B are the sublattice moment associated with A and B sublattices respectively. As the crystallographic environment of A and B sublattices are different from each other, therefore their respective molecular field and interactions are also different. According to the molecular field theory of FIM for $T > T_C$, the nature of inverse susceptibility is hyperbolic and can be characterized by the following expression [45, 46],

$$\chi^{-1} = \left(\frac{(T - \Theta)}{C}\right) - \left(\frac{\xi}{(T - \Theta')}\right) \tag{1.7}$$

Here, the first term is the hyperbolic asymptote in the high-temperature region and has a Curie-Weiss form and the second term stands for hyperbolic behavior near the FIM transition temperature. Here the parameter Θ is known as the asymptotic Curie temperature and it represents the strength of AFM exchange interaction between A and B sublattices. The parameter ξ, in the hyperbolic term represents the curvature in the inverse susceptibility plot and the characteristic temperature Θ' is close to T_C. All spinel chromites (ACr_2O_4) and spinel ferrites (AFe_2O_4) with magnetic A ion fall into this type of magnetism.

1.5.6 Magnetic Frustration, spin glass, spin liquid and spin ice

The first experimental evidence of SG behavior was found in the diluted magnetic alloy. These are the materials in which a very small percentage of a magnetic element (e.g. iron, manganese) is substituted at random locations inside a nonmagnetic metallic host such as copper, silver or gold. These materials also displayed unusual electrical conduction behavior. In general, resistivity of a metallic substance decreases with temperature and flattens as the temperature approaches absolute zero. However, in diluted metallic alloys, a sudden rise in resistivity is observed just above absolute zero temperature. This phenomenon (also known as *Kondo effect*) was explained by Japanese physicist Jun Kondo in 1964 [47]. In 1971 Cannella, Mydosh and Budnick observed a cusp in the susceptibility of gold–iron alloys and was the first and central experimental evidence of the SG system [48]. In the last decades, several experimental protocols have been carried out on SG which reveals several interesting properties. Most importantly, in the SG state spins are frozen and disordered. Unlike in the paramagnetic phase, where spins are randomly flips with time, here the spins are stuck in different orientations (quenched disorder) below the freezing temperature (T_f). The absence of long-range magnetic order and spin freezing features separated SG systems from all ordered magnetic systems such as FM, FIM or AFM.

Out of equilibrium and dynamic magnetic properties are the interesting features of SG system, which provides mathematical tools to analyze interesting and complicated real-world problems. For example, SG model can be used to understand neural networks and protein folding [4, 5], to design algorithms for image restoration and machine learning [6, 7]. In general, a system can be considered as non-equilibrium when its properties are changing with time or depends on how the system is been prepared i.e. a clear dependence of its history. There

are multiple ways to observe the dynamic properties of SG system. One approach is to study the decay of remanence magnetization with time, which is also known as relaxation of thermoremanent magnetization (TRM). Several models have been proposed to explain the magnetization relaxation with time. Some of them are logarithmic time decay ($\propto \ln t$) and stretched exponential function ($e^{-t^n}, with\ 0 < n < 1$) [49, 50]. The slow and long-lasting decay of TRM indicates that the process is governed by multiple relaxation timescales. Memory effects are another inherent characteristic of SG system and can be studied by performing different types of aging experiments. For example, a SG system is cooled to a temperature that is below T_f in zero magnetic field and after waiting for a certain time t_w an external magnetic field is applied. The rate of evolution of magnetization shows an inflection point at a time roughly equal to t_w, which indicates that SG remembers the waiting time. Memory effects can also be studied in temperature scale under zero field cooled (ZFC) and field cooled (FC) protocols and will be discussed in detail in Chapter 3.

In a magnetic system, frustration occurs when all spin-spin couplings are not satisfied simultaneously and hence leads to quasi-degenerate ground states. For example, in an Ising (spins either up or down) magnetic system with four spins at the corner of a square with three of the coupling ferromagnetic and one antiferromagnetic, the occurrence of magnetic frustration is shown in Fig. 1.8.

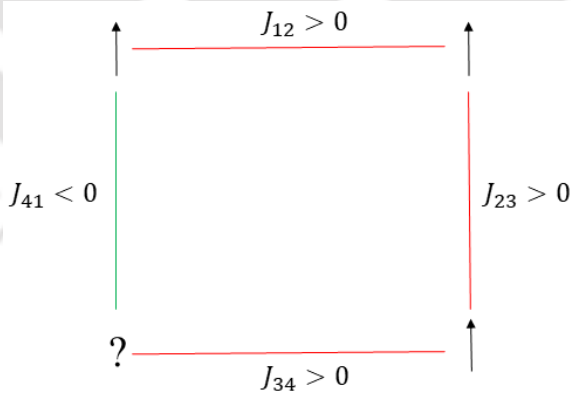

Fig. 1.8: Occurrence of magnetic frustration in a square network with three of the couplings ferromagnetic ($J_{xy} > 0$) and one antiferromagnetic ($J_{xy} < 0$).

From the above figure, it is clear that we are now running out of options in order to satisfy all the constraints (couplings). Such conflict is called magnetic frustration. In general, if we take

any closed cycle with N number of couplings, such conflict will occur if the product of the couplings is negative

$$\prod_{N} J_{xy}J_{yz} \ldots . J_{zx} < 0 \rightarrow \text{frustration} \tag{1.8}$$

where J are exchange integrals. J is positive for FM interaction and negative for AFM interaction. The occurrence of such frustration due to the geometry of the system is called geometrical magnetic frustration (GMF). For example, strong GMF is observed in spinel chromite due to the formation of corner-sharing tetrahedra by B site Cr^{3+} ions as shown in Fig. 1.9.

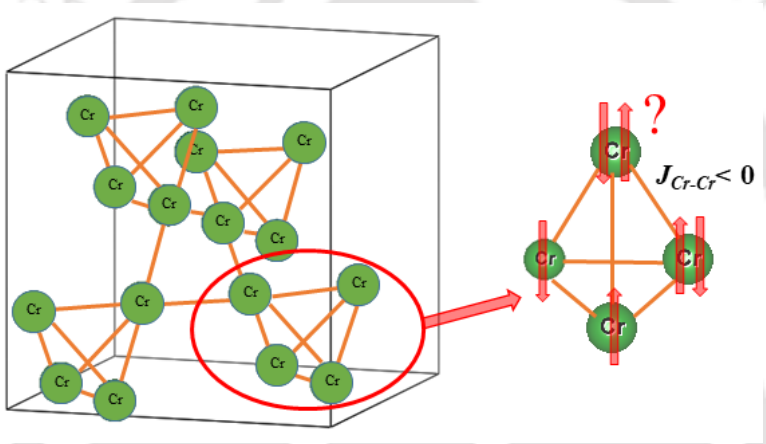

Fig. 1.9: Strong GMF in the corner sharing tetrahedra of a spinel chromite formed by antiferromagnetically coupled Cr^{3+} ions.

According to Lyons, Kaplan, Dwight and Menyuk (LKDM) theory [51], the strength of GMF can be estimated from the parameter,

$$u = \frac{4J_{BB}S_B}{J_{AB}S_A} \tag{1.9}$$

where J_{BB} and J_{AB} are nearest neighbor AFM superexchange interaction integral along B-O-B & A-O-B pathway, S_A and S_B are the magnitudes of moments at the A & B sublattices. Therefore, spinel chromite with nonmagnetic ions (Mg, Zn, Cd & Hg) at A sites shows strong GMF due to the small value of J_{AB} and S_A.

Spin liquid is another example of frustrated magnetic system in which spins are correlated but fluctuate strongly. These fluctuations are so strong that it prevents the ordering of the system even at absolute zero temperature $T = 0$ K. In addition to the lack of order, if the spins are highly entangled then the state is known as quantum spin liquid (QSL) state. Fractional, non-local, quasiparticle excitations as well as emerging gauge fields are some characteristic of QSL state. Since these states never order, they have no broken symmetries. The progress on QSL physics has been largely theoretical, but there is currently a great experimental search for these states. There are some QSL candidates, but none have been proven to be QSLs. Since QSLs have few experimental signatures, their identification is difficult.

Spin ices are materials that consist of regular corner-linked tetrahedra of magnetic ions, each of which has a non-zero magnetic moment, often abridged to spin, which must satisfy in their low-energy state a two-in, two-out rule on each tetrahedron. It is the very strong local magnetic anisotropy from the crystal field forcing the magnetic moments to point either in or out of a tetrahedron that renders ferromagnetic interactions frustrated in spin ices. Most importantly, it is the long-range magnetostatic dipole–dipole interaction, and not the nearest-neighbor exchange, that causes the frustration and the consequential two-in, two-out rule that leads to the spin ice phenomenology. The corresponding magnetization field has zero divergence. There is therefore no sink or source of the magnetization inside the tetrahedron, or no monopole. If a thermal fluctuation caused one of the bottom two magnetic moments to flip from "in" to "out", one would then have a 1 in, 3 out configuration; hence an outflow of magnetization, hence a positive divergence, that one could assign to a positively charged monopole of charge +Q. Flipping the two bottom magnetic moments would give a 0 in, 4 out configuration, the maximum possible "outflow" (i.e. divergence) of magnetization and, therefore, an associated monopole of charge +2Q.

1.6 Magnetic anisotropy

Magnetic anisotropy represents the variation in magnetic properties depending on the direction of the applied magnetic field. Magnetic anisotropy affects most of the magnetic parameters of material including coercivity (H_C), saturation magnetization (M_S), remanent

magnetization (M_R) etc. It may be intrinsic due to material crystal structure or extrinsic due to the choice of materials synthesis method or macroscopic dimension etc. Some commonly known magnetic anisotropies are explained below.

Magnetocrystalline anisotropy: It is an intrinsic anisotropy and represents the tendency of magnetization to orient along a preferred crystallographic direction. The preferred direction is also known as easy axis along which magnetization align easily or it takes less energy to magnetize the material. The other crystallographic directions are known as hard axis, where it takes more energy to magnetize the sample. Magnetocrystalline anisotropy mostly originated from the weak spin-orbital coupling of electrons. When an external magnetic field is applied, electron spin and orbital moment trends to align along the field direction but due to the strong orbital lattice coupling, the orbital moment resists the spin axis rotations. Even though the spin-spin coupling is strong in a magnetic material, it is independent of crystallographic orientation and does not contribute to the magnetocrystalline energy. The energy required to rotate the spin from its easy axis is known as anisotropic energy and can be expressed in terms of series expansion [33],

$$E = K_0 + K_1(\alpha_1^2\alpha_2^2 + \alpha_2^2\alpha_3^2 + \alpha_3^2\alpha_1^2) + K_2(\alpha_1^2\alpha_2^2\alpha_3^2) + \cdots \quad (1.10)$$

Here, K_0, K_1 and K_2 are constants for a particular crystal structure, and α_1, α_2 and α_3 are the direction cosines of the magnetization with respect to crystallographic axes *a*, *b* and *c*. The influence of K_0 is negligible as it is orientation-independent. For $K_2 = 0$, the direction of the easy axis can be estimated from the sign of K_1. If K_1 is positive, then $E_{100}<E_{110}<E_{111}$ and <100> is an easy axis. On the other hand, for negative K_1, $E_{111}<E_{110}<E_{100}$ with <111> as the easy axis. If $K_2 \neq 0$, then the easy axis is determined by both K_1 and K_2 [33].

Shape anisotropy: Shape anisotropy generally takes a predominant role in polycrystalline materials. For a spherical sample, the strength of the magnetic field required to saturate the sample in all directions is equal. However, if the sample is not perfectly spherical the required strength of the magnetic field will vary with the orientation of the sample in the magnetic field. This shape-dependent magnetization phenomenon is known as shape anisotropy. Shape

anisotropy is defined in terms of the demagnetization field. The demagnetization field H_d can be expressed as [52],

$$H_d = -N_d\vec{M} \tag{1.11}$$

where N_d is demagnetization factor and depends on shape of the sample.

Stress anisotropy: The change in domain structure due to the effect of stress can leads to one or more easy axis of magnetization in a magnetic material. The stress anisotropy energy can be written as [33],

$$E_\sigma = K_\sigma sin^2\theta \tag{1.12}$$

K_σ and θ represent the stress anisotropy constant and the angle between the axis in which the stress is applied and the magnetization.

Exchange anisotropy: Exchange anisotropy is generally observed at the interface between two different magnetic ordering. Exchange anisotropy can lead to exchange bias (EB) behavior in magnetic materials. Details of the EB phenomena is discussed in the next section.

1.7 Exchange bias

Exchange bias represents the shift in hysteresis loop as a result of anisotropic exchange interaction at the interface between FM-AFM, FIM-AFM or FM/FIM-SG phase. This effect was discovered by Meiklejon and Bean in 1956 [53]. They have observed a shift in hysteresis loop in cobaltous oxide coated Cobalt nanoparticles (20 nm) at 77 K after field cooling the sample through T_N. The shift in hysteresis loop along field (H_{EB}) and magnetization (M_{EB}) axis are expressed as,

$$H_{EB} = \frac{H_+ + H_-}{2} \tag{1.13}$$

and

$$M_{EB} = \frac{M_+ + M_-}{2} \tag{1.14}$$

where H_+ and H_- are field values where magnetization goes to zero. Similarly, $M_+$and M_- are the values of magnetization at zero magnetic field. A typical hysteresis loop with exchange bias behavior is shown in Fig. 1.10

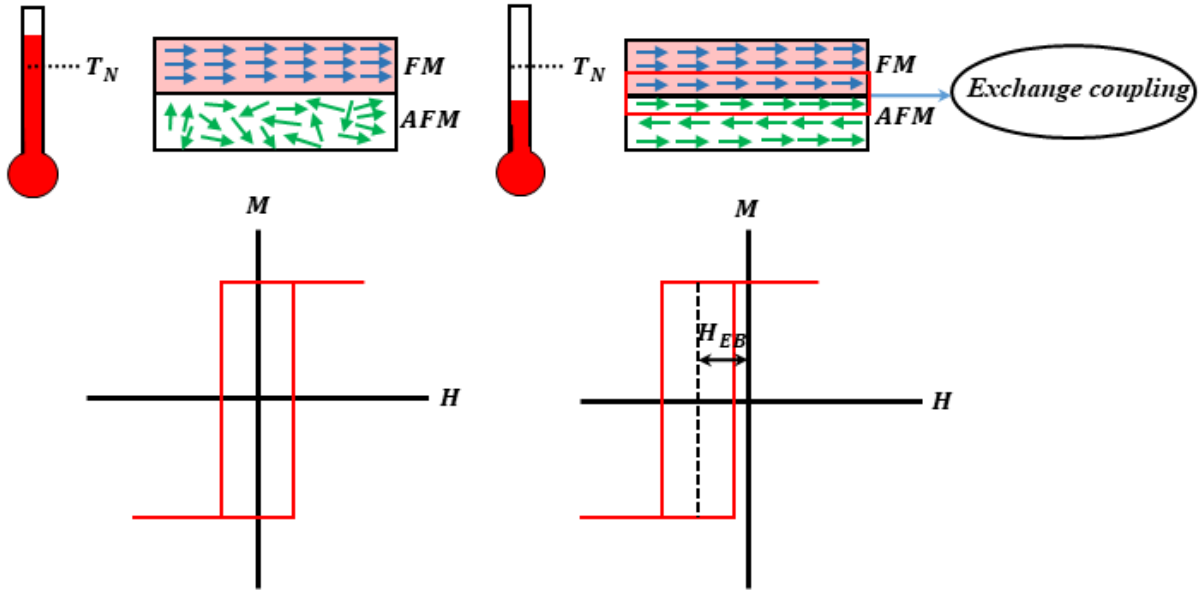

Fig. 1.10: Schematic representation of exchange bias with FM-AFM coupling.

When a sample consisting of both FM and AFM phases is cooled in a magnetic field down to $T_N < T < T_C$, the FM spins will align along field direction but the spins in the AFM part will remain in random orientation due to their PM behavior. When the sample cooled to $T < T_N$, the FM spins couple to AFM spins at the interface and as a result, the first layer of AFM spins aligns along the direction of FM spins in the first quadrant of hysteresis loop. However, the rest of the AFM spins deep inside follows the AFM behavior. In the second quadrant, when the field is revered the FM spins try to align themselves in the field direction but due to the sufficiently large AFM anisotropy, the AFM spins do not change their direction. As a result, these AFM spins exert a strong torque in the FM spins at the interface and force the FM spins to stay in their previous direction. Therefore, a larger negative magnetic field is required to align the spins along the negative field direction. However, when magnetic field changes to positive the FM spins will align easily along the field because the direction of the AFM torque and direction of field are same. Therefore, a smaller positive magnetic field is

needed to align the spins completely in the field direction. This asymmetric behavior in the ascending and descending branch of *M-H* loop gives rise to a shifted hysteresis loop.

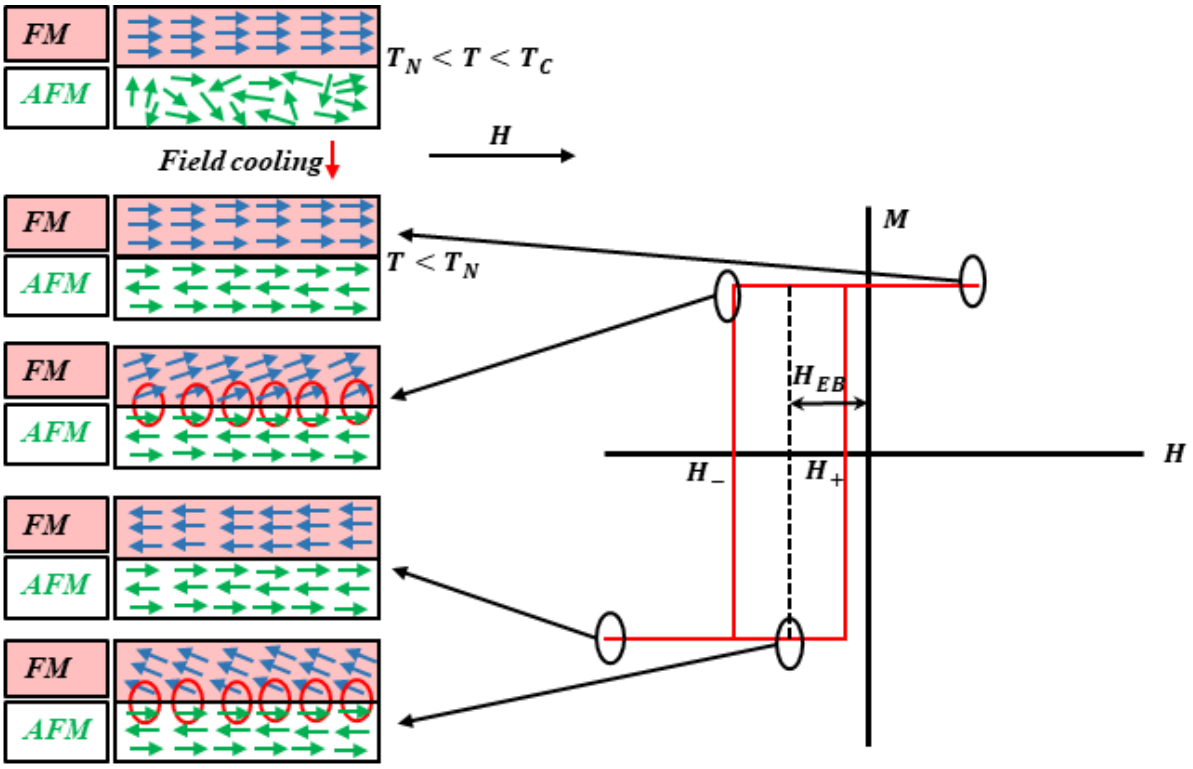

Fig. 1.11: Schematic diagram of FM-AFM coupling at different stages of a shifted hysteresis loop.

Exchange bias has significant importance in the area of spintronic. They can be used as read head in recording devices [54]. Other applications of EB are magnetic field sensor, magnetic random access memory (MRAM), spin valve and overcoming the superparamagnetic limit of memory devices [55-58]. Previous investigation reports EB phenomena in several spinel oxides in their bulk form as well as in nanoparticles. EB behavior observed in bulk $NiCr_2O_4$ is explained on the basis of anisotropic exchange interaction between FM-AFM components of canted spin structure [59]. EB in nanoparticles of $NiCr_2O_4$, $CoCr_2O_4$, $NiFe_2O_4$/NiO etc. is explained by exchange interaction between core and surface spin [60-63].

1.8 Magnetocaloric and Critical Exponents

The magnetocaloric effect (MCE) is the thermal response of a magnetic material under a changing magnetic field. When an external magnetic field is applied to a magnetic material, its domains try to align along the field direction and hence leads to decrease its entropy. But under an adiabatic demagnetization process in which an applied magnetic field is removed under adiabatic condition, the magnetic domains become disoriented and leads to a drop in temperature of the material. The magneto caloric effect can be defined in terms of change in entropy -ΔS_M and is calculated by considering the Maxwell equations of thermodynamics as stated below [64].

$$\Delta S_M\left(T, H_{0\to H_{max}}\right) = \mu_0 \int_0^{H_{max}} \left|\frac{dM}{dT}\right|_H dH \tag{1.15}$$

For magnetization isothermal taken at small discrete field and temperature intervals ΔS_M (T, H) can be evaluated as,

$$\Delta S_M = \sum \frac{M_i - M_{i+1}}{T_i - T_{i+1}} \Delta H_i \tag{1.16}$$

where M_i and M_{i+1} are magnetic moments at temperature T_i and T_{i+1} respectively under an applied magnetic field of $H_{i,k}$ and ΔH_i (=$H_{i,k+1}$-$H_{i,k}$) represents the change in an external magnetic field. The efficiency of a magnetocaloric material can also be characterized by relative cooling power (RCP) and is estimated from the following relation,

$$RCP = -\Delta S_M^{max}(T, H) \times T_{FWHM} \tag{1.17}$$

where T_{FWHM} is the full width at half maximum of entropy change over temperature scale.

In order to predict the nature of magnetic phase transition, normalization of entropy is needed. In case of a second-order magnetic transition the $\Delta S_M / \Delta S_M^{max}$ vs θ curves at different magnetic fields collapse into a common universal curve, where ΔS_M^{max} is the value of ΔS_M at $T = T_C$ and θ is the reduced temperature defined as $\theta = -\frac{T-T_C}{T_{r1}-T_C}$ for $T \leq T_C$ and $\theta = \frac{T-T_C}{T_{r2}-T_C}$ for $T > T_C$. T_{r1} and T_{r2} are the temperatures at full-width half maximum of entropy distribution over temperature scale [65].

According to Landau theory of second-order magnetic phase transition, Gibb's free energy G can be expressed as [66],

$$G(T,M) = G_0 - MH + aM^2 + bM^4 + \cdots \quad (1.18)$$

Here, a and b are temperature dependent coefficient. For ground state free energy $\frac{\partial G}{\partial M} = 0$ and the above expression can be reduced to

$$\frac{H}{M} = 2a + 4bM^2 \quad (1.19)$$

Therefore, M^2 vs H/M is expected to be a straight line with positive slope. According to scaling hypothesis the spontaneous magnetization M_S below T_C, initial susceptibility χ_0^{-1} above T_C and magnetization $M(H)$ at T_C follow the following equations [67],

$$M_S(T) = M_0(-\varepsilon)^{\beta} \ , \varepsilon < 0 \quad (1.20)$$

$$\chi_0^{-1}(T) = \Gamma(\varepsilon)^{\gamma} \ , \varepsilon > 0 \quad (1.21)$$

$$M(H) = DH^{1/\delta}, \varepsilon = 0 \quad (1.22)$$

where, M_0, Γ, D are critical amplitudes and β, γ, δ are critical exponents and $\varepsilon = \frac{T-T_C}{T_C}$.

According to Arrott and Noakes [68] for a more general case, the mean-field equation can be expressed as,

$$\left(\frac{H}{M}\right)^{1/\gamma} = a\frac{(T-T_C)}{T} + bM^{1/\beta} \quad (1.23)$$

Here, a and b are constants. For critical exponents corresponding to mean-field theory i.e. $\gamma = 1$ and $\beta = 0.5$, the above equation can be reduced to equation 1.19. A list of critical exponents for some important theoretical models are given in Table 1.1.

Table 1.1: Critical exponents corresponding to the different theoretical models.

Model	γ	β	δ
Mean-field	1.00	0.50	3.00
3 – d Heisenberg	1.336	0.365	4.80
3 – d Ising	1.241	0.325	4.82
Tricritical mean field	1.00	0.25	5.00

1.9 Dielectric Properties

Dielectric materials are very poor in electrical conductivity but generate electrostatic field and can store energy. These materials are very much useful for the development of capacitor technology (especially in the radio frequency range), memories, sensor, actuators etc. [69-71]. When a dielectric material is placed in a dc or ac electric field a limited displacement of the charges occurs, which leads to the formation of electric dipoles. This phenomenon is known as dielectric polarization. In the case of an uniform and isotropic dielectric material, the strength of polarization can be expressed as [72],

$$P = \varepsilon_0 \chi E \tag{1.24}$$

where ε_0 is the dielectric permittivity of free space and χ is dielectric susceptibility.

Depending on the origin of dipole formation, the polarization process is classified into five different categories such as electronic polarization, ionic polarization, orientational polarization, interface polarization, hopping polarization. The mechanism of different types of polarization and their operating frequency regions are shown in Fig. 1.12 and Fig. 1.13 respectively.

Electronic polarization: Electronic or atomic polarizaion represents the separation of centre of positive charge (nucleus) and negative charge (electron) of an atom under the application of

an electric field (Fig. 1.12 a). It is a very fast polarization phenomena and typically occurs at frequncies between $10^{13} - 10^{16}$ Hz.

Ionic polarization: This type of polarization takes place in polyatomic molecules with ionic bonding. When such materials are placed in an electric field, a small displacement of ions from their equilibrium position occurs and hence leads to the formation of electric dipoles. This polarization typically persists at frequencies between $10^{9} - 10^{13}$ Hz.

Orientational polarization: The orientation of molecules with permanent dipoles towards the direction of an external electric field is known as orientational polarization. Even though these materials have permanent dipoles but without an external electric field, the net dipole moment is zero because of the random orientation of dipoles due to thermal randomization. This type of polarization generally occurs below 10^{9} Hz.

Interface polarization: Interface polarization generally take place in polycrystalline or amorphous materials at their grain boundaries or interface such as electrode-material interface. This usually happens at the interface of two phases having different conductivities and permittivity. Interface polarization typically occurs at a low frequency (~10 Hz).

Hopping polarization: This type of polarization occurs due to the hopping of charge carriers across a potential barrier from one site to another site

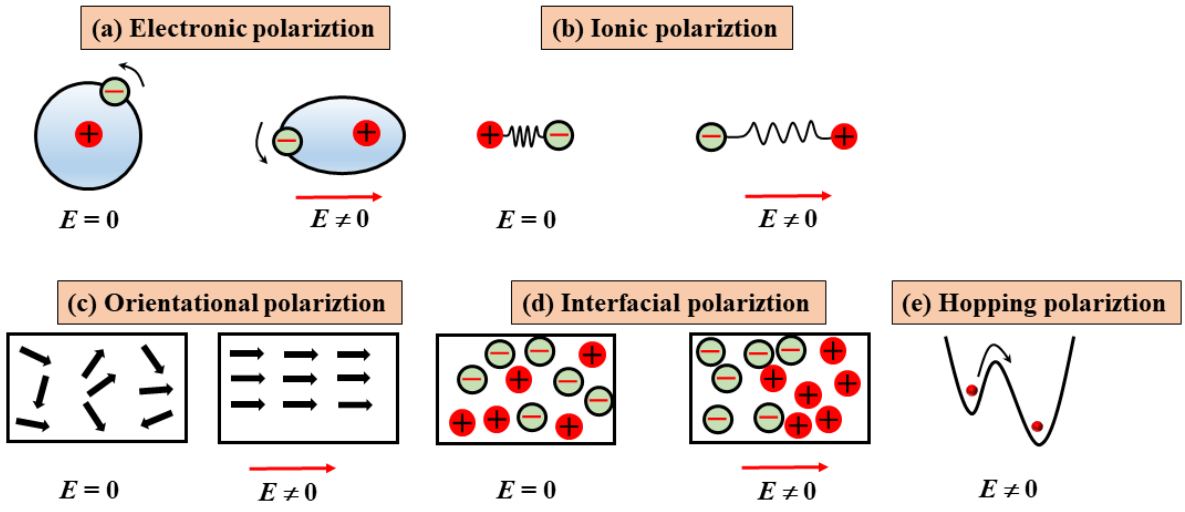

Fig. 1.12: Schematic diagram of different types of polarization.

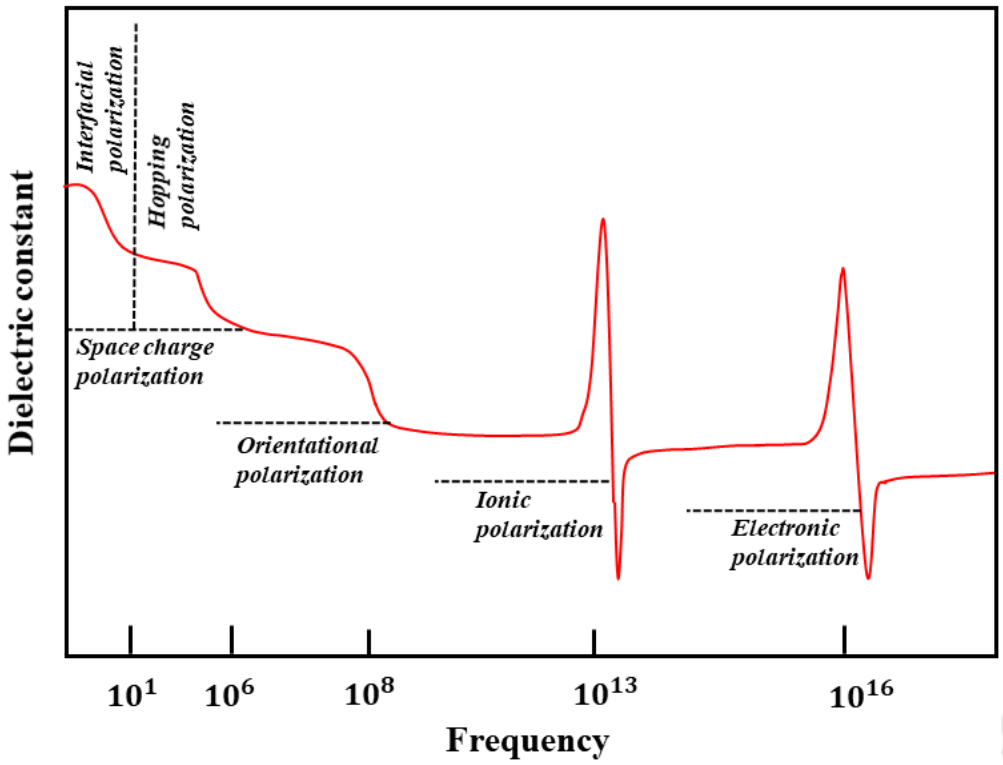

Fig. 1.13: Schematic figure between dielectric constant vs frequency showing various polarization mechanism.

1.9.1 Complex impedance spectroscopy

Impedance spectroscopy (IS) is an important analytical tool to characterize the electrical properties of dielectric materials and hence plays a significant role in applied electrochemistry and material science. IS spectroscopy is generally utilized to study the static and dynamic characteristics of charge carriers. It can predict aspect of performance of the chemical sensors, fuel cells and can be used to investigate the membrane behavior of the living cells. Impedance spectroscopy was first introduced by Oliver Heaviside in terms case of vector diagrams and further developed by A E Kennelly, C P Steinmetz in terms of complex representation [73]. In the case of alternating current (ac) signal, resistance can be expressed in a general form known as impedance (Z^*),

$$Z(\omega) = Z' - jZ'' = \frac{V^*(\omega)}{I^*(\omega)} \tag{1.25}$$

where Z' and Z'' are the real and imaginary components of complex impedance. $V^*(\omega)$ is the voltage across the dielectric substance and $I^*(\omega)$ is the current through it. A schematic representation of the Z' and Z'' as a function of frequency (f) is shown in Fig. 1.14. The frequency at which Z'' is showing a maximum is known as the relaxation frequency of charge carrier with a relaxation time of $\tau = 1/2\pi f$.

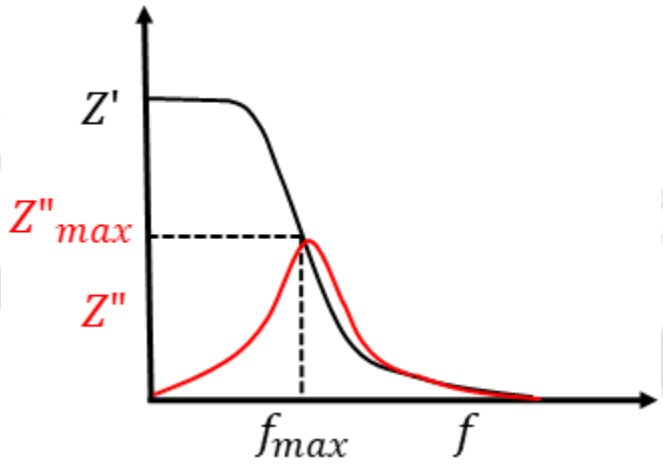

Fig. 1.14: Frequency dependent of Z' and Z'' showing dispersion and relaxation behaviour.

To represent Z^* on a complex plane, Nyquist plot (Z'' vs Z') is used. The plot helps to characterize certain elements or combinations of elements in the equivalent circuit of the materials. For an ideal resistance-capacitance (*RC*) case, the Nyquist plot is a semicircle with a radius equal to resistance (*R*) and center on Z' axis as shown in Fig. 1.15 (a). However, in reality, such an ideal case is not observed in dielectric materials. Therefore, the Nyquist plot is a depressed semicircle with a center that lies below the Z' axis as shown in Fig. 1.15 (b). Such deviation can be addressed by introducing a factor known as the constant phase element (CPE, denoted by *Q*) in the equivalent circuit. The impedance associated with CPE can be expressed as [73],

$$Z_{CPE} = \frac{1}{A}(j\omega)^{-m} \tag{1.26}$$

where A is a constant and m is the relaxation time distribution factor with values lies in the range $0 \leq m \leq 1$.

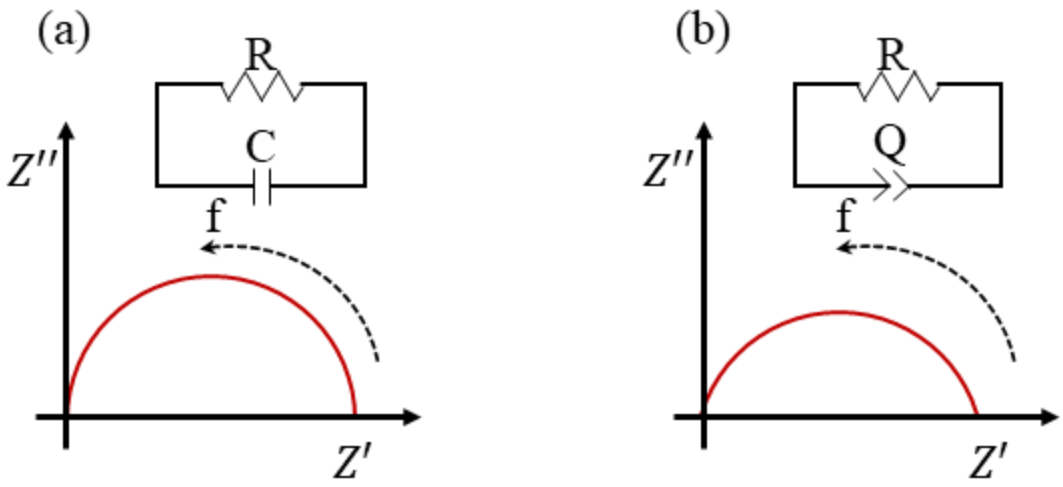

Fig. 1.15: Schematic representation of Nyquist plot at different conditions.

1.9.2 Complex dielectric spectroscopy

The dielectric constant (ε_r) of a material can be expressed as,

$$\varepsilon_r = \frac{C}{C_0} \tag{1.27}$$

where C and C_0 are the material capacitance and geometrical capacitance. For a parallel plate assembly with surface area A and separation d, $C_0 = \varepsilon_0 A/d$.

Similar to the impedance, the dielectric constant is also a complex quantity and can be expressed as,

$$\varepsilon^* = \varepsilon' - j\varepsilon'' \tag{1.28}$$

where ε' and ε'' are the real and imaginary parts of the dielectric constant. The dissipation of electrical energy due to different physical phenomena such as electrical conduction, dielectric relaxation and resonance *etc.* can be expressed in terms of dielectric loss tangent ($tan\delta$),

$$tan\delta = \frac{\varepsilon''}{\varepsilon'} \tag{1.29}$$

Dielectric constant can also be expressed in terms of impedance,

$$\varepsilon^* = \frac{1}{j\omega Z^*} \tag{1.30}$$

With real and imaginary parts as,

$$\varepsilon' = \frac{-Z''}{\omega C_0 (Z'^2 + Z''^2)} \tag{1.31}$$

$$\varepsilon'' = \frac{Z'}{\omega C_0 (Z'^2 + Z''^2)} \tag{1.32}$$

1.9.3 AC conductivity

The conductivity of dielectric material in response to an ac current with angular frequency ω can be expressed as [74],

$$\sigma_{ac}(\omega) = \omega \varepsilon'' \varepsilon_0 \tag{1.33}$$

The typical behavior of ac conductivity is shown in Fig.1.16 (a) The lower frequency region (dc conductivity) is almost independent of frequency and attributed to translational motion of charge carriers assisted by successful hoping of charge carriers (Fig. 1.16(b)). The increase in conductivity in the higher frequency region is due to the increase in the ratio of successful to unsuccessful hoping as shown in Fig. 1.16 (c) [75].

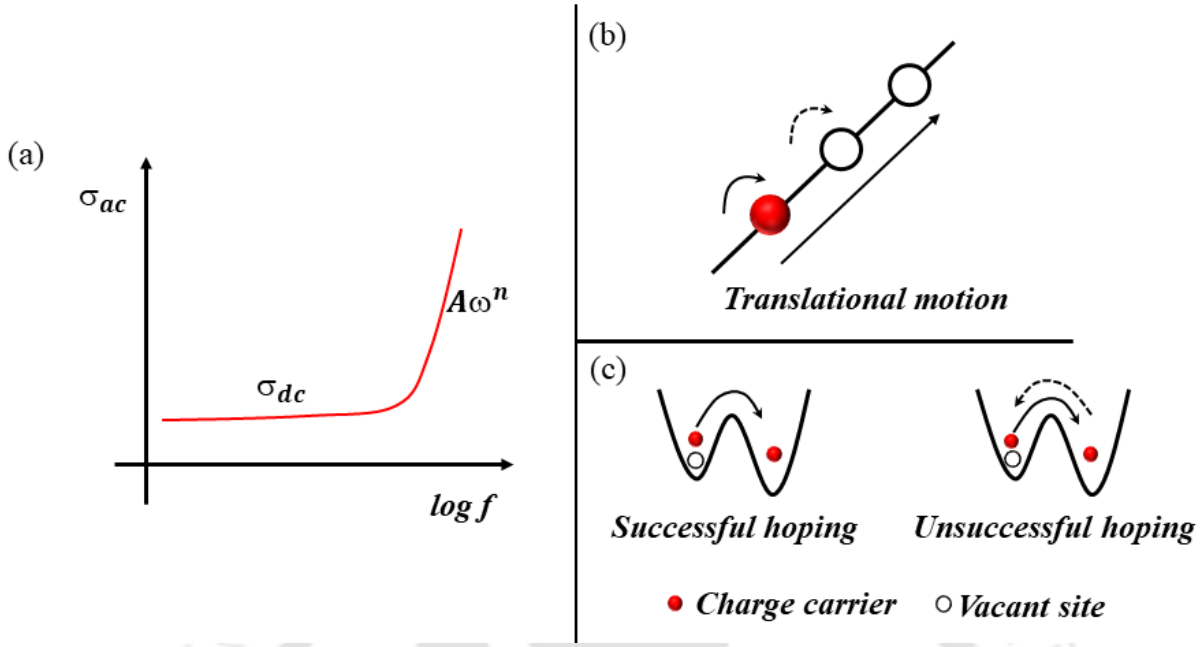

Fig. 1.16: Typical frequency dependent (a) ac conductivity spectra, (b) long range translational motion, and (c) successful and unsuccessful hoping of charge carriers.

The ac conductivity mechanism can be investigated by Jonscher power law (JPL) [76], given as,

$$\sigma_{ac}(\omega) = \sigma_{dc} + A\omega^{n} \tag{1.34}$$

where σ_{dc} is associated with the frequency independent part and $A\omega^{n}$ represent the frequency dependent part at higher frequency. The exponent n gives the information about the origin of conduction mechanisms in a dielectric system. For $n < 1$, conductivity mainly corresponds to the translational motion of the charge carrier and for $n > 1$, it is attributed to localized or reorientational hopping motion due to the back and forth movement of electrons between two defect sites [72].

1.10 Review of $NiCr_2O_4$ based compounds

$NiCr_2O_4$ is a normal spinel with Ni^{2+} ions at the tetrahedral (A) sites and Cr^{3+} ions at octahedral (B) sites. The compound crystallizes in cubic phase at high temperature with space group $Fd\bar{3}m$. With lowering the temperature, the symmetry of the nickel chromite decreases to tetragonal ($I4_1/amd$) at 320 K driven by the cooperative JT effect associated with the Ni^{2+} cations in the tetrahedral position [77]. The detailed crystal structure has been investigated by Crottaz *et al.* from single crystal and powder X-ray diffraction measurements [24]. They reported cubic structure at T = 353 ± 3 K with lattice parameter a = 8.3155 Å and tetragonal structure with lattice parameter $a = b$ = 5.8369 Å, c = 8.4301 Å at T = 298 K. With lowering the temperature, the compound undergoes a magnetic transition from PM to FIM phase at T_C = 65 K [77]. Klemme *et al.* discovered another transition at 29 K from heat capacity measurement [78] and later it is confirmed as AFM transition (T_N = 31K) from neutron diffraction measurement by Tomiyasu and Kogomiya [79]. According to them, below T_N two A sites are grouped into a single sublattice while four B sites are grouped into two sublattices with each sublattice having both longitudinal and transverse components of the magnetic moment. The longitudinal components give rise to M_S = 0.3 μ_B/f. u. and FIM transition, while the transverse components result in AFM transition. A schematic representation of the canted magnetic structure of $NiCr_2O_4$ is shown in Fig. 1.17. The total magnetization per formula unit can be expressed as $M = |\uparrow \mu_{A1-A2} + \uparrow \mu_{B1-B3} - \downarrow \mu_{B2-B4}|$, where $\uparrow \mu_{A1-A2}$, $\uparrow \mu_{B1-B3}$ and $\downarrow \mu_{B2-B4}$ are longitudinal components of the magnetic moment of A1 – A2, B1 – B3 and B2 – B4 sublattices along the filed direction. Ishibashi and Yasumi found a signature of magneto-structural coupling driven by tetragonal to orthorhombic transition at FIM transition temperature T_C = 74 K [80]. The AFM ordering is also further accompanied by the discontinuity in size of lattice parameters of the orthorhombic structure as observed from high-resolution synchrotron x-ray diffraction measurements at different temperatures [81].

After the discovery of its basic structural and magnetic properties, many researchers have tried to explore other possible multifunctional properties in $NiCr_2O_4$. Spinel chromite generally exhibits diverse exotic properties such as multiferroic, magnetodielectric and spin-lattice coupling etc. Apart from these interesting properties, spinel chromites are also studied

extensively for their rich physical behavior such as exchange bias, negative magnetization, bipolar switching, magnetic frustration and reentrant spin glass etc. They have received great deal of attention due to their promising application as electrode in supercapacitors [82], catalyst materials [83], humidity sensor [84], spintronic [85], microwave absorber [86] and as antibacterial drug [87] etc. Mufti *et al.* have studied the magnetodielectric coupling in $NiCr_2O_4$ and reported a clear anomaly in the dielectric constant in the vicinity of T_N [88]. Signature of EB behavior was observed in $NiCr_2O_4$ and explained on the basis of exchange anisotropy between FIM and AFM components of the canted spin structure [59]. Kocsis *et al*. studied the dynamical properties of lattice structure by optical spectroscopy and confirmed magnetostructural coupling at T_C and T_N [11]. Evidence of electrical polarization in the FIM state has been reported by Maignan *et al.* in $NiCr_2O_4$ [10].

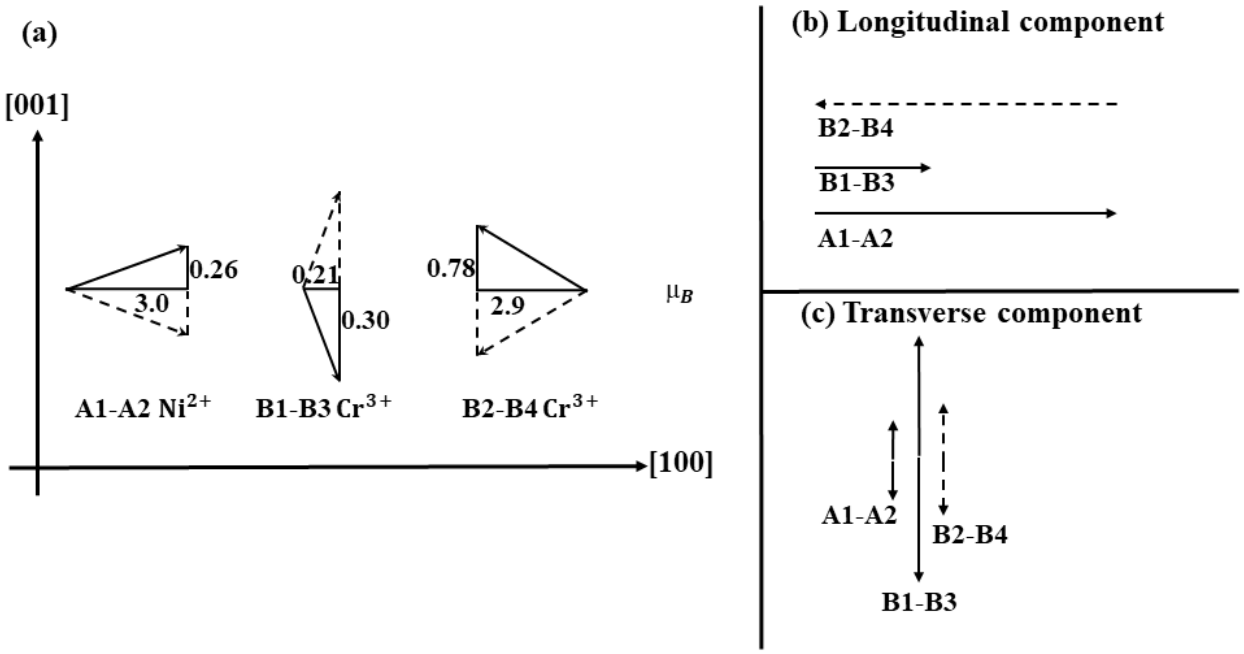

Fig. 1.17: Schematic diagram of magnetic structure of $NiCr_2O_4$ below T_N [96], (b) longitudinal (c) transverse components of sublattices.

To improve the physical properties of $NiCr_2O_4$, several researchers are performing the cation substitution at Ni and Cr sites. A large value of spontaneous EB ($H_{EB} = 2.6$ kOe) and

peculiar magnetic phase transitions such as spin spiral and spin lock-in were reported in $NiCr_{1.8}Fe_{0.2}O_4$ [89]. Interesting magnetization reversal phenomena has been reported in $NiCr_{2-x}Fe_xO_4$ (x = 0-0.20) and $NiCr_{2-x}Mn_xO_4$ (x = 0-0.50) series [90, 91]. Tunable magnetization reversal and exchange bias behavior have been reported in Ga substituted $NiCr_2O_4$ nanoparticles [92]. Enhanced magnetodielectric response was reported in Dy modified $NiCr_2O_4$ compounds [93]. Although investigation of substitutional effect at Cr site is carried out by several researchers [94-99], very few studies have been carried out on substitution effect at Ni sites. A variety of rich phenomena such as magneto dielectric, ferroelectricity, and spin-lattice coupling are observed in low (x = 0.05) Zn-substituted bulk $Ni_{1-x}Zn_xCr_2O_4$ magnetic system [100]. Theoretical analysis was carried out in $Ni_{1-x}M_xCr_2O_4$ (M = Cu & Fe) system to study the effect of cooperative JT distortion [101]. Dynamical structural disorder driven ferroelectric properties were studied in $Co_{1-x}Ni_xCr_2O_4$ solid solution [102]. The study of JT active Cu substituted $Ni_{1-x}Cu_xCr_2O_4$ provides insight into the interplay between the JT effect, geometrical frustration and long-range magnetic order in the magnetic system [103].

1.11 Review of $NiFe_2O_4$ based compounds

In addition to nickel chromite, $NiFe_2O_4$ is another interesting spinel and falls under inverse spinel structure [23]. In 1953, Hastings et al. reported its chemical and magnetic properties for the first time by using neutron diffraction measurement at room temperature [104]. However, the material is getting more attention among scientists and researchers after 1990 due to their new field of applications, such as magnetic recording media [105, 106], spintronics and actuators [107], magnetic memories [108, 109], microwave devices [110, 111], catalysts [112, 113], magnetic sensors [114] and biotechnology [115, 116] etc. Youseef *et al.* confirmed the inverse crystal structure and collinear FIM nature by using polarised neutron diffraction data [117]. The spinel ferrite exhibits ferrimagnetism (FIM), as a result of the anti-parallel alignment of magnetic moments of Fe^{3+} ions at tetrahedral (A) sites and those of Ni^{2+} and Fe^{3+} ions at octahedral (B) sites. Hence, at low temperature, the magnetic moment per formula unit for the inverse spinel nickel ferrite can be represent as,

$$M = M_B - M_A \tag{1.35}$$

where M_A and M_B are the magnetic moments of (A) and [B] sublattices respectively. Depending on the synthesis process, the material can exhibit several interesting properties. Shi et al. reported cluster glass like behavior along with strong uni-directional anisotropy and coercivity of 10 kOe in mechanically milled $NiFe_2O_4$ nanoparticles [118]. Evolution of structural and magnetic properties with Fe concentration at the tetrahedral site were investigated by Sepelak et al. in milled $NiFe_2O_4$ particles [119]. Misra el al. used micro emulsion technique to obtain narrow size distribution of particles which makes the material suitable for application in magneto-optical devices [120].

The Co substituted $NiFe_2O_4$ has attracted much attention due to its interesting magnetic properties such as high coercivity, moderate saturation magnetization, super paramagnetism (SPM), Verwey transition etc. [121-126]. The spinel ferrite exhibits good chemical stability which makes it suitable for application as a binder and magnetic filter in electromagnetic shielding [127]. Moreover, cobalt substituted nickel ferrites are highly resistive and magnetostrictive. Kamble et al. prepared $Ni_{1-x}Co_xFe_2O_4$ ($x = 0 – 0.8$) by ceramic technique and reported the lattice parameters in the range 8.33 – 8.38 Å, while particle size was in the range 1.53-3 μm. Both these structural parameters were reported to increase with Co content (x) [128]. Khan prepared the same series by co-precipitation method and reported its magnetic and microwave absorption properties [129, 130]. Chakradhary et al. presented high coercivity Co doped Ni ferrites, prepared by using heat treatment for application in magnetic data recording [126]. Ati et al. and Rodrigues et al. reported an increase in coercivity with Co substitution due to higher anisotropy associated with Co ions [131]. Influence of Co^{2+}- Co^{2+} pair on anisotropy constant (K) in $Ni_{1-x}Co_xFe_2O_4$ with higher dopant level of Co ($x \geq 0.4$) was presented by Wohlfarth et al [132]. Maqsood et al. observed enhancement in permittivity and permeability with increase in Co substitution and explained in terms of distortion of octahedral sites [133]. Kamble et al. reported a decrease in DC resistivity with increase in cobalt substitution and explained in terms of formation of Fe^{2+} ions and lattice distortion [134]. Co substituted nickel ferrite nanoparticle prepared by co-precipitation method shows vertical shift and exchange bias phenomena as a result of surface spin disorder and the role played by bulk and surface anisotropy of the system [135]. Moreover, Co substitution in spinel ferrite leads to better optimization of dielectric constant and dielectric loss and hence results in good insulator [136].

Even though Co substitution is known to play a major role in the modulation of several physical properties, the detailed analysis of site occupation of Co ions and its influence on structural and magnetic property are yet to be explained. In my thesis work we have prepared $Ni_{1-x}Co_xFe_2O_4$ (x = 0 – 0.50) compounds by sol-gel technique and investigated the evolution of structural and magnetic properties. We have also used the quantum – mechanical method [137] to estimate the cation distributions at tetrahedral and octahedral sublattices and their effect on lattice parameters and magnetic properties.

1.12 Motivation

As per the above literature survey, it is clear that choice of A site cation or partial substitution at A site can results in interesting magnetic properties in these spinels due to the modulation of different exchange interactions between the sublattices. Although there are many reports available on the magnetic properties of nickel chromite spinel system, systematic study of the effect of magnetic and nonmagnetic ions substitution on spin frustration, magneto caloric effect, critical behavior and low temperature dielectric and conduction mechanism are still lacking. A study on interplay between geometric spin frustration and effect of nanoparticle size is also lacking in this chromite system. In addition, a comprehensive study of effect of cation distribution and ionic states on basic magnetic properties of nickel spinel ferrite system would be introduced here in my thesis.

Therefore, in the present thesis we have focused on the following series of mostly bulk samples to study the above objectives.

6) $Ni_{1-x}Mg_xCr_2O_4$ (x = 0 to 0.50)
7) $Ni_{0.85}Mg_{0.15}Cr_2O_4$ nanoparticles
8) $Ni_{1-x}Mn_xCr_2O_4$ (x = 0 to 0.50)
9) $Ni_{1-x}Cd_xCr_2O_4$ (x = 0 to 0.30)
10) $Ni_{1-x}Co_xFe_2O_4$ (x = 0 to 0.50)

Chapter 2

Experimental Techniques

This chapter discusses different types of sample synthesis methods, characterization of the samples using sophisticated instruments and measurements of physical properties. During my research work, samples were synthesized by sol-gel and hydrothermal routes followed by presintering and sintering using high temperature furnace. The samples were characterized by several sophisticated equipments such as X-ray Diffractometer (XRD) to record powder diffraction patterns for phase identification and crystal structure analysis; Field Emission Scanning Electron Microscope (FESEM) and Field – Emission Transmission Electron Microscope (FETEM) to study the microstructural morphology and Energy Dispersive X-ray (EDX) spectroscopy to carry out compositional analysis. X – ray photoelectron spectroscopy (XPS) was used to investigate the possible oxidation states of the ions in the samples. Micro-Raman spectrometer was used to analyze vibration modes. Magnetic properties were studied by using Vibrating Sample Magnetometer (VSM) and Physical Properties Measurement System (PPMS). LCR meter was used to record the frequency and temperature variations of complex impedance spectra. The details of the above mentioned experimental techniques are elaborated as follows.

2.1 Sample Preparation

2.1.1 Sol-gel Method

Here the starting compounds used for sample preparation were mostly in their nitrate or acetate form such as nickel nitrate ($Ni(NOO_3)_2.6H_2O$), chromium nitrate ($Cr(NO_3)_3.9H_2O$), ferric nitrate ($Fe(NO_3)_3.9H_2O$), cobalt nitrate ($Co(NO_3)_2.6H_2O$), magnesium nitrate ($Mg(NO_3)_2.6H2O$), manganese acetate ($C_4H_6MnO_4.4H_2O$) and $Cd(NO_3).4H_2O$. In this method, first stoichiometric ratio of the starting materials were dissolved in distilled water and then mixed together. The mixture was then transferred into a glass beaker and it is kept on a hot plate with magnetic stirrer which was set at 90-100 ^{0}C. An adequate amount of citric acid

and ethylene glycol were then added to the solution. Citric acid acts as a chelating agent which can bind up only metal ions and remove the non-metallic ions, while ethylene glycol helps to form a dense gel. The solution was then kept under constant stirring for 6-7 hours for homogeneity and for another 12 hours at the same temperature to complete the evaporate of the water and acid. The obtained metal citrate gel was then kept in an oven operated at 300 ^{0}C to remove the volatile compound trapped in the pores of the gel, organic ligands etc. and to obtain fine powders. The precursor powders were grinded thoroughly for better contact between the surfaces of the reactant and presintered at 600 ^{0}C for 12 hours. After several intermediate heating and grinding process, these powders were pressed into pellet form. The final heat treatment was performed at 1100 ^{0}C for 24 hours. High temperature furnace was used for presintering and final sintering of the samples.

2.1.2 Hydrothermal Method

Hydrothermal method is one of the widely used synthesis process for the preparation of nanoparticles, nanorods, nanotubes, hollow nanospheres and graphene nanosheets etc. The method is based on an aqueous solution and reactions take place inside a hydrothermal autoclave reactor at high-pressure and high-temperature conditions. The solvent is usually water and the metal hydroxide such as NaOH is added as a mineralizer. This method can be used to change particle morphology and grain size, surface chemistry and crystalline phase by optimizing the temperature, pressure, solvent and aging time. The schematic diagram of the general preparation steps of the hydrothermal method is shown in Fig. 2.1. In this procedure, first stoichiometric ratio of the starting materials were dissolved in distilled water and then mixed together. The pH value of the mixture was adjusted to 13 by dropwise addition of 2 M NaOH solution. The mixture was then transferred into an autoclave reactor. The autoclave reactor was made up of thick and steel-walled cylindrical vessels having hermetic sealing and therefore safe to use at high temperature and high-pressure conditions. To kick off the hydrothermal reaction, the autoclave was then placed into a hot air oven at 150^0 C for 20 h and allowed to cool naturally after the hydrothermal reaction was over. The resultant precipitate was extracted by several centrifugations followed by washing with distilled water to remove water soluble salts. The precipitate was dried at 90^0 C in an oven in order to get the powder

form of the sample. The as synthesized powders were heated at 700^0 C for 4 hours to get final product.

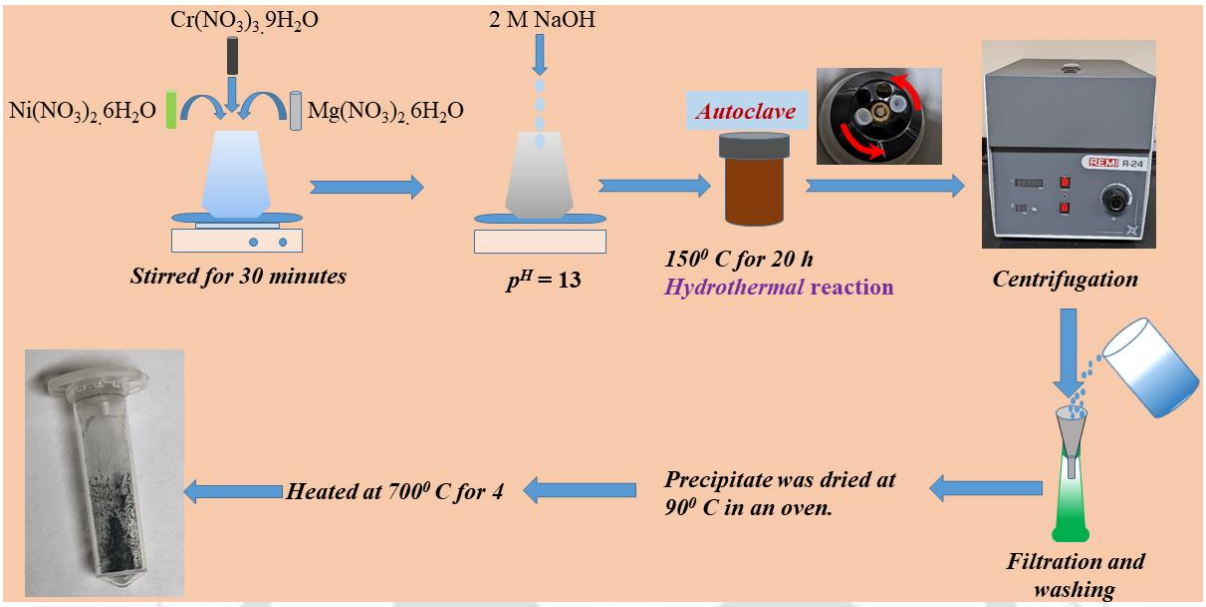

Fig. 2.1: Schematic diagram of the general preparation steps of the hydrothermal method.

2.2 High Temperature Furnace

In the present research work, the heat treatment of the sample was carried out by Nabertherm made high temperature furnace (Model HTCT 03/15) with a maximum operating temperature of 1773 K. The external and internal dimensions ($W \times D \times H$) of the furnace are 400×535×530 mm and 120×210×120 mm respectively. The schematic diagram of the furnace is shown in Fig. 2.2. The furnace is made up of stainless steel outer jacket with dual shell housing to avoid heat leakage to the external atmosphere and high stability. The temperature was controlled using PID programmable temperature controller (Model no. C450) with 10 programs and 20 segments facility. The S-type thermocouple (Platinum Rhodium - 10% / Platinum) was used as temperature sensor. The high-quality Silicon-Carbide (Si-C) rods were used as a heating element. A solid-state relay was used as a switching system to control the power to the Si-C rod. The accuracy of the temperature controller is ± 1 K and the operating voltage of the furnace is 380 V - 400 V (50 Hz - 3 Phase) with a current rating of 20 A.

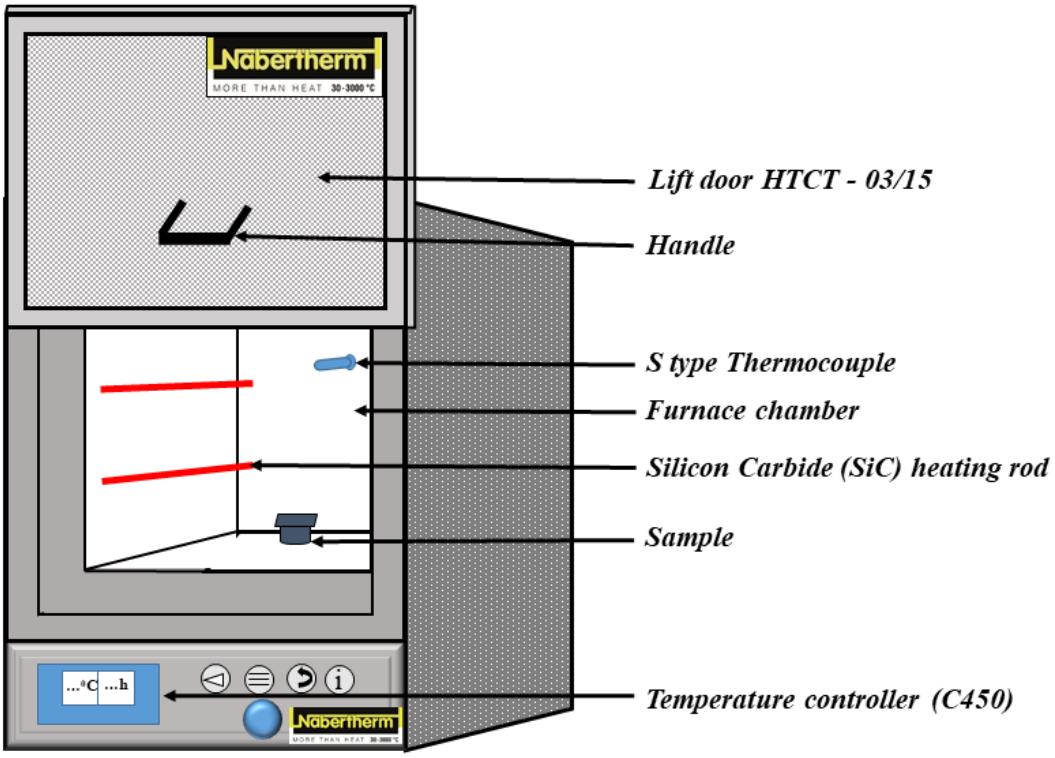

Fig. 2.2: Overview of high temperature furnace setup (model: HTCT 03/15).

2.3 Structural Characterization

2.3.1 X-ray Diffraction

X-ray diffraction (XRD) is a powerful characterization tool to study the crystal structure of materials. This technique gives information about the sample purity, phase, structural parameters such as lattice constant, bong length, bond angle etc. When a monochromatic X-ray incident on a polycrystalline sample, diffraction occurs due to the X-ray's comparable wavelength with inter lattice spacing (Fig. 2.3 (a)). However, constructive interference takes place only from those planes which fulfill Bragg's condition i.e.,

$$2dsin\theta = n\lambda \quad (2.1)$$

where λ is the wavelength of the X-ray, d is the inter planer spacing corresponding to the particular miller indices (hkl), n is the order of diffraction and θ is the glancing angle [138]. In my thesis work, the XRD patterns were recorded at room temperature by Rigaku made TTRAX III diffractometer with CuK_α radiation ($\lambda = 1.5406$ Å). To produce the X-rays, the generator

voltage and current values were set at 50 kV and 200 mA respectively. The schematic diagram of Bragg-Brentano geometry on which the instrument is based is shown in Fig. 2.3 (b).

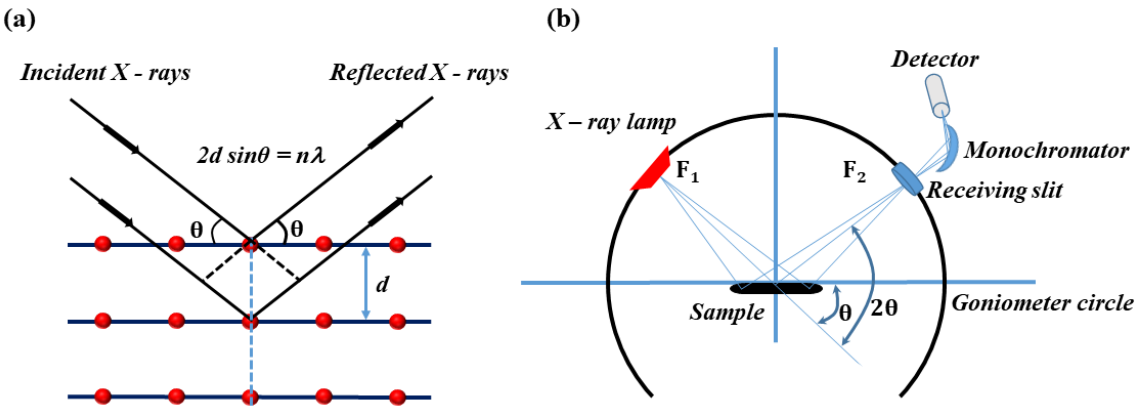

Fig. 2.3: (a) Schematic representation of Bragg's Law and (b) Bragg-Brentano geometry of XRD.

In this setup, both the X-ray generator and detector are placed at equidistance from the sample holder. The X-ray source (F_1) and receiving slit (F_2) reside on the circle with the center positioned on the surface of the sample. The data were collected by scanning the samples in the 2θ angle range of 20^0-70^0 with a step size of 0.03^0 and a scan speed of 3^0/min.

The recorded XRD data were analyzed by the Rietveld refinement method using Fullprof software. This method minimizes the difference between experimental and theoretical diffraction profiles by optimizing different parameters such as coefficient of background polynomials, scaling factor, half-width parameter (*u*, *v*, *w*), lattice constant (*a*, *b*, *c*), crystallographic position of atoms (*x*, *y*, *z*), occupancy values, etc. The peak shape was refined by the Pseudo-Voigt function. The quality of refinement is based on values of reliability parameters such as R_p, R_{wp}, R_{exp}, R_{Bragg}, R_F and χ^2 and they can be expressed as [139],

Profile factor, $$R_p = 100 \frac{\sum_{i=1,n} |y_i - y_{c,i}|}{\sum_{i=1,n} y_i} \quad (2.2)$$

Here, y_i is the experimental data and $y_{c,i}$ is the calculated data and *n* represents the number of data points,

Weighted profile factor, $$R_{wp} = 100\left[\frac{\sum_{i=1,n}\omega_i|y_i - y_{c,i}|^2}{\sum_{i=1,n}\omega_i y_i^2}\right]^{1/2} \quad (2.3)$$

Here, $\omega_i = \frac{1}{\sigma_i^2}$, σ_i^2 is the variance of y_i and can be expressed as $\sigma^2 = \langle(y_i - \langle y_i\rangle)^2\rangle$, where <> represent the average value.

Expected weighted factor, $$R_{exp} = 100\left[\frac{|n-p|}{\sum_{i=1,n}\omega_i y_i^2}\right]^{1/2} \quad (2.4)$$

Here, (n - p) gives the number of degrees of freedom, where n is the total number of experimental data points and p is the number of refined parameters.

Reduced chi-square, $$\chi^2 = \left[\frac{R_{wp}}{R_{exp}}\right]^2 \quad (2.5)$$

Bragg factor, $$R_{Bragg} = 100\frac{\sum_h |I_{obs,h} - I_{calc,h}|}{\sum_h I_{obs,h}} \quad (2.6)$$

Here, h represents the particular hkl Bragg peak. The $I_{obs,h}$ and $I_{calc,h}$ are the observed and calculated integrated intensities, respectively.

Crystallographic R_F factor, $$R_F = 100\frac{\sum_h |F_{obs,h} - F_{calc,h}|}{\sum_h F_{obs,h}} \quad (2.7)$$

$F_{obs,h}$ and $F_{calc,h}$ are the observed and calculated structural factors, respectively. Bond length and bond angles were estimated by visualization of electronic and structural analysis (VESTA, version 4.3.0) software.

2.3.2 Field Emission Scanning Electron Microscope

Field emission scanning electron microscope (FESEM) is commonly used to analyze surface morphology and elemental composition on a nanometric scale. A schematic diagram of the FESEM setup is shown in Fig. 2.4. This instrument uses a high energetic electron beam to study any biological or chemical samples. FESEM can produce clearer and less distorted

images with spatial resolution down to 1nm as compared to a scanning electron microscope (SEM). The electron gun is a zirconium oxide coated tungsten (ZrO_2/W) emitter, which operates in a thermally assisted Schottky emission mode. This type of gun provides narrower probing beams as well as high electron energy, resulting in both improved spatial resolution and minimized sample damage due to charging. Extreme vacuum and high electrical field gradient are created for the acceleration of the electrons. The acceleration voltage between electron gun and anode is generally in the order of 0.5-30 kV.

The primary electrons moving in the high vacuum are focused and deflected by the second condenser lens (magnetic lens) to produce a narrow scan beam that bombards the specimen. This bombardment results in different types of emitted electrons from the sample as shown in Fig. 2.5 (a). Upon electron impingement on the sample, the interaction volume resumes as a drop shape. The dislodged electrons scattered from the surface are known as secondary electrons. A highly efficient annular in-lens detector receives the secondary electrons and an image of the sample surface is constructed. Apart from these secondary electrons (SE), the backscattered electrons (BSE), characteristic X-rays, cathode-luminescence, Auger electrons and continuum X-rays are also generated from the sample surface. BSE are more energetic as compared to SE and have a definite direction. All emissions above 50 eV are considered as BSE and they cannot be collected by a SE detector, unless the detector is directly in their travel path. This imaging is useful in distinguishing one material from another since the yield of the collected BSE increases monotonically with the specimen's atomic number Z ($\sim 0.05\ Z^{1/2}$). Backscattered imaging can distinguish elements with an atomic number difference of at least 3. The energy spectrum of electrons emitted from the specimen surface is shown in Fig. 2.5 (b). In order to make the samples conducting, they were coated with a thin layer (1.5-3.0 nm) of gold. ZEISS make FESEM (model: Sigma 300) was used to carry out the analysis in the present thesis work.

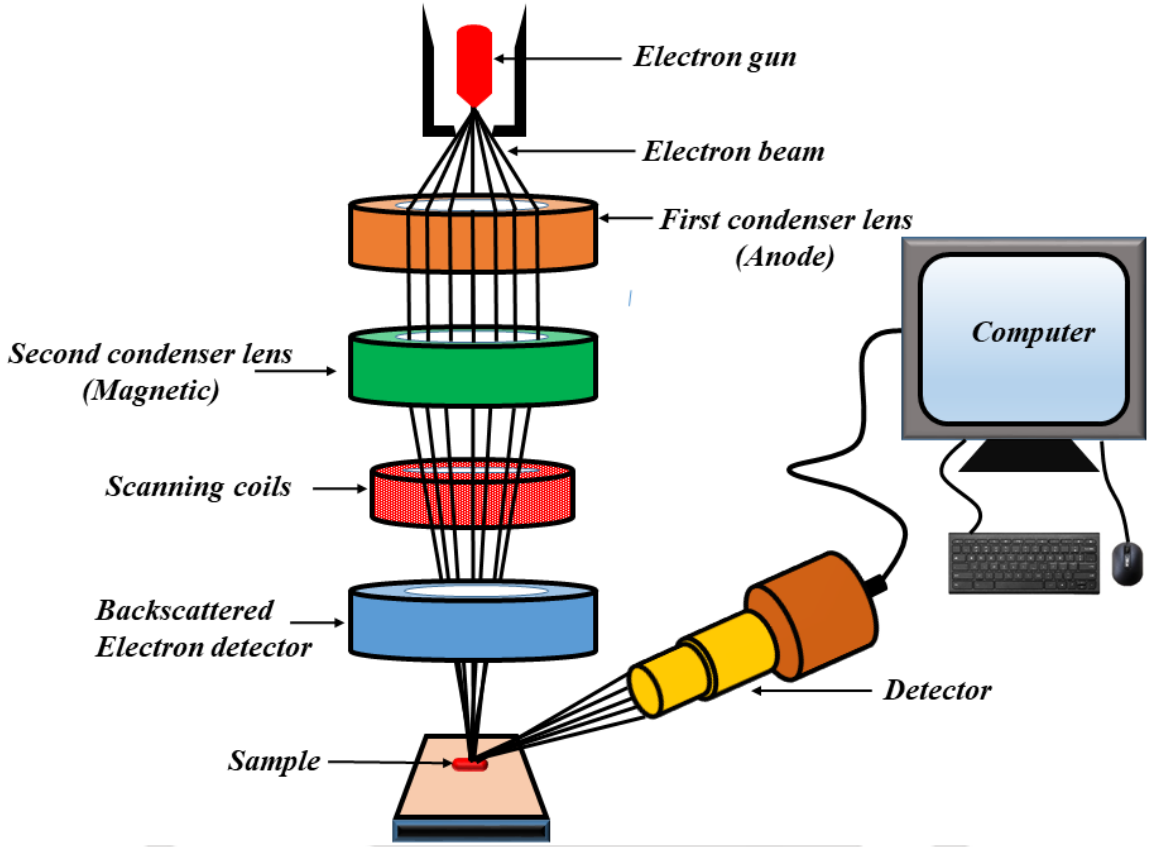

Fig. 2.4: Schematic diagrm of the FESEM setup.

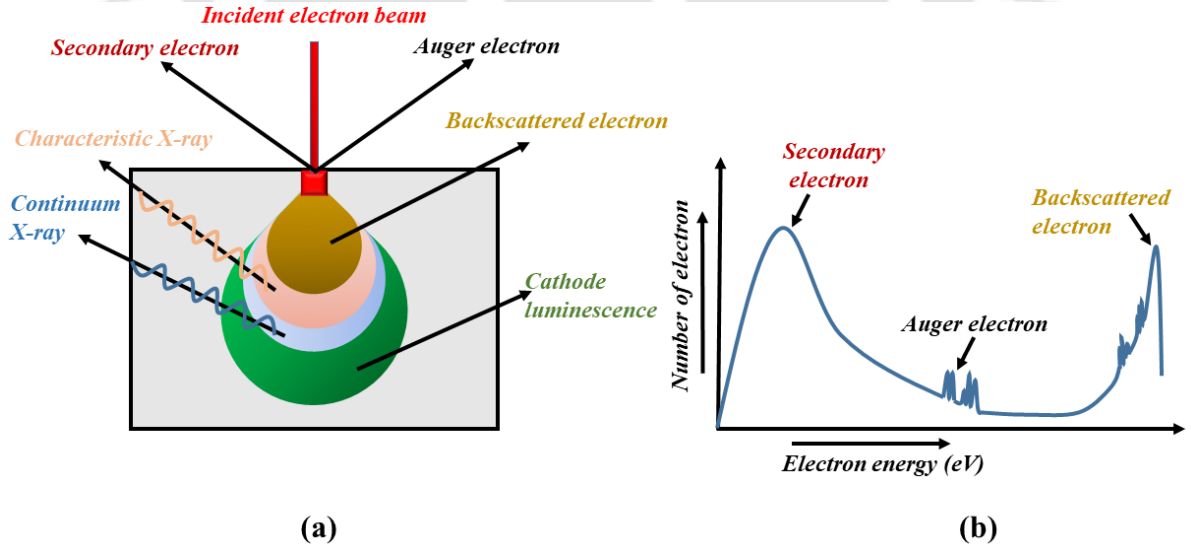

Fig.2.5: (a) The scattering of electron and photon from the drop-shaped interacting volume of the sample (b) the energy spectrum of electrons emitted from the specimen.

2.3.3: Energy Dispersive X-ray Spectroscopic Technique

Energy Dispersive X-ray Spectroscopic (EDS) is an instrument that provides elemental or compositional information of a specimen. The instrument is usually attached to the FESEM facility. The characterization technique is based on fact that each element has a definite atomic structure and emits its unique characteristic X-ray. To simulate the emission of characteristic X-rays from the sample, a high energy beam of charged particles such as electrons or protons is focused on the sample being studied. Such excitation leads to hole or electron vacancy of some inner shell and it is further filled by some outer core electrons by emitting the characteristic X-rays. Thus, by estimating the amount of energy released by X-rays released by the sample, one can identify the elements. Hence, we get a spectrum as an output, which displays peaks corresponding to the energy levels. The peak position and its intensity give information about the elements and their relative concentration. In the present thesis, the EDX spectra of the samples were recorded by using ZEISS make FESEM (SIGMA) equipped with an oxford EDX facility.

2.3.4: Raman Spectroscopy

Raman spectroscopy is a non-destructive technique and it is generally used to study vibrational modes of molecules to access crucial information such as bond structure, crystalline phase, strain, defects, etc. of a compound. Raman scattering was discovered by C. V. Raman in 1928 and for which, he won the prestigious Novel Prize in 1930.

The principle of Raman scattering is based on the quantum theory of radiation. When a monochromatic light with frequency ν_0 incident on a sample it interacts with molecular vibration. In the case of elastic scattering, the frequency of incident light and scattered light are the same (Rayleigh scattering). However, a small portion of the incident photons transfer to or receive energy from the sample due to changes in vibrational or rotational modes of the molecules, causing a change in the frequency of the scattered frequency (Raman scattering). If ν_s is the frequency of the scattered light, then the Raman shift can be expressed as $\Delta\nu = \nu_0 - \nu_s$. If the incident light transfers energy to the molecules, the scattered light has a red-shifted frequency and is referred to as stokes shift ($\Delta\nu = +ve$). However, in some cases, the molecule

is already in an excited energy state and transfer of energy takes place from molecules to the incident photons. Therefore, the scattered light has a blue-shifted frequency and is referred to as anti-stokes shift ($\Delta\nu$ = - *ve*). The Raman activity of a compound is decided by the polarizability of its molecule. The intensity of Raman scattering is proportional to the degree of polarization of the molecules due to the stretching or bending of the bonds. According to the Raman selection rule, the displacement of the constituent atoms from the equilibrium positions leads to molecular vibration and hence change in molecular polarizability [140].

Raman spectrometer is generally classified into two types dispersive and non-dispersive. The dispersive technology is based on the light scattered from a sample using a diffraction grating, while non-dispersive technology is based on the Michelson interferometer. In the present thesis, the Raman spectra of the samples are recorded by using a micro Raman spectrometer (LabRam HR 800, Horiba Jobin Yvon) at room temperature. The exciting wavelength of the laser (Argon laser) used for carrying out the analysis is 514 nm. A schematic diagram of dispersive Raman spectrometer is shown in Fig. 2.6. The beam splitter splits the laser beam coming out from the source into two parts with equal intensity. When the laser incident on the sample both Rayleigh and Raman scattering occurs. However, the notch filter only allows the Raman scattered wavelength to pass. The scattered light was allowed to pass through the grating and etalon, which in turn resolve the weak inelastic scattered wavelength coming from the sample more efficiently. The beam was then allowed to enter into a charge coupled device (CCD), where it detects the change in polarizability of the sample from the change in wavelength and converts into the intensity profile.

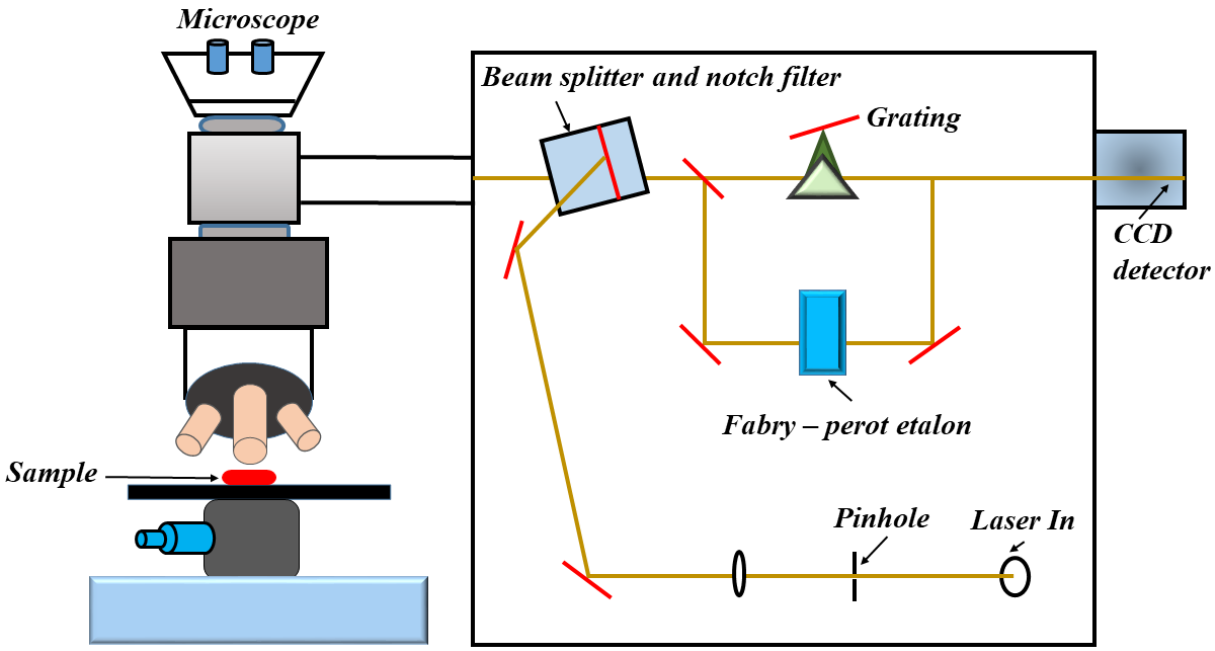

Fig. 2.6: Schematic diagram of Raman spectrometer.

2.3.5 X-ray Photoelectron Spectroscopy

X-ray photoelectron spectroscopy (XPS) is surface science technique for measuring elemental compositions, oxidation state and their binding energy. Typically, XPS probes to a depth of 10 nm on the surface of a specimen. The XPS spectra is obtained by irradiating the sample with X-ray and measuring the kinetic energy of emitted electrons from the top of the material. All the surface atoms have their characteristic peaks in the XPS spectrum. The binding energy along with intensity of these peaks enables the identification of electron configuration (e.g., 1*s*, 2*s*, 2*p*, 3*s* etc.) and elements present in the material. The relation between different energy parameters is represented by the following equation [141],

$$E_{kinetic} = E_{photon(h\nu)} - E_{binding} - \phi \qquad (2.8)$$

where $E_{kinetic}$ is the kinetic energy of the photoelectron, E_{photon} is the energy of the incident photon, $E_{binding}$ is the binding energy corresponding to a particular electron in a state and ϕ is the work function (the energy difference between vacuum energy (E_v) level and the Fermi energy (E_f) level of a solid). The schematic diagram of XPS setup is shown Fig. 2.7.

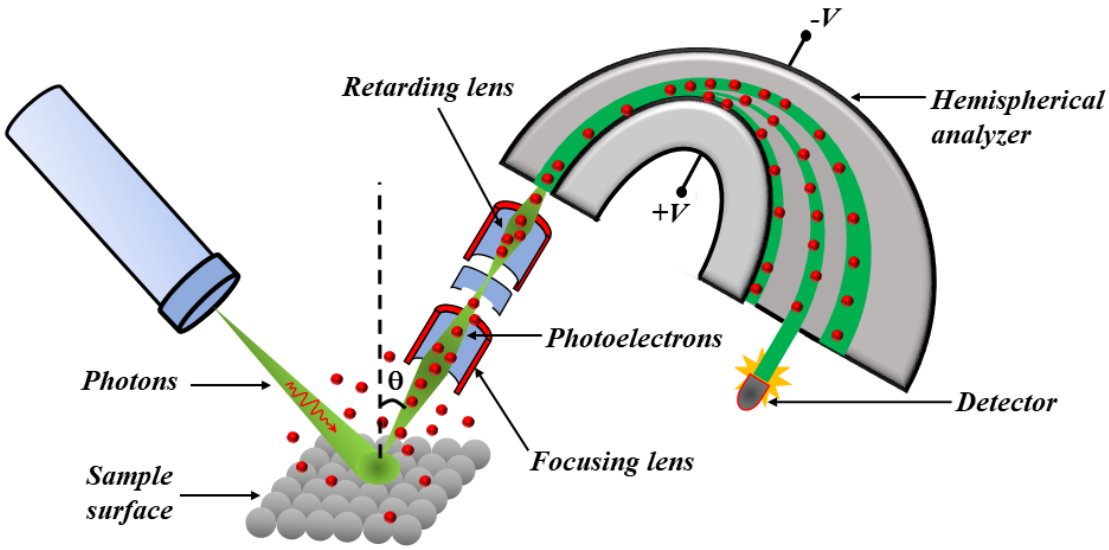

Fig. 2.7: Schematic diagram of XPS instrument.

As shown in Fig. 2.7 the incident X-ray illuminates the sample causing the electron to leave the surface with a range of energies and directions. A portion of these emitted photoelectrons are collected by a set of magnetic and multielement electrostatic input lenses and transfer to the analyzer. Electrostatic fields within the hemispherical analyzer are established to only allow electron with specific energy to arrive at the detector. Energy of a specific initial kinetic energy are measured by setting voltages for the lens system that focus onto the entrance slit of the required initial energy and retards their velocity so that their kinetic energy after passing through the transfer lenses matches the pass energy of the hemispherical analyzer. In the present thesis work, Thermo Fisher Scientific make XPS (Model: ESCALAB Xi+) with Al K_α and Mg K_α X-ray source was used to carry out the measurements.

2.4 Physical Measurements

The magnetic and dielectric behaviors are the physical properties that have been investigated in the present thesis work. For magnetic characterizations, we have used Quantum Design DynaCool model of physical property measurement system (PPMS) and Lakeshore make vibrating sample magnetometer (VSM) (model 7410). The dielectric and impedance data were recorded by using Wayne Kerr make LCR meter (Model: 1J4300R/43100R) in the frequency range of 20 Hz to 10^5 Hz. We have used Advanced Research System (ARS) make

closed cycle refrigerator (CCR) cryostat (model DMX-19) paired with a Lake Shore temperature controller (model 331) to create a low temperature environment for study the samples in the temperature range of 28 K to 300 K.

2.4.1 Physical Properties Measurement System

The physical property measurement system (PPMS) is used to study the magnetic and electrical transport properties of a specimen in an environment where the magnetic field and temperature are well-controlled. The type of specimens are typically in bulk, thin-film or powder form. In the present thesis work, we have used Quantum Design make DynaCool model of PPMS equipped with VSM. The instrument uses a two-stage pulse tube cooler to cool both the superconducting magnet and temperature control system. Therefore, the setup can provide continuous low-temperature control, precise field and temperature sweep modes. The integrated cryo-pump evacuates the sample chamber to less than 10^{-4} Torr in under 10 minutes and the system is capable of cooling a sample from 300 K to 1.9 K in less than 40 minutes. The accuracy in temperature and magnetic moment are quoted as ± 1% and ± 0.5% respectively. The PPMS is equipped with a superconducting magnet and includes a hybrid digital/analog magnet controller to precisely control the magnet field. The bipolar design allows smooth continuous ramping through zero field. The field uniformity is quoted as 0.01% within the sample volume.

The vibrating sample magnetometer (VSM) mode uses a puck-based first-order gradiometer coil set and a high-resolution linear transport motor that allows the system to study magnetic materials. The lock-in measurement approach isolates the sample signal from external noises and hence provides precise data. The static (DC) magnetic moment of the samples can be measured as a function of temperature or field. The basic principle of VSM is that changing magnetic flux will induce a voltage in a pickup coil. The induced voltage can be expressed as,

$$V_{coil} = \frac{d\Phi}{dt} = \left(\frac{d\Phi}{dz}\right)\left(\frac{dz}{dt}\right) \tag{2.9}$$

where Φ is the magnetic flux enclosed by the pick up coil, z is the vertical position of the sample with respect to the coil and t is the time. For a vibrating sample, the output voltage is based on the following equation,

$$V_{coil} = 2\pi f C m A \sin(2\pi f t) \tag{2.10}$$

Here, C is the coupling constant, m is the dc magnetic moment of the measured sample, A is the amplitude of oscillation with a frequency f. The magnetic moment of the sample is estimated by measuring the coefficient of the voltage response from the detecting coil. A block diagram of different steps involve in VSM mode is illustrated in Fig. 2.8.

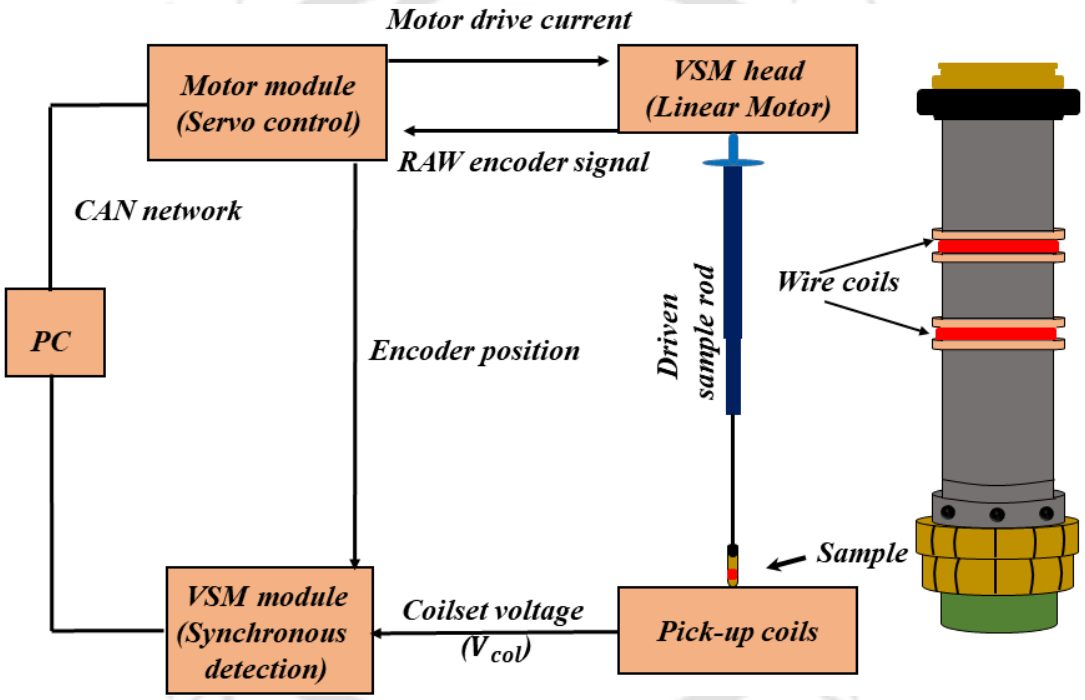

Fig. 2.8: Block diagram of VSM mode operation of PPMS and schematic view of VSM coil set.

The sample is attached to the end of the sample rod that is driven sinusoidally. The oscillation of the sample is positioned at center of the gradiometer pick-up coil (Fig. 2.8) by calibrating the sample. The position and amplitude of oscillation is controlled by VSM motor module. The voltage induced in the pick-up coil is amplified and lock in detected in the VSM detection module.

The cryostat is the most important part of the PPMS system and is responsible for keeping all the necessary components of the system at the correct temperature. The schematic diagram of the cryostat control system is shown in Fig. 2.9. The pulse tube cryocooler consists of two stages and provides all necessary mechanisms required for cooling. The first stage typically operates at 45 K, while the second stage runs roughly at 4.2 K. The main components cooled by the two stages are discussed below

Main radiation shield: The heat loads from the room temperature are intercepted by the main radiation shield to prevent excess heat load on the 4 K plate. The main radiation shield is cooled by conduction through a small gas gap to the first stage of cryocooler. All other first-stage components are cooled by solid contact to the main radiation shield.

4 K plate: The 4 K plate is cooled by contact with approximately 150 cc of liquid helium in the bottom of the bucket. All other second-stage components are cooled by solid contact to the 4 K plate.

Annulus radiation shield: The cooling annulus is surrounded by the annulus radiation shield. Thermal radiation from the cooling annulus that shines on the annulus radiation shield is conducted up the annulus shield to the main shield, and then to the pulse tube cryocooler's first stage.

Cooling annulus: The DynaCool sample chamber resides inside the annulus tube. The space between the sample chamber and annulus tube is called the cooling annulus. When the circulation loop is set to Circulating, helium flows up the cooling annulus in order to cool the sample chamber and provide a bias of cooling power for temperature control.

Bucket and liquid helium: The pulse tube cryocooler in DynaCool resides in helium gas in a cryogenic tank usually called the bucket. The 4 K Plate is cooled by contact with approximately 150 cc of liquid helium in the bottom of the bucket. Heat loads from second stage components cause small amounts of liquid helium to evaporate from the bottom of the bucket. The evaporated helium then condenses on the second stage of the cryocooler and falls back onto the 4 K Plate, creating a classic thermosiphon.

Circulation pump, main and low temperature flow: In order to circulate helium for chamber cooling, the circulation loop is configured with the circulation pump turned on, the bypass valve closed, the circulation/exhaust valve set to circulation, and the helium fill valve closed. Main flow starts as 4.2 K helium gas in the bucket. The He gas then flows up the counter-flow heat exchanger (CFE), through the mass flow controller, back down the CFE, through connecting tubing, and into the cooling annulus. The flow then runs through the annulus pumping line to the circulation pump, then through the return gas line back to the bucket.

The low temperature flow system provides 1.7 K helium gas to cool the sample chamber when it is below about 10 K. In this mode, the main flow is set to zero and 4.2 K liquid from the bucket is expanded through the capillary flow impedance. The inlet of the impedance is at bucket pressure, about one atmosphere, and the outlet is at annulus pressure, about 10 Torr. As the helium undergoes expansion in the impedance, some of it evaporates, resulting in an impedance outlet flow that is a mixture of liquid and gas at about 1.7 K. This mixture flows through connecting tubes to the bottom of the cooling annulus, also known as the pot.

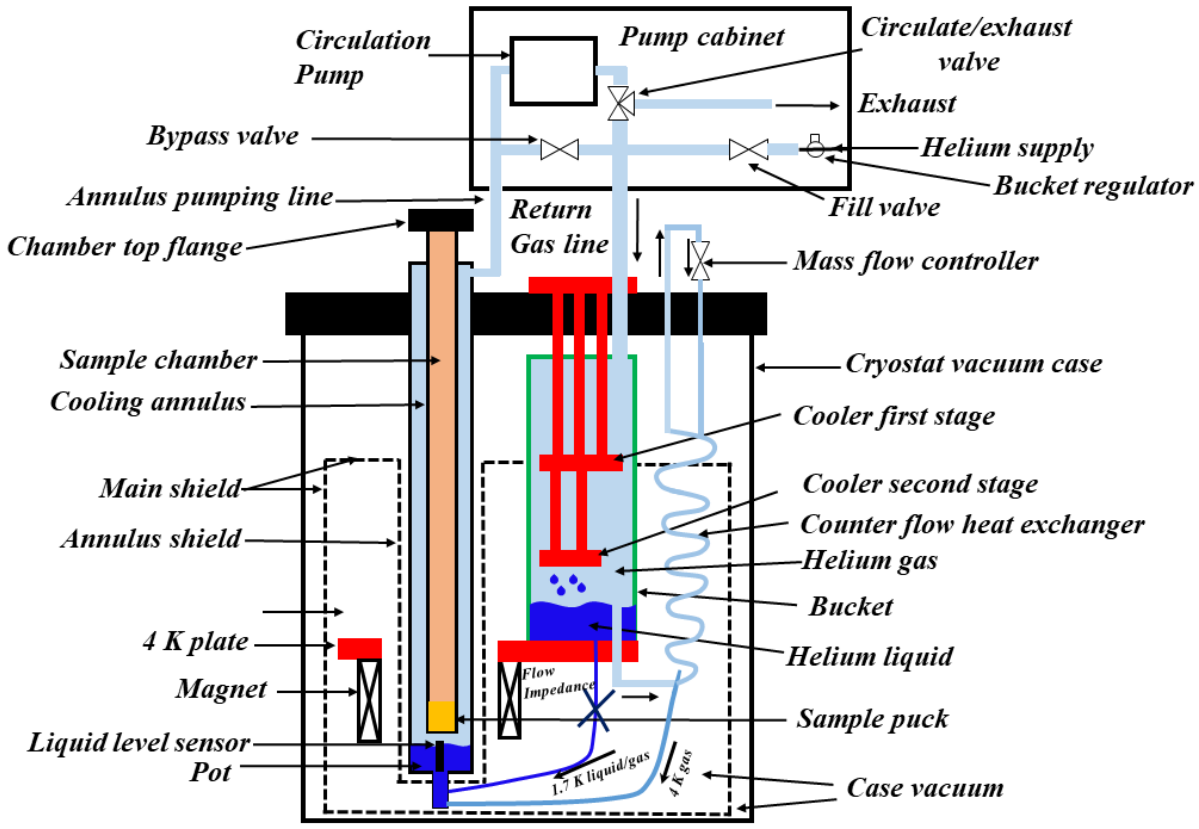

Fig.2.9: Schematic diagram of DynaCool cryostat system.

2.4.2: Electromagnet Based Vibrating Sample Magnetometer

Another extensively used sophisticated instrument for investigating the magnetic characteristics of a wide range of magnetic materials is the vibrating sample magnetometer (VSM). In my thesis work, temperature variations of magnetization above room temperature were recorded by using the Lakeshore make VSM (model no. 7410) with a maximum applied field of 1.5 T. The model has a very flexible design such that sample can be changed rapidly even at any operating temperature. VSM generally used to measure dc magnetic moment as a function of time, temperature and magnetic field. The schematic diagram of the VSM instrument is shown in Fig. 2.10.

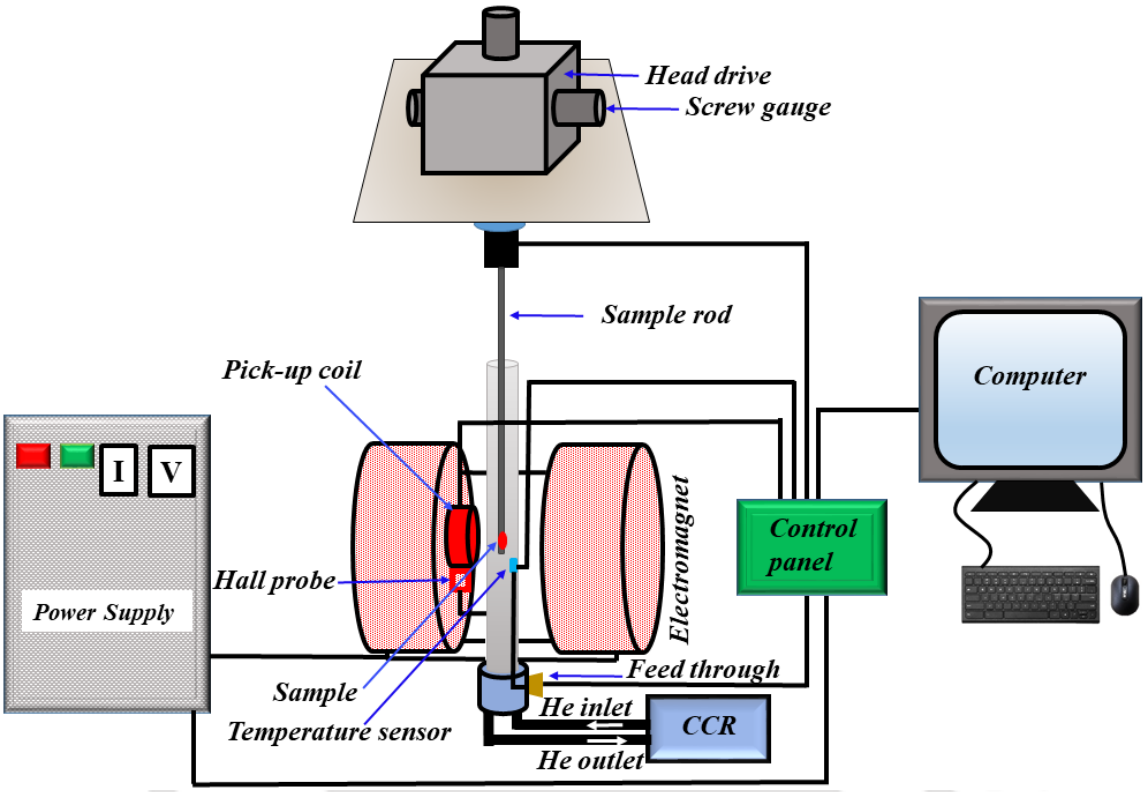

Fig. 2.10: Block diagram of VSM along with accessories.

The working principle of VSM is also based on Faraday's law, according to which changing magnetic flux can generate electromotive force (emf) in a coil or conductor. The sample is attached to a vertical quartz rod and placed in between the pole pieces of an electromagnet that producing a uniform magnetic field. When the magnetic sample is vibrated (80 Hz) vertically the number of magnetic flux changes. This induces an emf in the pick-up coil mounted on the pole pieces of the electromagnet, which is proportional to the magnetic moment of the sample. The magnetic field is measured by Gauss-meter with analog output capabilities. A Hall probe is mounted between the magnetic pole pieces close to the sample location. Various parts of the instrument are interfaced to a computer and parameters such as magnetic field, temperature are controlled by using IDEAVSM software. A proportional, integral and derivative (PID) temperature controller has been used to control the temperature precisely in between 300-1000 K. To perform the magnetic measurements above room temperature, a high-temperature oven setup equipped with a heater was used. During the measurement, Nitrogen/Argon gas was supplied to the oven continuously to avoid any possible

oxidation of the sample and overheating of the chamber. The temperature is measured by using a type K thermocouple attached to the oven. Before performing the measurement, calibration was carried out by using a standard Ni sample with a moment of 6.92 emu for 5000 Oe.

2.4.3 Dielectric Measurement Setup

The dielectric and impedance data were recorded by using Wayne Kerr make LCR meter (Model: 1J4300R/43100R) in the frequency range of 20 Hz to 10^5 Hz and temperature range of 27 K to 300 K. The AC voltage was set at 1 V throughout the measurements. The LCR data were recorded by using a software provided by Wayne Kerr through the RS232 interface. To study the dielectric properties, samples were taken in cylindrical pellet form with thickness of 1-1.5 mm and diameter of roughly 10 mm. Screw gauge and Vernier calliper were used to estimate the sample diameter and thickness precisely. To make the electrode, silver paste (Sigma Aldrich) was used on the surface of the pellet. The schematic diagram of the setup is shown in Fig. 2.11. The thin walled stainless steel (SS) chamber tube with an inner diameter of 13 mm and length of 800 mm is coupled to the sample holder made up of a nylon rod of length 700 mm. The sample was placed between two conducting plates at the bottom of the nylon rod. At the top of the SS tube chamber, electrical feedthrough was mounted for electrical connection to the temperature sensor and electrodes. The measurement was carried out in a parallel plate capacitor arrangement by employing four-terminal methods. The LCR meter was connected with the four leads and these leads are connected to sample holding plates in such a way that the top electrode is connected as I_H, V_H, while the bottom electrodes are connected to the I_L and V_L terminals. All the electrical connections from the electrical feed through to the electrodes and sensor were established by using copper wires.

For dielectric measurement at low temperature, Advanced Research System (ARS) make closed cycle refrigerator (CCR) cryostat (model DMX-19) equipped with a Lake Shore temperature controller (model 331) was used. Helium gas was purged into the sample chamber for a good thermal contact and temperature uniformity over the sample. The temperature was measured using a silicon diode sensor.

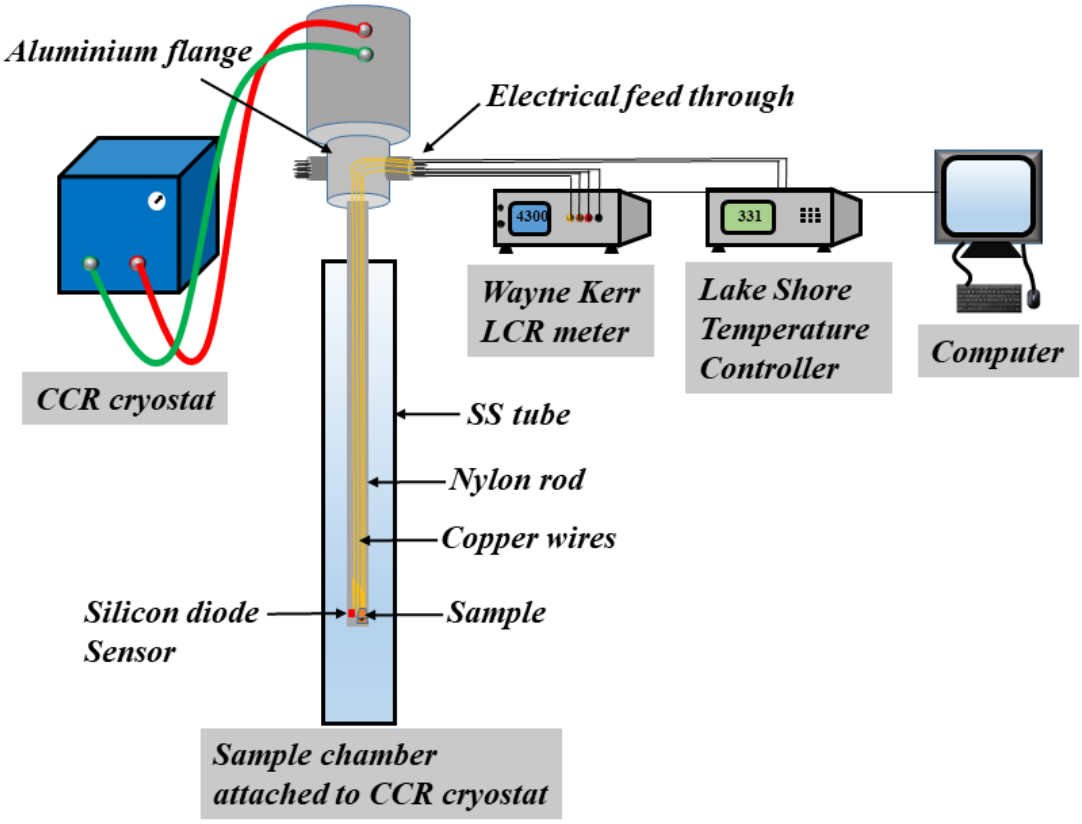

Fig. 2.11: Schematic diagram of dielectric measurement system.

The LCR meter detects the voltage across the device by transmitting current at a specific frequency (*f*) and computing the sample's impedance using the formula,

$$Z^*(f) = \frac{V^*(f)}{I^*(f)} \tag{2.11}$$

where Z^*, $V^*$and I^* represent the complex impedance, voltage and current, respectively. The real (Z') and imaginary (Z'') parts of the impedance data were directly obtained from LCR meter. Other dielectric parameters such as real and imaginary parts of dielectric constant (ε' and ε''), loss tangent ($tan\delta$), conductivity (σ_{ac}) were estimated by using following relations,

$$\varepsilon' = \frac{-Z''}{2\pi f C_0 (Z'^2 + Z''^2)} \tag{2.12}$$

$$\varepsilon'' = \frac{Z'}{2\pi f C_0 (Z'^2 + Z''^2)} \tag{2.13}$$

$$tan\delta = \frac{\varepsilon''}{\varepsilon'} \tag{2.14}$$

$$\sigma_{ac}(\omega) = 2\pi f \varepsilon'' \varepsilon_0 \tag{2.15}$$

where C_0 is the geometrical capacitance of the sample having thickness t and area A and can be expressed as,

$$C_0 = \frac{\varepsilon_0 A}{t} \tag{2.16}$$

Chapter 3

Mg Substituted $NiCr_2O_4$ series

As discussed in the introduction section, normal spinel nickel chromite ($NiCr_2O_4$), which crystallizes in tetragonal crystal structure attracts much attention due to their rich physical and chemical properties. It is ferrimagnetic (FIM) in nature with Curie temperature T_C = 70 K [77]. An additional transition occurring at T_N = 31 K is due to the antiferromagnetic (AFM) ordering of the transverse components of the magnetic moment [78]. In the spinel chromite, Ni^{2+} $\left(e_g^4 t_{2g}^4\right)$ cations are distributed in the tetrahedral sites, while octahedrally coordinated Cr^{3+} $\left(t_{2g}^3 e_g^0\right)$ cations form a corner sharing pyrochlore lattice, where spins are governed by geometrical frustraction due to antiferromagnetic exchange interaction among them. This compound crystallizes in cubic phase at high temperature with space group $Fd\bar{3}m$. When lowering the temperature, the symmetry of the nickel chromite decreases to tetragonal at 310 K driven by the cooperative Jahn-Teller (JT) effect associated with the Ni^{2+} cations in the tetrahedral position [26]. As a result, despite the presence of pyrochlore lattice formed by Cr^{3+} ions, the possibility of frustration is canceled out by the JT distortion. However, with non-JT magnetic A^{2+} (Mn^{2+}, Co^{2+}) ions, the system can survive frustration and can lead to spin glass like spiral ordering [1]. ACr_2O_4 (A = Zn^{2+}, Mg^{2+}, Cd), with a non-magnetic A^{2+} cations can give rise to frustrated AFM [142]. So, the choice of A site cation and the substitution at A site can result in interesting magnetic properties due to the modulation of different exchange interactions between the sublattices. The magnetic structure of $NiCr_2O_4$ contains two magnetic sublattices at tetrahedral (A) and octahedral (B) sites respectively. Two A sites are grouped into a single sublattice while four B sites are grouped into two sublattices with each sublattice having both longitudinal and transverse components of magnetic moment [79].

In this chapter, we have investigated the evolution of structural and magnetic properties of $NiCr_2O_4$ upon Mg substitution in bulk as well as in nanoparticle form for one composition. The present system is interesting because substitution of nonmagnetic Mg at JT active Ni site may trigger the frustration of corner sharing tetrahedra and hence could lead to exotic magnetic

phase. Apart from this, finite size of the particles may also play a prominent role in determining the magnetic structure of the system. So, in the present chapter, we present the structural and magnetic properties of bulk $Ni_{1-x}Mg_xCr_2O_4$ (x = 0-0.50) and nanoparticles of $Ni_{0.85}Mg_{0.15}Cr_2O_4$.

3.1 $Ni_{1-x}Mg_xCr_2O_4$ (x = 0 - 0.50) Bulk Series

The present section deals with the synthesis of Mg substituted $NiCr_2O_4$ bulk samples and the study of their structural and magnetic properties. We have carried out a detailed investigation on time, temperature and field dependent magnetic properties of these compounds.

Polycrystalline samples of $Ni_{1-x}Mg_xCr_2O_4$ (x = 0.0 – 0.50) were synthesized by using sol-gel method as discussed in Chapter 2. Stoichiometric ratio of $Ni(NO_3)_2{\cdot}6H_2O$, $Mg(NO_3)_2{\cdot}6H_2O$ and $Cr(NO_3)_3{\cdot}9H_2O$ of 99% purity were used as starting compounds for the synthesis. The precursors obtained by sol-gel method were presintered at 600 ^{0}C and 800 ^{0}C for 12 hours. Final sintering was performed at 1100 ^{0}C for 24 hours in pellet form. Room temperature XRD patterns, FESEM, EDX and magnetic data were obtained as per the details given in Chapter 2.

3.1.1 Structural Study

Room temperature powder XRD patterns for the parent and Mg substituted samples are displayed in Fig 3.1. We have observed shifting of (311) peak position towards lower 2θ value with Mg substitution, which generally suggests the increase in lattice parameters. To confirm the phase purity and to obtain the structural parameters, we have carried out Rietveld refinement for all the samples. The typical Rietveld refinements (black solid line) for x = 0, 0.05, 0.30 & 0.50 along with recorded patterns (red open circle) are shown in Fig 3.2 & Fig. 3.3. All the samples are in single-phase form with tetragonal structure ($I4_1/amd$) for x = 0 and cubic structure ($Fd\bar{3}m$) in Mg doped samples. For x = 0, the lattice parameters are found to be $a = b$ = 5.8299 Å and c = 8.4363 Å and they are comparable to earlier reports [24, 59]. The lattice parameters, reliability factors, unit cell volume and occupancy of all the samples are presented in Table 3.1. The occupancy values of the samples are normalized to formula units. All Mg substituted samples exhibit cubic structure with lattice constant varying from a

= 8.3186 Å for x = 0.05 to a = 8.3252 Å for x = 0.50. The increase in lattice parameters in the Mg substituted cubic systems can be understood in terms of the replacement of smaller Ni^{2+}(0.55 Å) ions by Mg^{2+}(0.57 Å) ions [143]. The structural transformation confirms that some of the JT active Ni^{2+} ions are replaced by JT inactive Mg^{2+} ions such that it drives the system into a higher-symmetric cubic crystal structure at room temperature.

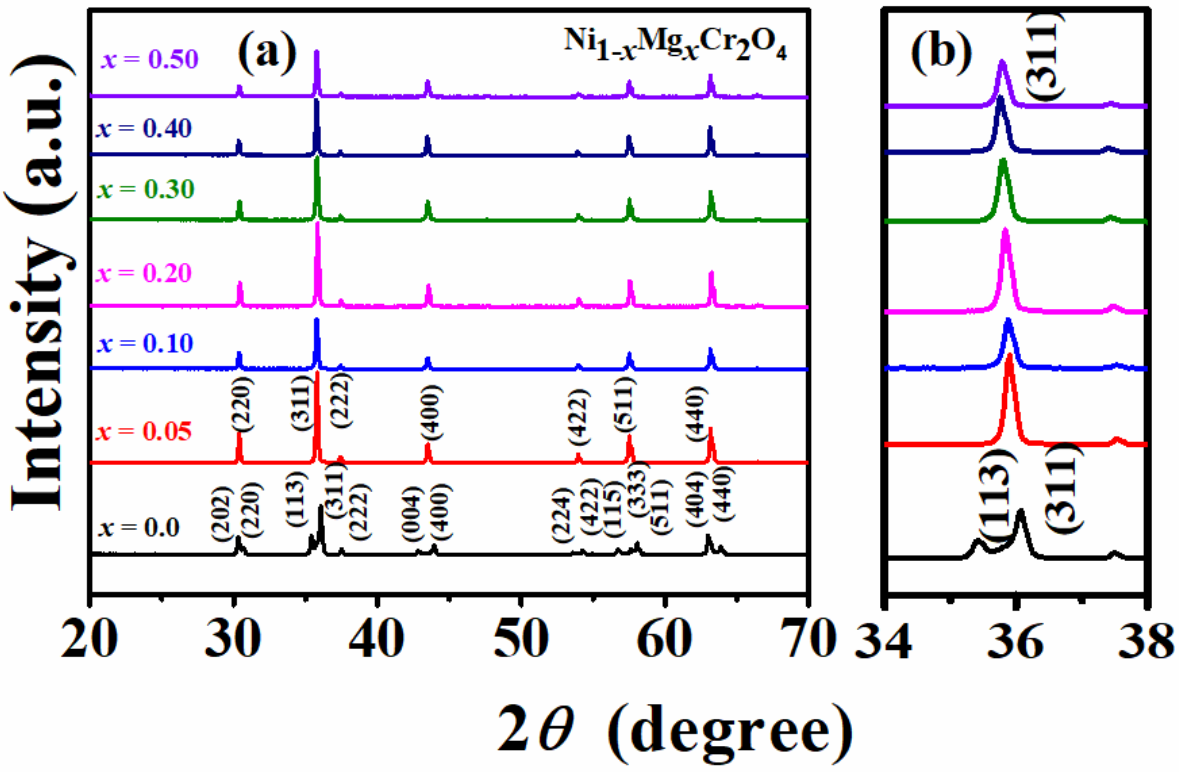

Fig. 3.1: (a) XRD patterns of $Ni_{1-x}Mg_xCr_2O_4$ (x = 0 – 0.50) series and (b) shifting of (311) peak position.

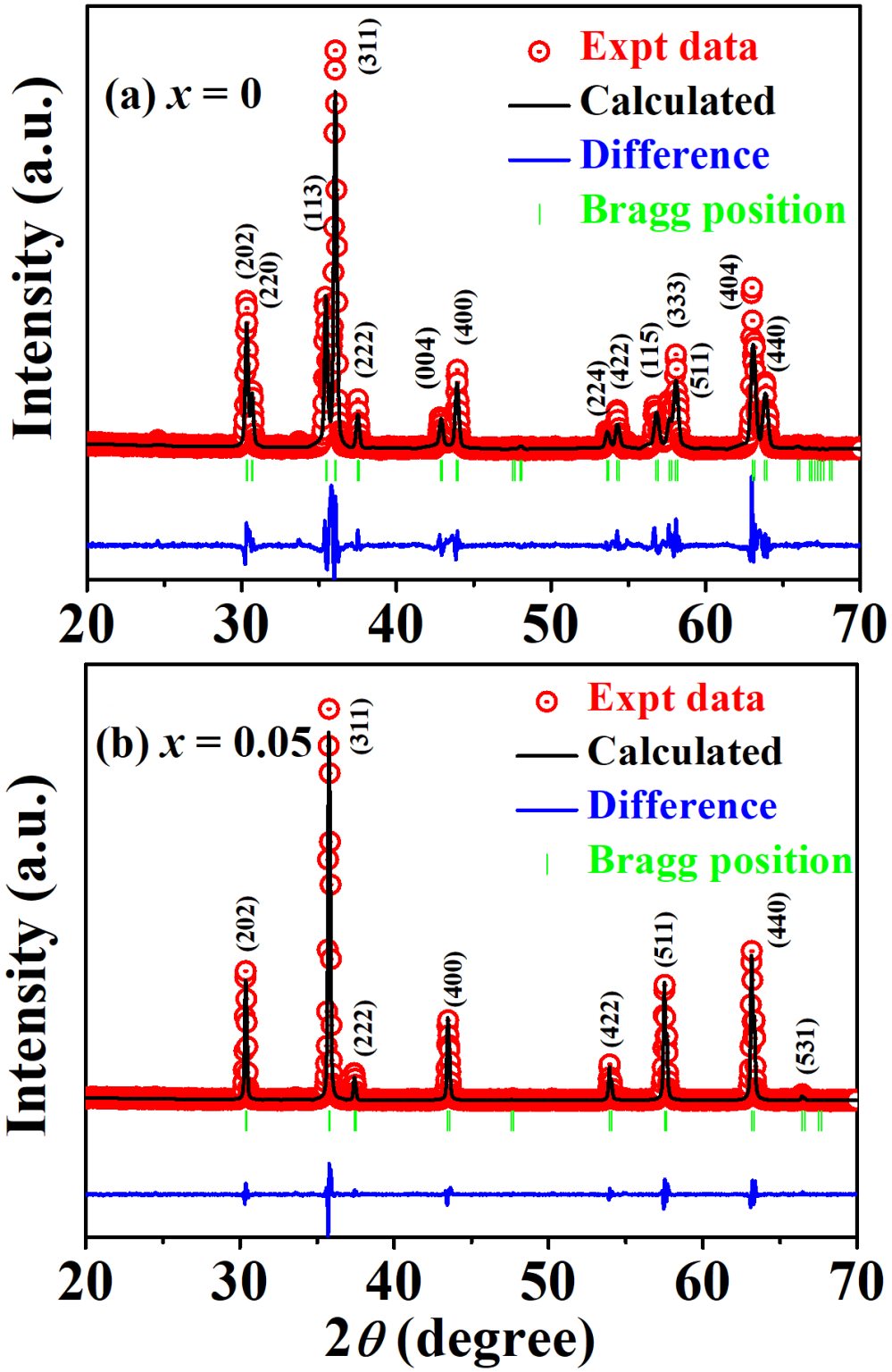

Fig 3.2: Rietveld refinement of the XRD patterns of (a) $x = 0$ and (b) $x = 0.05$ samples. The red open circles are the experimental data and the black solid lines are the fitted data. The bottom line shows the difference between experimental and refined data.

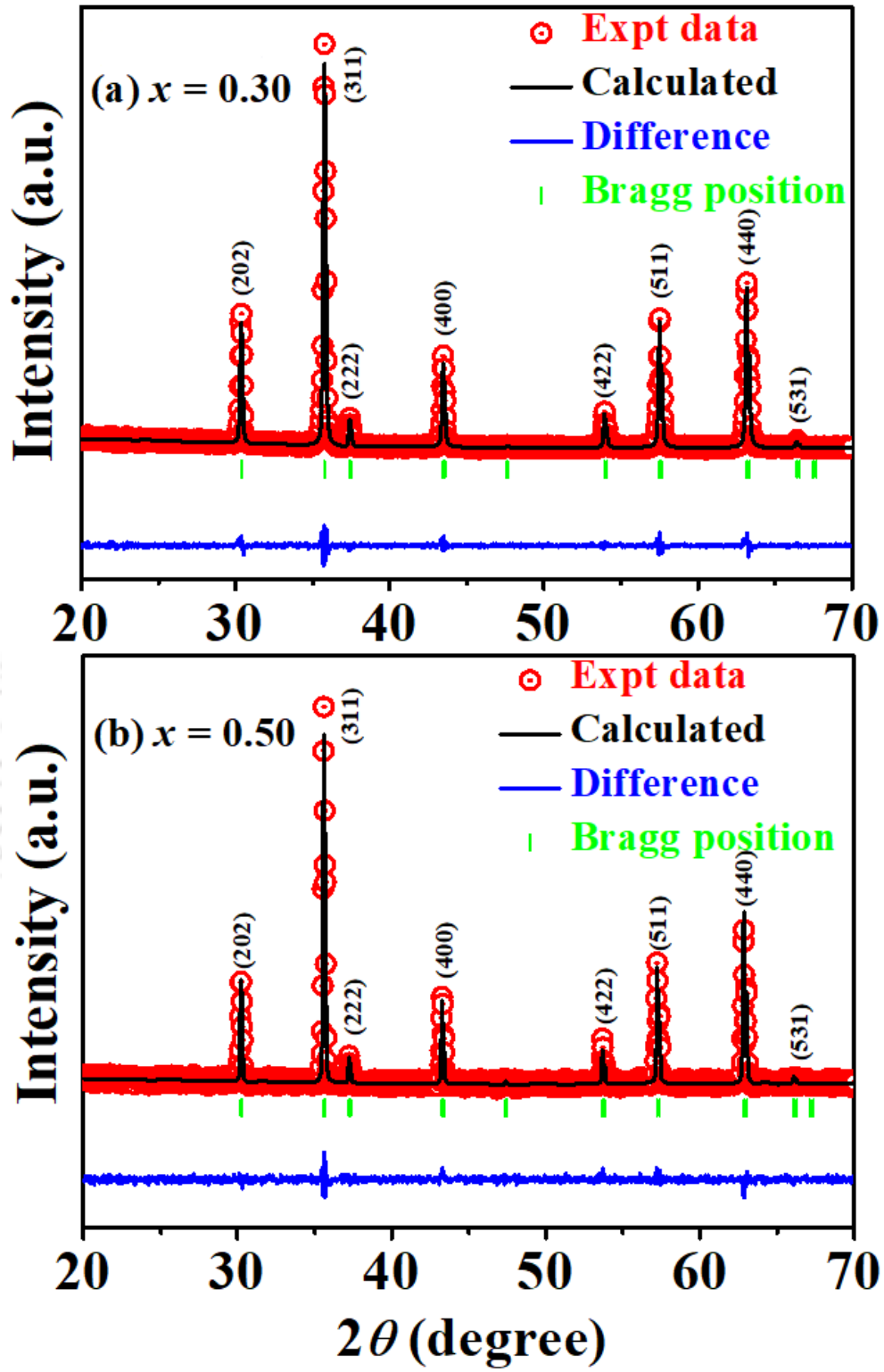

Fig 3.3: Rietveld refinement of the XRD patterns of (a) $x = 0.30$ and (b) $x = 0.50$ samples. The red open circles are the experimental data and the black solid lines are the fitted data. The bottom line shows the difference between experimental and refined data.

Table 3.1: Structural and reliability parameters obtained from the Rietveld refinement of XRD patterns of $Ni_{1-x}Mg_xCr_2O_4$ (x = 0 – 0.50).

Sample/ Parameters	x = 0	x = 0.05	x = 0.10	x = 0.20	x = 0.30	x = 0.40	x = 0.50
Space group	$I4_1/amd$	$Fd\bar{3}m$	$Fd\bar{3}m$	$Fd\bar{3}m$	$Fd\bar{3}m$	$Fd\bar{3}m$	$Fd\bar{3}m$
a (Å)	5.8299 (0.0002)	8.3186 (0.0001)	8.3206 (0.0004)	8.3214 (0.0003)	8.3222 (0.0001)	8.3248 (0.0003)	8.3252 (0.0001)
c (Å)	8.4363 (0.0005)	-	-	-	-	-	-
Volume (Å^3)	286.7	575.6	576.0	576.2	576.3	576.9	577.0
R_F (%)	3.7	1.8	2.1	2.2	2	2.6	3.1
R_{Bragg} (%)	5.3	2.1	2.2	3.1	2.4	3.9	4.2
R_P (%)	15.6	6.9	8.9	9.0	8.4	8.0	8.3
χ^2	8.0	2.5	2.4	3.8	2.5	2.35	2.3
Ni/Mg/Cr Occupancy	1.033 /0.000 /2.046	0.901 /0.109 /1.998	0.899 /0.110 /1.996	0.802 /0.189 /1.990	0.721 /0.284 /1.991	0.633 /0.395 /1.994	0.524 /0.501 /1.989

The typical FESEM micrographs of the samples are shown in Fig. 3.4(a - d). The particle sizes of the samples were determined by using ImageJ software. The variation of average particle size (d_{av}) with Mg substitution is estimated by fitting the size distribution histogram (Fig. 3.4(e-h)) to log normal distribution function [144],

$$f(l,\mu,\sigma_s) = \frac{1}{l\sigma_s\sqrt{2\pi}} exp\left(-\frac{(lnl-\mu)^2}{2\sigma_s^2}\right) \quad (3.1)$$

Where, μ is the logarithmic mean, l is the cross-sectional length of the particle, and σ_s represents the standard deviation. FESEM micrographs reveal that they exhibit broad particle size distribution.

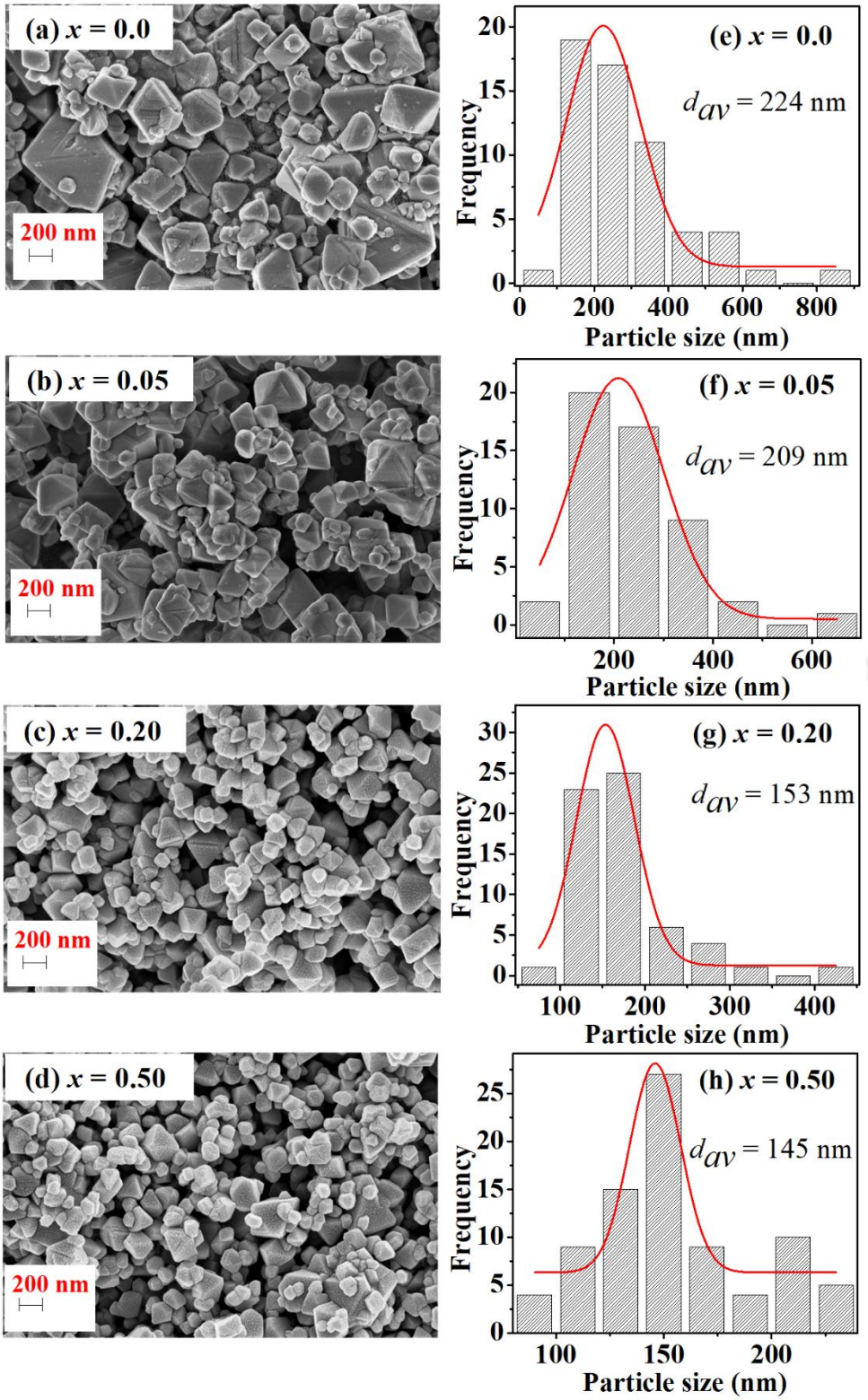

Fig. 3.4: FESEM micrograph (a-d) along with particle size distribution (e-h) for x = 0.0, 0.05, 0.20 & 0.50 samples.

We have observed a decrease in average particle size with increase in Mg concentration in the present series. All samples show similar kind of morphology with most of the particles having bi-pyramidal shape. The EDX spectra along with elemental mapping is shown in Fig. 3.5 for $x = 0$ & 0.05 samples. The cationic ratio Ni:Mg:Cr for $x = 0$ & 0.05 are found to be 1.04:0:2.00 and 0.96:0.03:2.00 respectively and are comparable to normal starting composition. The elemental mapping further confirms purity and the uniform distribution of various elements throughout the particles in these samples.

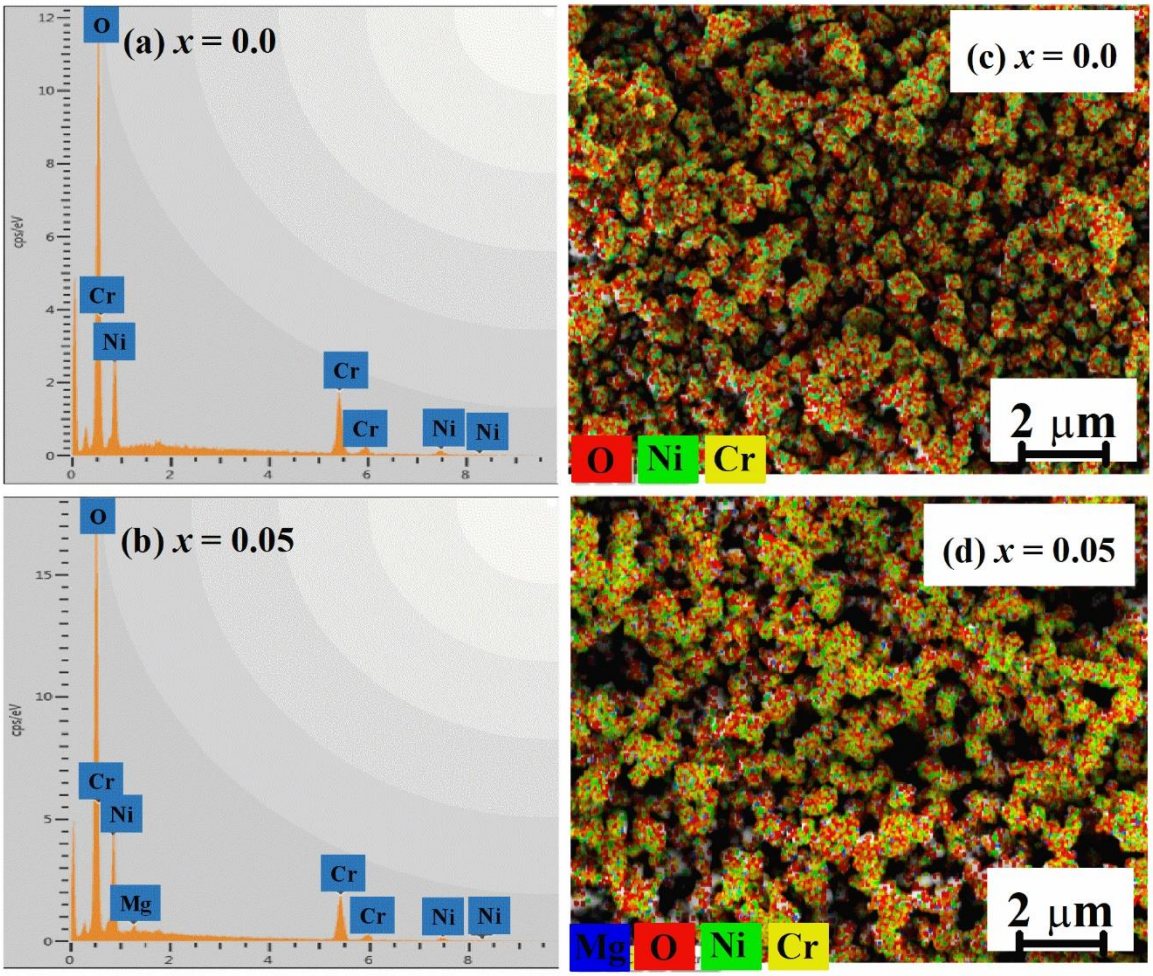

Fig. 3.5: EDX spectra (a, b) along with elemental mapping (c, d) for $x = 0$ & 0.05.

Raman spectroscopic study was carried out for all the samples in order to further understand the structural properties. Raman spectra of $Ni_{1-x}Mg_xCr_2O_4$ (x = 0-0.50) samples are shown in Fig. 3.6. For $NiCr_2O_4$, we have observed three Raman peaks at 688 cm^{-1}, 520 cm^{-1}

and 430 cm^{-1} and these can be assigned to $A_{1g}(1)$, $T_{2g}(2)$ and E_g modes, respectively [145]. With the increase in Mg substitution, the $T_{2g}(2)$ peak is found to shift towards a higher wavenumber due to the occupation of lighter Mg (24.30 u) atoms in the tetrahedral positions of Ni (58.69 u) atoms.

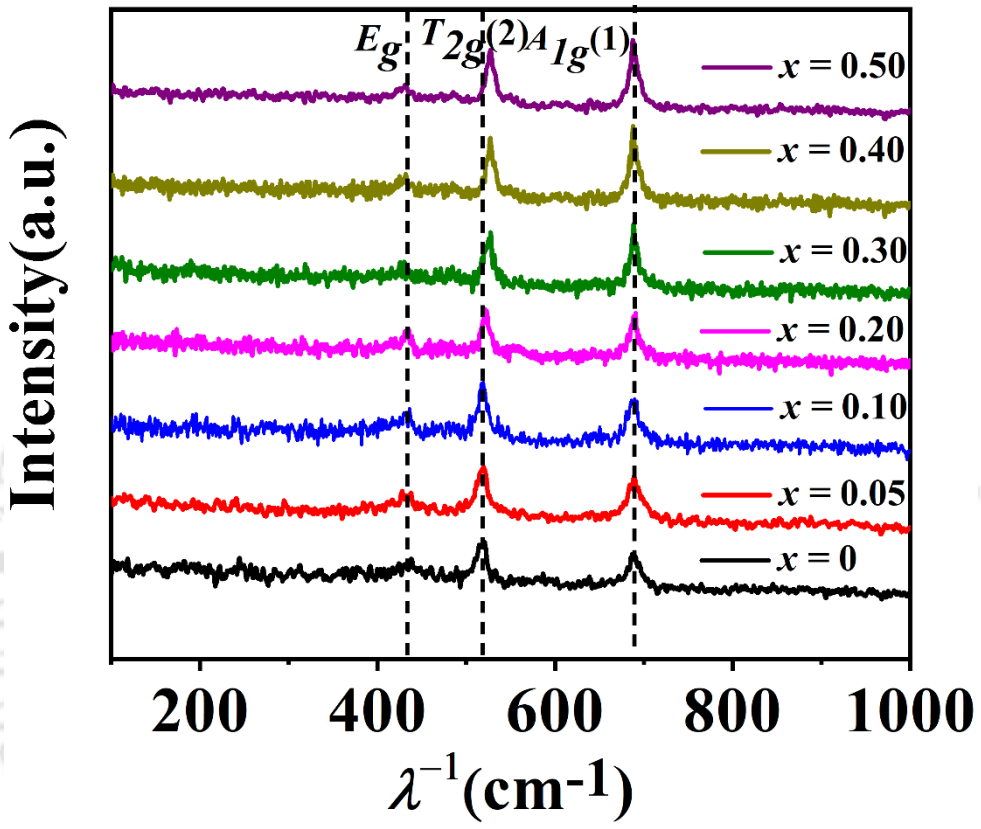

Fig. 3.6: Raman Spectra of $Ni_{1-x}Mg_xCr_2O_4$ (x = 0-0.50) at room temperature.

3.1.2 Temperature and Time Dependent Magnetic Properties

Susceptibility ($\chi = M/H$) as a function of temperature measured under zero field cooled (ZFC) and field cooled (FC) conditions for an applied field of H = 200 Oe are shown in Fig. 3.7 and Fig 3.8. Samples with x = 0.0, 0.05 and 0.10 are show typical FIM behavior while the rest of the samples i.e., for $0.20 \leq x \leq 0.50$ behave antiferromagnetically. For $T < T_C$, significant irreversibility between ZFC and FC curves appears for x = 0, 0.05 & 0.10. At 10 K for H = 200 Oe, the value of irreversibility in susceptibility is found to be $\Delta\chi/\chi_{ZFC}$ =

$(\chi_{FC} - \chi_{ZFC})/\chi_{ZFC} = 9.72$, for x = 0.0 sample. These values for x = 0.05 and 0.10 samples are found to be 11.41 and 22.08 respectively. The increase in irreversibility parameter confirms the enhancement of effective magnetic anisotropy with Mg substitution in these samples. The FIM transition temperature (T_C) values for the samples x = 0.0, 0.05 and 0.10 are found to be 70 K, 57 K and 42 K respectively. The T_C value for the parent compound is comparable to that reported in literature [80, 146]. We have observed a clear inflection in the $\chi - T$ plots of x = 0.0, 0.05, 0.10 samples at 29 K, 27 K and 22 K respectively due to the ordering of AFM component (T_N) of spin structure. In addition to the observed FIM and AFM transitions in x = 0.10 sample, we have observed a step like transition around T_f = 34 K as shown in Fig.3.7 (d) in an expanded scale. This may be due to the short-range glassy magnetic phase as a result of enhancement of frustration triggered by the substitution of nonmagnetic Mg.

From the ZFC and FC susceptibility (χ) curves of x = 0.20 and 0.30 samples, a peak like structure around 34 K followed by an enhancement in its value for T < 22 K have been observed as shown in Fig. 3.8. Recently, a similar type of complex magnetic transition has been reported in the FIM $Ni_{0.95}Zn_{0.05}Cr_2O_4$ compound and is explained in terms of short-range glass like magnetic structure due to the canting nature of magnetic moments [100]. However, in our system, magnetic behaviors in both x = 0.20 and x = 0.30 samples are dominated by the strong AFM interaction.

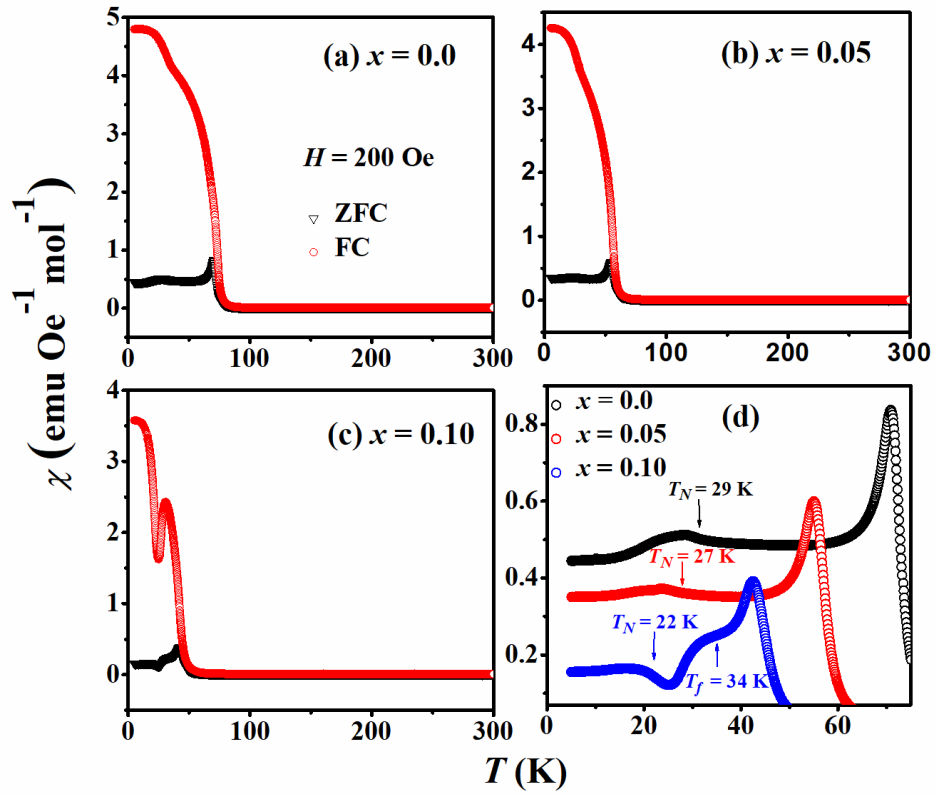

Fig. 3.7: Temperature dependent susceptibility (χ) under zero field cooled (ZFC) and field cooled (FC) conditions for (a) x = 0.0, (b) x = 0.05 and x = 0.10 samples. (d) ZFC $\chi - T$ plots in the expanded scale in the low temperature region.

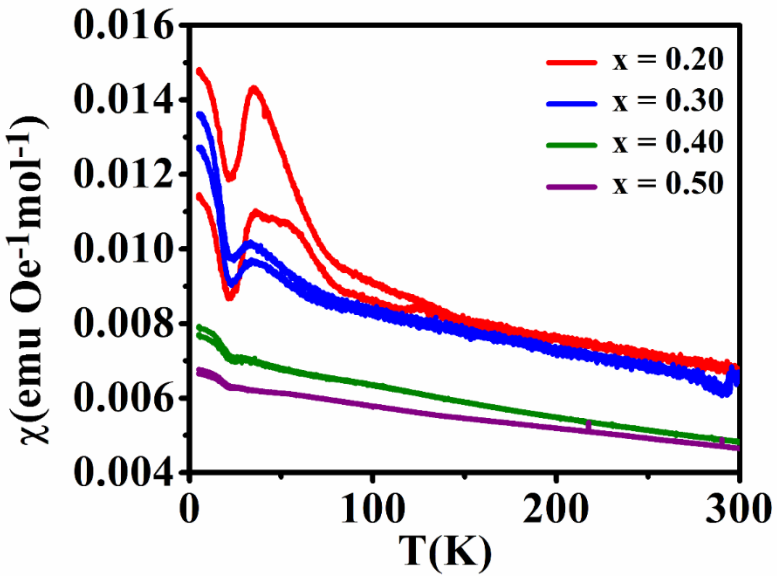

Fig. 3.8: Temperature dependent susceptibility (χ) under zero field cooled (ZFC) and field cooled (FC) conditions for x = 0.20, 0.30, 0.40, and 0.50.

In order to justify and investigate the nature of glassy magnetic phase in x = 0.10, 0.20 and 0.30 samples we have studied the relaxation of isothermal remanent magnetization (IRM) at T = 25 K, i.e., below the spin glass transition temperature (Fig. 3.9). For this study, the samples were first ZFC to T = 25 K and then a magnetic field of 6 T was applied. After reducing the applied field to zero, the remanent magnetization $M(t)$ was measured as a function of time upto $t = 10^3$ s. Glassy magnetic system shows long-lasting magnetization relaxation. Fig. 3.9 (a) & (b) show the normalized magnetization decay ($M(t)/M(t_0)$) for the FIM and AFM samples respectively. Where $M(t_0)$ stands for initial magnetic moment at t = 0 s. It can be noted, $M(t)/M(t_0)$ rapidly drops to a nearly constant value for non-spin glass sample, while it keeps continuously decreasing for spin glass systems [147]. From Fig. 3.9, it is clear that x = 0.10, 0.20 and 0.30 samples are showing promising behavior of relaxation of IRM. Additionally, even though all other samples are also showing relatively weak relaxation of IRM, we did not observe any distinct glassy transition in their respective temperature dependent susceptibility data.

The time dependent thermoremanent magnetization curve can be well explained by a stretched exponential function [148],

$$M(t) = M_0 + M_{sg} exp(-(t/\tau)^{1-n}) \quad (3.2)$$

Here, M_0 is related to the intrinsic FIM component and M_{sg} is attributed to the contribution from glassy magnetic phase. Fig. 3.9 (c&d) shows the fitting of thermoremanent magnetization data of x = 0.10, 0.20 & 0.30 to Eq. 3.2. The rate of relaxation is defined by the parameters τ and n, where n lies in the range of 0 to 1. The values of all the fitted parameters are presented in Table 3.2. The fitted values of n are considerably smaller than one which indicates that relaxation is due to the activation against multiple anisotropy barriers as observed in spin glass system [149]. The relaxation in thermoremanent magnetization suggests that the competition between FIM and AFM coupling leads to the cluster glass state due to the significant frustration in magnetic system.

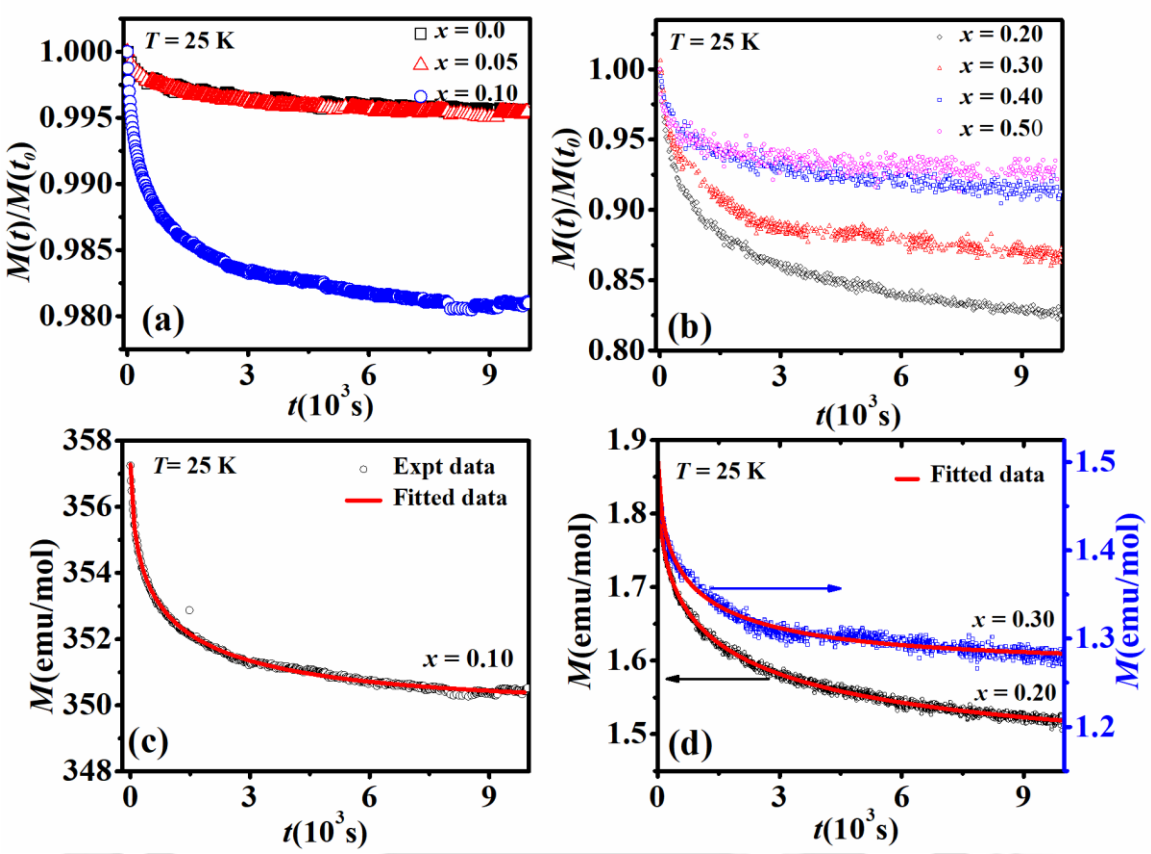

Fig. 3.9: Normalized relaxation of thermoremanent magnetization of (a) x = 0.0 - 0.10 (b) x = 0.20 - 0.50 along with fitted data for (c) x = 0.10, (d) x = 0.20 and x = 0.30.

Studying the temperature dependence of inverse susceptibility by using molecular field theory is an excellent approach to understand the magnetic properties. According to the molecular field theory of ferrimagnetism for $T > T_C$, the hyperbolic nature of inverse susceptibility can be characterized by the following expression [46],

$$\chi^{-1} = \left(\frac{(T-\Theta)}{C}\right) - \left(\frac{\xi}{(T-\Theta')}\right) \tag{3.3}$$

Here, the first term is the hyperbolic asymptote in the high temperature region and has a Curie-Weiss form and the second term stands for hyperbolic behavior near the FIM transition temperature. We fitted our experimental data to Eq. 3.3 as shown in Fig. 3.10 and the fitted parameters are presented in Table 3.2. A clear kink at T = 232 K observed in the inverse susceptibility curve of x = 0.05 (Fig. 3.10 b), can be attributed to the decreased JT transition temperature from 320 K for x = 0 sample due to the substitution of JT inactive Mg^{2+} ions.

However, we did not observe any such kink for the x = 0.10 sample in the paramagnetic (PM) region. Thus, the Mg substituted samples are more stable in the cubic crystal structure at room temperature due to the shifting of JT distortion below the room temperature. In order to fit the inverse susceptibility of x = 0.05 sample we consider the PM region below the onset of JT distortion i.e. for T < 232 K. Here the parameter Θ, is known as the asymptotic Curie temperature and it represents the strength of AFM exchange interaction between Ni^{2+} and Cr^{3+}. The characteristic temperature Θ' should be close to T_C [150]. The closeness of Θ' and T_C confirms the long-range FIM ordering in these samples. The difference between Θ' and T_C generally gives an idea of broadening of magnetization about FIM transition temperature. With increase in broadening, the magnetic disorder increases and the FIM state changes from long-range to short-range order [151]. Although there is an overall FIM ordering in the sample but considerable short-range order can produce cluster glass like dynamics below T_C. From earlier reports, it is confirmed that magnetic interaction in bulk $NiCr_2O_4$ is long range FIM in nature, so closeness of Θ' and T_C is expected. However, for x = 0.10, the difference between these two temperatures is distinguishable. The difference can be attributed to the increase in magnetic disorder in the sample. The parameter ξ, in the hyperbolic term represents the curvature in the inverse susceptibility plot. If $\xi \rightarrow 0$, Eq. 3.3 takes the form of a straight line i.e. the typical Curie-Weiss law. The ξ value is found to decrease with Mg substitution as given in Table 3.2 and it confirms domination of Curie-Weiss law term.

The spin only effective magnetic moment per formula unit of $NiCr_2O_4$ is 6.16 μ_B which is small as compared to the value obtained from the molecular field theory fitting (6.6 μ_B/f. u.). Though, the angular momentum of the system is largely quenched by the JT distortion at T = 320 K, but some contribution from partially quenched orbital magnetic moment cannot be neglected [146, 152]. We have observed a larger effective magnetic moment for x = 0.10 compared to the expected value of μ_{eff} = 6.10 μ_B per formula unit, which further confirms the unquenched orbital magnetic moment of Ni^{2+} in the tetrahedral sites of cubic structure due to considerable suppression of JT distortion by Mg^{2+} substitution. The electronic configuration of Ni^{2+} in the tetrahedral environment is $e_g^4 t_{2g}^4$. Due to the triply degenerate energy levels of t_{2g} caused by the similar shape of orbitals d_{xy}, d_{yz} and d_{zx}, one orbital can be transformed into another orbital by simple 90^0 rotation about proper axis. This orbital motion of electron gives

rise the orbital magnetic moment and contribute to the total magnetic moment of the system. In $NiCr_2O_4$, t_{2g} energy levels split into two energy levels due to the JT distortion taking place just above the room temperature. Therefore, the orbital magnetic moment is partially quenched. But with Mg substitution the JT distortion decreases and contribution from the orbital magnetic moment is higher compared to that of $NiCr_2O_4$.This is one of major possible reasons behind the high value of experimental effective magnetic moment of $x = 0.10$. In case of $x = 0.05$, we have fitted the inverse susceptibility data below ($T < 232$ K) the onset of JT distortion transition temperature and the experimental effective magnetic moment is close to the theoretical spin only magnetic moment (6.13 μ_B). Considering spin-orbital coupling in the system the theoretical effective magnetic moment of ions can be expressed as $\mu_{eff} = g\sqrt{J(J+1)}$ in the unit of μ_B. With $L = 3$, $S = 1$ and $g = 5/4$ for Ni^{2+} the effective magnetic moment is 5.59 μ_B, while that is for Cr^{3+} is 3.87 μ_B (spin only). Hence, the resultant effective theoretical magnetic moment for $x = 0.10$ compound is found to be 7.62 μ_B/f. u. and is close to our experimental value of 7.5 μ_B/f. u..

From the fitting of inverse susceptibility data, we can see that the frustration index (f = 16) for $x = 0.10$ compound is much higher than those of the other two FIM samples. Therefore, it is possible that such a frustrated magnetic behavior gives rise to a glassy state below the transition temperature $T_f = 34$ K.

Table 3.2: Magnetic parameters obtained from temperature and time dependent magnetization measurements and fittings.

Sample/ Parameters	x = 0.0	x = 0.05	x = 0.10	x = 0.20	x = 0.30	x = 0.40	x = 0.50
T_C (K)	70	57	42	-	-	-	-
T_N (K)	29	27	22	19	20	18	17
T_f (K)	-	-	34	30	29	-	-
τ (s)	-	-	750 ± 4	1460 ± 10	685±18	-	-
n	-	-	0.41	0.39	0.42	-	-
M_0 (emu/mol)	-	-	349.93	1.46	1.27	-	-
M_{sg} (emu/mol)	-	-	8.40	0.45	0.26	-	-
Θ (K)	-720	-403	-670	-	-	-	-
Θ' (K)	72	61	56	-	-	-	-
ξ (Oe mol K/emu)	1058	602	460	-	-	-	-
μ_{eff} (μ_B/f.u.)	6.6	6.1	7.5	-	-	-	-
$f = \left\|\frac{\theta}{T_C}\right\|$	10	7	16	-	-	-	-

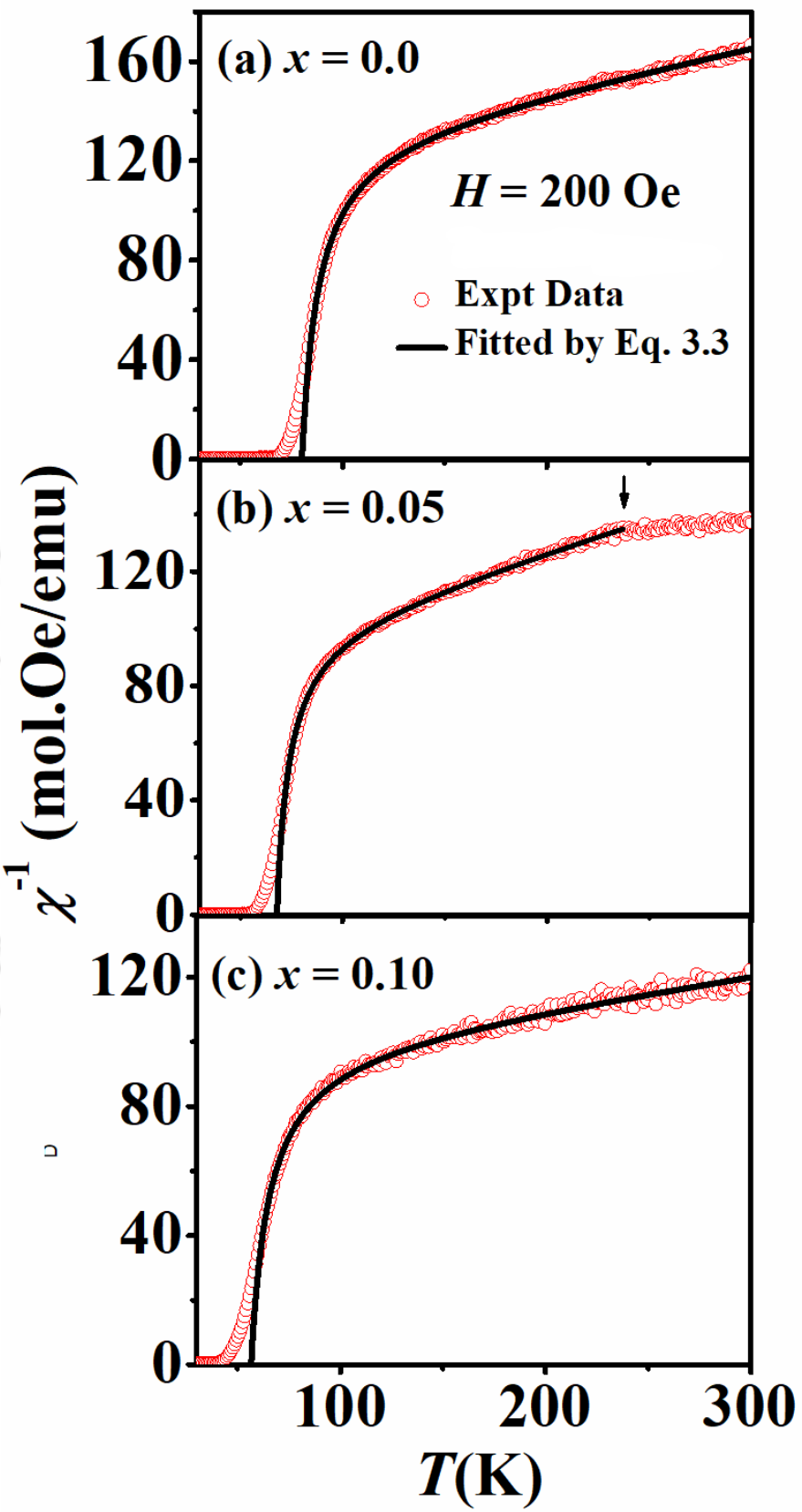

Fig. 3.10: Fitting of inverse susceptibility with Molecular field theory.

3.1.3 Field Dependent Magnetization and Exchange Bias studies

Magnetization as a function of applied magnetic field was recorded for all the samples at T = 5 K as shown in Fig. 3.11 (a & b). The unsaturated hysteresis loops for $x \leq 0.10$ samples indicate the presence of non-collinear magnetic structure of these compounds. The values of saturation magnetization (M_S) for $x \leq 0.10$ were estimated by using Law of Approach to saturation (LAS) for our polycrystalline samples. According to this law, the value of magnetization for high applied magnetic field $H >> H_C$ (H_C is coercivity) can be described by the following expression [153],

$$M = M_s\left(1 - \frac{8K_1^2}{105\mu_0^2 M_S^2 H^2}\right) + cH \tag{3.4}$$

where M_S is the saturation magnetization, H is the applied magnetic field, μ_0 is the free space magnetic permeability and K_1 is the effective magnetic anisotropy. The numerical coefficient 8/105 corresponds to polycrystalline material with cubic symmetry. The term cH represents force magnetization due to increase of saturation magnetization at high applied magnetic field. For $NiCr_2O_4$ the value of spontaneous magnetization is found to be 0.26 $\mu_B/f.u.$ at T = 5 K and is comparable to earlier report [79]. The value of saturation magnetization is found to decrease with Mg substitution and is 0.24 & 0.23 μ_B/f. u. for x = 0.05 and 0.10 respectively. The reduction in spontaneous magnetization can be understood by the substitution of nonmagnetic Mg^{2+} ions in place of magnetic Ni^{2+} ions in the system. The value of coercivity at 5 K for the parent compound is found to be 7384 Oe. An increase in coercivity is observed with Mg substitution which may be due to the enhancement of effective magneto crystalline anisotropy with Mg substitution. The value of coercivity for x = 0.05 & 0.10 is found to be 8486 & 7855 Oe respectively. The appearance of similar hysteresis loop and comparable coercivity values for x = 0.05 and 0.10 samples confirm the FIM nature of these samples. The observed large value of coercivity indicates the existence of competing AFM component along with a long-range FIM interaction. For $x \geq 0.20$ the predominant linear behavior of *M-H* curves confirm the strong AFM interaction in these samples.

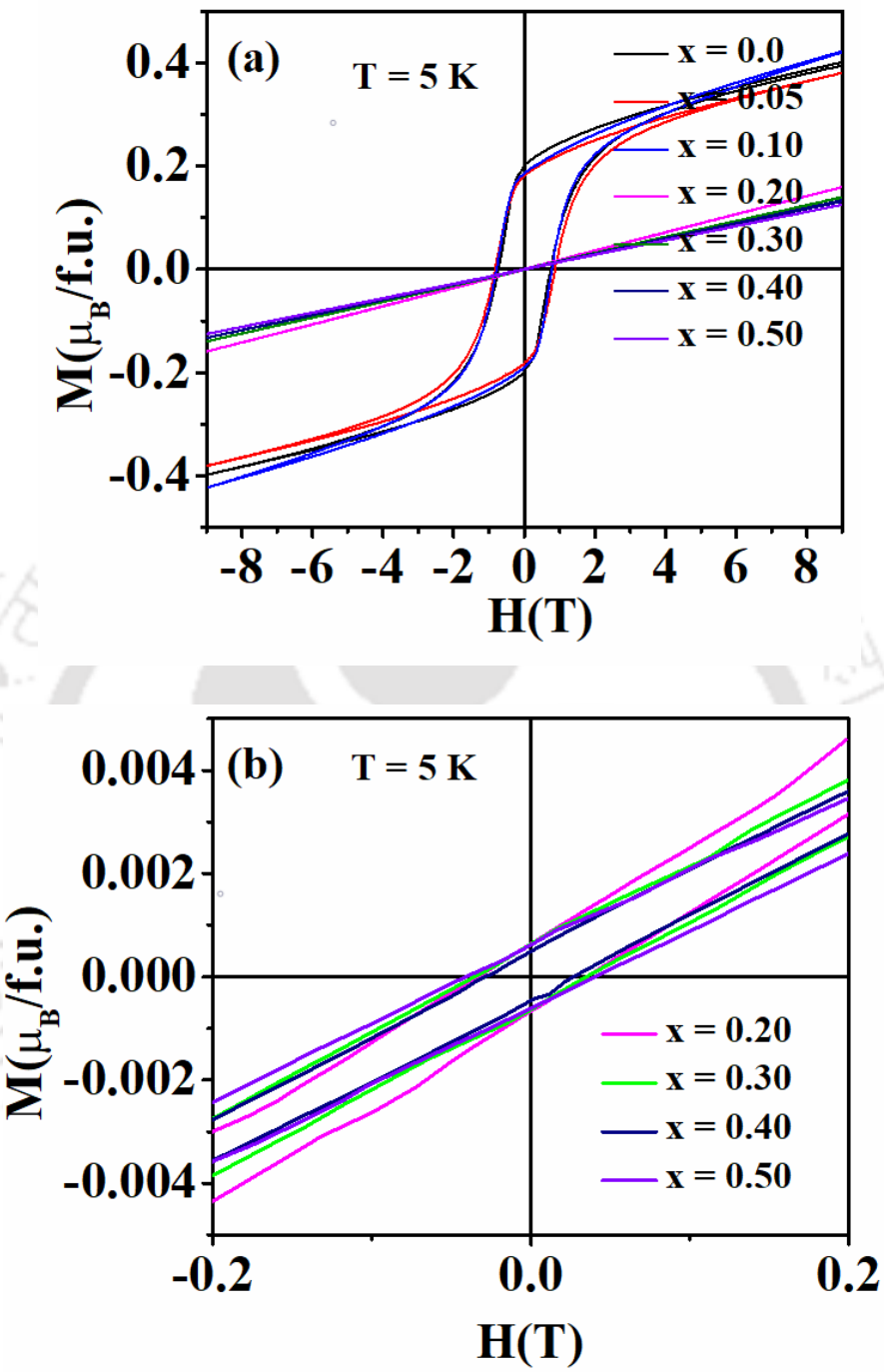

Fig. 3.11: (a) ZFC *M-H* curves at 5 K and (b) the magnified view of *M-H* loops near coercive field for $x \geq 20$.

The typical ZFC *M-H* loops recorded at different temperatures for x = 0 & 0.05 are shown in Fig. 3.12. (a & b). Both the samples exhibit FIM loops with considerable coercivity even as the temperature increases close to their corresponding FIM transition. The variation of

saturation magnetization and coercivity with temperature are shown in Fig 3.12 (c & d). As expected, both saturation magnetization and coercivity are found to decrease with increase in temperature for these samples.

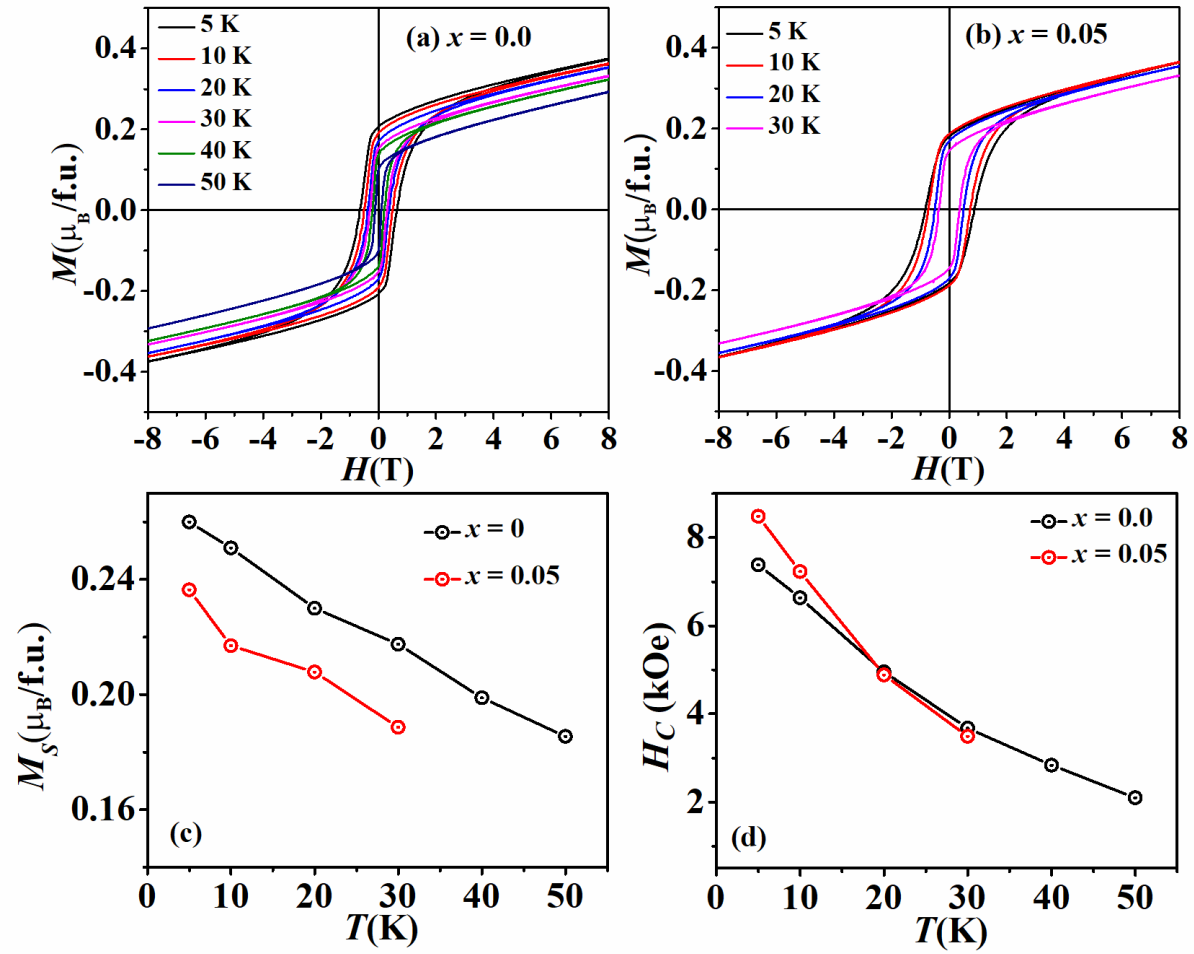

Fig 3.12: *M-H* loops recorded for (a) $x = 0$ and (b) $x = 0.05$ at different temperatures. Variation of (c) saturation magnetization (M_S) and (d) coercivity (H_C) as a function of temperatures for $x = 0$ & 0.05 samples.

Based on various temperature, time and field dependent magnetic properties as described above, the complete magnetic phase diagram can be constructed for the series as shown in Fig. 3.13. The magnetic structure of $x = 0$, 0.05 & 0.10 compounds are found to governed by long range magnetic interactions with distinct FIM and AFM transition temperatures. The intermediate compositions $x = 0.10$, 0.20 & 0.30 are showing the presence

of short range cluster glass like magnetic phases. We have observed dominant antiferromagnetic interactions in the end compositions x = 0.40 & 0.50 of the series.

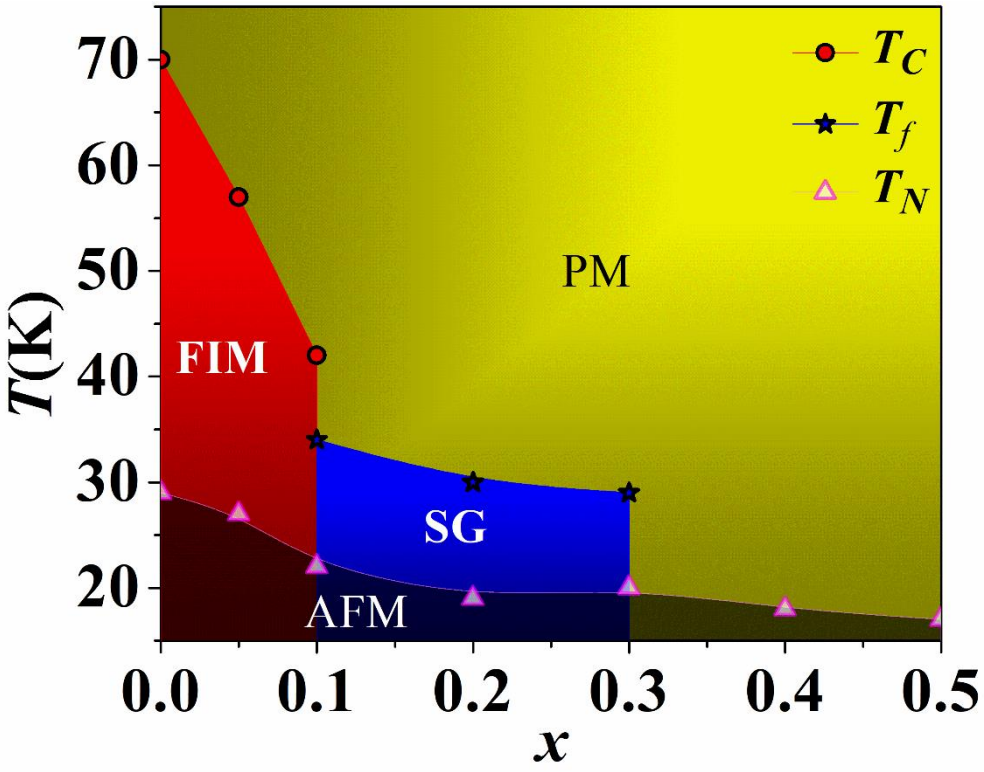

Fig. 3.13: Magnetic phase diagram of $Ni_{1-x}Mg_xCr_2O_4$ series.

It is a great deal of interest to explore the EB behavior in a magnetic system that shows FIM and AFM ordering. The presence of exchange bias behavior in magnetic materials provides technological application in spintronic devices [154, 155]. In order to investigate the EB effect in these FIM compounds, the magnetic hysteresis loops were recorded at T = 5 K after FC the samples at an applied field of 0.5 T from room temperature. We have observed shifting of *M-H* loop for all the FIM samples along the negative *H* axis as shown in Fig. 3.14. However, the shifting in the *M-H* loop for the parent compound is small as compared to the Mg substituted samples. The value of EB field (H_{EB}) and effective coercive field (H_C^{eff})were estimated by using the following relations as discussed in Chapter 1,

$$H_{EB} = (H_+ + H_-)/2 \quad (3.5)$$

$$H_C^{eff} = (H_+ - H_-)/2 \tag{3.6}$$

It is noted that the value of EB field also depends on maximum measuring field and FC field. The values of EB field at T = 5 K are found to be 91, 590 and 747 Oe for x = 0, 0.05 and 0.10 respectively for a maximum measuring field of 9T and FC field of 0.5T.

The shifting of hysteresis loop can be attributed to the presence of competing FIM and AFM moments in the system and can be explained by the model proposed by Tomiyasu and Kagomiya as discussed in Chapter 1 [79]. According to this model A sublattices are classified in to A1 - A2 pairs and B sublattices are classified into B1 - B3 and B2 - B4 pairs for FIM (longitudinal) ordering along {100} and AFM (transverse) ordering along {001}.

In spinel chromite uncompensated magnetic moment can exist due to the magnetic frustration occurring in the octahedral (B) pyrochlore sublattice [14, 156]. In $NiCr_2O_4$, for $T < T_C$, A sublattices moment μ_A (= $\mu_{A1\text{-}A2}$) is aligned along the field direction and dominates over the net B sublattices moment μ_B (= $\mu_{B1\text{-}B3}$ - $\mu_{B2\text{-}B4}$). So, under FC condition far above from the Curie temperature, the net magnetic moment of the sublattices is oriented along the field direction. Therefore, in the first quadrant of the hysteresis loop (initial curve) at a particular temperature, the uncompensated magnetic moment contributes to the total magnetic moment in the positive direction. As the direction of magnetic field is gradually reversed (second quadrant), it is quite difficult to align μ_A along the field direction due to the strong AFM interaction with μ_B. The substitution of nonmagnetic Mg^{2+} ions in the A sites further decreases μ_A and hence the value of μ_B component becomes quite dominant. As the μ_B component exerts a torque on the μ_A of ions, a relatively larger negative magnetic field is required to align the magnetic moment in the reverse direction. This asymmetric behavior in the ascending and descending branches of *M*-*H* loop gives rise to shift in hysteresis loop towards the negative field axis. With decrease in temperature the AFM interaction is strengthened and it gives rise to larger exchange bias field (H_{EB}).

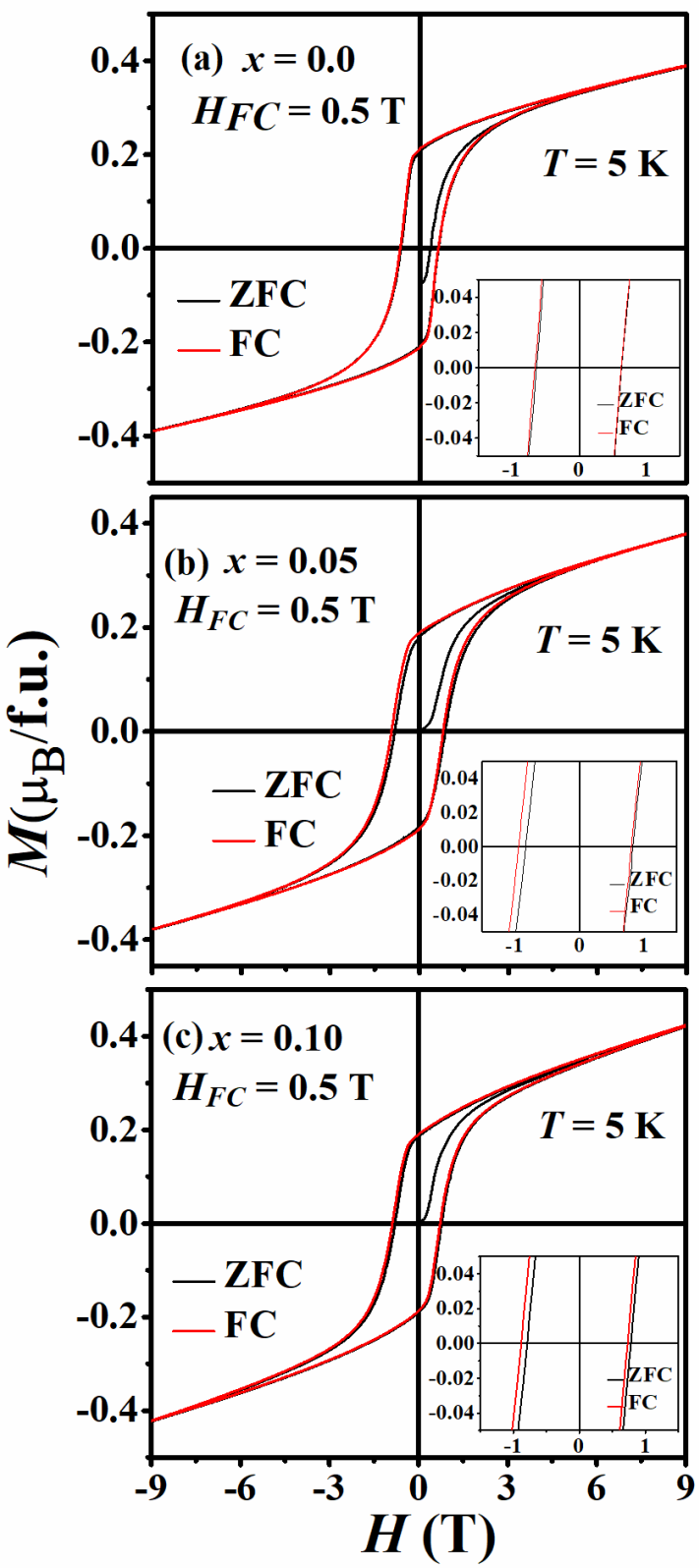

Fig. 3.14: Magnetic hysteresis loop recorded at 5 K under ZFC and FC conditions for (a) x = 0.0, (b) x = 0.05 and (c) x = 0.10. Insets show the loop in expanded scale close to H_C.

In order to understand the effect of temperature on H_{EB} and H_C^{eff}, we have taken taken several *M-H* loops at different temperatures for x = 0.10 sample. For this study, *M-H* loops were recorded with a maximum measuring field of ± 6 T after field cooling the sample at 0.5 T field. As shown in Fig. 3.15 (a), the exponential rise in magnitude of H_{EB} with decrease in temperature can be fitted to the exponential function of the form [90],

$$H_{EB} = H_{EB}(0)exp(-T/T_1) \tag{3.7}$$

where H_{EB} (0) is the value of $H_{EB,}$ at T = 0 K and T_1 is a constant. The best fitted parameters are found to be H_{EB}(0) = 2241 ± 5 Oe and T_1 = 4.99 ± 0.09 K. The exponential rise of H_{EB} with decrease in temperature can be undestood by growth of long range AFM ordering and corresponding increase in exchange anisotropy between FIM and AFM components at low temprature. The temperature dependance of H_C^{eff} is found to follow modified Kneller's law [157],

$$H_C^{eff} = H_C(0)[1 - (T/T_B)^{\alpha}] \tag{3.8}$$

where H_C (0) is the coercivity at T = 0 K, T_B is the blocking temperature and α is a constant. In case of nanoparticles (single domain), T_B represent the superparamagnetic blocking temperature and α = 0.5. Since, we are dealing with polycrystalline (multi domain) particles, therefore a deviation from original Kneller's law can be expected. From the fitted data as shown in Fig. 3.15 (b), the value of H_C (0) is found to be 10554 Oe. The estimated values of T_B and α are found to be 41.2 K and 0.64 respectively.

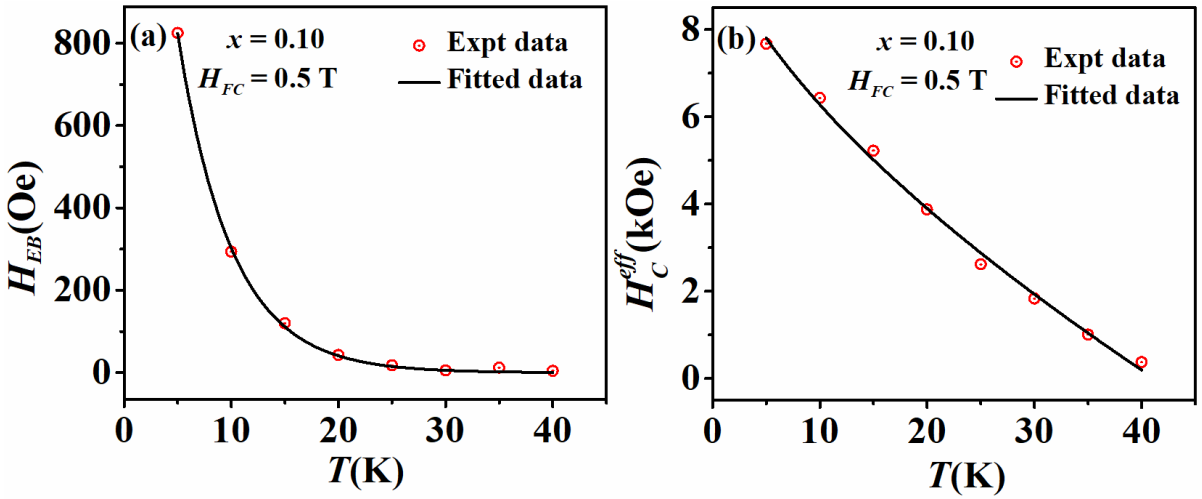

Fig. 3.15: Temperature dependence of (a) exchange bias (H_{EB}) and (b) coercivity (H_C) for x = 0.10.

EB behavior depends on both cooling field (H_{FC}) and maximum measuring field (H_{max}). Fig. 3.16 (a) & (b) show the variation of H_{EB} for x = 0.10 sample with respect to H_{FC} and H_{max} respectively. In order to study the effect of H_{FC} on H_{EB}, we recorded M-H data after cooling the sample at 0.05, 0.1, 0.5, 1, 3 and 5 T respectively. As shown in the inset of Fig. 3.16 (a), the initial increase in H_{EB} for H_{FC} upto 1 T can be atributed to the consolidation of magnetic domains due to applied higher cooling magnetic field. However, for cooling field H_{FC} > 1T the H_{EB} value decreases due to possible permanent allignment of some of the components of magnetic moment along the field direction, thereby reducing the anisotropic exchange interaction between FM and AFM components. Fig. 3.16 (b) shows hysteresis loops recorded at various maximum measuring field. For each loop, the sample was cooled down to 5 K from room temperature at a field 0.5 T and measurements were carried out in the field ranges H_{max} = ± 1, ± 2, ± 3, ± 6 and ± 9 T. To avoid the remanence effect, each hystersis loop was recorded after demagnetizing the sample by warming to room tempearture, removing of the stray magnetic field in oscillating mode and field cooling to 5 K again. We have observed a monotonic decrease in H_{EB} with increase in measuring field. For $H_{max} \leq 3$ T, mostly minor loop is observed with considerable vertical shift in magnetization. The decrease of H_{EB} with increase in measuring field can be understood in terms of dominant Zeeman energy which overcomes the exchange anisotropy.

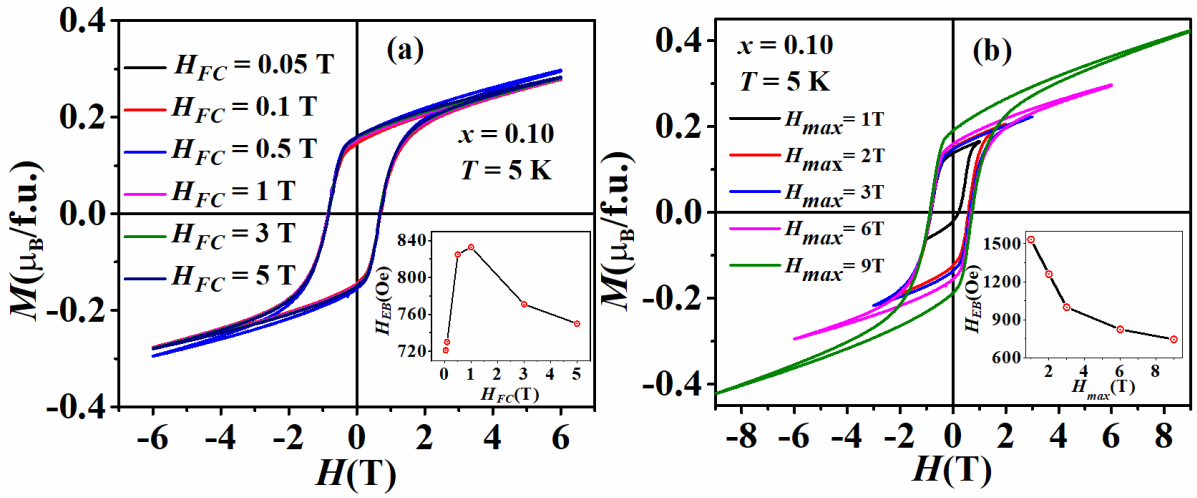

Fig. 3.16: (a) Cooling field (H_{FC}) dependence of exchange bias and (b) the maximum measuring field (H_{max}) dependence of exchange bias for x = 0.10.

3.1.4 Training Effect

Training effect is an interesting characteristic of EB phenomena. The training effect refers to the gradual and monotonous decrease of H_{EB} when the sample is cycled through consecutive hysteresis loops at a fixed temperature. Training effect was first observed by Paccard *et. al.* in 1966 in three systems exhibiting FM – AFM coupling with uniaxial anisotropy [158]. Usually, the shift in first loop appears to be more as compared to the others. Also, this decrease in the shift is more prominent of the left branch of *M-H* loop than the right hand one, resulting a decrease in coercivity of hysteresis loops. In general, training effect can be classified into two categories. The first is a considerable decrease in H_{EB} from n = 1 to n = 2 loop, and the second is a minor decrease in H_{EB} as the number of subsequent hysteresis loops increases when n > 2. For n > 2, training effect follows a power law [159],

$$H_{EB}(n) - H_{EB}(\infty) \propto 1/\sqrt{n} \tag{3.9}$$

In order to investigate training effect in x = 0.05 compound eight consecutive hysteresis loops (n = 8) have been recorded at 5 K after field cooling through T_N with H_{FC} = 0.5 T. Consecutive hysteresis loops are shown in Fig. 3.17 (a), where the inset shows the plot in the expanded scale close to M = 0. Fig. 3.17 (b) shows the decrease in H_{EB} with increase in loop numbers.

The observed training effect may be due to the relaxation of AFM components along an equilibrium configuration by each reversal process.

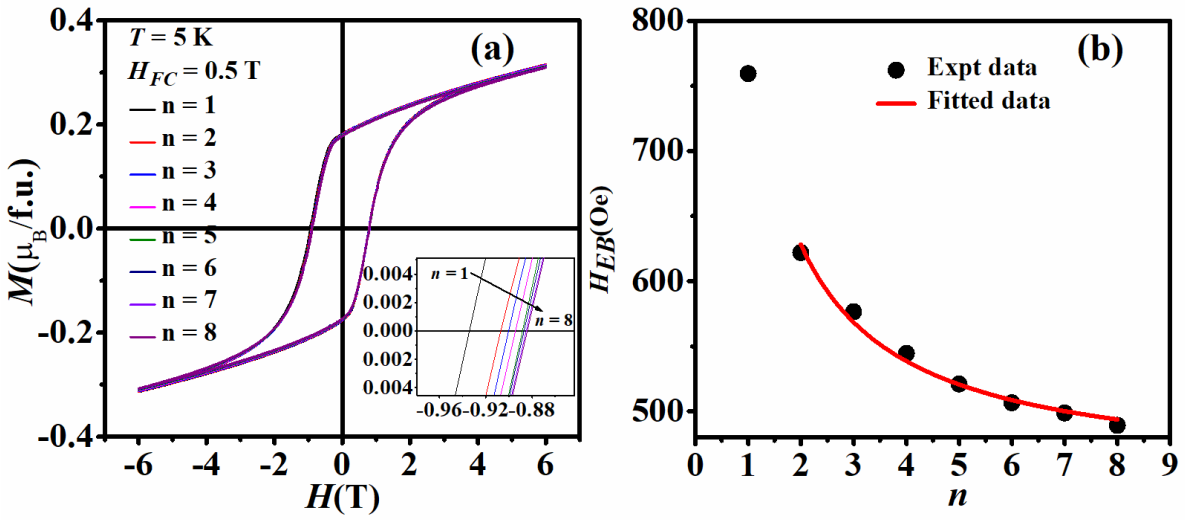

Fig 3.17: (a) Consecutive *M-H* loops recorded at T = 5 K for x = 0.05 with index n = 1 to n = 8. Inset shows the loops in expanded scale (b) H_{EB} as a function of n along with fitted data using Eq. 3.9.

3.2 Magnetic Properties of $Ni_{0.85}Mg_{0.15}Cr_2O_4$ Nanoparticles

As discussed in the previous section, investigations on Mg substituted bulk $NiCr_2O_4$ systems revels that substitution of nonmagnetic Mg at JT active Ni sites enhanced the frustration and hence led to a cluster glass like magnetic phase in the system. However, such properties may not be observed in its nano counterpart, as size of the particles also play a prominent role in determining the magnetic structure of a system. Several effects, such as randomly oriented uncompensated surface spin, dominant surface anisotropy, spin-glass like state may occur in nanomagnetic systems [160, 161]. Previous investigations on magnetic nanoparticle systems also suggested the possibilities of complex magnetic structures as a result of the anisotropic exchange interaction between these disordered surface spins and ordered core magnetic moments [162, 163]. In this context, a detailed study has been carried out by means of magnetization measurement to investigate the various exchange interactions inside the core and the possible effect of disordered surface spins. In this section, preparation of 15 atm % of Mg substituted $Ni_{0.85}Mg_{0.15}Cr_2O_4$ nanoparticles and their structural, static and dynamic magnetic properties are presented.

$Ni_{0.85}Mg_{0.15}Cr_2O_4$ nanoparticles are synthesized by hydrothermal route as discussed in Chapter 2. The as synthesized powder was heated at 700^0 C for 4 hours to get final product as polycrystalline $Ni_{0.85}Mg_{0.15}Cr_2O_4$ nanoparticles. For phase identification powder X-ray diffraction pattern was recorded at room temperature using a Rigaku X-ray diffractometer (XRD) (TTRAX III) using Cu-Kα (λ = 1.5406Å) radiation. The particle size and microstructure of samples were analyzed by recording microstructural images using ZEISS make FESEM (ΣIGMA) and JEOL make FETEM (2100F) systems. The magnetization data were recorded by using Vibrating Sample Magnetometer (VSM) probe installed in Quantum Design Physical Property Measurement System (PPMS) fitted with a superconducting magnet of 9T capacity.

3.2.1 Structural and particle size analysis

Room temperature XRD pattern along with Rietveld refinement for $Ni_{0.85}Mg_{0.15}Cr_2O_4$ nanoparticles is illustrated in Fig. 3.18 (a). The sample is showing single phase form with cubic crystal ($Fd\bar{3}m$) structure. From Rietveld refinement, the lattice constant is found to be a =

8.3560(6) Å. To estimate the bond angles and understand the underlying exchange interactions, we have used VESTA software by applying the results of Rietveld refinement as shown in Fig. 3.18 (b). Generally, in collinear spinel system the standard bond angles of A – O – B & B – O – B networks should be 125^0 & 90^0 respectively [164]. The bond angles of Ni/Mg – O – Cr & Cr – O – Cr networks in our present system are found to be 124.9^0 & 90.5^0 respectively, which indicates the possibilities of collinear spin configuration in the system. However, structural change and influence of the strong antiferromagnetic Cr – Cr direct exchange interaction can't be ruled out at low temperature, which are primely responsible for canted or spiral like spin structure in most of the bulk spinel chromite system [1, 79].

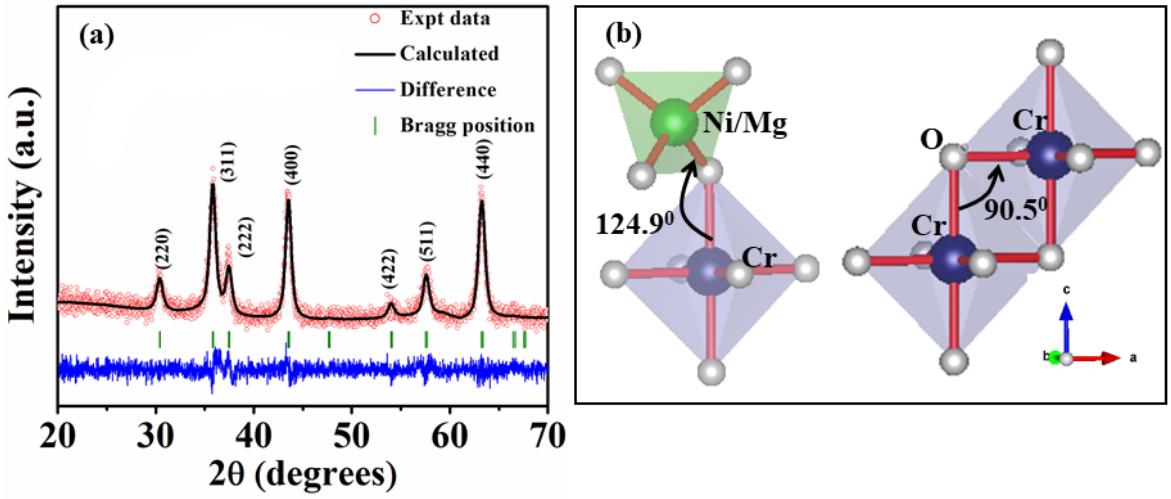

Fig. 3.18: (a) Room temperature X - ray diffraction pattern along with Rietveld refinement of $Ni_{0.85}Mg_{0.15}Cr_2O_4$. (b) Bond angles of Ni/Mg – O – Cr and Cr – O – Cr networks obtained from VESTA program.

FESEM micrograph and particle size distribution as shown in Fig. 3.19 (a&b) reveal strongly agglomerated nanoparticles with an average particle size of 46 nm. The TEM image (Fig. 3.19 (c)) also shows the agglomeration of nanoparticles. The high resolution TEM image shown in Fig. 3.19 (d) clearly demonstrates (220) plane with an interplanar spacing of 0.297 nm and it is comparable to the d spacing of 0.295 nm, estimated by using $d = \frac{a}{\sqrt{h^2+k^2+l^2}}$ (where a = 8.3560 Å as per XRD refinement). The selected area electron diffraction (SAED) pattern of the sample is shown in Fig. 3.19 (e), where clear diffraction rings corresponding to various (hkl) planes are seen. These patterns indicate the polycrystalline nature of agglomerated

nanoparticles. The interplanar spacing estimated from SAED pattern for different (hkl) planes can be fitted by using $d = \frac{a}{\sqrt{h^2+k^2+l^2}}$ as shown in Fig. 3.19 (f). The lattice constant obtained from the fitting is found to be a = 8.395 ± 0.035 Å, which is comparable to the lattice constant estimated by Rietveld refinement and hence confirms the reliability of our (hkl) plane identification and crystal structure at microscopic level.

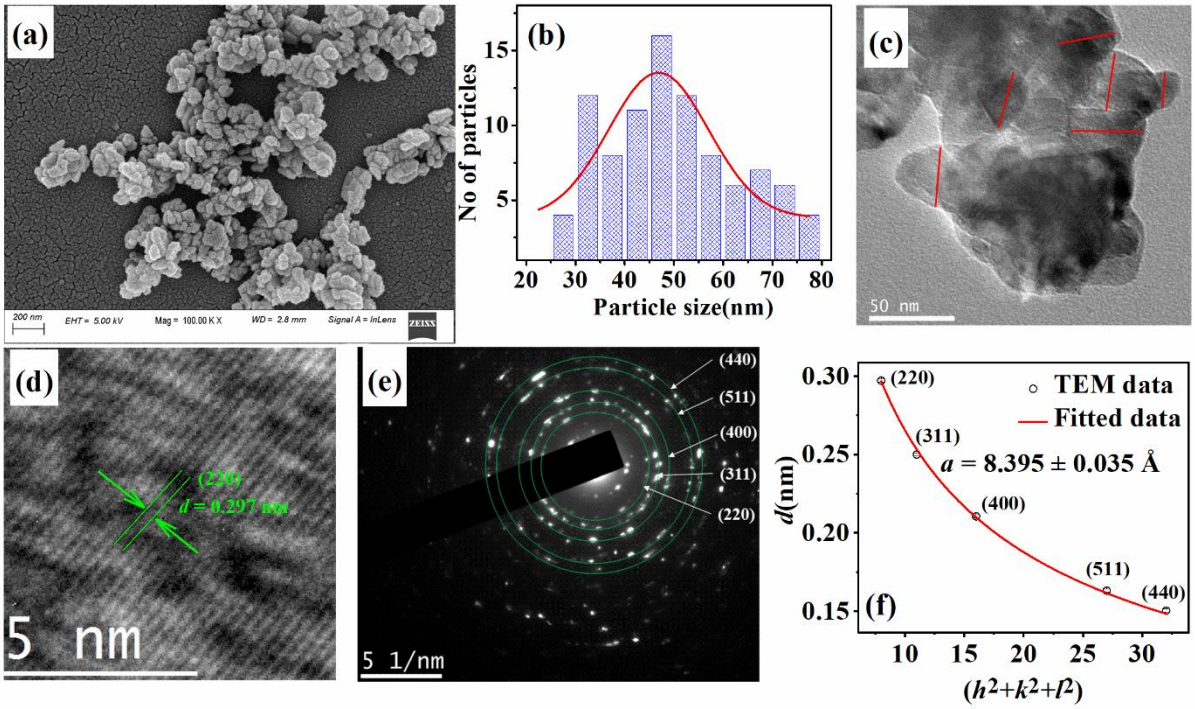

Fig. 3.19: (a) FESEM micrograph (b) particle size distribution fitted to Lorentz distribution (c) TEM image (d) HRTEM image with (220) planes. (e) SAED pattern and (f) estimation of lattice constant from d – spacing obtained from SAED pattern for $Ni_{0.85}Mg_{0.15}Cr_2O_4$ nanoparticles.

The EDX spectrum of $Ni_{0.85}Mg_{0.15}Cr_2O_4$ nanoparticles is shown in Fig. 3.20. The cationic ratio of Ni:Mg:Cr is found to be 0.85:0.19:2.0 and it is comparable to the normal starting composition.

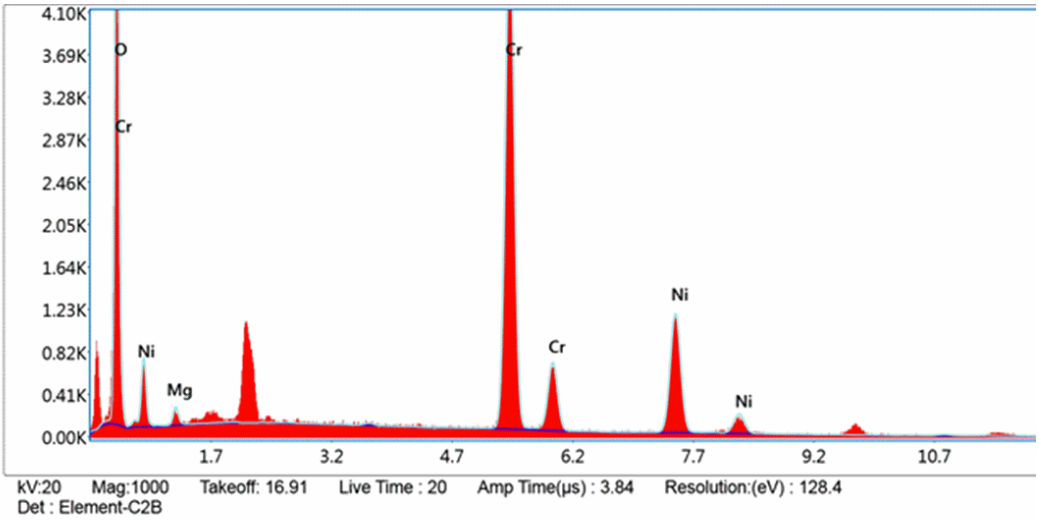

Element	Weight %	Atomic %	Error %	Net Int.	K Ratio	Z	A	F
O K	30.72	59.09	6.81	1692.63	0.1707	1.1621	0.4783	1.0000
Mg K	2.07	2.62	17.01	62.94	0.0036	1.0800	0.1614	1.0010
Cr K	45.33	26.82	1.89	3284.58	0.4239	0.9098	1.0035	1.0243
Ni K	21.88	11.47	3.56	898.56	0.1867	0.9161	0.9209	1.0115

Fig. 3.20: EDS spectrum of $Ni_{0.85}Mg_{0.15}Cr_2O_4$ nanoparticles.

In order to understand the possible ionic states of cations, we have carried out XPS studies for the samples. In Fig 3.21 the high-resolution core level photoelectron spectra of (a) Ni 2p (b) Mg 2pand (c) Cr 2p are shown respectively. All the spectra were calibrated against the C 1s reference peak at 284.8 eV. The binding energies of the Ni 2p doublet were found to be 856.2 eV ($2p_{3/2}$) and 874.2 eV ($2p_{1/2}$), respectively, leading to a difference of binding energy of 18 eV. The peak positions and shape and energy separation indicating that Ni is in the 2+ oxidation state. In addition to main sublevels, satellite peaks were also observed at higher binding energies relative to these sublevels. This could be the result of shake-up and multiplet splitting processes involved in Ni 2p levels. Similarly, the core level spectrum peak of Mg 2p at 49.5 eV suggest Mg^{2+} ionic state in the sample. Fig. 3.21 (c) depicts the Cr 2p core levels with energy separation between the Cr $2p_{3/2}$ and Cr $2p_{1/2}$ levels about 10 eV suggesting Cr is in 3+ oxidation state.

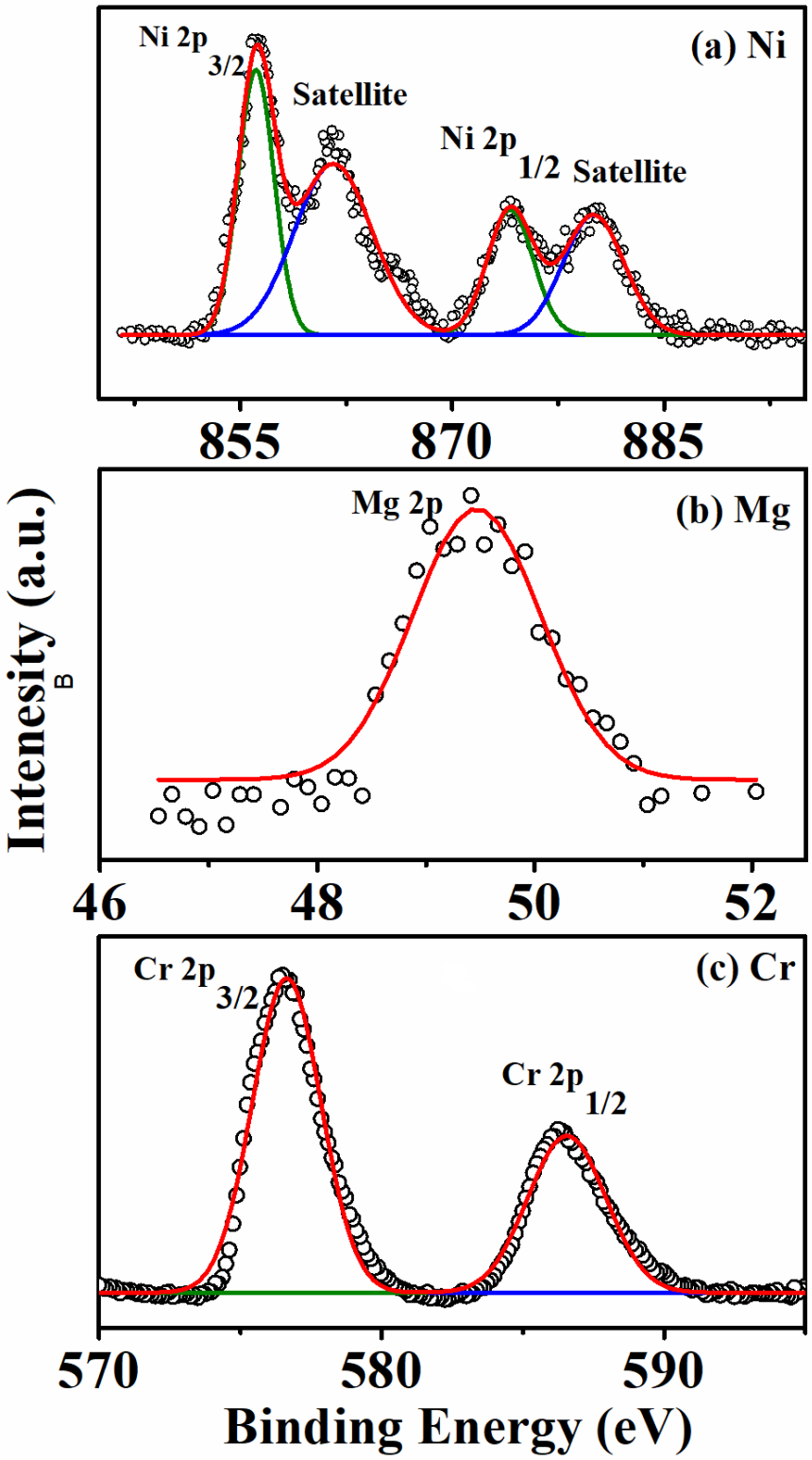

Fig 3.21: Core level XPS spectrum of (a) Ni (b) Mg and (c) Cr ions of $Ni_{0.85}Mg_{0.15}Cr_2O_4$.

3.2.2 Magnetic Characterization

Temperature dependent dc magnetization data measured under zero field cooled (ZFC) and field cooled (FC) conditions for H = 200 Oe are shown in Fig. 3.22 (a). The temperature-dependent magnetization (M vs T) shows three distinct features: Irreversibility between ZFC and FC magnetization starting from T_{irr} = 125 K, a broad maximum of ZFC magnetization around T_C = 76 K and a sharp maximum of ZFC magnetization at T_f = 9.5 K. As shown in the inset of Fig. 3.22 (a), the blocking phenomenon of ferrimagnetic nanoparticles is often suggested by the magnetic irreversibility between ZFC and FC magnetization at T_{irr} [153]. The broad magnetic transition around T_C is attributed to the ordering of ferrimagnetic (longitudinal) components of magnetic spin structure. The broadening of magnetization near T_C often indicates magnetic disorder in a system. With increasing broadening, the magnetic disorder increases, as observed in the present system. According to the core-shell model of ferrimagnetic nanoparticles, such disorder is related to the contribution of surface spins and long-range ferrimagnetic order associated with core spins [150, 165]. Below 30 K, progressive freezing of surface spin occurs and leads to a frozen cluster glass like state for $T < T_f$ [162, 163]. Therefore, the magnetic behavior in the present system is governed by both particle core and surface spins.

In order to further explore the low temperature peak, we have measured ZFC susceptibility (M/H) as a function of temperature (T) for different applied magnetic fields H = 100 Oe to 1000 Oe. These plots especially in the low temperature region are shown in Fig. 3.22 (b). The peak temperature T_f is found to shift towards low temperature with increase in applied field. At low temperatures (T < 6 K), ZFC M/H curves measured at different magnetic field appears to be field independent as typically observed in spin glass like materials [166].

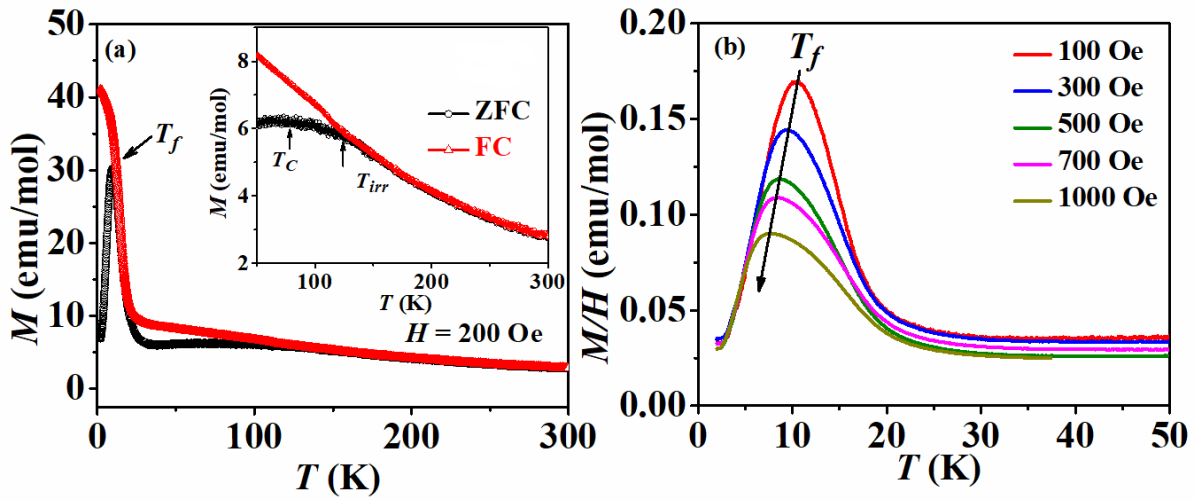

Fig. 3.22: (a) Temperature variation of ZFC and FC magnetization data of $Ni_{0.85}Mg_{0.15}Cr_2O_4$ compound at H = 200 Oe. Inset shows the enlarged view of the same data near T_C and T_{irr}. (b) M/H vs T at different magnetic field.

Temperature dependence of inverse susceptibility (χ^{-1}) in the high temperature region i.e. $T > T_{irr}$ is studied by Curie –Weiss (CW) law [167],

$$\chi = \frac{C}{T - \theta_C} \tag{3.10}$$

Here, C and θ_C are the Curie constant and Curie temperature respectively. The temperature dependence of inverse susceptibility fitted to CW law curve is shown as solid line in Fig. 3.23 along with measured data. The estimated value of $\theta_C = -24.9 \pm 0.4\ K$ and its negative sign indicates that the magnetism in the sample is governed by AFM or FIM superexchange interactions. The estimated value of θ_C is reported to be -557 K for bulk $NiCr_2O_4$ [59]. The small magnitude of θ_C in the present system further suggests the presence of relatively weak superexchange interactions. In addition, frustration index $f\left(=\frac{|\theta_C|}{T_C}\right)$ is found to be 0.3 as compared to 7.8 for bulk $NiCr_2O_4$. From Monte Carlo simulation, it is found that θ_c is proportional $(3J_{BB} + 6J_{AB} + J_{AA})$ [168], where, J_{AA}, J_{AB} & J_{BB} are the nearest neighbor AFM superexchange integrals along A – O – A , A – O – B & B – O – B pathway. On the other hand, T_C is only proportional to J_{AB} [150]. Since J_{AA} is very small as compared to J_{BB} and J_{AB},

therefore frustrated index f is proportional to the ratio $\frac{J_{BB}}{J_{AB}}$. A weak frustration index therefore indicates the dominance of J_{AB} over J_{BB}. As discussed in Chapter 1, according to Lyons, Kaplan, Dwight and Menyuk (LKDM) theory [51], strength of geometrical magnetic frustration (GMF) for spinel structure can also be estimated from 'u' parameter,

$$u = \frac{4J_{BB}S_B}{3J_{AB}S_A} \tag{3.11}$$

where, S_A & S_B are the magnitude of magnetic moment of A & B sublattices respectively. $u = \infty$ signifies large GMF [169], $\infty > u > 1.298$ signifies weak GMF and results in short range spiral ordering as observed in $MnCr_2O_4$ and $CoCr_2O_4$ [1]. Long range spiral configuration is observed for $1.298 \geq u \geq 8/9$. Neel type collinear FIM or AFM ordering prevails when $u < 8/9$ as observed in spinel ferrites. The strong domination of J_{AB} over J_{BB} confirms the tendency of spin structure towards collinearity in the present system, rather than spin canting (observed in bulk $NiCr_2O_4$). As a result, no distinct AFM ordering of the transverse component is observed in the system, which is a signature of the canted spin structure of bulk $NiCr_2O_4$. The experimental effective paramagnetic moment can be determined from Curie constant $C = N\mu_{eff}^2/3k_B$, obtained from the fitting. The theoretical effective moment is estimated by using $\mu_{theo} = \sqrt{(0.85)\mu_{Ni}^2 + 2\mu_{Cr}^2}$, where μ_{Ni} and μ_{Cr} are the theoretical moment of Ni^{2+} and Cr^{3+} ions in high spin state calculated by considering spin only contribution. The experimental value is found to be $\mu_{expt} = 6.05\ \mu_B$ and it is comparable to the theoretically calculated spin only magnetic moment $\mu_{theo} = 6.06\ \mu_B$.

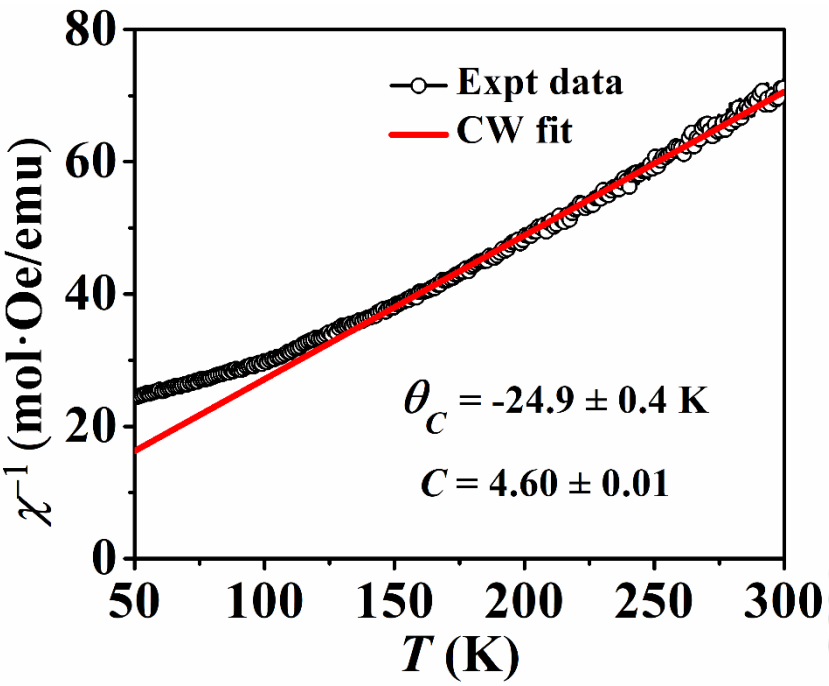

Fig. 3.23: Curie –Weiss fitting of temperature dependence inverse susceptibility (χ^{-1}) data of FC magnetization at H = 200 Oe.

Memory effect, aging and out-of-equilibrium dynamics:

The memory effect in spin configuration and the corresponding magnetization is a characteristic feature of superparamagnetic and glassy nanomagnetic system. Memory effect studied in FC condition is shown in Fig. 3.24 (a). In FC investigation, the sample was cooled in an external field of H = 200 Oe from 150 K down to 2 K with a slow cooling rate of 1 K/min. Below T_f, we interrupted the cooling process at T_1 = 8 K and T_2 = 5 K for a duration of t_w = 1 hour each. At each stopping temperature, the magnetic field was turned off and the system was allowed to relax. After the lapse of waiting time (t_w), the same magnetic field was reapplied and resumed the cooling process. The magnetization curve obtained from this process is referred as M_{FCC}^{stop} (FCC: field cooled cooling data). After reaching T = 2 K, sample was warmed up to paramagnetic region in the same magnetic field and the memory magnetization curve (M_{FCW}^{mem}) (FCW: Field cooled warming data) was recorded. The conventional FC magnetization curve during cooling was also recorded for the compound and is depicted as M_{FCC}^{ref}. From Fig. 3.24 (a), it is clear that the obtained M_{FCW}^{mem} curve is exhibiting a clear signature of the past

history by attempting to follow the M_{FCC}^{stop} curve. This indicates that the previous behavior of the spins during the cooling protocol is imprinted as a memory in the system.

In a glassy magnetic system, the spin-spin correlation length grows during the halting time, even in zero magnetic field, and shows a memory dip in zero field cooled warming (ZFCW) data at halting temperature upon reheating. Therefore, memory effect under the ZFC condition is unique to SG or cluster glass only and is not observed in a superparamagnetic state. To study ZFC memory effect, the sample was cooled from 150 K down to 2 K at a constant cooling rate of 1 K/min in the absence of external magnetic field. The cooling process was interrupted at $T = 6$ K for a duration of time of 4 h. After reaching 2 K, a probing magnetic field of 200 Oe was applied and the magnetization (M_{ZFCW}^{mem}) was measured as a function of temperature during warming. The conventional ZFC magnetization curve (M_{ZFCW}^{ref}) was also recorded with the same rate for reference. As shown in the inset of Fig. 3.24 (b), the temperature dependence of the difference in magnetization $\Delta M = M_{ZFCW}^{mem} - M_{ZFCW}^{ref}$ between the memory and reference data does not indicate clear evidence of memory dip at 6 K in the ZFC protocol. However, the observed non-zero ΔM between 2 K and 25 K, indicating the magnetic moment configuration rearranges spontaneously toward an equilibrium state due to the growth of correlation length during the imposed waiting period as observed in typical SG materials. This indicates that a glass-like correlation is taking place in the present nanoparticles system. The absence of clear evidence of the ZFC memory effect confirms the possibility of weak interparticle interactions to retain the ZFC memory effect in the present system. Apart from interparticle interactions, it is also notated that in nanoparticles, the glass-like magnetic phase may also appear due to the frustrated surface spins or due to the random freezing of surface spins. Gandhi et al. have explained the absence of the ZFC memory effect in NiO nanoparticles by taking into account the effect of unidirectional anisotropy (UA) associated with the strongly pinned surface spins [170]. A similar type of non-zero value of ΔM has been reported near halting temperature in the ZFC memory of Fe_2O_3 nanoparticles with a surface spin glass like state [171]. UA mediated FC only memory effect has been observed in Cr_2O_3 nanorods [172].

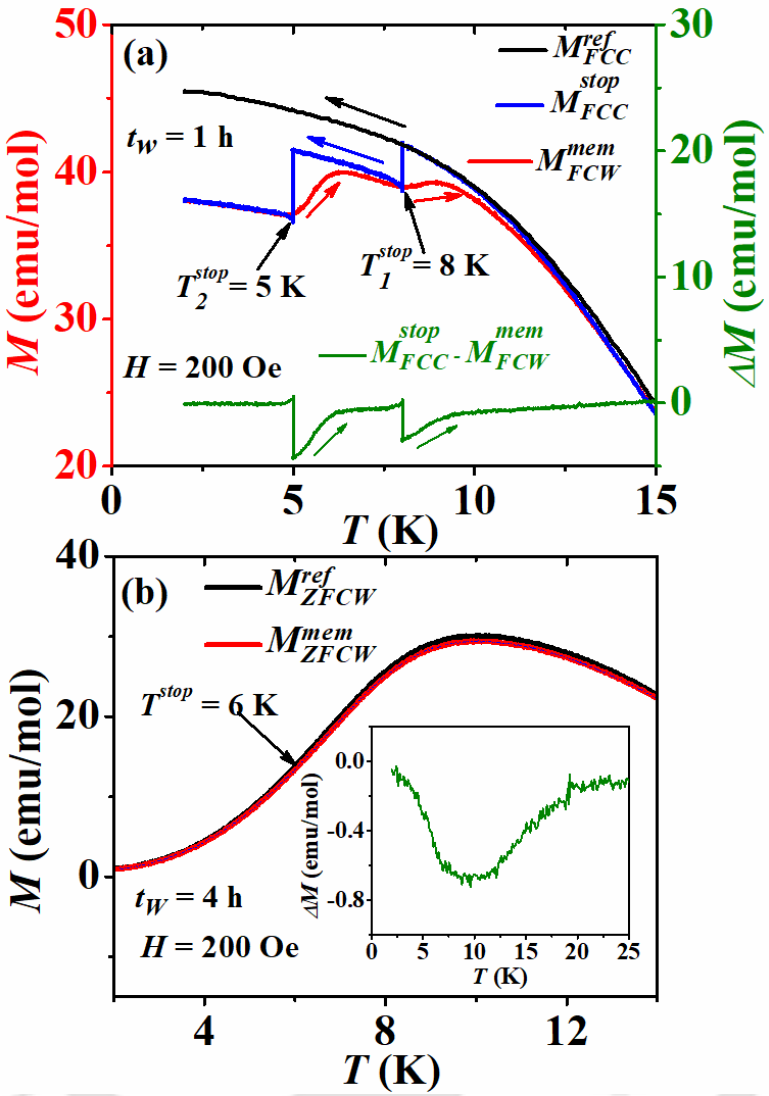

Fig. 3.24: Memory effect in magnetization of $Ni_{0.85}Mg_{0.15}Cr_2O_4$ as a function of temperature in (a) FC and (b) ZFC protocol at H = 200 Oe.

The Magnetization vs field (*M-H*) loop recorded at *T* = 5 K is shown in Fig. 3.25. The saturation magnetization (M_S) value is estimated by fitting the experimental data to the law of approach to saturation (LAS) and is found to be 0.03 μ_B/f. u.. The parent bulk compound exhibits a saturation magnetization of 0.3 μ_B/f. u. as observed from high field magnetization measurement. The decrease in saturation magnetization can be attributed to the substitution of nonmagnetic Mg at Ni sites and the random canting nature of frozen surface spin clusters from the net magnetization direction as observed in core shell type nanoparticles [173]. Moreover,

the squareness ratio $Q = \frac{M_R}{M_S}$ (defined as the ratio of remanent magnetization to saturation magnetization) is found to be 0.4, which is significantly smaller than cubic (Q = 0.81) magneto crystalline anisotropy and close to uniaxial anisotropy (Q = 0.5). The smaller Q value indicates the strong effect of surface magnetic anisotropy that randomizes the surface spin as observed in typical core shell type nanoparticles [175, 175].

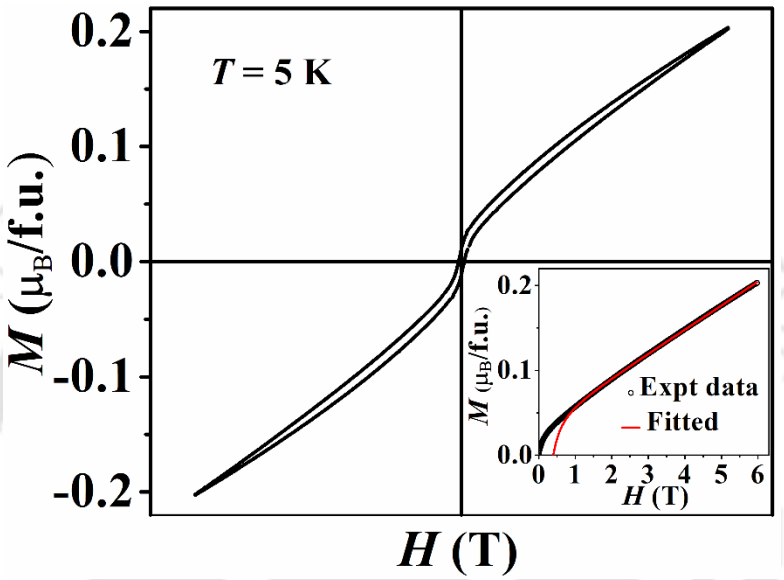

Fig. 3.25: *M* - *H* loop recorded at *T* = 5 K. Inset shows the fitting of initial magnetization curve with law of approach to saturation.

In order to support the evidence of surface spins freezing nature and their interactions with the core spins, we have recorded several field-dependent magnetizations (*M* vs *H*) loops at different temperatures. *M*-*H* loops recorded at *T* = 20, 12 & 5 K are shown in Fig. 3.26 (a, b & c). Above T_f, the unfrozen surface spin generally follows the direction of the core magnetic moment under the application of a magnetic field and hence the shape of the *M*-*H* loops is regular (Fig. 3.26 (a)). Remarkably around T_f, narrowing of the *M*-*H* loops near the coercive region and decrease in H_C values have been observed (Fig. 3.26 (b)). This distortion in the *M*-*H* loop can be explained on the basis of the freezing characteristic of the surface spins as previously discussed in a few nanoparticle systems [162, 163, 176]. As the temperature approach T_f, the exchange interaction among surface spin cluster grow and their random freezing behavior tends to demagnetize the sample. Therefore, a low negative (reverse)

magnetic field is required in order to achieve the zero magnetic moment (complete demagnetization) of the sample, which results a smaller H_C value near T_f (Fig. 3.26 (b)). At sufficiently low temperatures such as at 5 K, the shape of the hysteresis loop again starts to become regular due to the growth of surface spin cluster into a disordered frozen state and their strong exchange interaction with the core gives rise to an increase in H_C value (Fig. 3.26 (c). The variation of coercivity (H_C) and remanent magnetization (M_r) with respect to temperature is shown in Fig. 3.26 (d). The M_r value is found to increase continuously with decreasing temperature. Similar behavior of thermal variations of H_C and M_r are also confirmed by Monte Carlo simulations in $(Fe_{0.26}Ni_{0.74})_{50}B_{50}$ nanoparticle system having frozen surface spin state [176].

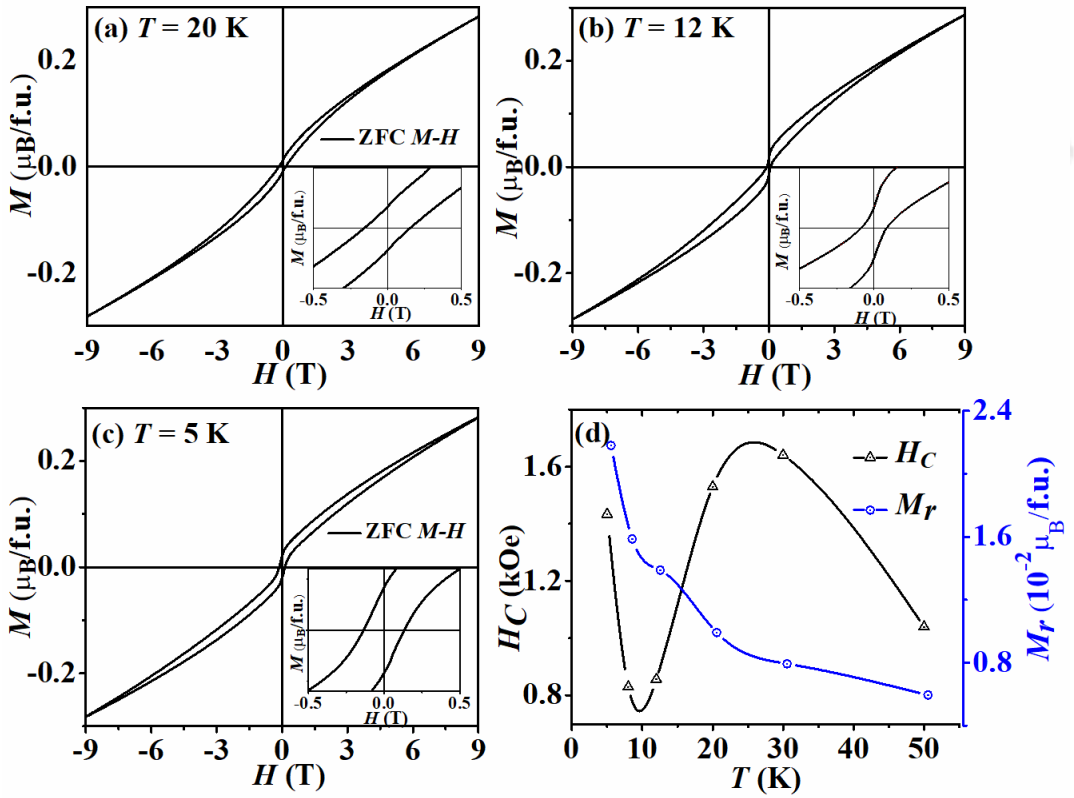

Fig.3.26: *M-H* loops recorded at different temperatures and variation of H_C and M_r as a function of temperature.

The relaxation of ZFC isothermal remanent magnetization (IRM) dynamics is an inherent property of a SG or cluster glass magnetic system. Here, the relaxation refers to the

slow decay of magnetization with time after removal or reduction of an applied magnetic field. In order to study the relaxation dynamics in our system, first we have cooled the sample in ZFC mode to 5 K (below T_f) and then a field of H = 9 T was applied. After reducing the magnetic field to zero, the remanent magnetization was measured as a function of time up to t = 10^4 s. Magnetic materials having SG nature shows slow and long-lasting drop of IRM, however in non - SG system, it rapidly drops in to a nearly constant value. The signature of slow and continuous drop (Fig. 3.25) of IRM even after t = 10^4 s confirms the glassy magnetic behavior in our system.

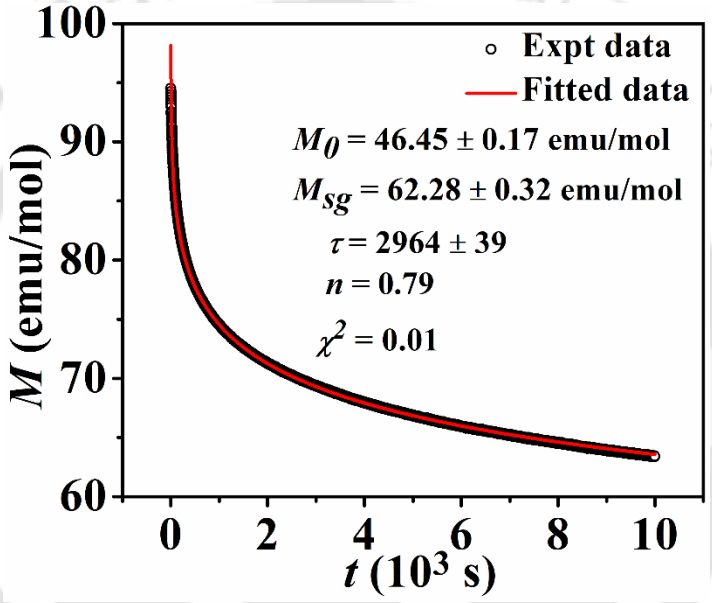

Fig. 3.27: Relaxation of ZFC magnetization measured at T = 5 K. The solid line (red) represent the fit using stretched exponential decay function.

The time dependent IRM data can be analysed by a stretched exponential function given in Eq. 3.2. The non-zero value of M_0 confirms the presence of ferrimagnetic component in our system and taking part in the relaxation dynamics. The high value of mean relaxation time τ = 2964 s further confirms presence of cluster glass state in the system. The rate of relaxation is defined by the exponent n and lies in the range $0 < n \leq 1$. The value of n generally indicates the distribution of anisotropy barriers in the system. For a single energy barrier, the value of n = 0. However, with a large value of n = 0.79 confirms the relaxation

dynamics involving activation against multiple anisotropy barriers as observed in typical spin glass system.

In order to understand the memory effect in the relaxation dynamics, we have carried out different experimental protocols below the glassy magnetic transition temperature. As shown in Fig. 3.26 memory effect has been studied in both ZFC and FC modes at T = 3 & 5 K with an intermediate cooling i.e. $T - \Delta T$ (negative T cycle) and heating i.e. $T + \Delta T$ (positive T cycle) for a duration of 3000 s.

Negative T cycle: Here, in the ZFC magnetic relaxation protocol (Fig. 3.28 a), the sample was first cooled down to the measuring temperature T = 5 K in zero magnetic field and then a magnetic field of H = 200 Oe was applied and $M(t)$ was measured for 3000 s. It is found to increase with t. The sample was then quenched to a lower temperature T = 3 K (ΔT = 2 K) in the same magnetic field and $M(t)$ was recorded for 3000 s (t_2), which is almost independent of t. Finally, the sample was warmed back to T = 5 K and magnetization data were collected for another 3000 s (t_3) in the same magnetic field, which again increases exponentially with t. From the inset of Fig. 3.28 (a) it is clear that when the temperature is raised back to its earlier value of 5 K, the magnetization $M(t_3)$ almost coincides with the $M(t_1)$ and thereby following the earlier growth curve. This phenomenon clearly illustrates the presence of memory effect in the given magnetic system. In FC protocol (Fig. 3.28 b) the sample was cooled down to T = 5 K in a field of H = 200 Oe and $M(t)$ was measured for 3000 s after reducing the field to zero. In the second step, sample was further cooled down to T = 3 K and $M(t)$ was recorded for another 3000 s. Finally, the sample was warmed back to T = 5 K and $M(t)$ was recorded again for 3000 s. As shown in the inset of Fig. 3.28 (b) the magnetization nearly returns to the same value after the temporary halt at low temperature T = 3 K. Study of the memory effect in both ZFC and FC protocol indicates that the magnetic state of the sample is recovered even after experiencing a perturbation in energy barrier and hence change in magnetization in negative T cycle. These growth and decay curves were fitted by the stretched exponential function (Eq. 3.2) as shown in the inset of Fig. 3.28 (a & b).

Positive T cycle: Similar to negative T cycle, memory effect was also studied in both ZFC (Fig. 3.28 c) and FC (Fig. 3.28 d) modes for the positive T cycle. In ZFC mode, sample was first zero field cooled to T = 3 K. At 3 K, a field of 200 Oe was applied and $M(t)$ was recorded for

3000 s (t_1). The sample was then heated to T = 5 K in the presence of the same magnetic field and $M(t)$ was recorded for another 3000 s (t_2). Finally, the sample was cooled back to the initial temperature T = 3 K and $M(t)$ was collected again for 3000 s (t_3). Surprisingly unlike the negative T cycle, $M(t)$ data recorded at the beginning of t_3 do not match with that at the end of t_1. In FC mode, the sample was cooled in a magnetic field of H = 200 Oe down to T = 3 K. At T = 3 K the field was switched off and same sequence (as for ZFC) was followed. From Fig. 3.28 (c & d) it is clear that relaxation of $M(t)$ during t_1, t_2 and t_3 are quite different from each other. During the t_1 and t_2 duration, $M(t)$ data are found increase (ZFC mode) or decrease (FC mode) gradually with t, while they are almost independent of time during t_3 duration. Thus, positive T cycle rejuvenates the relaxation process at high temperature and no memory effect is observed when the temperature is restored.

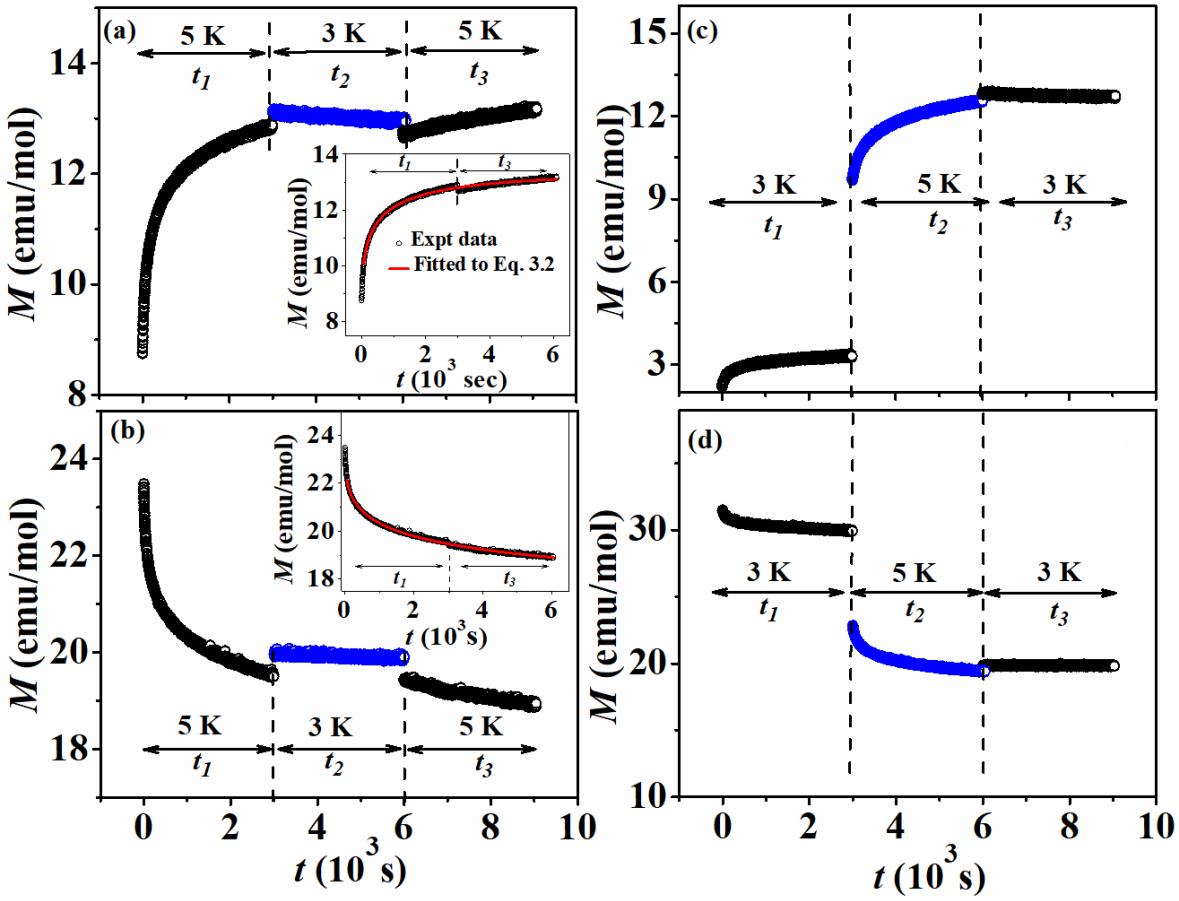

Fig. 3.28: Magnetic relaxation measurements in Negative T cycle for (a) ZFC mode and (b) in FC mode. Similar measurement in positive T cycle for ZFC (c) and FC (d) condition. Insets shows the fitted data using Eq. 3.2.

The asymmetric response of magnetic relaxation with respect to positive and negative *T* cycle is in accordance with hierarchical model, which was originally proposed for interacting magnetic nanoparticles such as spin glass or super spin glass system. Additionally, recent studies also suggest that the above protocols may also be applicable for non-interacting superparamagnetic as well as for exchange coupled systems [178, 179]. Tian et al. explained the observed asymmetric response and memory effects in $NiFe_2O_4$-NiO nanosystem by considering the distribution of energy barriers due to the interfacial exchange anisotropy between ferrimagnetic core and spin glass like surface [178]. Xu et al. also studied the asymmetric temperature cycles in $NiFe_2O_4$/NiO nanocomposite by field pulse technique and confirmed the effect of exchange interactions between FIM (core) and AFM (shell) phase on temperature cycle [179]. According to these previous reports, during the negative *T* cycle, when temperature of the system is lowered to $T-\Delta T$, only the spin clusters with smaller energy barriers associate with ferrimagnetic nanoparticles or weakly exchange coupled ferrimagnetic and surface spins can respond to the temperature change. Whereas spins associate with larger ferrimagnetic nanoparticles and strongly exchange coupled interfacial spins are frozen. As a result, the system relaxes to a new state with a selected number of spin configurations. However, when the temperature is heated back to the original temperature, the spin cluster with smaller energy barriers responds rapidly and the system back to its original state and relaxes with time. This results in the recovery of magnetization after negative *T* cycle. In positive *T* cycle, all the spin clusters respond to the increase in temperature ($T+\Delta T$) irrespective of their energy scale and hence the system achieves a new magnetic state. However, when temperature return to its original value, spins associated with the larger ferrimagnetic particles and strongly exchange coupled ferrimagnetic and surface spins don't respond at all, this leading to an absence of memory effect under positive *T* cycle. Therefore, the observed asymmetric response with respect to change in temperature in the present system is may be mediated by ferrimagnetic particle size distribution and exchange coupling between ferrimagnetic core and glassy surface spin.

Aging effect in ZFC magnetization is a characteristic signature of SG system [179]. When a magnetic field is applied to a glassy magnetic system which was cooled in zero field through the T_f, the time evolution of magnetization depends on the time spent by the system at

that particular temperature before application of the field. For this study, the sample was cooled in ZFC mode down to T = 5 K (< T_f) and a magnetic field H = 200 Oe was applied after a waiting time t_w. The time evolution of the magnetization was then fitted to Eq. 3.2. As shown in Fig 3.29, we have collected the magnetic relaxation data for three different waiting times t_w = 100, 1000 & 2000 s at T = 5 K and the parameters estimated from the fitting are presented in Table 3.3. The increase in relaxation time τ with increase in t_w indicates the stiffening of spin relaxation with time. This further confirms the non-equilibrium dynamics of the spins and aging effect of the glassy magnetic phase. The stretching factor n is found to be nonzero ($n > 0$), as multiple anisotropy barriers are distributed in the system. In the relaxation process the contribution from both FIM and glassy component is found to increase with t_w. In addition, the ratio of $M_0(t_w)/M_{sg}(t_w)$ found to decrease from 3.02 for t_w = 100 s to 2.57 for t_w = 2000 s, which confirms the enhancement in contribution from glassy phase as compared to core FIM component in relaxation mechanism with increase in waiting time.

In classical SG system, the plot of magnetic viscosity $S(t) = (1/H)dM(t)/d(ln\, t)$ versus t shows an inflection point at $t \approx t_w$. Which is generally assigned as a crossover from quasi-equilibrium dynamics for $t < t_w$ to non-equilibrium dynamics for $t > t_w$ on time scale. Fig. 3.29 (d) shows the dependence of magnetic viscosity $S(t)$ for various waiting time t_w at T = 5 K. Unlike the conventional SG system, the peak position of $S(t)$ known as effective time (t_{eff}) is higher than t_w. Shifting of t_{eff} towards longer time scale with increasing in waiting time is also observed in the system. The deviation of t_{eff} from t_w can be understood by the presence of surface cluster glass along with ordered core rather than canonical SG in the system.

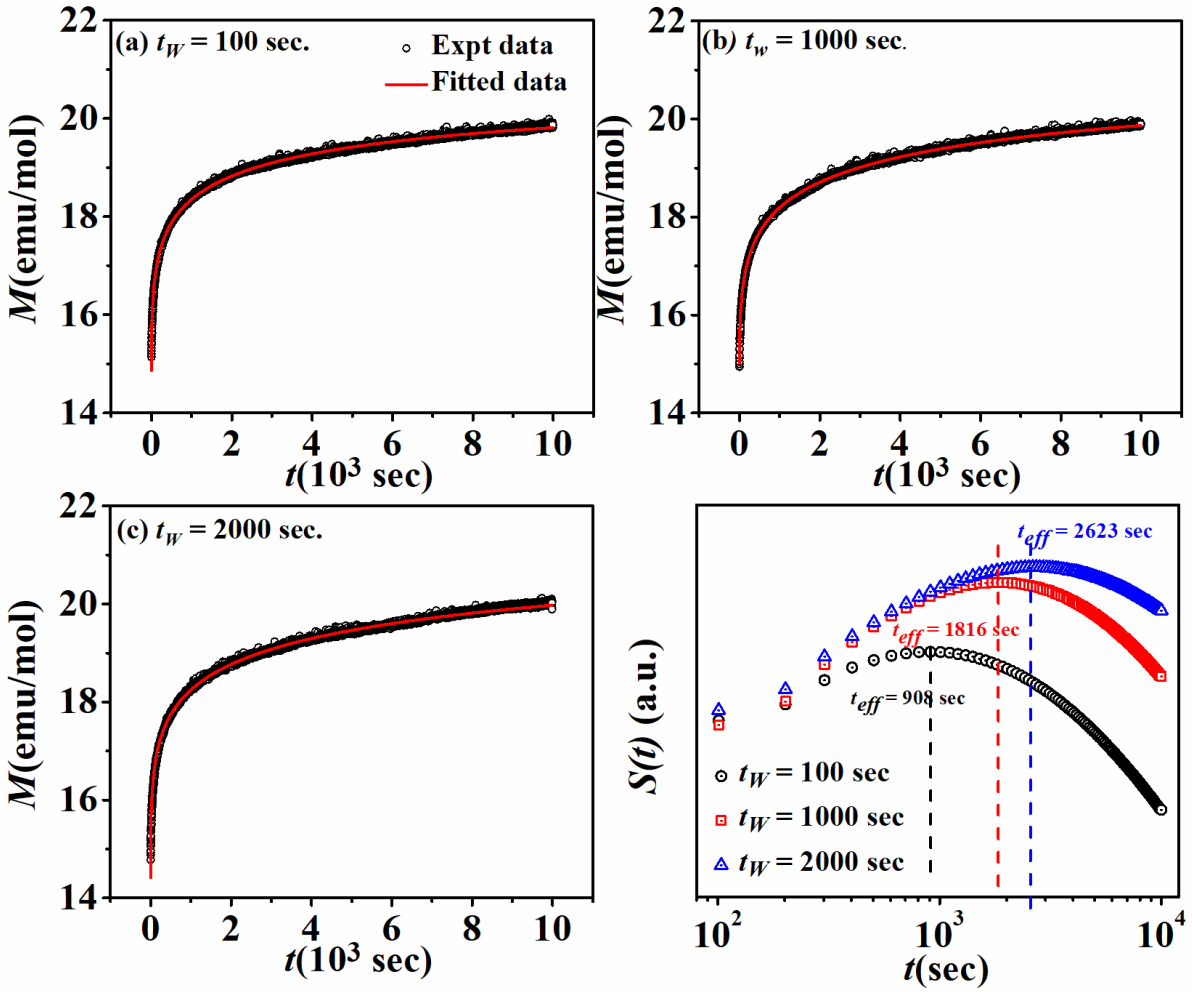

Fig. 3.29: Relaxation of zero-field-cooled (ZFC) magnetization for (a) t_w = 100 s (b) t_w = 1000 s and (c) t_w = 2000 s wait times at T = 5 K, (d) plot of magnetic viscosity $S(t)$ as a function of time for different waiting period at T = 5 K.

Table 3.3: Estimated relaxation parameters obtained from different waiting period at T = 5 K.

t_w (s)	M_0 (t_w) (emu/mol)	M_{sg} (t_w) (emu/mol)	τ (s)	n
100	20.84±0.01	6.91±0.03	901±8	0.79
1000	21.34±0.02	7.34±0.03	1852±8	0.72
2000	22.16±0.04	8.63±0.06	2696±56	0.76

3.3 Conclusion

To summarize, we have investigated the crystal structure, particle size and morphology, temperature and time dependent magnetic properties, magnetic frustration, glassy nature and exchange bias behavior of $Ni_{1-x}Mg_xCr_2O_4$ (x = 0-0.05) bulk polycrystalline series and $Ni_{0.85}Mg_{0.15}Cr_2O_4$ nanoparticles in this chapter.

We have successfully synthesized single phase bulk polycrystalline samples of Mg substituted $NiCr_2O_4$ by sol-gel method. Rietveld refinement of room temperature XRD pattern confirms the tetragonal crystal structure of $NiCr_2O_4$ with space group $I4_1/amd$. XRD patterns of all the Mg substituted samples can be refined by using cubic $Fd\bar{3}m$ space group. FESEM micrograph shows broad particle size distribution (50-850 nm) with most of the particles bi-pyramidal in shape. Temperature dependent magnetization reveals FIM nature of $NiCr_2O_4$ with T_C = 70 K and an antiferromagnetic ordering at T_N = 29 K. With Mg substitution, the FIM transition temperature T_C is found to decrease to 42 K for x = 0.10 sample. The decrease in T_C with Mg substitution confirms the reduction in superexchange interaction with Mg substitution. A crossover from FIM to AFM nature for Mg substation $x \geq 0.20$ is observed in the series. We have observed glassy magnetic phase for the intermediate compositions x = 0.10, 0.20 & 0.30 samples due to competing FIM and AFM component of magnetic moment. The observed glassy magnetic phase was established with stretched type relaxation of thermoremanent magnetization (TRM) and significant frustration in the systems. The anisotropic exchange interaction between FIM and AFM components of magnetic moment gives rise to the EB behavior in x = 0, 0.05 & 0.10 samples. The H_{EB} value is found to increase with Mg substitution from 91 Oe to 747 Oe. Temperature variation of H_{EB} and H_C^{eff} were analyzed based on exponential and modified Kneller's law respectively. In addition, the effects of H_{FC} and H_{max} on H_{EB} for the x = 0.10 sample are also investigated in detail. Training effect of H_{EB} follows the typical power law behavior.

Motivated by the interesting outcomes of Mg substituted bulk $NiCr_2O_4$ series, single phase nanoparticles of $Ni_{0.85}Mg_{0.15}Cr_2O_4$ were synthesized by hydrothermal route. It is crystallized in cubic crystal structure with space group $Fd\bar{3}m$. Estimated bonds angles of the superexchange networks indicates the possibilities of collinear spin structure in the system.

FESEM and FETEM micrographs reveal strongly agglomerated nanoparticles with an average particle size of 46 nm. From temperature dependence magnetization measurement at 200 Oe, we have observed a broad ferrimagnetic transition around 76 K followed by a sharp cluster glass like transition around 9.5 K. The occurrence of cluster glass phase is attributed to the interaction between disordered surface spin and ordered FIM core structure. In contrast to the bulk nickel chromite system, where the substitution of nonmagnetic and non-JT active ions at the Ni site increases geometric spin frustration, our nanosystem shows tendency towards collinear ferrimagnetism with a frustration index of only 0.3. The reduction in frustration can be attributed to the domination of Ni-O-Cr superexchange interaction over Cr-O-Cr superexchange and Cr-Cr direct exchange interaction. Field dependent $M - T$ measurement, relaxation of thermoremanent magnetization and memory effect support the metastability of our cluster glass system. The peculiar variation of temperature dependent coercivity (H_C) has been explained on the basis of spin freezing characteristic of surface spins and their interactions with core ferrimagnetism. We have observed asymmetric response of magnetic relaxation with respect to change in temperature below the glassy transition temperature. Below T_f, wait-time dependent ageing phenomena is observed.

Chapter 4

Mn and Cd substituted $NiCr_2O_4$ series

In the previous Chapter, we have observed that substitution of non-magnetic Mg at the Ni sites of $NiCr_2O_4$ highly influenced the structural and magnetic properties of the system. The transition of its crystal structure (from tetragonal to cubic) and magnetic structure (from ferrimagnetic (FIM) to antiferromagnetic (AFM) dominant) with Mg substitution is the important aspect of this series. Additionally, observed exchange bias (EB), magnetic frustration and glass-like magnetic properties are interesting characteristics of these materials. In the current Chapter, we are going to discuss about the effect of substitution of Mn and Cd at Ni sites of $NiCr_2O_4$ compound. Interestingly, the multiferroic spinel chromite $MnCr_2O_4$ shows a considerable magnetocaloric effect (MCE), where the critical phenomenon cannot be described by the existing universality classes [180]. Though MCE of $NiCr_2O_4$ has already been reported earlier [181], there is a lack of report on their critical exponent behavior close to the FIM transition. Therefore, it will be interesting to investigate the evolution of structural properties, magnetic properties, MCE and critical phenomena of $Ni_{1-x}Mn_xCr_2O_4$ system. In addition, a series of Cd substituted $NiCr_2O_4$ samples were synthesized by the sol-gel method and their structural, magnetic and dielectric properties have been discussed in this chapter. As discussed in Chapter 1, even though magnetodielectric coupling has been reported in $NiCr_2O_4$ at T_C, there is a lack of detailed investigation of its dielectric and impedance properties near T_C. The $CdCr_2O_4$ spinel chromite shows a transition from paramagnetic (PM) cubic phase to an AFM tetragonal state at low temperature [182]. Therefore, it is also interesting to study the possibility of enhancing the value of EB field and magnetic frustration by Cd substitution as a result of competing AFM and FM components of the magnetic moment. To our knowledge, no systematic study of structural, magnetic and dielectric or impedance properties are available in these two series.

4.1 $Ni_{1-x}Mn_xCr_2O_4$ (x = 0 - 0.50) Series

This section deals with the preparation of Mn substituted nickel chromite series ($Ni_{1-x}Mn_xCr_2O_4$ (x = 0 - 0.50) and the investigation of their structural and magnetic properties.

Polycrystalline samples of $Ni_{1-x}Mn_xCr_2O_4$ were synthesized by using sol-gel method. Stoichiometric ratio of $Ni(NO_3)_2{\cdot}6H_2O$, $C_4H_6MnO_4{\cdot}4H_2O$ and $Cr(NO_3)_3{\cdot}9H_2O$ of 99% purity were used as the starting materials for the preparation of the sample. The as synthesized samples were grinded and pre-sintered at 600 ^{0}C followed by a sintering at 800 ^{0}C for 12 hours. Final sintering was performed at 1100 ^{0}C for 24 hours.

4.1.1 Structural Study

XRD patterns (Fig. 4.1) recorded at room temperature reveal the single-phase polycrystalline nature of these samples. The typical Rietveld refinement of x = 0 and 0.05 are shown in Fig. 4.2, while those of x = 0.30 and 0.50 are shown in Fig. 4.3. The Rietveld refinements confirm the tetragonal ($I4_1/amd$) crystal structure for x = 0 and cubic structure ($Fd\bar{3}m$) in Mn doped samples. The lattice parameters for $NiCr_2O_4$ are found to be $a = b$ = 5.8296 Å, c = 8.4367 Å. The lattice parameters are presented in Table 4.1 and they are found to increase with Mn concentration for $x \geq 0.05$ due to the larger ionic size of Mn^{2+} (0.66 Å) as compared to Ni^{2+}(0.55 Å) [143]. The occupancy values normalized to formula units are also given in Table 4.1.

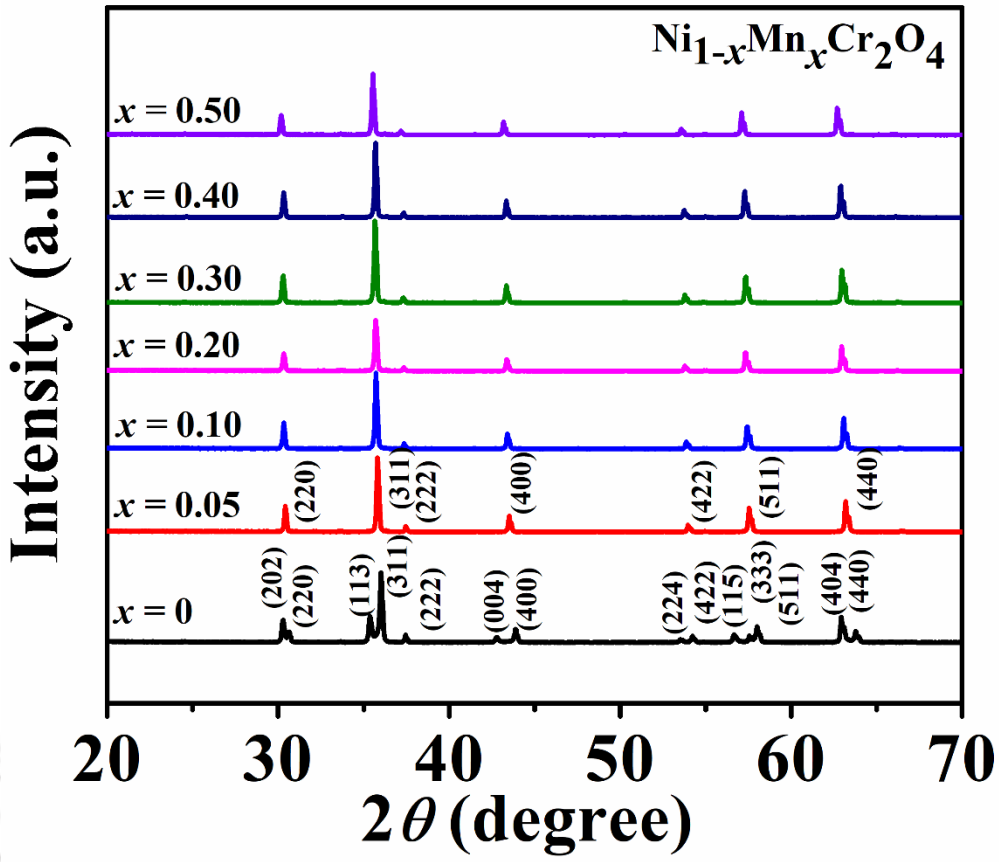

Fig. 4.1: XRD patterns of $Ni_{1-x}Mn_xCr_2O_4$ (x = 0 – 0.50).

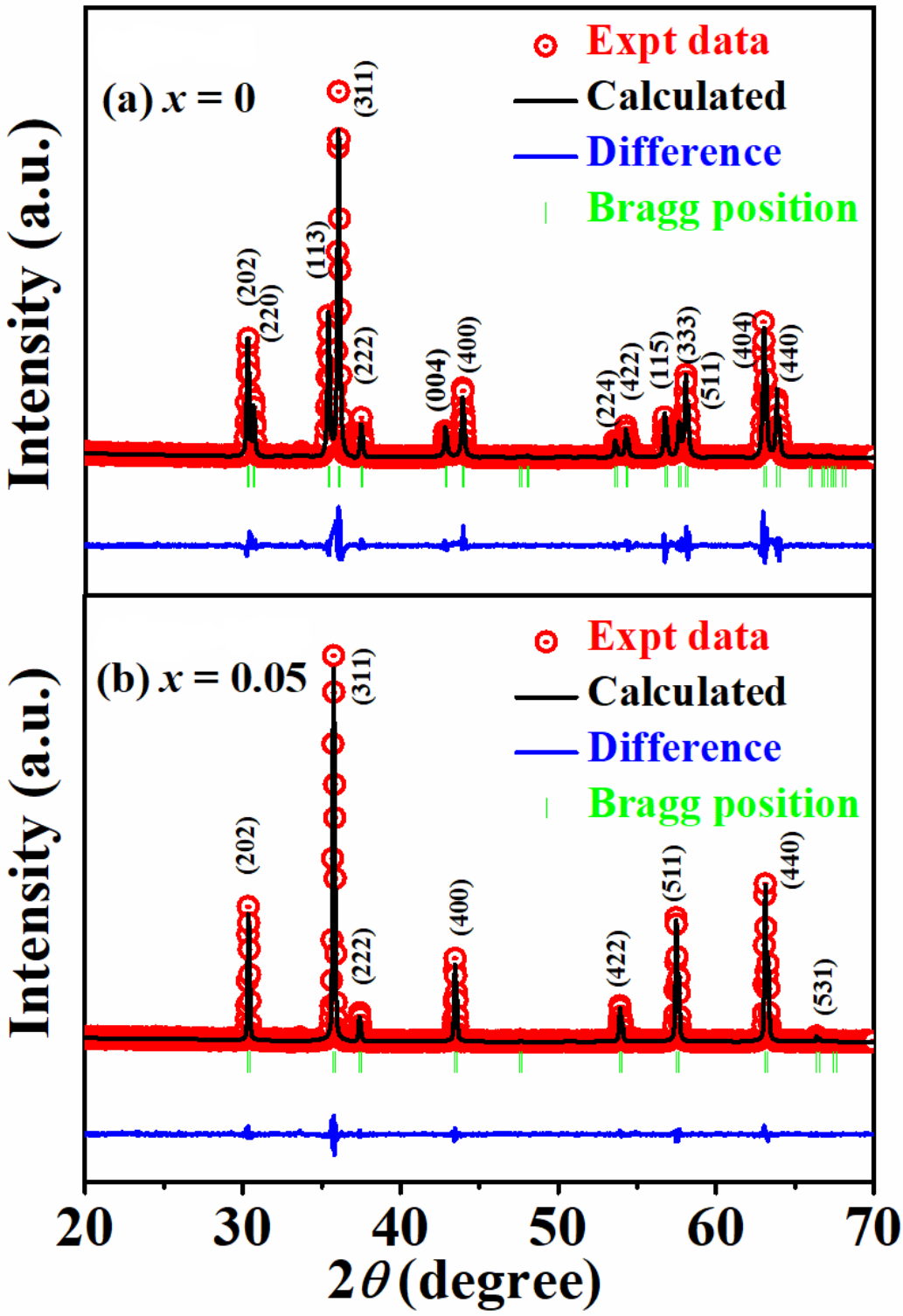

Fig. 4.2: Rietveld refinement of the XRD patterns of (a) $x = 0$ and (b) $x = 0.05$ samples. The red open circles are the experimental data and the black solid lines are the fitted data. The bottom line shows the difference between experimental and refined data.

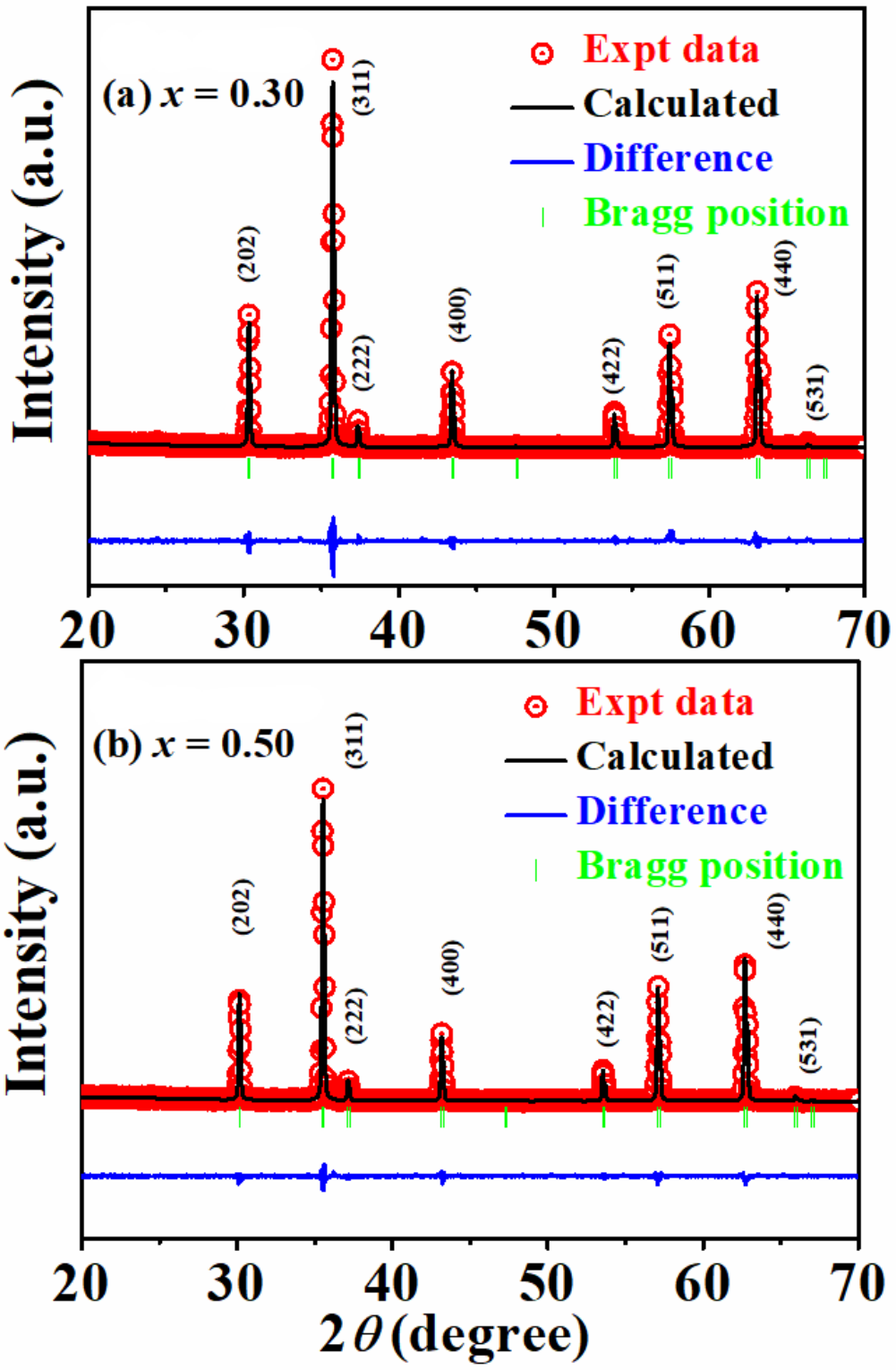

Fig. 4.3: Rietveld refinement of the XRD patterns of (a) $x = 0.10$ and (b) $x = 0.50$ samples. The red open circles are the experimental data and the black solid lines are the fitted data. The bottom line shows the difference between experimental and refined data.

Table 4.1: Structural and reliability parameters obtained from the Rietveld refinement of XRD patterns of $Ni_{1-x}Mn_xCr_2O_4$ (x = 0 – 0.50).

Sample/ Parameters	x = 0	x = 0.05	x = 0.10	x = 0.20	x = 0.30	x = 0.40	x = 0.50
Space group	$I4_1/amd$	$Fd\bar{3}m$	$Fd\bar{3}m$	$Fd\bar{3}m$	$Fd\bar{3}m$	$Fd\bar{3}m$	$Fd\bar{3}m$
a (Å)	5.8265 (0.0003)	8.3234 (0.0002)	8.3290 (0.0004)	8.3400 (0.0001)	8.3533 (0.0001)	8.3621 (0.0002)	8.3762 (0.0001)
c (Å)	8.4389 (0.0006)	-	-	-	-	-	-
Volume (Å^3)	286.54	576.64	580.09	582.87	582.87	584.72	587.68
R_F (%)	2.8	1.7	2.5	2.4	1.8	2.3	1.3
R_{Bragg} (%)	4.7	2.13	3.3	3.4	2.9	3.4	2.0
R_P (%)	15.4	7.8	9.8	9.5	7.4	8.6	7.4
χ^2	6.1	3.9	4.5	3.6	3.2	2.7	3.6
Ni/Mg/Cr Occupancy	0.968 /0.000 /1.932	0.965 /0.062 /1.980	0.706 /0.148 /1.686	0.812 /0.195 /1.977	0.707 /0.300 /1.981	0.643 /0.385 /1.977	0.392 /0.532 /1.832

The FESEM micrographs of the samples are shown in Fig. 4.4. All samples show similar kinds of morphology with most of the particles having bi-pyramidal shapes. FESEM micrographs reveal that they mostly exhibit broad particle size distribution over a scale of 50 nm to 450 nm. The average particle sizes were estimated by fitting the size distribution histogram (Fig. 4.4 (e-h)) to the log-normal distribution function (Eq. 3.1) as described in the previous Chapter. We have observed a decrease in average particle size (d_{av}) with increase in Mn concentration from 220 nm for x = 0.0 to 162 nm for x = 0.50 in the series.

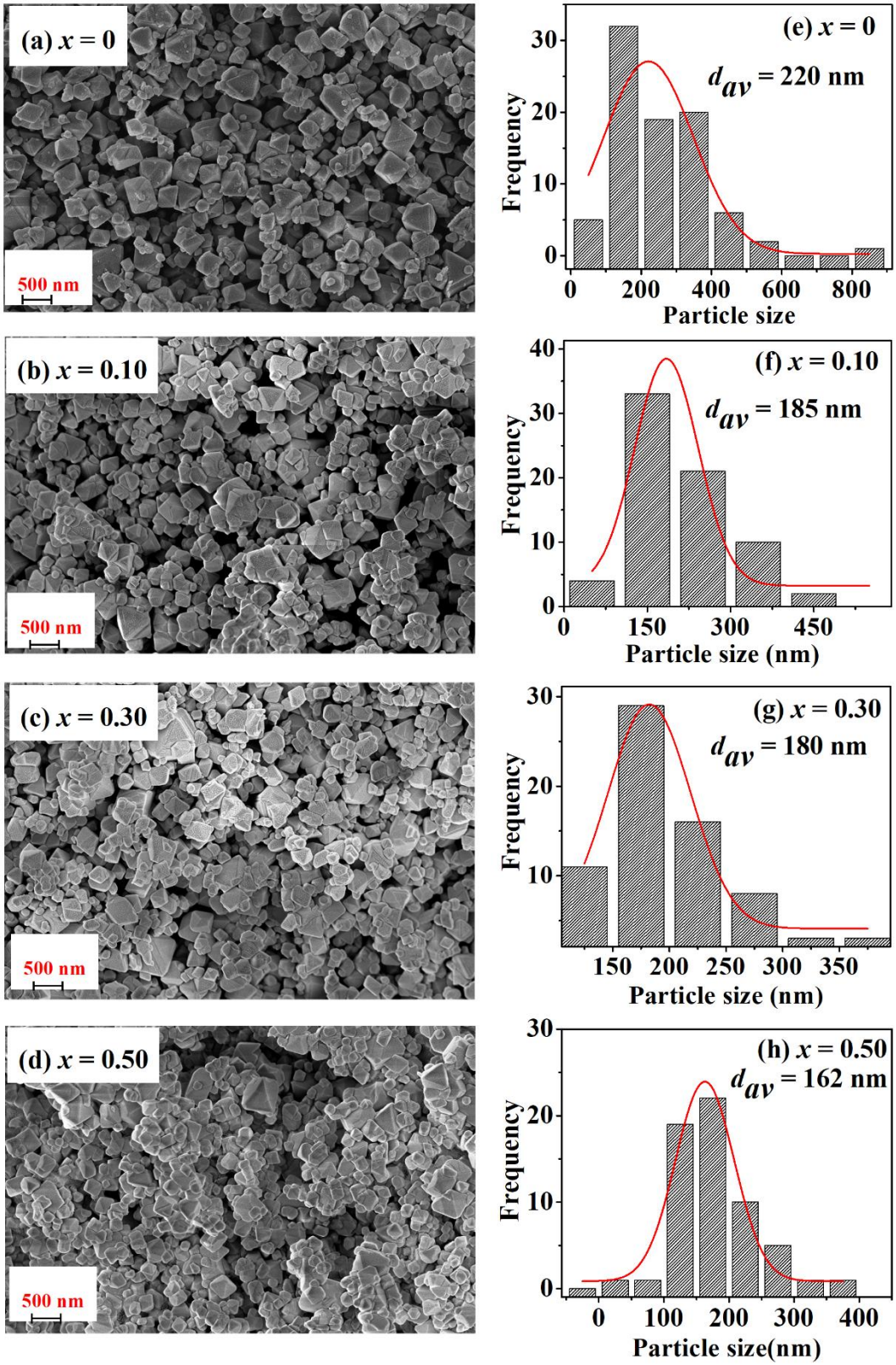

Fig. 4.4: FESEM micrograph (a-d) along with particle size distribution (e-h) for x = 0.0, 0.10, 0.30 & 0.50 samples.

The EDX spectra along with elemental mapping is shown in Fig. 4.5 for x = 0.05 & 0.30 samples. The cationic ratio Ni:Mn:Cr for x = 0.05 & 0.30 are found to be 0.92:0.04:2.0 and 0.72:0.26:2.0 respectively and is comparable to normal starting composition. The elemental mapping further confirms the purity and the uniform distribution of various elements throughout the samples in these systems.

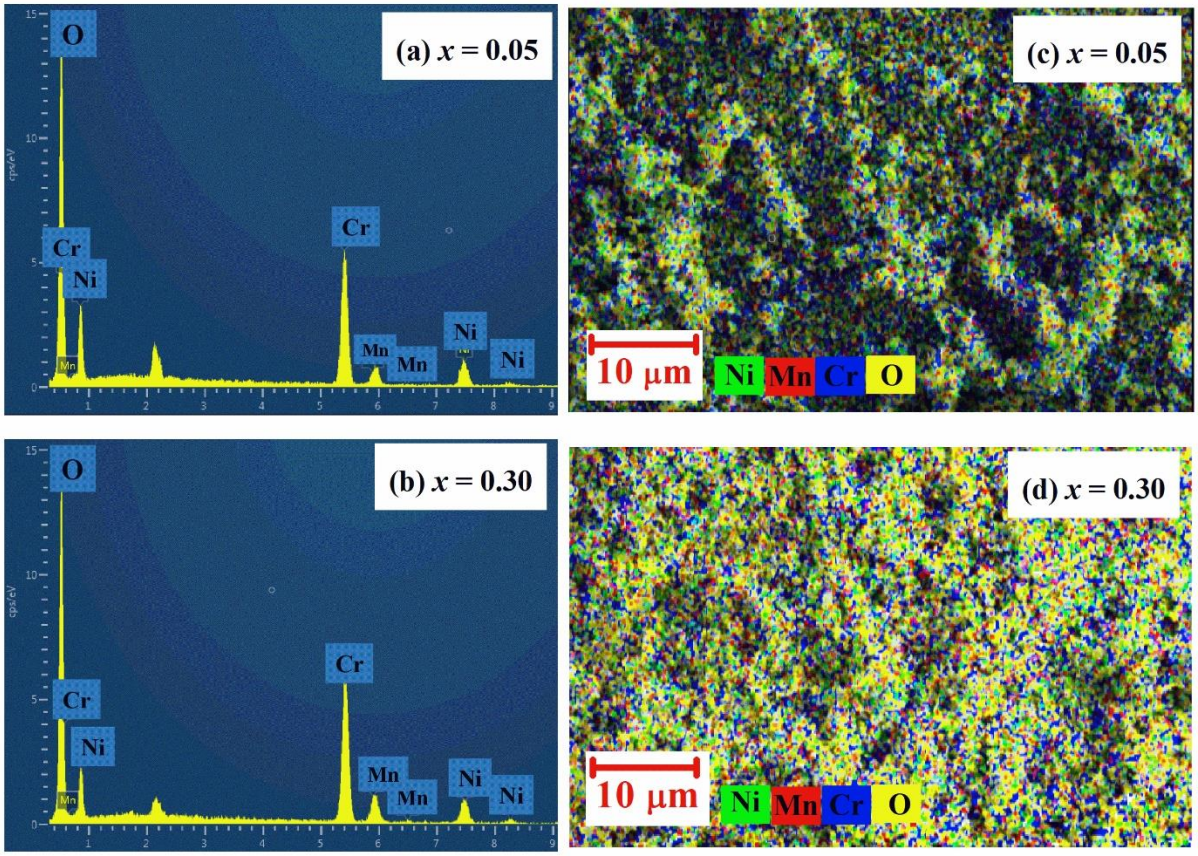

Fig. 4.5: EDX spectra (a, b) along with elemental mapping (c, d) for x = 0.05 and 0.30.

Raman spectroscopic study was carried out for all the samples as shown in Fig. 4.6. We have observed four Raman peaks at 687 cm^{-1}, 629 cm^{-1}, 518 cm^{-1} and 430 cm^{-1} and these peaks can be assigned to $A_{1g}(1)$, $T_{2g}(3)$, $T_{2g}(2)$ and E_g modes, respectively. We have observed variation in intensity and area of all the modes with Mn substitution. Such behaviors of the modes are related to the change in mass, bond length, charge etc.

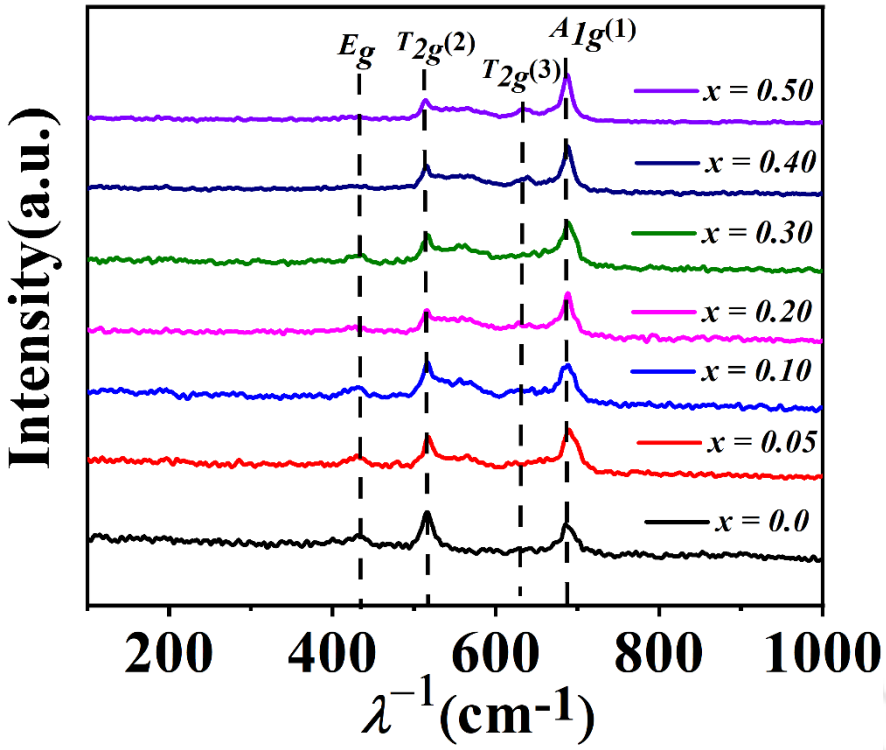

Fig. 4.6: Raman Spectra of $Ni_{1-x}Mn_xCr_2O_4$ (x = 0-0.50) at room temperature.

4.1.2 Temperature and Field Dependent Magnetic Studies

Magnetization as a function of temperature is measured under both zero field cooled (ZFC) and field cooled (FC) conditions at a DC magnetic field of 200 Oe. All the samples show paramagnetic to ferrimagnetic (PM – FIM) transition with a decrease in transition temperature (T_C) from T_C = 72 K for x = 0 to T_C = 38 K for x = 0.50 (Fig. 4.7). The T_C value of the parent compound is comparable to the earlier report [59, 79]. The transition temperature, T_C values are determined from dM/dT versus T plots. The AFM ordering of $NiCr_2O_4$ at 30 K is found to be suppressed with increase in Mn concentration. The systematic decrease in T_C with increase in Mn concentration is due to the weakening of superexchange interaction through Ni^{2+}/Mn^{2+}-O-Cr^{3+} networks. However, the effect of antiferromagnetic exchange interaction through Mn^{2+}-O-Mn^{2+} networks cannot be ruled out. The weakening of superexchange interaction and magnetic frustration can be understood from Currie-Weiss fitting as discussed below. The large enhancement in the FC magnetization data and the observed significant irreversibility between ZFC and FC curves for $T < T_C$ indicates the non-

collinear ferrimagnetism and the presence of competing AFM interactions in these samples. In $NiCr_2O_4$, the B site is divided into two groups B1-B3 and B2-B4 sublattices with their resultant moment antiparallel to the A site moment. Thus, the resultant magnetization per formula unit can be written as $M = |\uparrow \mu_{A1-A2} + \uparrow \mu_{B1-B3} - \downarrow \mu_{B2-B4}|$, where $\uparrow \mu_{A1-A2}$, $\uparrow \mu_{B1-B3}$ and $\downarrow \mu_{B2-B4}$ are the longitudinal component of magnetic moment of A1-A2, B1-B3 and B2- B4 sublattices respectively with respect to the field direction [59, 80]. The increase in magnitude of FC magnetization for x = 0.50 confirms the predominant occupation of Mn^{2+} ions in the tetrahedral A1-A2 site.

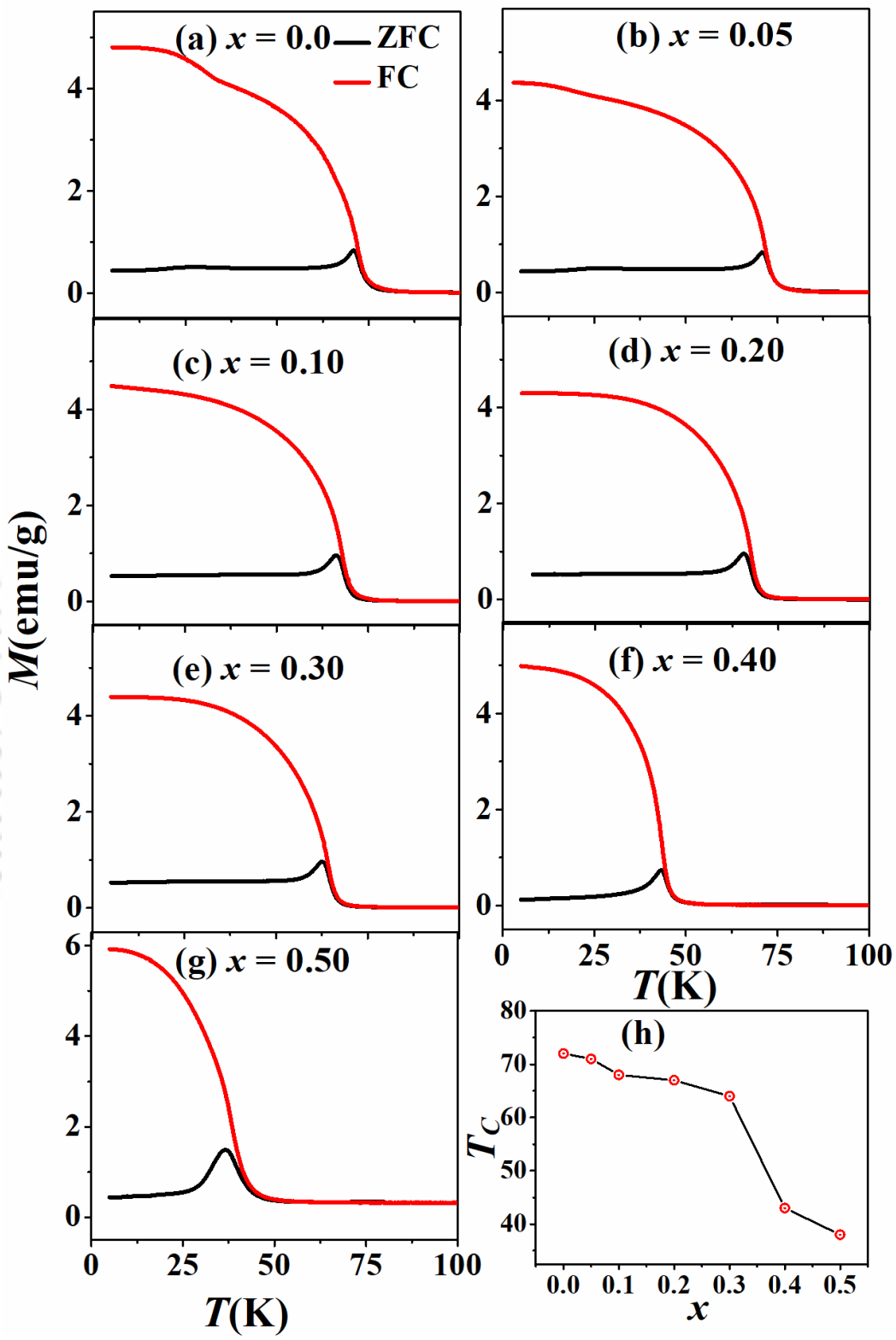

Fig. 4.7: Temperature dependent magnetization under zero field cooled (ZFC) and field cooled (FC) processes for x = 0 – 0.50 (a - g) under an applied field of H = 200 Oe., (h) variation of T_C with Mn concentration.

According to molecular field theory of ferrimagnetism for $T > T_C$ the hyperbolic nature of inverse susceptibility can be characterized by Eq. 3.3 as discussed in Chapter 3. We fitted our experimental data to Eq. 3.3 as shown in Fig. 4.8 and the fitted parameters are presented in Table 4.2. The parameter Θ represents the strength of AFM exchange interaction between Ni^{2+}/Mn^{2+} and Cr^{3+} ions. The magnitude of Θ is found to decrease with increase in Mn concentration and is consistent with expected reduction in superexchange interaction. The closeness of characteristic temperature Θ' and T_C confirms the long-range FIM ordering in these samples. The difference between Θ' and T_C generally gives an idea of broadening of magnetization about FIM transition temperature. With Mn substitution, the difference between these two temperatures are found to be decreased and can be attributed to the suppression of magnetic disorder in the sample. The parameter ξ, in the hyperbolic term represents the curvature in the inverse susceptibility plot. The ξ value is found to decrease with Mn substitution and it confirms the domination of Curie-Weiss law term. The effective paramagnetic moment (μ_{eff}) can be determined from the Curie constant $C = N\mu_{eff}^2/3k_B$. The experimental μ_{eff} values as given in Table 4.2 are almost comparable to the theoretically calculated values using the relation, $\mu_{theo} = \sqrt{(1-x)\mu_{Ni}^2 + x\mu_{Mn}^2 + 2\mu_{Cr}^2}$, where μ_{Ni}, μ_{Mn} and μ_{Cr} are the theoretical spin only magnetic moment of Ni^{2+}, Mn^{2+} and Cr^{3+} ions in high spin state. The frustration index ($f = \left|\frac{\Theta}{T_C}\right|$) is decreased with Mn substitution and hence more magnetically ordered as compared to the parent compound.

Table 4.2: Parameters obtained from the fitting of inverse susceptibility of $Ni_{1-x}Mn_xCr_2O_4$ (x = 0 – 0.50).

Sample/ Parameters	Θ (K)	C (emu K/Oe mol)	ξ (Oe mol K/emu)	Θ' (K)	μ_{eff} (μ_B)	$f = \left\|\frac{\Theta}{T_C}\right\|$
x = 0	-705±4	4.88±0.02	958±6	79	6.23	10
x = 0.10	-593±4	5.23±0.05	884±7	70	6.45	9
x = 0.20	-530±2	5.84±0.02	620±9	67	6.81	7
x = 0.30	510±3	6.11±0.04	570±7	62	6.97	8
x = 0.40	-360±4	6.32±0.03	405±5	45	7.11	8
x = 0.50	-322±5	6.63±0.10	359±8	40	7.26	8

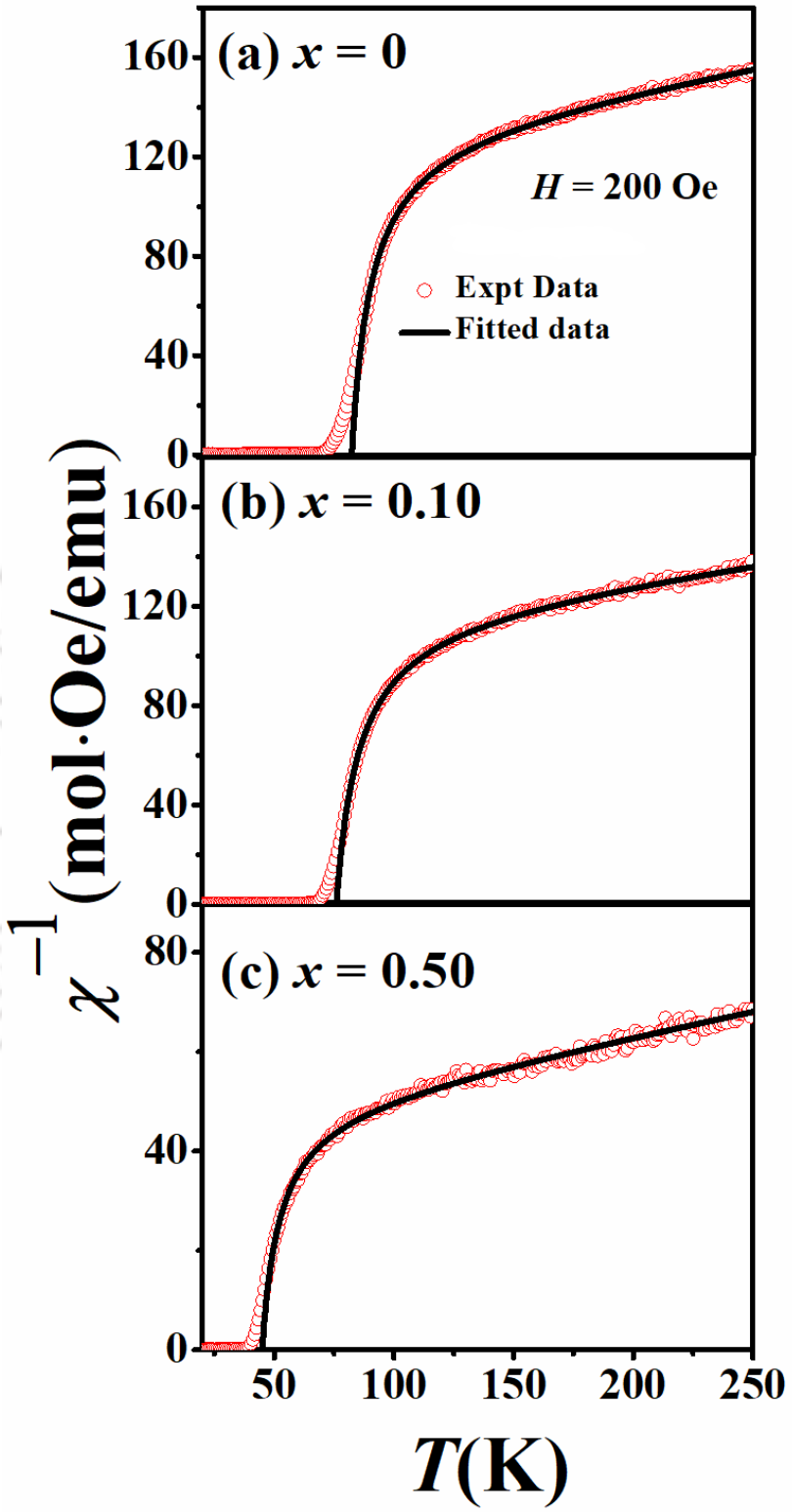

Fig. 4.8: Fitting of FC inverse susceptibility with Molecular field theory for (a) $x = 0$, (b) $x = 0.10$ and (c) $x = 0.50$ samples.

Magnetization (M) as a function of applied magnetic field (H) is recorded at 5 K as shown in Fig. 4.9. The value of saturation magnetization is determined by using Law of Approach to Saturation (LAS) as discussed in the previous Chapter (Eq. 3.4). The estimated values of H_C, M_S, M_R and remanent ratio ($R = M_R/M_S$) with Mn substitution is presented in Table 4.3.

Table 4.3: Parameters estimated from $M - H$ loops recorded at T = 5 K.

Sample/ Parameters	H_C (Oe)	M_S (emu/g)	M_R (emu/g)	$R = M_R/M_S$
x = 0	6429	6.15	4.91	0.92
x = 0.05	12186	6.37	5.05	0.87
x = 0.10	12858	6.84	5.28	0.88
x = 0.20	12983	6.14	5.33	0.86
x = 0.30	14182	6.96	5.22	0.88
x = 0.40	11982	7.42	5.62	0.82
x = 0.50	9360	10.30	8.37	0.81

The value of saturation magnetization for x = 0 is found to be 6.15 emu/g which is comparable to earlier report [79]. The increase in saturation magnetization with Mn concentration can be understood in terms of higher magnetic moment associated with Mn^{2+} ions. The H_C values are found to increase systematically with Mn substitution up to x = 0.30. However, a decrease in its values has been observed for x = 0.40 & 0.50 samples and can be attributed to possible tendency of their spin structures toward $MnCr_2O_4$ compound. Earlier reports suggest that $MnCr_2O_4$ has a larger M_S and a smaller H_C value as compared to $NiCr_2O_4$. The abrupt increase in M_S value for x = 0.50 compound also pointed toward possibilities of such tendency in their spin structure. The remanent ratio $R = M_R/M_S$ for the samples are found to be in the range from 0.8 to 0.9, which is generally observed in particles with cubic magnetocrystalline anisotropy [183].

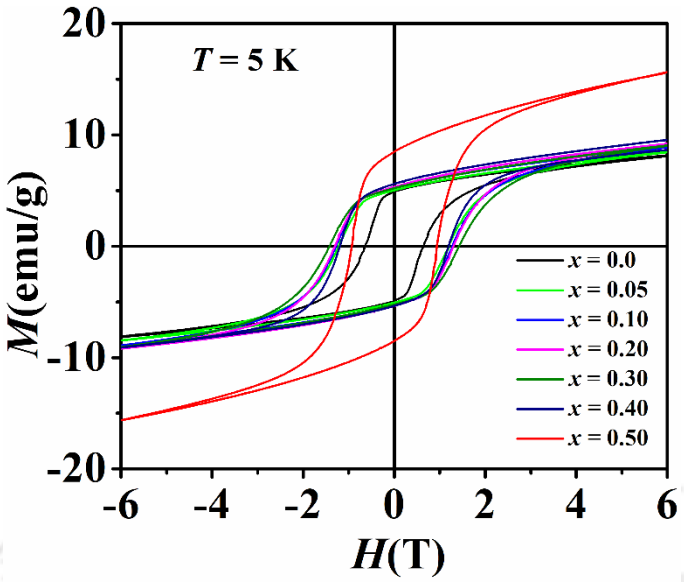

Fig. 4.9: *M* - *H* loops recorded at *T* = 5 K for $Ni_{1-x}Mn_xCr_2O_4$ (*x* = 0 - 0.50).

4.1.3 Critical Exponent and Magnetocaloric Effect Study

In order to estimate the magnetic entropy change (ΔS_M), a series of isothermal magnetization curves are recorded for *x* = 0, 0.10 and 0.50 about their respective FIM-PM transition temperature (Fig. 4.10 (a, b, & c)). All the initial *M-H* curves are recorded with a maximum measuring field of 9 T and the difference in temperature between two successive isotherms is ΔT = 2 K. The non-saturating M-H nature is due to the competing AFM phase in the samples. In order to avoid stray remanence magnetic moment, samples were warmed up to far above from their respective T_C after taking every initial isotherm. For the precision of the data, we have also considered a demagnetization field of $-\frac{1}{3}4\pi M$ for our spherically shaped samples. Now, in order to check the nature of magnetic transition in these samples, magnetization data are plotted in the form of Arrott plots (M^2 vs H/M) (Fig. 4.10 (d, e, & f)). According to Banerjee criterion a magnetic transition is of first order in nature if Arrott plots have negative slope and second order in nature if it is positive [184]. The presence of positive slope confirms the second order FIM-PM transition in this series.

The Landau expression of free energy (*f*) for two coupled order parameters can be expressed as [185],

$$f = \frac{a}{2}\sigma_1^2 + b\sigma_1\sigma_2 + \frac{c}{2}\sigma_2^2 + O(\sigma^4) \tag{4.1}$$

Here, σ_1 and σ_2 are the order parameters. For our magnetic system σ_1 and σ_2 can be considered as the magnetic moments of the two sublattices. Now, considering the magnetic system in an external magnetic field *H* the above equation can be rewritten as [185],

$$f = f_0 + \frac{a}{2}\sigma_1^2 + b\sigma_1\sigma_2 + \frac{c}{2}\sigma_2^2 + \frac{1}{4}A\sigma_1^4 + \frac{1}{4}C\sigma_2^4 - H\sigma_1 - H\sigma_2 \tag{4.2}$$

Now, in order to get the ground state values of magnetization we have differentiated the free energy expression with respect to σ_1 and σ_2, which gives

$$a\sigma_1 + A\sigma_1^3 - H + b\sigma_2 = 0 \tag{4.3}$$

$$c\sigma_2 + C\sigma_2^3 - H + b\sigma_1 = 0 \tag{4.4}$$

From eq. 4.3 & 4.4 we can see that the magnetization of second sublattice acting as an effective magnetic field for the first sublattice and vice versa. In addition, σ_1 and σ_2 will be nonlinear function of *H* which results in nonlinear Arrott plots (*H/M* vs M^2) in our system. In general, Arrott plots for ferromagnetic material in the paramagnetic state ($T > T_C$) are linear parallel lines, but the observed strong curvature in the Arrotts plots for $T > T_C$ confirms the significant antiferromagnetic coupling between the sublattices in our system.

Moreover, the curves are not straight and parallel to each other in the high field regime. This indicates that the magnetization data deviate from the meanfield model ($\beta = 0.5$, $\gamma = 1$) significantly. Therefore, it is necessary to estimate the critical exponents and entropy scaling in order to get more details about the deviation from meanfield and other universality classes.

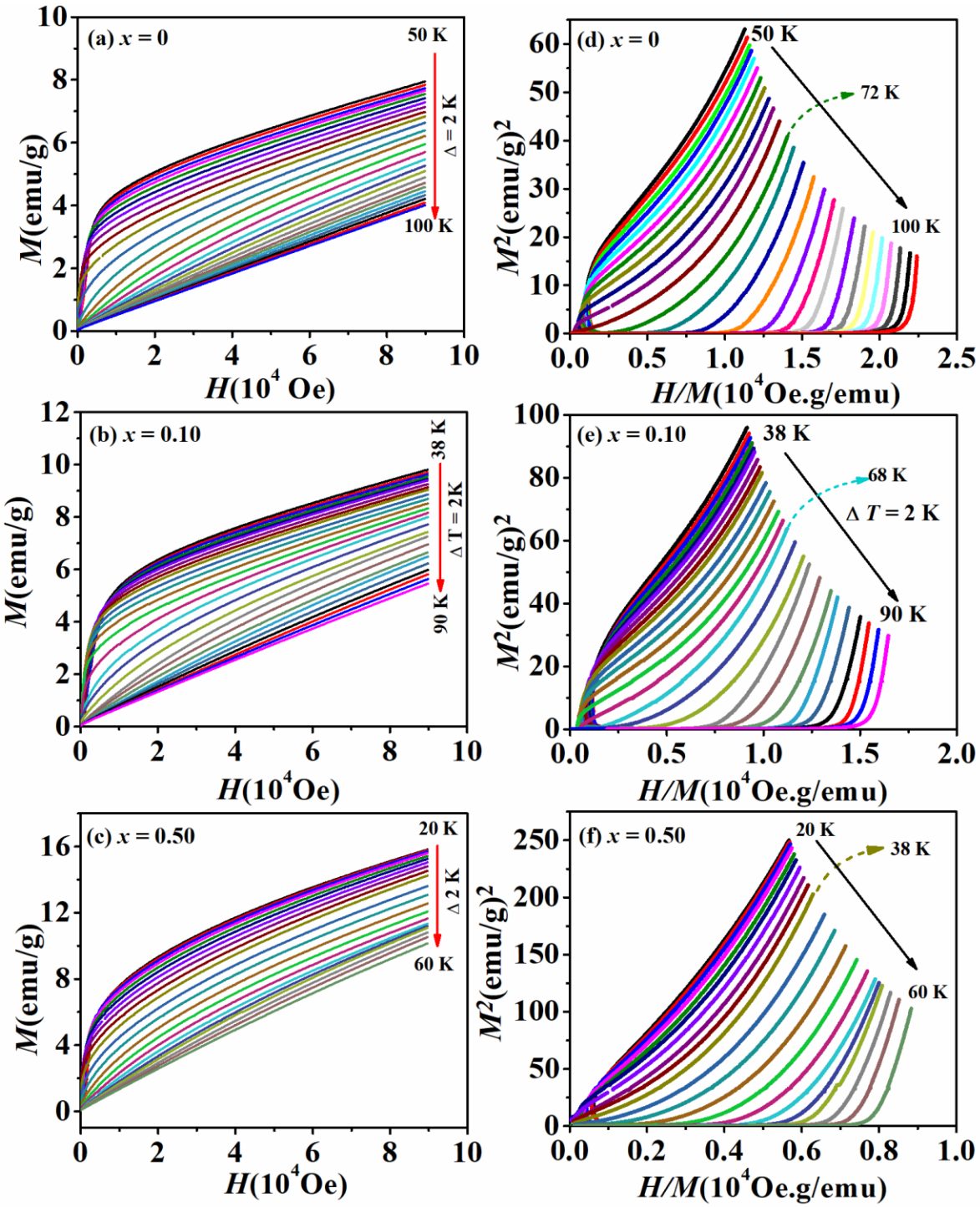

Fig. 4.10: Isothermal magnetization recorded at different temperatures for (a) $x = 0$, (b) $x = 0.05$, (c) $x = 0.10$ and (d, e, f) their corresponding Arrott plots.

According to scaling hypothesis the spontaneous magnetization M_S below T_C and initial susceptibility χ_0^{-1} above T_C follow the following equations [67],

$$M_S(T) = M_0(-\varepsilon)^{\beta} \ , \varepsilon < 0 \tag{4.5}$$

$$\chi_0^{-1}(T) = \Gamma(\varepsilon)^{\gamma} \ , \varepsilon > 0 \tag{4.6}$$

where, M_0, Γ are critical amplitudes and β, γ are critical exponents and $\varepsilon = \frac{T-T_C}{T_C}$. As one can notice that the Arrott plots (Fig. 4.10) for x = 0, 0.10 and 0.50 are found to be nonlinear and hence we have chosen modified Arrott plot on the basis of Arrott Noakes equation [68],

$$\left(\frac{H}{M}\right)^{1/\gamma} = a\frac{(T-T_C)}{T} + bM^{1/\beta} \tag{4.7}$$

Here, a and b are constant. The isotherms of modified Arrott plots $\left(M^{1/\beta} \ vs \ H/M^{1/\gamma}\right)$ should be straight lines and parallel to each other at high-field regime, which can be seen in our system (Fig. 4.11 (a, b & c)). The trial values we have chosen for β and γ are corresponding to mean field theory (β = 0.5, γ = 1). At first, these values of β and γ are substituted in Eq. 4.7 and subsequent $\left(\frac{H}{M}\right)^{1/\gamma} vs \ M^{1/\beta}$ plots are generated. Linear extrapolation of these isotherms gives $M_S(T)$ and $\chi_0^{-1}(T)$ as an intercept on $M^{1/\beta}$ and $\left(\frac{H}{M}\right)^{1/\gamma}$ axes respectively. In the second step, these data were analyzed based on Eq. 4.5 & 4.6 in order to extract new β and γ values. These new β and γ values are then used to construct new modified Arrott plot and this process is repeated for several times until linear isotherms and stable values of critical exponents are achieved. The extracted values of $M_S(T)$ and $\chi_0^{-1}(T)$ from modified Arrott plots are plotted as a function of temperature as shown in Fig. 4.11 (d, e & f). These data are fitted by using equations 4.5 & 4.6 to estimate the critical exponents β and γ, which are presented in table 4.4. In order to find the critical exponent δ, we have used Widom's scaling given by $\delta = 1 + \frac{\gamma}{\beta}$. The estimated critical exponent from Windom's scaling are found to be 1.62, 1.95 and 2.05 for x = 0, 0.10 and 0.50 respectively. It is also noted that critical exponent δ associated with critical magnetization at $T = T_C$ as $M_{T=T_C} \propto H^{1/\delta}$ [67]. As shown in Table 4.4, the values of δ

estimated from fitting (Fig. 4.12) of *M-H* curves at $T = T_C$ are found to be very close to the δ values as estimated by Widom's scaling, which confirms the reliability of our critical exponents. Importantly, the final critical exponents (Table 4.4) we have obtained are found to be significantly deviated from mean field approximation.

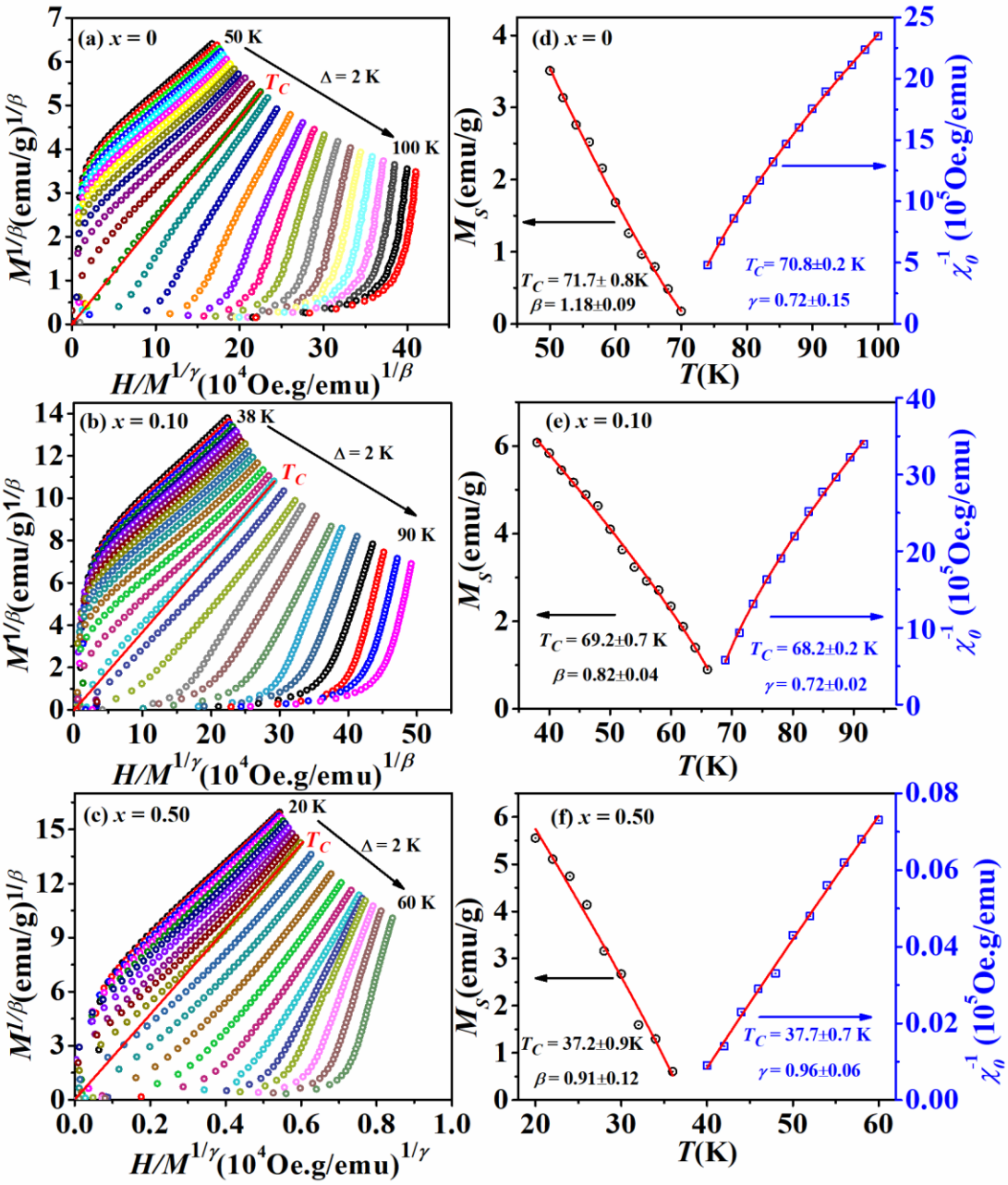

Fig. 4.11: Modified Arrott plots ($M^{1/\beta}$ vs $H/M^{1/\gamma}$) of (a) x = 0, (b) x = 0.10 and (c) x = 0.50 around critical regime. (d, e, f) Spontaneous magnetization and inverse susceptibility along with fitted data using Eq. 4.5 and 4.6 for x = 0, 0.10 & 0.50 respectively.

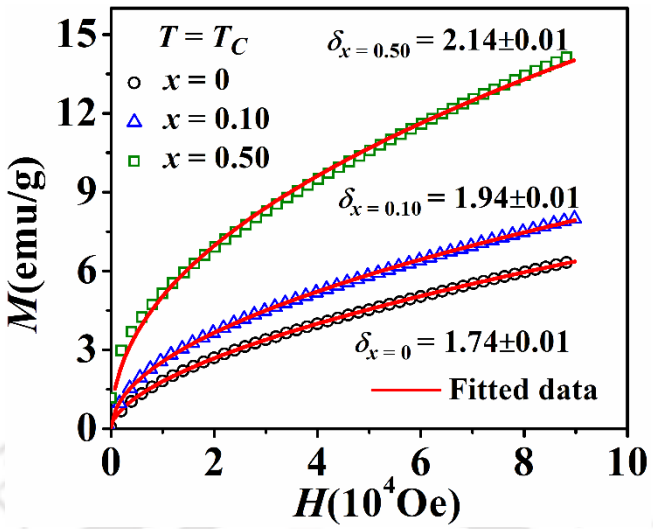

Fig. 4.12: Fitting of isothermal magnetization data at Curie temperature for x = 0 (circle), x = 0.10 (triangle) and x = 0.50 (square) samples.

The reliability of our calculated critical exponent (β, γ & δ) can also be confirmed by scaling hypothesis. The static scaling theory predicts that M (H, ε) can be written as [186],

$$M(H,\varepsilon)|\varepsilon|^{-\beta} = f_{\pm}\left(H|\varepsilon|^{-(\beta+\gamma)}\right) \qquad (4.8)$$

Where, f_+ and f_- are regular analytical functions for $\varepsilon > 0$ and $\varepsilon < 0$, respectively. According to Eq. 4.8, plots of M (H, ε)$|\varepsilon|^{-\beta}$ versus $H|\varepsilon|^{-(\beta+\gamma)}$ would lead to universal curves, one for temperatures $T > T_C$ ($\varepsilon > 0$) and the other for $T < T_C$ ($\varepsilon < 0$). Fig. 4.13 (a, b & c) shows the scaling plot on a linear scale and the inset shows the same data in the logarithmic scale for x = 0, 0.10 & 0.50 respectively. All the data points in the entire range of variables fall into two curves, depending upon the sign of ε. Thus, it confirms that the obtained values of the critical exponents are reasonably accurate.

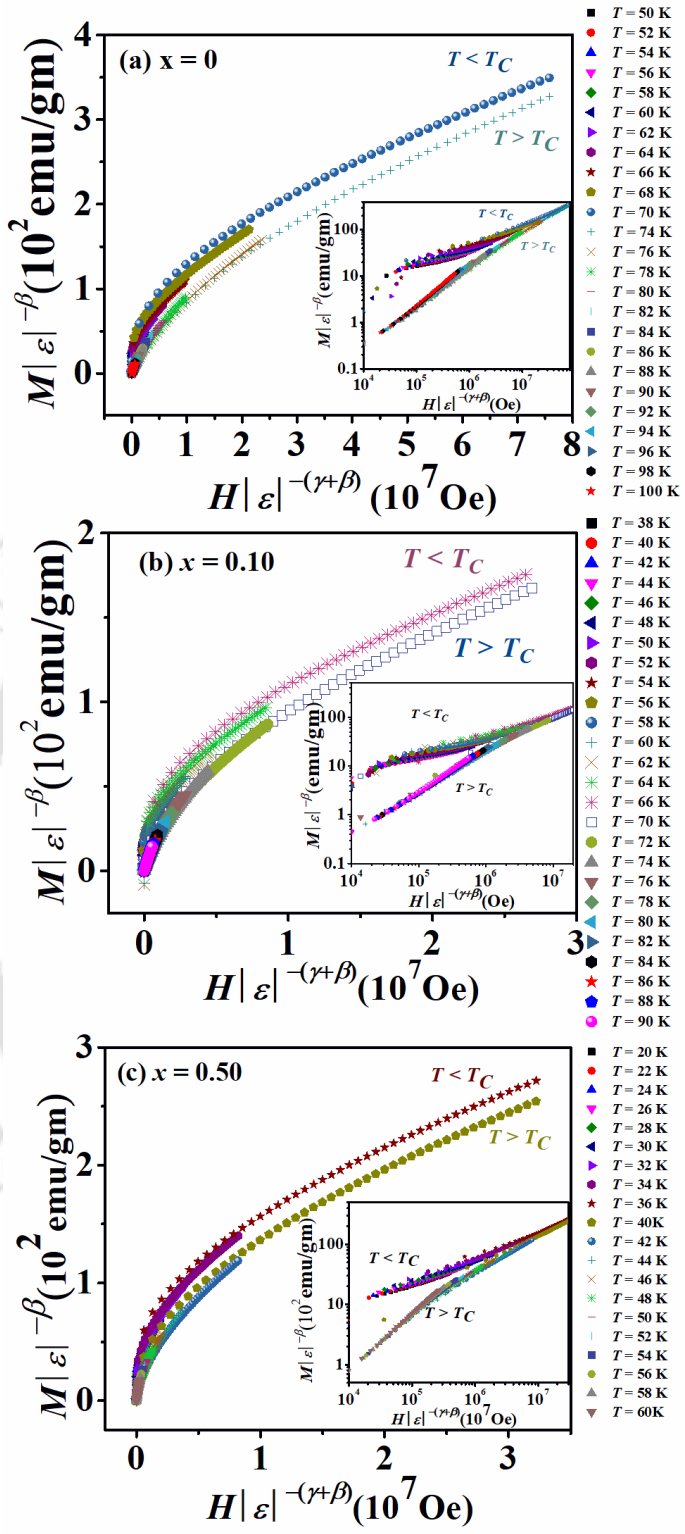

Fig. 4.13: Scaling plots of $M\,|\varepsilon|^{-\beta}$ versus $H\,|\varepsilon|^{-(\gamma+\beta)}$ with β, γ and δ values obtained from modified Arrott plot for (a) x = 0, (b) x = 0.10 and (c) x = 0.50. Different symbols represent data taken at different temperatures. Insets shows the respective plots in logarithmic scale.

The extracted critical exponents using the set of power laws are found to be deviated from universal classes in our case. However, such type of unusual critical exponents have already been reported in previous works on different magnetic systems [186-189]. For example, in case of nano $La_{0.5}Ca_{0.5}MnO_3$ system, the deviation of critical exponents has been explained by possible surface disorder or unsuitability of the theory in nano-system [186]. Unusual critical exponent observed in polycrystalline $La_{0.4}Pr_{0.3}Ba_{0.3}MnO_3$ is explained by the presence of magnetic disorder in the system [187]. In a previous study, the unusual critical behavior observed in $Cu_{1-x}NMn_{3+x}$ (x = 0.1 & 0.3) is explained by the presence of short range antiferromagnetic ordering in the system which vanishes for x = 0.40 [189]. In our system, also the evaluated critical exponents deviate significantly from mean-field values (β = 0.5, γ = 1.0, δ = 3.0) and other universality classes where $\beta < 0.5$ and $\delta > 3.0$. Critical exponent β generally implies how ordered moment grows below T_C, with smaller values indicating faster growth; γ describes the divergence of initial magnetic susceptibility upon approaching T_C from above, with smaller values yielding sharper divergence; and δ describes the curvature of $M(H)$ at T_C, with smaller values reflecting less curvature and slower saturation. In our present system the observed larger values of β suggested a slower increase of the ordered magnetic moment than mean field or other classical magnetic system, which may be due to the significant influence of canted spin structure in our system. On the other hand, the sharper divergence of initial magnetic susceptibility for x = 0 at T_C as compared to x = 0.50 leads to a smaller value of γ (< 1) for x = 0 sample. Similarly, a smaller value of δ for x = 0 as compared to Mn substituted samples implies a slower saturation due to the presence of competing antiferromagnetic ordering.

The MCE is the thermal response of a magnetic material under a changing magnetic field. When a magnetic material is exposed to an external magnetic field, its domains attempt to align along the field direction, resulting in a drop in entropy. But the magnetic domains get disoriented and the material's temperature drops during an adiabatic demagnetization process, in which an applied magnetic field is removed under adiabatic conditions. The magnetocaloric effect can be defined in terms of change in entropy $-\Delta S_M$ and is calculated by considering the Maxwell equations of thermodynamics as discussed in Chapter 1.

For magnetization isothermal taken at small discrete field and temperature intervals ΔS_M (T, H) can be evaluated as [64],

$$\Delta S_M = \sum \frac{M_i - M_{i+1}}{T_i - T_{i+1}} \Delta H_i \tag{4.9}$$

where M_i and M_{i+1} are magnetic moment at temperature T_i and T_{i+1} respectively under an applied magnetic field of $H_{i,k}$ and ΔH_i ($=H_{i,k+1}$-$H_{i,k}$) represent the change in the external magnetic field. Fig. 4.14 shows the distribution of entropy change over temperature scale in the vicinity of T_C for x = 0, 0.10 & 0.50 samples. The magnitude of the peak of $-\Delta S_M$ increases with increasing magnetic field as expected. The value of maximum magnetic entropy changes (ΔS_M^{max}) for x = 0 is found to be 1.5 $JKg^{-1}K^{-1}$ at its T_C for an applied field of 9 T and is comparable to earlier report on $NiCr_2O_4$ [181]. With Mn substitution, this value increases to 2.9 $JKg^{-1}K^{-1}$ for x = 0.50. The efficiency of a magneto caloric material can also be characterized by relative cooling power (RCP) as discussed in Chapter 1 (Eq. 1.17). The estimated values of magneto caloric parameters are presented in Table 4.4 for all the samples. Here, the error is estimated by considering the uncertainties in Temperature (T), magnetic field (H) and magnetic moment (M) of PPMS as discussed in Chapter 2 and by following ref. [190]. Hence, with Mn substitution both width and peak values of ΔS_M increase, which makes it a potential application for magnetic refrigeration.

In order to predict the nature of magnetic transition in the vicinity of FIM-PM transition temperature, we have calculated the normalized change in entropy as described below. In case of a second order magnetic transition the $\Delta S_M / \Delta S_M^{max}$ vs θ curves at different magnetic fields collapse into a common universal curves, where ΔS_M^{max} is the value of ΔS_M at $T = T_C$ and θ is the reduced temperature defined as $\theta = -\frac{T-T_C}{T_{r1}-T_C}$ for $T \leq T_C$ and $\theta = \frac{T-T_C}{T_{r2}-T_C}$ for $T > T_C$. T_{r1} and T_{r2} are the temperatures at full width half maximum of entropy distribution over temperature scale [65]. As shown in Fig. 4.14, the plots of $\Delta S_M / \Delta S_M^{max}$ vs θ at different magnetic fields nearly collapse onto a single universal curve for the all the samples, which further confirms the magnetic transition in the present set of samples is of second order in nature [65].

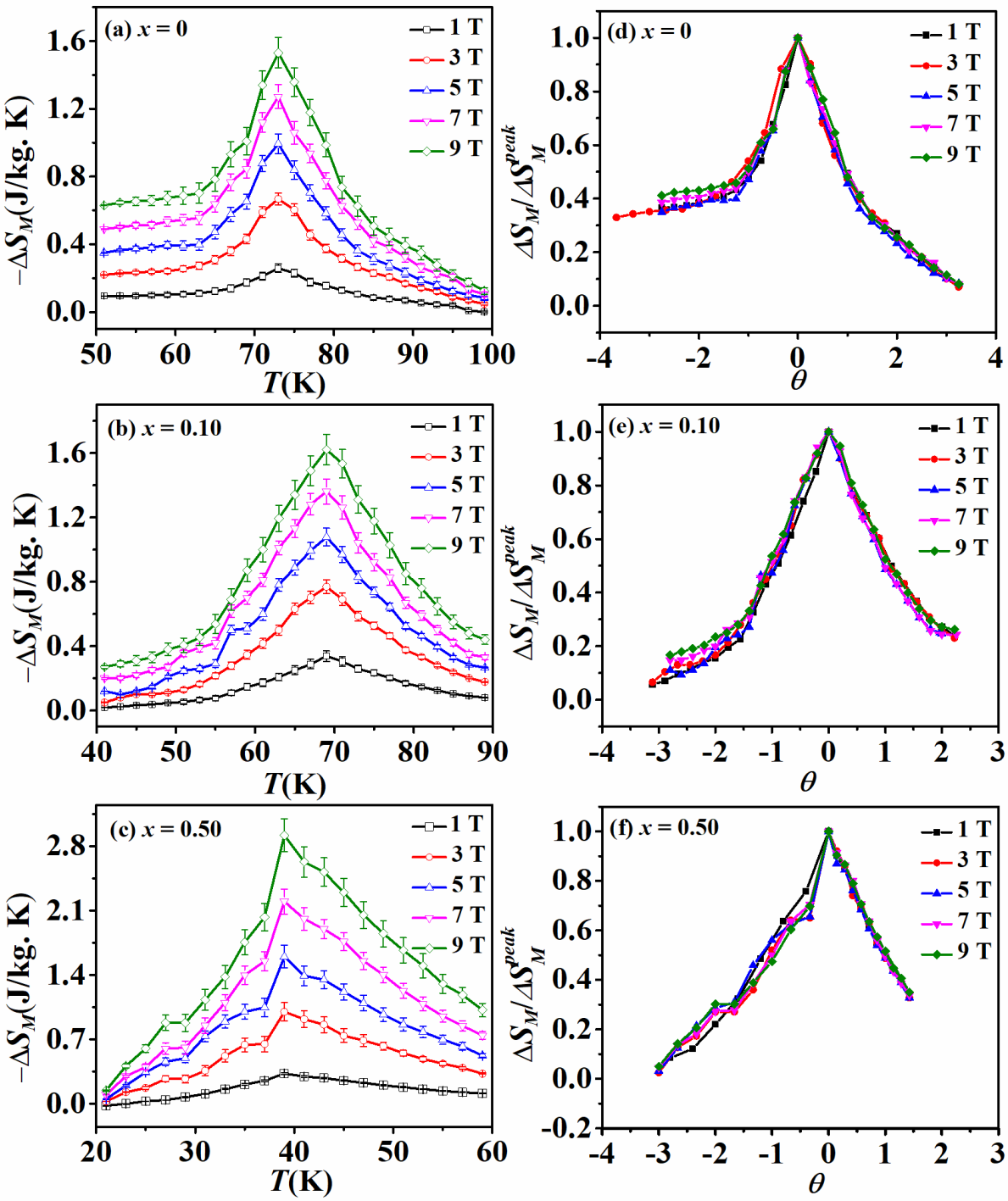

Fig. 4.14: Temperature dependence of MCE for (a) x = 0, (b) x = 0.10, (c) x = 0.50 and their respective (d, e & f) $\Delta S_M / S_M^{max}$ vs θ plots.

Table 4.4: Magnetocaloric parameters and critical exponents of $Ni_{1-x}Mn_xCr_2O_4$ (x = 0, 0.10 and 0.50) at an applied maximum field of 9 T.

Sample	$-\Delta S_M$ ($J \cdot Kg^{-1} \cdot K^{-1}$)	RCP ($J \cdot Kg^{-1}$)	β	γ	δ
x = 0	1.5±0.1	26.0±0.2	1.18±0.09	0.72±0.15	1.74±0.01
x = 0.10	1.6±0.1	29.2±0.2	0.82±0.04	0.72±0.02	1.94±0.01
x = 0.50	2.9±0.2	58.2±0.3	0.91±0.12	0.96±0.06	2.14±0.01

In a magnetic system with a second - order phase transition, the field dependent magnetic entropy change (ΔS_M) at transition temperature (T_C) obeys a power law given by [191],

$$\Delta S_M(H) \propto H^n \tag{4.10}$$

According to mean field approach, the value of exponent n at T_C is estimated to be 2/3 [186, 192]. Though, the determined values of n exponent for x = 0 and x = 0.10 are found close to n = 2/3, a significant deviation is observed for x = 0.50 sample, which is showing a linear dependence ($n \approx 1$) on applied magnetic field (Fig. 4.15). This deviation can be attributed to the specific magnetic microstructure of the system, which is affected by various factors like chemical homogeneity, distribution of crystal defects, lattice stresses, distribution of grain sizes and shapes [193]. Previous study also shows that critical phenomena of $MnCr_2O_4$ cannot be described within the framework of existing universality classes and probably belongs to a separate class [180]. Therefore, a deviation from n = 2/3 can be also taken as the indication of deviation of critical exponents from the known theoretical models.

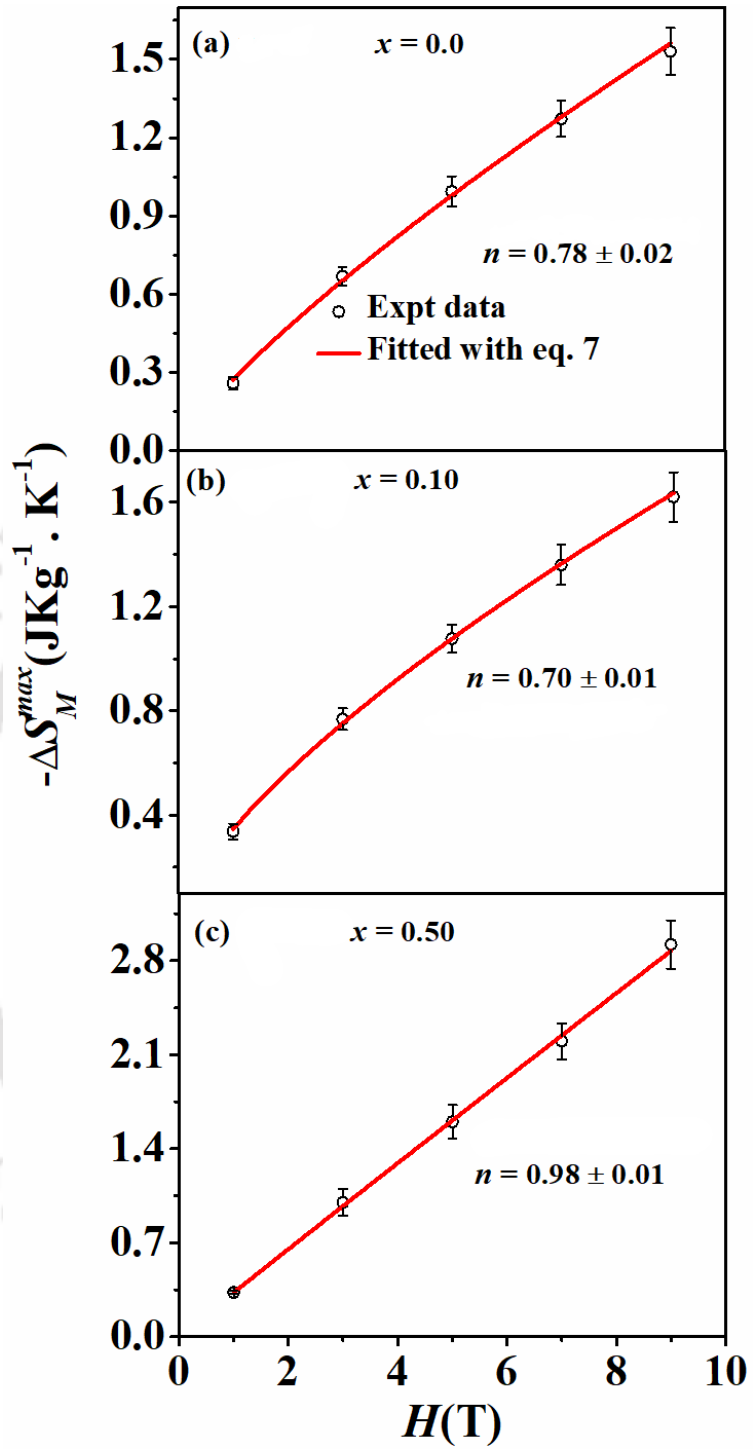

Fig. 4.15: Maximum entropy change vs applied magnetic field for (a) x = 0, (b) x = 0.10 and (c) x = 0.50 samples.

4.2 Cd Substituted $NiCr_2O_4$ Series

In this section, we have described the preparation of Cd substituted $Ni_{1-x}Cd_xCr_2O_4$ (x = 0-0.30) compounds and study of their structural, magnetic and dielectric properties. Various important properties such glass like magnetic phase, reversible magnetocaloric effect, dielectric properties and impedance spectroscopy of this series have been discussed in details.

The Cd substituted samples were synthesized by using sol-gel method. Stoichiometric ratio of $Ni(NO_3)_2{\cdot}6H_2O$, $Cd(NO_3)_2{\cdot}4H_2O$ and $Cr(NO_3)_3{\cdot}9H_2O$ of 99% purity were used as the starting materials for the preparation of the samples. The as synthesized samples were grinded and pre-sintered at 600 ^{0}C followed by a sintering at 800 ^{0}C for 12 hours. Final sintering was performed at 1100 ^{0}C for 24 hours.

4.2.1 Structural Properties

For structural characterization, XRD patterns were recorded for all the samples at room temperature as shown in Fig. 4.16. Rietveld refinement confirms the single phase tetragonal ($I4_1/amd$) for the parent (x = 0) and cubic ($Fd\bar{3}m$) crystal structure for Cd substituted samples (Fig. 4.17 (a, b & c)). For x = 0 compound, the estimated lattice parameters are a = b = 5.8271 (3) Å, c = 8.4392 (6) Å. As shown in Fig. 4.18 (a), the increase in lattice constant with Cd substitution is attributed to the larger ionic size of Cd^{2+} (0.78 Å) as compared to Ni^{2+} (0.55 Å) ion [143]. The results of Rietveld refinements were further utilized in VESTA software to estimate the bond length (Fig. 4.18 (b)) and bond angles (Fig. 4.18 (c)) of lattice structures. The variations in bond length and bond angles are expected due to lattice expansion with Cd substitution. The bond angles corresponding to the A-O-B network decreases and that of B-O-B increases with Cd substitution.

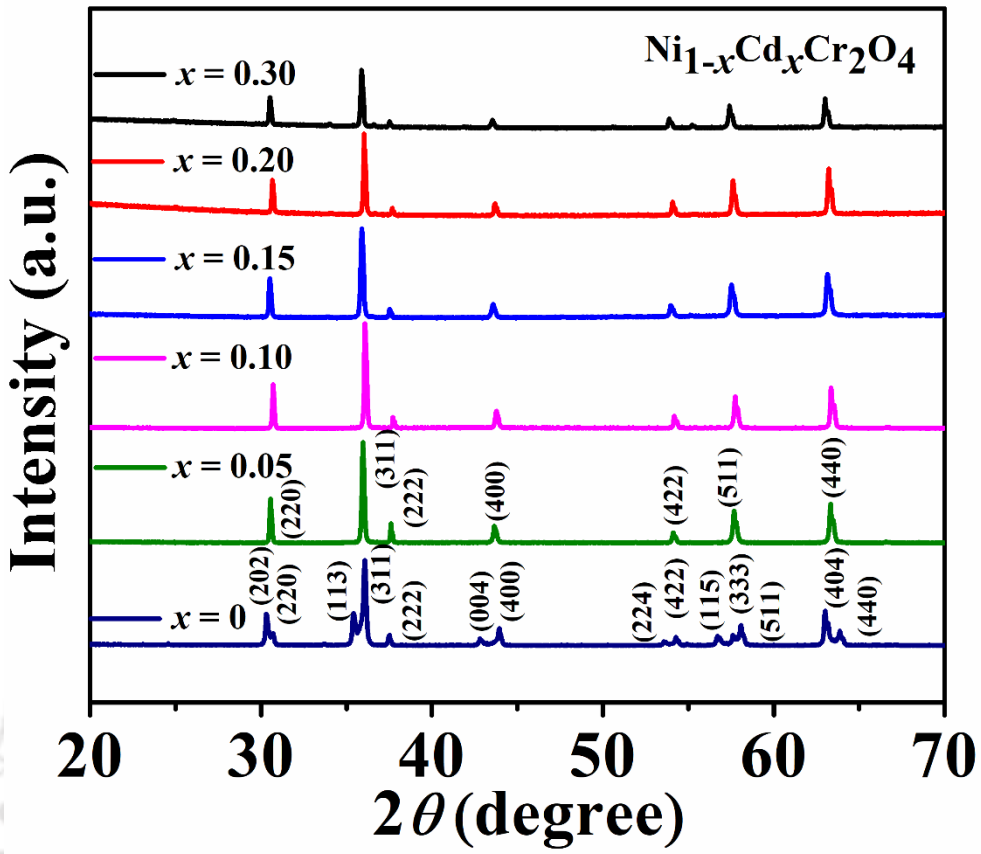

Fig. 4.16: XRD patterns recorded at room temperature for $Ni_{1-x}Cd_xCr_2O_4$ (x = 0 – 0.30).

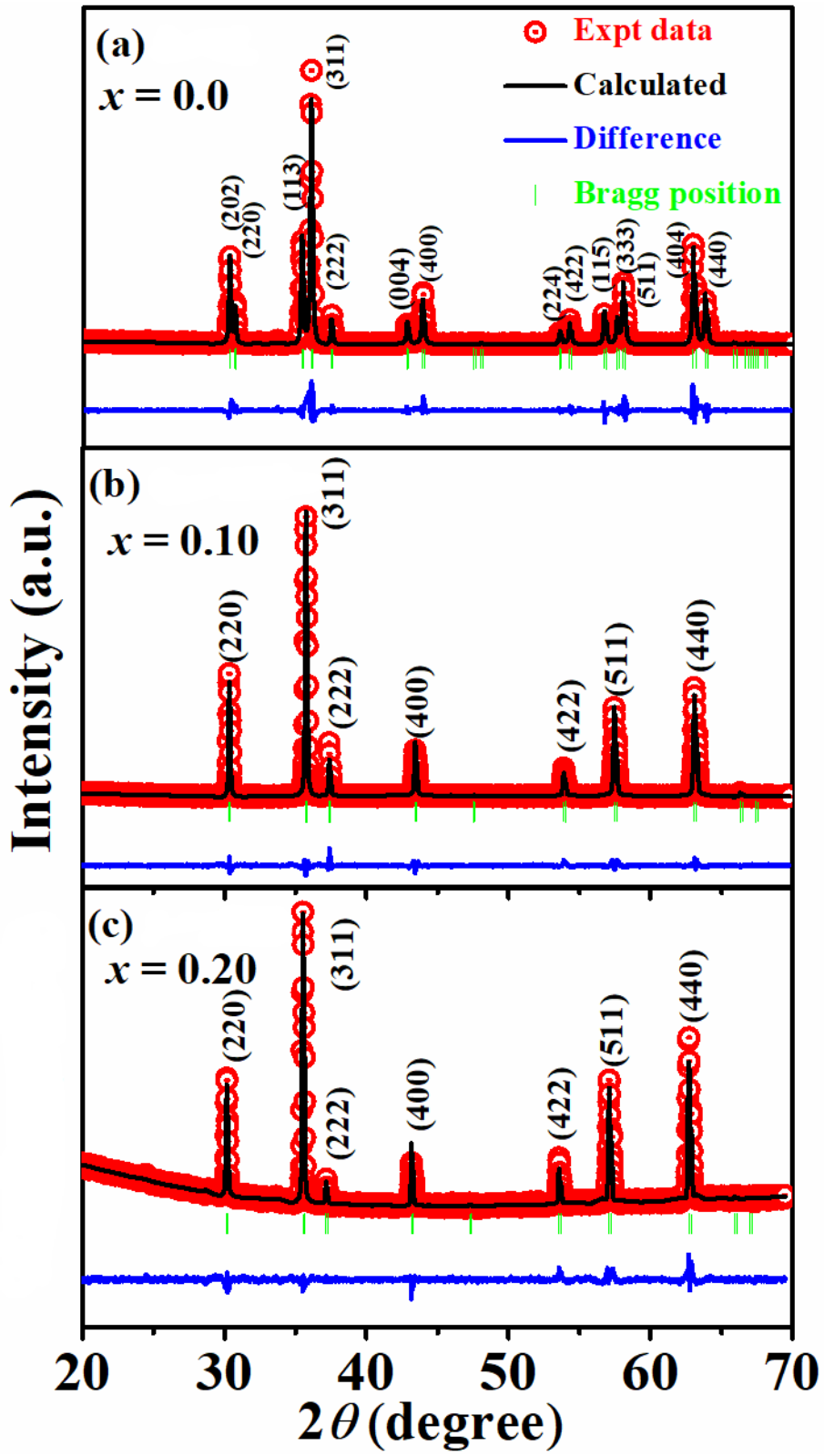

Fig. 4.17: Typical XRD patterns (open red circle) along with Rietveld refined data (black solid line) for (a) $x = 0$, (b) $x = 0.05$ & (c) $x = 0.20$ samples.

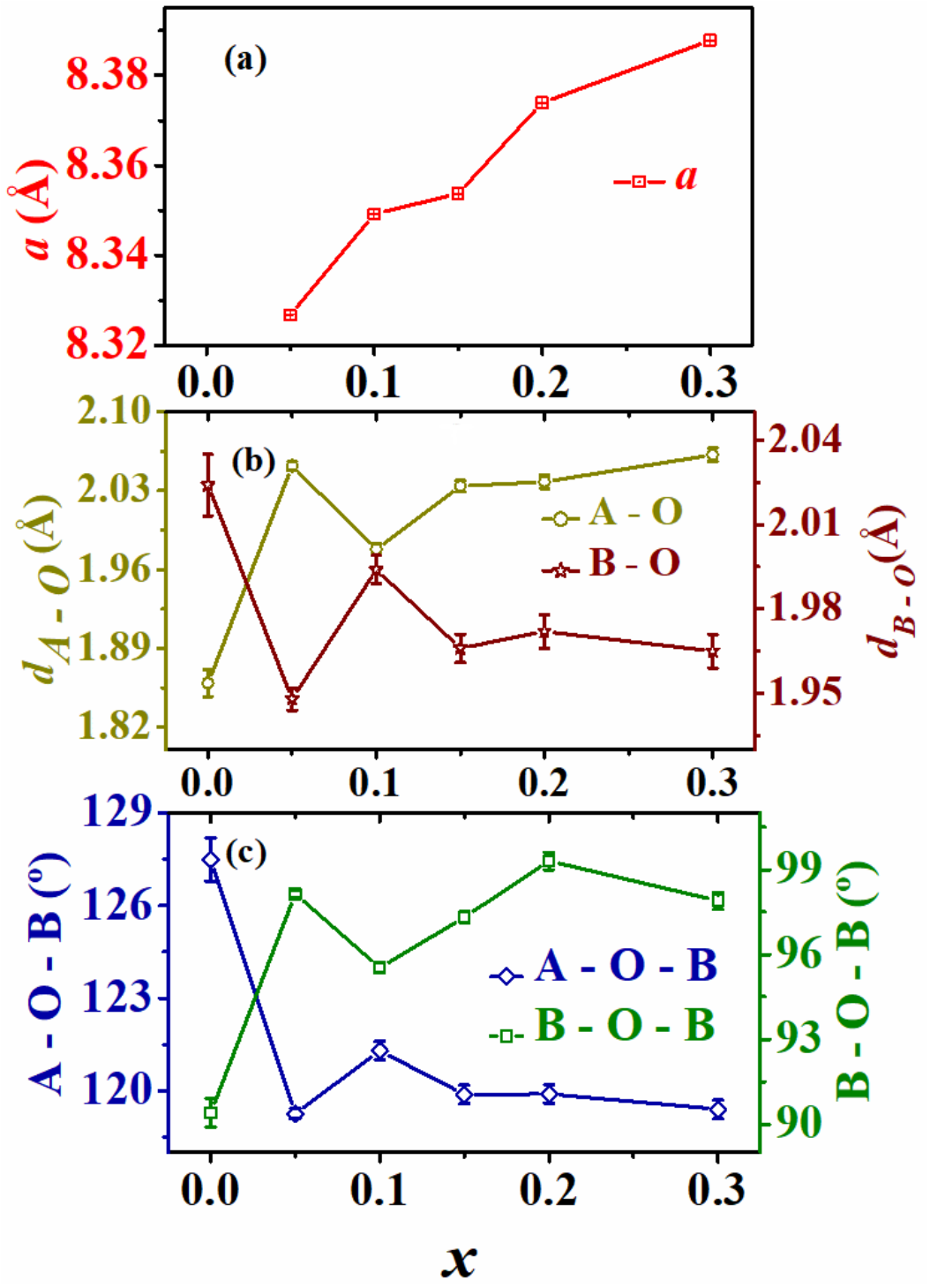

Fig.4.18: Estimated (a) lattice parameters, (b) bond length and (c) bond angles of $Ni_{1-x}Cd_xCr_2O_4$ (x = 0 – 0.30).

The EDX spectra performed for x = 0.30 samples are shown in Fig. 4.19 (a). The cationic ratio of Cd:Ni:Cr is found to be 0.3:0.6:2.0 respectively and it is almost comparable to normal starting composition. The EDX spectra further confirm the absence of any impurity elements in the sample. The elemental mapping (Fig. 4.19 (b)) indicates the uniform distribution of these elements in the sample. FESEM micrograph of the samples are shown in Fig. 4.20 (a-d). All the samples are showing a similar kind of morphology with bi-pyramidal shape grains. The average particle size of samples is estimated from the size distribution histogram as shown in Fig. 4.20 (e, f). We have observed an increase in the average size of the particles with Cd substitution.

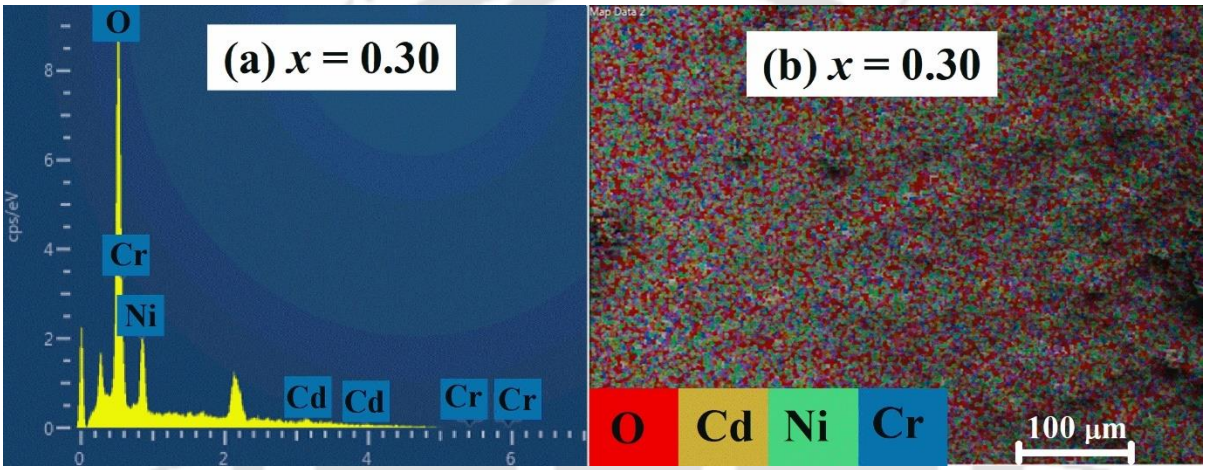

Fig. 4.19: EDX spectra (a) and elemental mapping (b) for x = 0.30 sample.

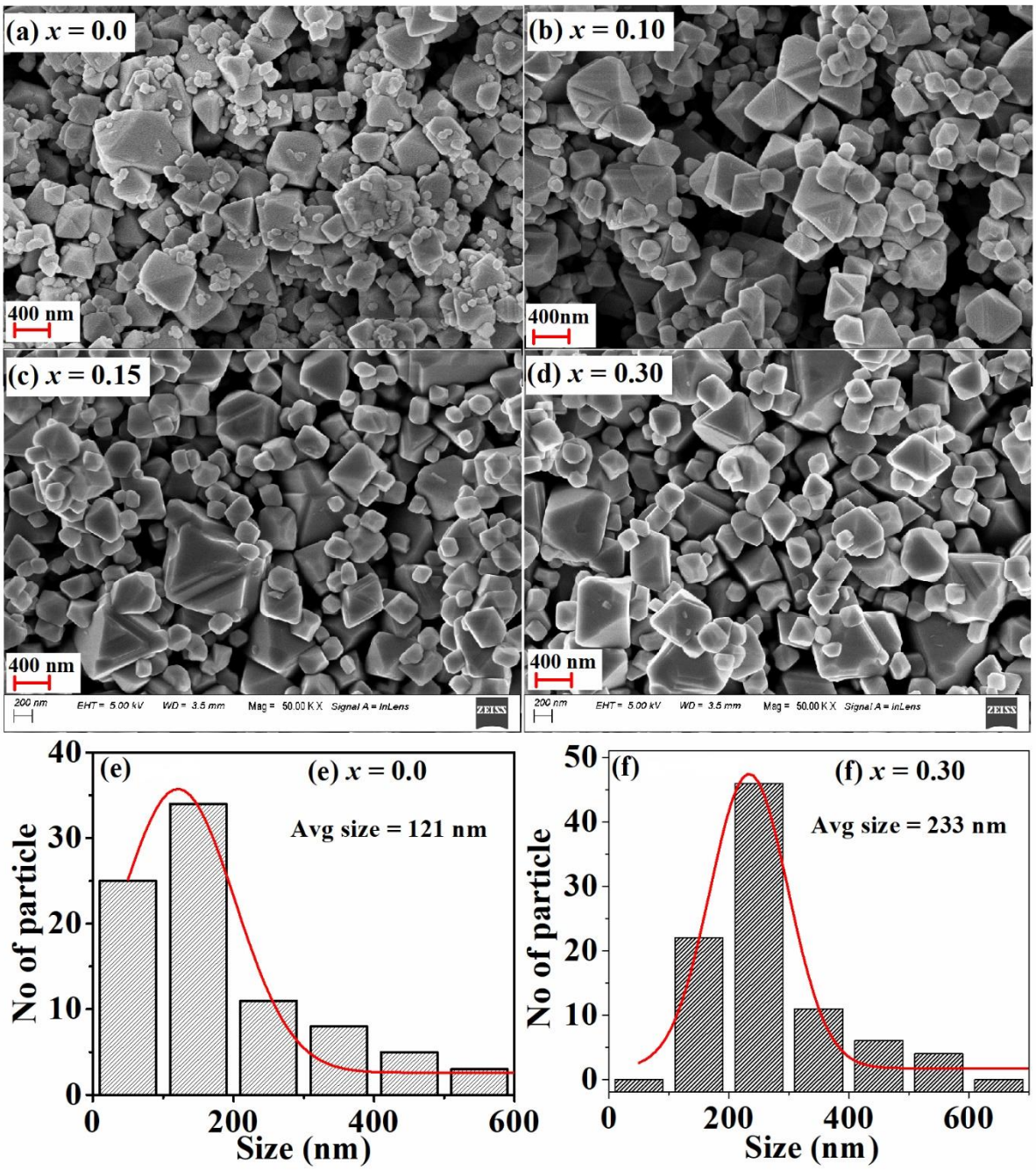

Fig. 4.20: FESEM micrographs of $Ni_{1-x}Cd_xCr_2O_4$ samples (a-d) and particle size distribution histogram (e, f).

4.2.2 Temperature Dependent Magnetic Properties

Temperature dependent magnetization (M vs T) measurements under zero field cooled (ZFC) and field cooled (FC) conditions were carried out at H = 200 Oe as shown in Fig. 4.21. The parent compound is showing a FIM transition near T_C = 70 K and an AFM transition at T_N = 29 K. As suggested by Neutron diffraction study [80], the observed FIM and AFM transitions can be attributed to the ordering of longitudinal and transverse magnetic components of canted spin structure of $NiCr_2O_4$. With Cd substitution, we observe that the low temperature AFM transition at 29 K has completely disappeared and instead another transition near the FIM T_C with irreversibility between ZFC and FC magnetization is observed. This transition can be attributed to the ordering of transverse components of magnetic moment as a result of possible enhancement of their magnitude due to the increase in spin canting structure. For x = 0.20 sample, we have observed an additional transition in the ZFC magnetization curve at 34 K and it is accompanied by a sudden drop in FC magnetization curve. This transition can be attributed to the possible formation of short range magnetic phase as a result of competing exchange interaction between different magnetic components of the canted spin structure. The x = 0.30 sample shows a glass like magnetic transition around T_f = 22 K. The broadening of M-T curves near transition temperatures indicates the enhancement of spin disorderness for the samples x = 0.20 & 0.30. Therefore, the magnetism in these two samples (x = 0.20 & 0.30) is mostly governed by short-range magnetic correlation rather than any strong FIM or AFM ordering.

Temperature dependent inverse FC susceptibility data in the paramagnetic region were analyzed with the help of molecular field theory fitting (Eq. 3.3) for x = 0 – 0.20 samples as shown in Fig 4.22. The fitted parameters are presented in Table 4.5. Here, the parameter Θ represent the strength of AFM super exchange-interaction through A-O-B networks and it is found to decrease with Cd substitution. The reductions in T_C with Cd substitution further reflects the weakening of super exchange interactions. The parameter ξ represent the curvature in the inverse susceptibility plot. A smaller value of ξ, generally leads to a less curvature in the inverse susceptibility and the system shows tendency towards anti-ferromagnetism. The reduction in ξ with Cd substitution confirms the enhancement of AFM nature in these samples. The experimental value of effective paramagnetic moment is also presented in Table 4.5.

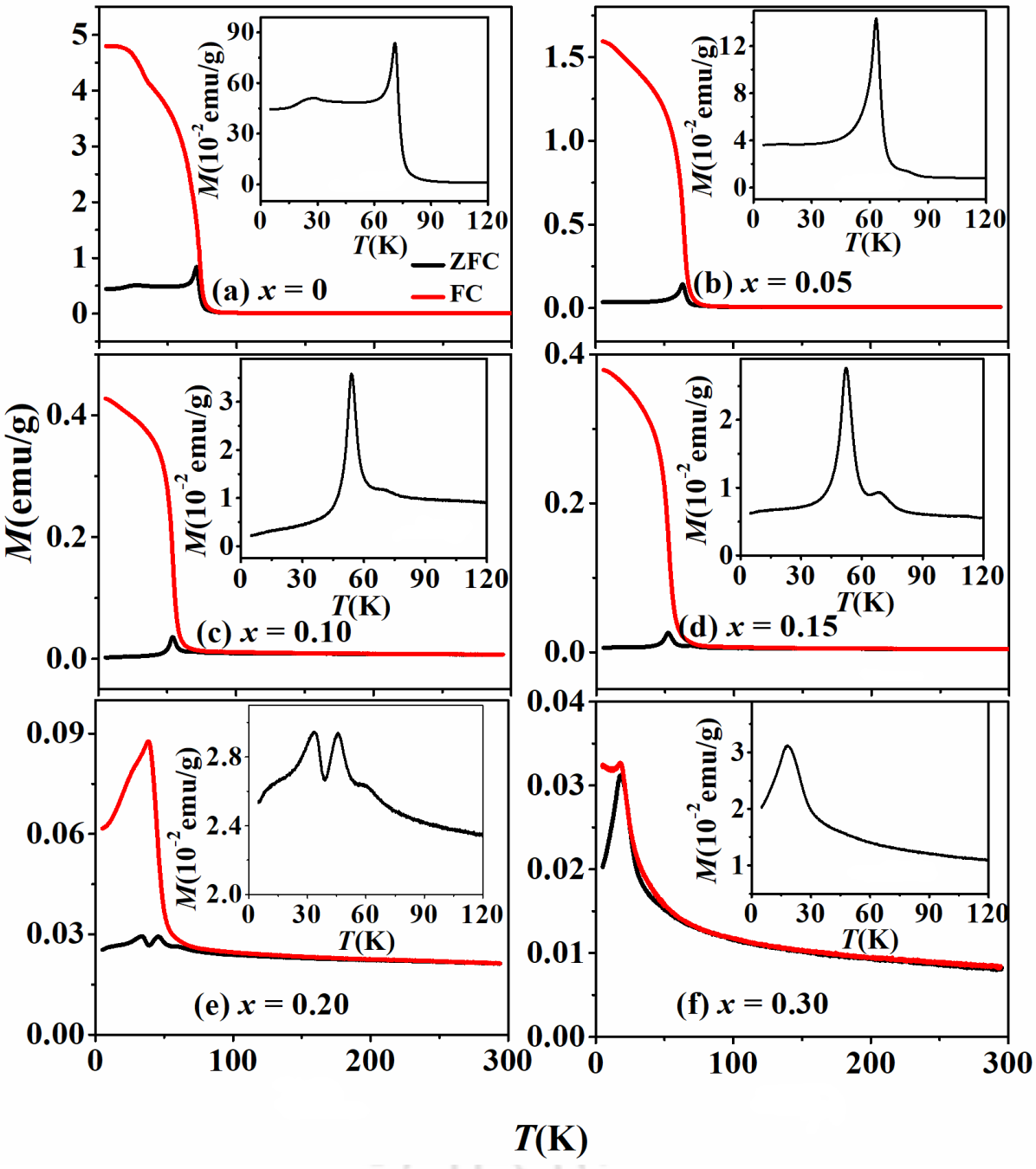

Fig. 4.21: Temperature (*T*) dependence of magnetization (*M*) under zero field cooled (ZFC) and field cooled (FC) conditions.

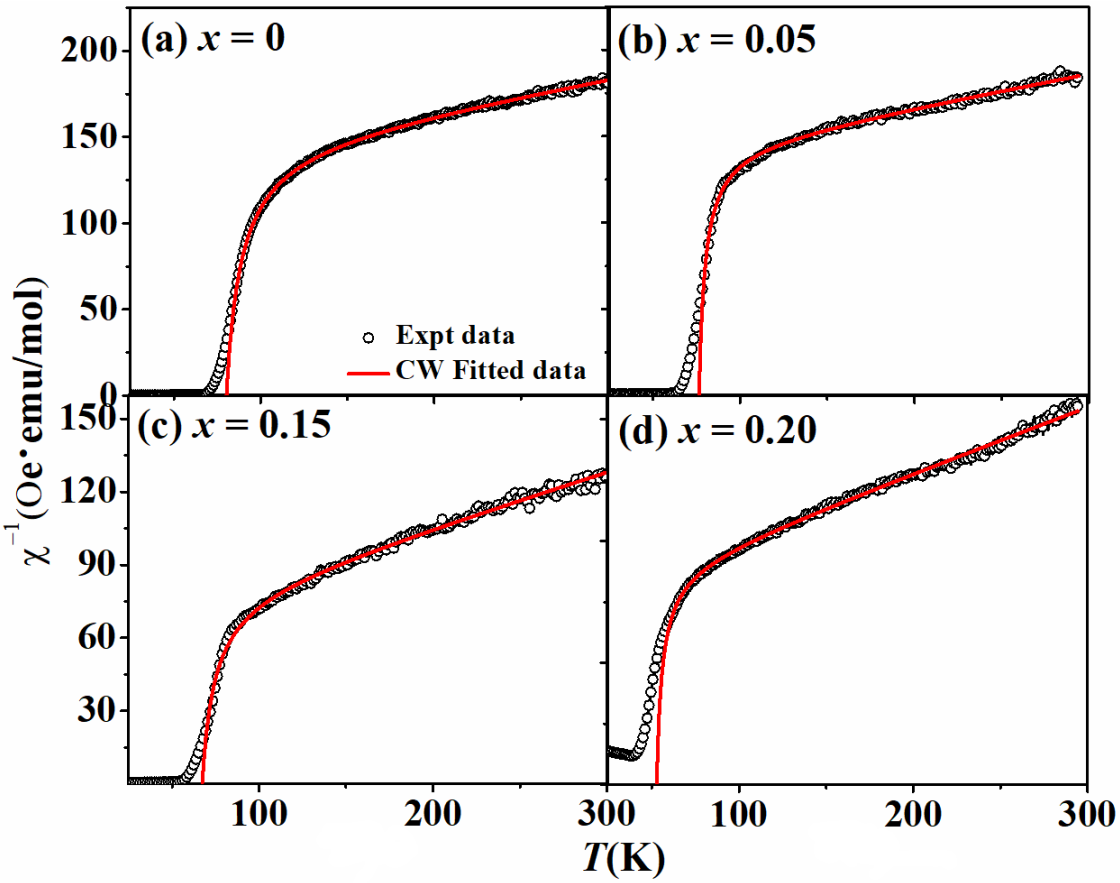

Fig. 4.22: Fitting of inverse susceptibility with molecular field theory.

Table 4.5: Parameters estimated from molecular field theory fitting of $Ni_{1-x}Cd_xCr_2O_4$ (x = 0-0.20).

Parameters	x = 0	x = 0.05	x = 0.10	x = 0.15	x = 0.20
θ (K)	-768 (3)	-705(5)	-373(2)	-289(2)	-280 (2)
C (emu K/Oe mol)	5.67(2)	5.34(3)	5.01(2)	4.5(2)	3.72(1)
ξ (Oe mol K/emu)	1246(9)	504(9)	357(7)	544(17)	273(14)
Θ' (K)	72	73	61	60	50
μ_{eff}(μ_B/f.u.)	6.67	6.47	6.27	5.94	5.42
T_C (K)	70	64	58	55	45

4.2.3: Memory Effect and Relaxation Dynamics

In order to confirm the short-range cluster glass phase, memory effect under ZFC and FC conditions were investigated for x = 0.30 sample (Fig. 4.23). In ZFC condition, the sample was cooled from room temperature down to 5 K at a constant cooling rate of 1 K/min in the absence of an external magnetic field. The cooling process was interrupted at $T_1^{stop} = 15$ K and $T_2^{stop} = 10$ K for a duration of time of 1 h. After reaching 5 K, a probing magnetic field of 200 Oe was applied and the magnetization (M_{ZFCW}^{mem}) was measured as a function of temperature during warming. The conventional ZFC magnetization curve (M_{ZFCW}^{ref}) was also recorded with the same cooling rate for reference. As shown in Fig. 4.23 (a), the temperature dependence of the difference in magnetization $\Delta M = M_{ZFCW}^{mem} - M_{ZFCW}^{ref}$ between the memory and reference data indicates clear evidence of memory dip at halting temperatures 10 K and 15 K. In a glassy magnetic system, the spin-spin correlation length grows during the halting time, even in zero magnetic field, and shows a memory dip in zero field cooled warming (ZFCW) data at halting temperature upon reheating.

To study the memory effect under FC condition, the sample was cooled in an external field of H = 200 Oe from room temperature down to 5 K with a slow cooling rate of 1 K/min. Below T_f, we interrupted the cooling process at T_1 = 15 K and T_2 = 10 K for a duration of t_w = 1 hour each. At each stopping temperature, the magnetic field was turned off and the system was allowed to relax. After the lapse of waiting time (t_w), the same magnetic field was reapplied and resumed the cooling process. The magnetization curve obtained from this process is referred as M_{FCC}^{stop}. After reaching T = 5 K, sample was warmed up with a same heating rate of 1 K/min to paramagnetic region in the same magnetic field and the memory magnetization curve (M_{FCW}^{mem}) was recorded. The FC magnetization curve during cooling was also recorded for the compound and is depicted as M_{FCC}^{ref}. From Fig. 4.23(b), it is clear that the obtained M_{FCW}^{mem} curve is exhibiting a clear signature of the past history by attempting to follow the M_{FCC}^{stop} curve. These behaviors indicate that the previous behavior of the spins during the cooling protocol is imprinted as a memory in the system.

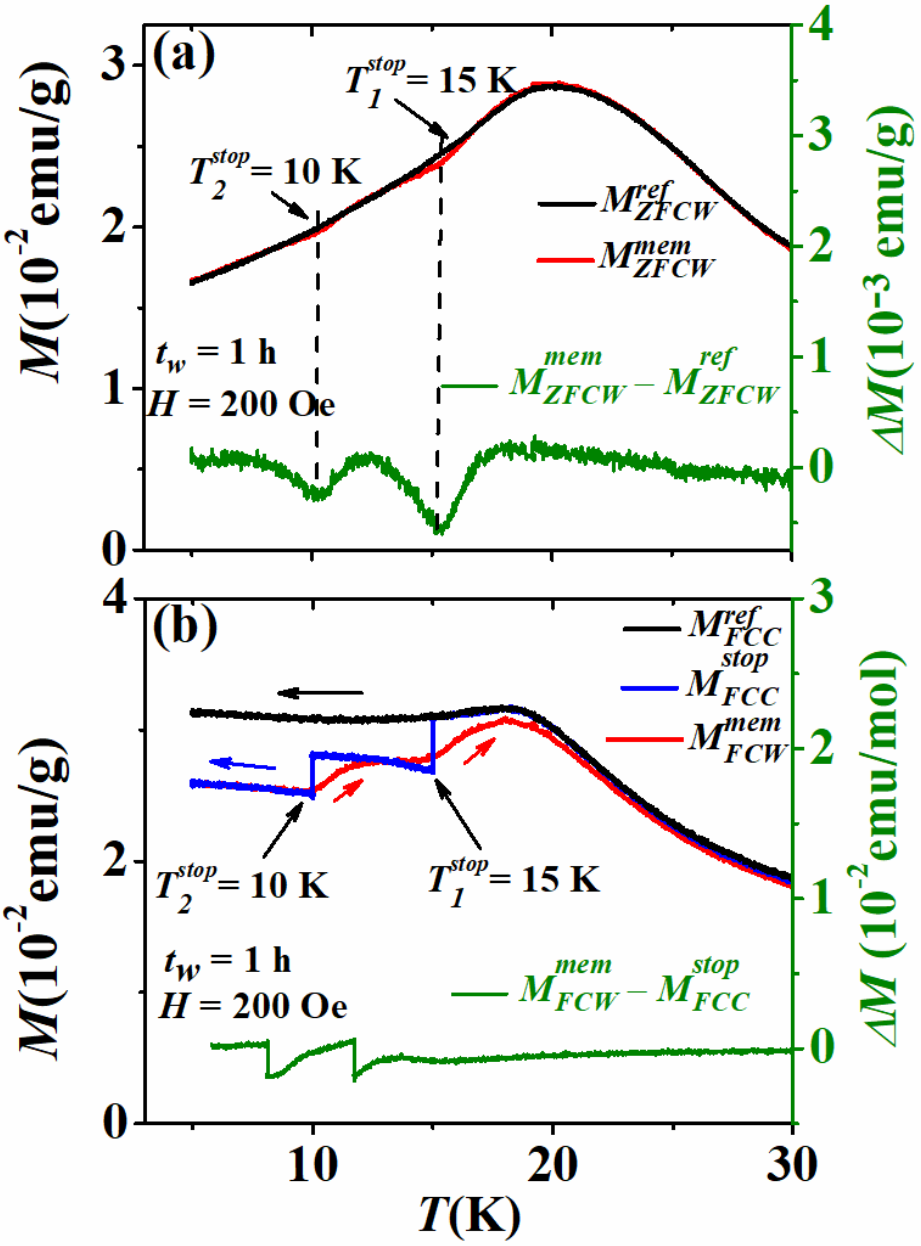

Fig. 4.23: (a) Memory effect in magnetization under (a) ZFC and (b) FC protocols at H = 200 Oe for x = 0.30 sample.

To study the relaxation of isothermal remanent magnetization, the sample was first cooled down to T = 15 K and a magnetic field of 6 T was then applied. After reducing the magnetic field to zero, magnetization was recorded for a period of time t = 6000 s. Fig. 4.24 shows the decay of magnetization with time. The relaxation data was analyzed by the stretched exponential function (Eq. 3.2). The ratio of M_{sg}/M_0 is found to be 1.2 and confirms the

dominant glassy component in the system. The rate of relaxation is defined by the parameters n and τ. The value of n (= 0.37) lies in the range $0 < n < 1$ and indicates the activation of relaxation against multiple anisotropy barriers. The value of relaxation time is found to be τ = 835 s.

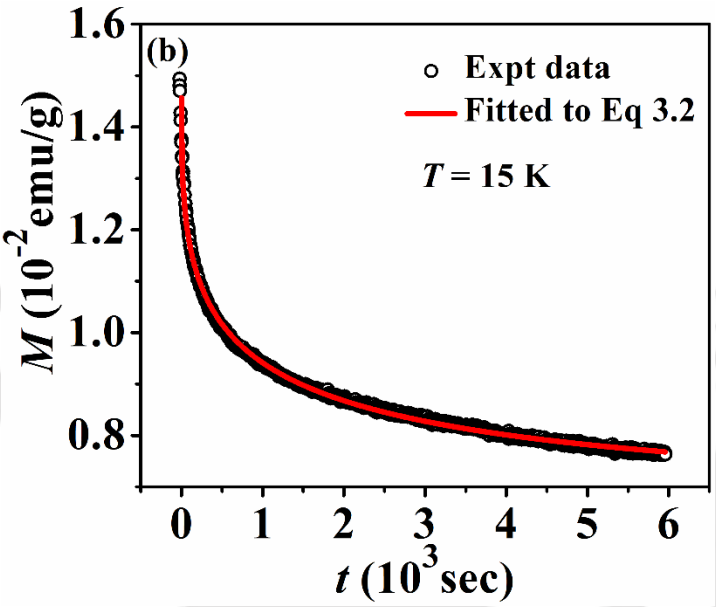

Fig. 4.24: Relaxation of ZFC isothermal remanent magnetization measured at T = 15 K. The solid line (red) represent the fit using stretched exponential decay function (Eq. 3.2).

4.2.4: Field Dependent Magnetization and Exchange Bias studies

The field dependent magnetization (M-H) loops recorded at T = 5 K are shown in Fig. 4.25. Large coercivity is observed for x = 0 & 0.05 samples, which can be attributed to the existence of competing long range AFM and FIM interactions. On the other hand, almost linear loop is observed for x = 0.10 – 0.30 samples due to dominant AFM interaction which completely overtakes the FIM interaction. For the parent compound, the estimated value of M_S is found to be 0.26 μ_B/f. u. and it is comparable to the value (0.30 μ_B/f. u.) observed from neutron diffraction measurement [79]. The drastic reduction in M_S with Cd substitution (M_S = 0.08 μ_B/f. u. for x = 0.05) can be attributed to the nonmagnetic nature of Cd and enhancement

in canting nature of the spin structure. The ordering of AFM components at much higher temperature in the Cd substituted samples as compared to the parent compound further confirms the enhancement in spin canting nature.

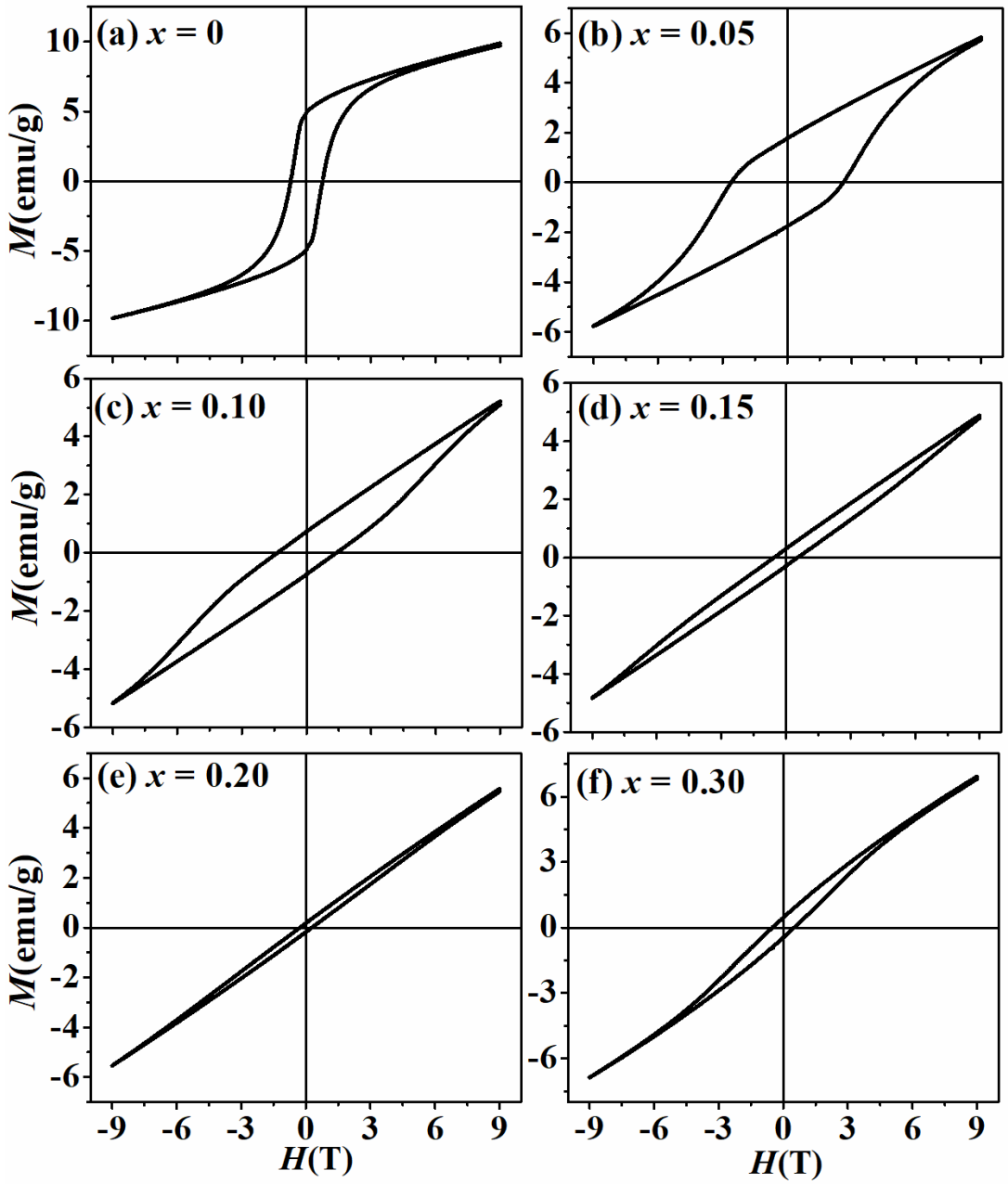

Fig. 4.25: ZFC field dependent magnetization (*M-H*) loops recorded at T = 5 K.

In order to investigate the EB behavior, *M-H* loops were recorded at T = 5 K after cooling the samples under an external magnetic field of $H = \pm 0.5$ T from room temperature.

As shown in Fig. 4.26, we have observed shifting in the *M-H* loops along *H* axis. The estimated values of exchange bias field (H_{EB}) for the Cd substituted samples x = 0.05 & 0.15 are found to be 1.65 kOe and 7.47 kOe respectively and they are found to be quite large as compared to the parent compound (H_{EB} = 91 Oe for x = 0).

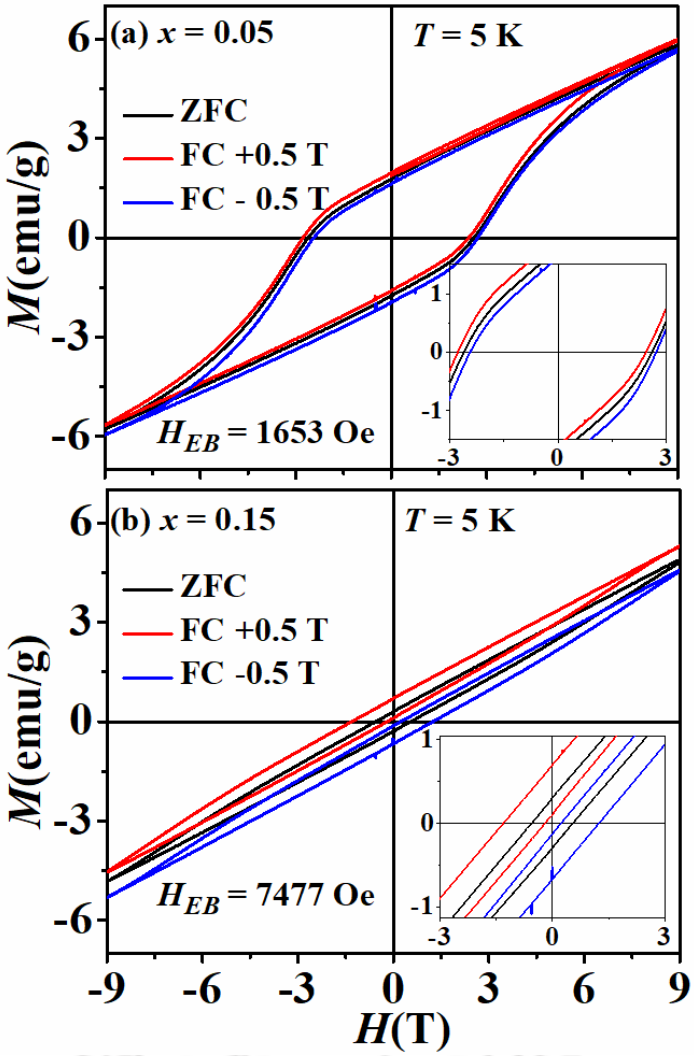

Fig. 4.26*:* *M-H* loops recorded at T = 5 K after FC at H = ± 0.5 T for (a) x = 0.05 and (b) x = 0.15 sample.

The MCE is investigated for x = 0.20 sample that exhibits peculiar multiple magnetic transitions. The magnetic entropy change, $-\Delta S_M$ is estimated from the isothermal magnetization measurements at several temperatures and using Eq. 4.9. As shown in Fig. 4.27, we have taken several initial *M-H* curves in between 2 K to 50 K. All the initial *M-H* curves

are recorded with a maximum measuring field of 9 T and the difference in temperature between two successive isotherms is ΔT = 2 K. The non-saturating *M-H* nature is due to the dominant competing AFM phase in the sample. The distribution of entropy change over temperature scale is shown in Fig. 4. 27 (b). We have observed both normal and inverse MCE for this sample and can be used to maintain a constant temperature bath in solid state refrigeration devices. The $-\Delta S_M$ is showing a positive (normal MCE) maxima near the ferrimagnetic transition temperature T_C. The value of $-\Delta S_M$ decreases as temperature approaches T_f, and changes to negative (inverse MCE) below 20 K. The observed inverse MCE effect can be attributed to the existence of short range magnetic phases in the system. The maximum entropy change at T = 2 K is found to be $-\Delta S_M = -0.431(3)$ J·kg^{-1}·K^{-1}.

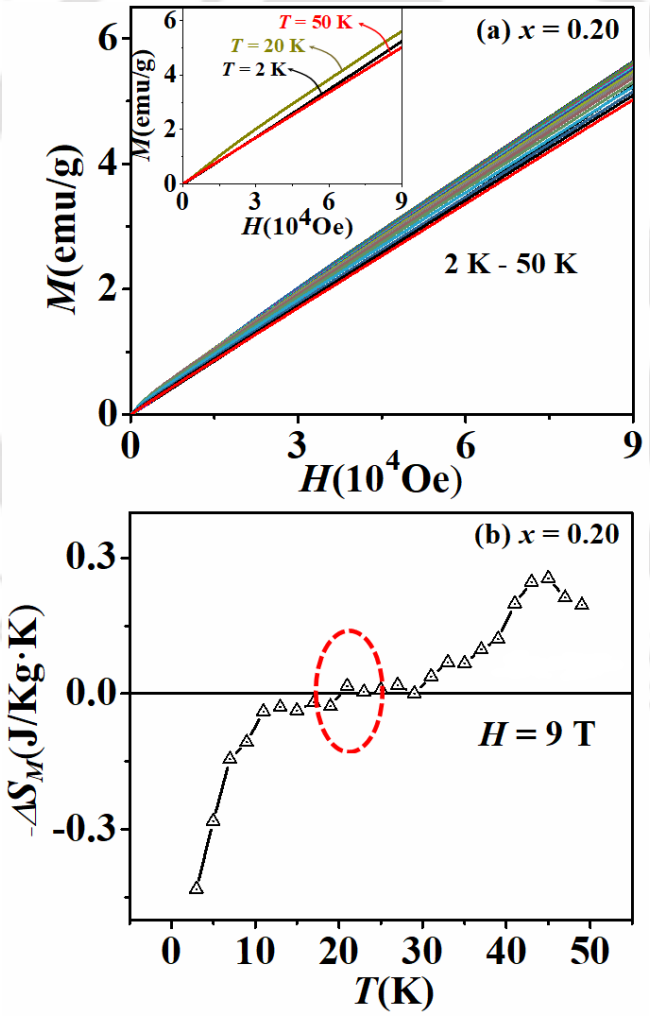

Fig. 4.27: (a) Isothermal magnetization recorded at different temperatures and (b) entropy distribution over temperature scale for x = 0.20 sample.

4.2.5 Dielectric and Impedance Spectroscopy Study

To study the dielectric properties, temperature and frequency dependent dielectric constant (ε') and loss ($tan\ \delta$) have been investigated in the samples over a temperature scale of 30 K to 300 K. Fig. 4.28 shows the temperature dependent ε' and $tan\ \delta$ at a frequency of f = 500 Hz. For all the samples we have observed a very small increase in ε' and $tan\ \delta$ with temperature up to around 200 K and it increases abruptly afterwards. The increase in dielectric constant with temperature can be attributed to the increase in concentration of charge carriers and their polarization [194, 195].

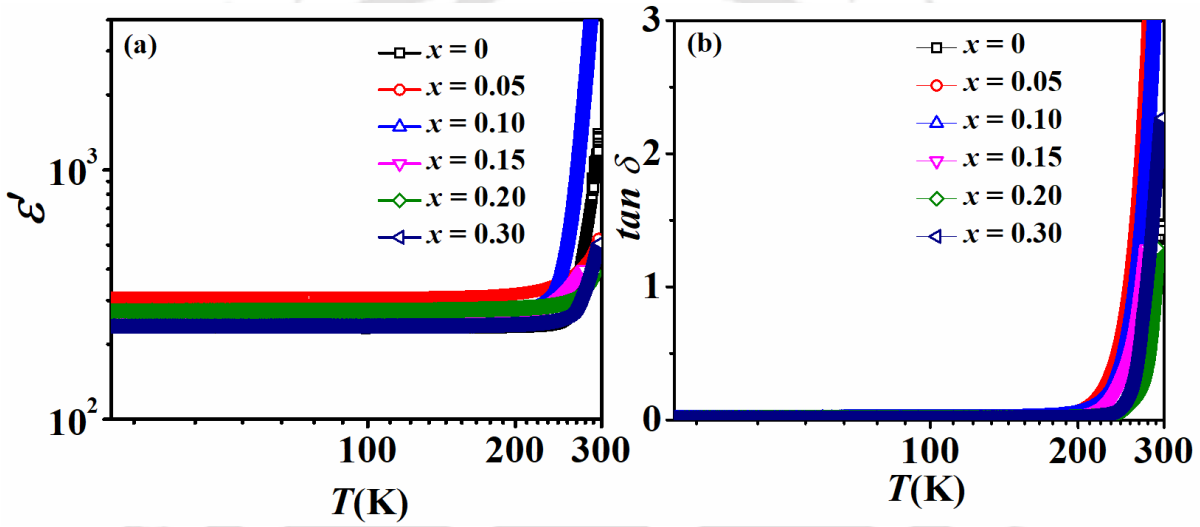

Fig. 4.28: Temperature dependent dielectric constant (ε') and loss tangent ($tan\ \delta$) measured at f = 500 Hz.

The temperature dependent dielectric constant measured at different frequencies at the low temperature regime are shown in Fig. 4.29. The observed anomalies in ε' near the magnetic transition temperature suggests the magneto dielectric coupling in these systems. The anomaly is found to be more distinct for x = 0.05 sample as compared to the parent compound and it indicates the possible enhancement in magneto dielectric response for this sample. Previous reports suggest that $NiCr_2O_4$ shows magneto dielectric coupling transition at both FIM and AFM transition temperatures. The observed anomalies in the present compounds are found to be broad over temperature scale and therefore it is difficult to predict the exact nature of magnetic transition (FIM or AFM) at that corresponding temperatures.

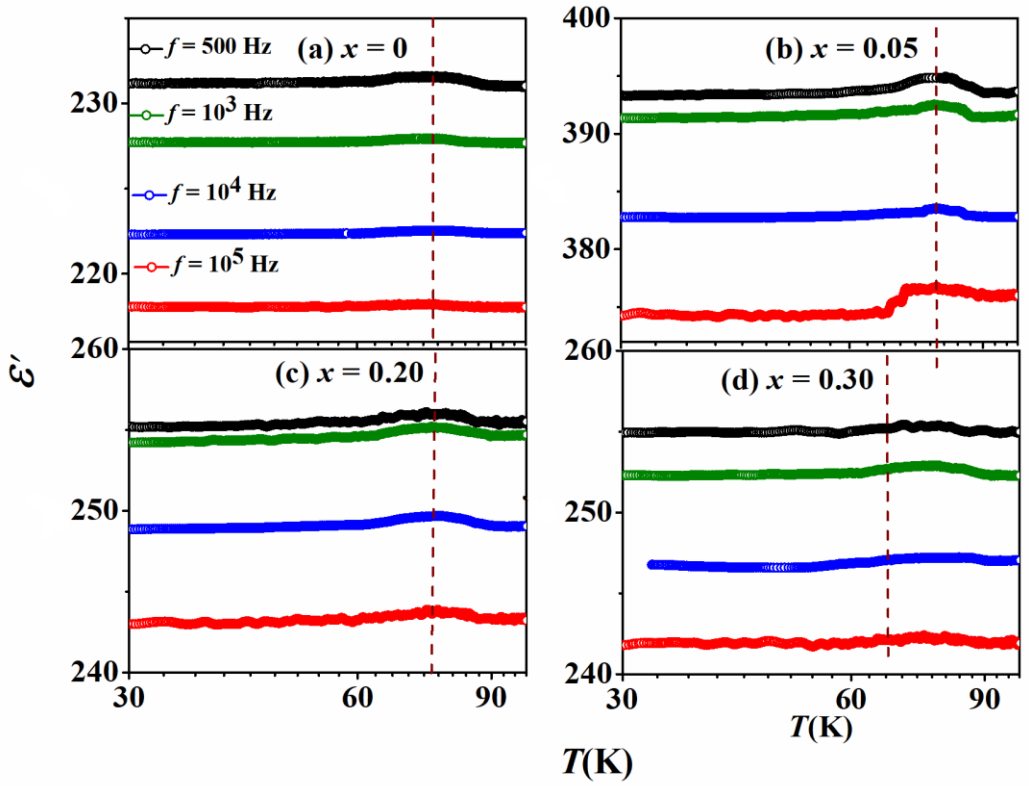

Fig. 4.29: Temperature dependent dielectric constant (ε') near magnetic transition temperature at four different frequencies for (a) x = 0, (b) x =0.05 (c) x = 0.20 and (d) x = 0.30 samples.

The frequency dependent of real (Z') and imaginary (Z'') components of impedance at different temperature (27 K-300 K) for x = 0, 0.10 & 0.30 samples are shown in Fig. 4.30. The Z' value is found to fall quite sharply with increase in frequency up to 10^3 Hz and almost constant in the frequency range 10^3 to 10^5. Thus, the conduction process increases with increase in frequency. The observed high magnitude of Z' value at low frequency can be attributed to space charge carriers [196]. The characteristic frequency (frequency at sharp fall) shifts towards the higher frequency regime as the temperature is raised. In order to understand the relaxation process, we have measured $-Z''$ as a function of frequency at different temperatures. The relaxation peak is found to shift towards higher frequency with increase in temperature and it indicates that the conduction process is thermally activated [196].

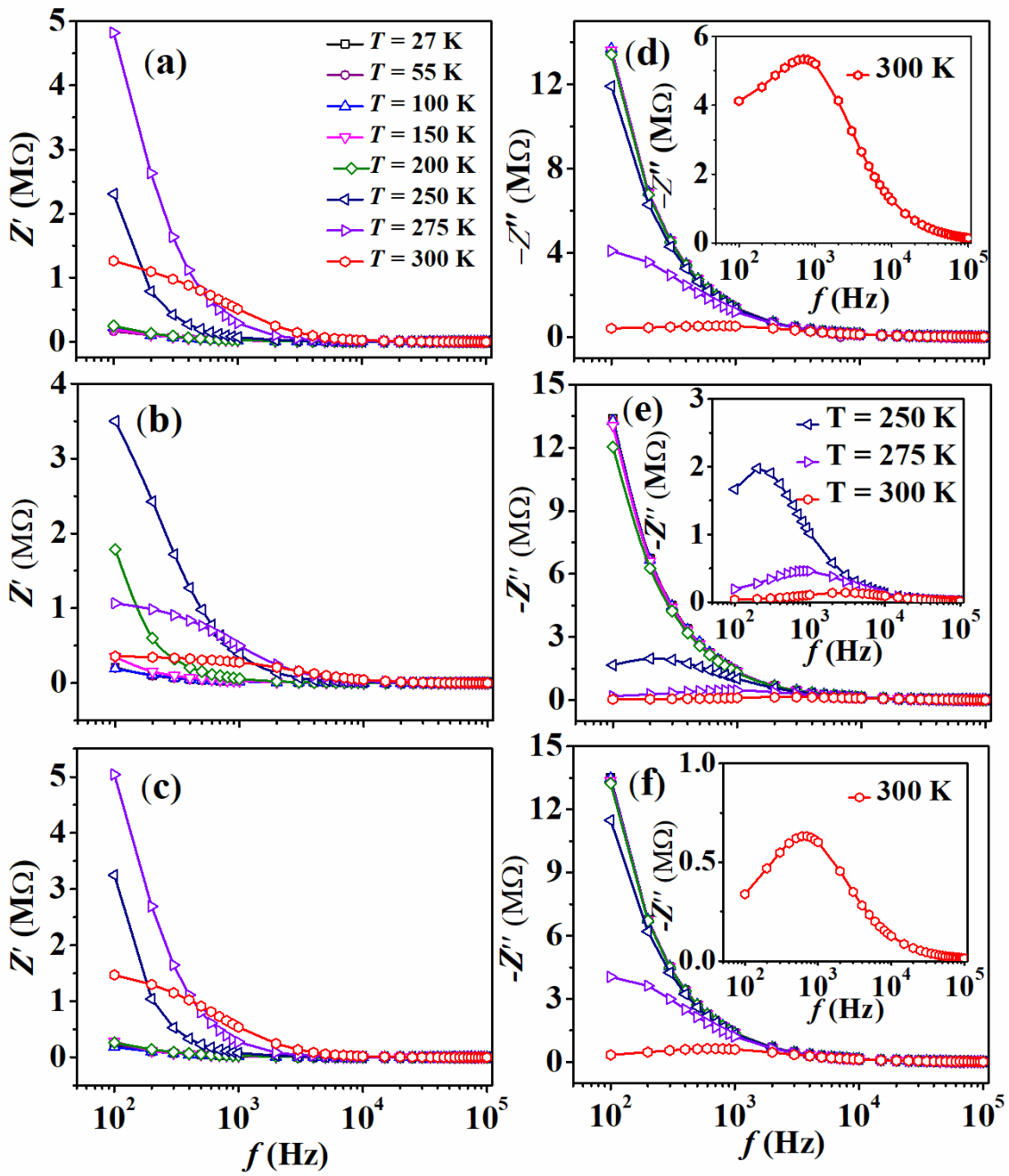

Fig. 4.30: (a, b & c) Z' and (d, e, & f) Z'' for x = 0, 0.10 & 0.30 samples. Inset shows the relaxation behavior of Z'' at higher temperatures.

Complex impedance plane plots ($-Z''$ vs Z': Nyquist plots) have been studied in order understand the contribution of grains (Gs) and grain boundaries (GBs) in conduction mechanism for the samples x = 0, 0.10 & 0.30 (Fig. 4.31). We have observed almost linear nature of $-Z''$ values for temperature up to T = 200 K and nearly semicircular arc for $T \geq 250$

K. The linear behavior and lack of complete semicircular characteristic of Z'' below room temperature is mainly due to their relaxation frequency values falling below the measured frequency range. An equivalent circuit model was proposed to investigate the electrical properties of the materials. The equivalent circuit includes two parallel combinations designated as ($R_{GB}C_{GB}Q_{GB}$)(R_GC_G) as shown in Fig. (d), where R_{GB}, C_{GB}, Q_{GB}, R_G and C_G represent the resistance of GBs, capacitance of GBs, constant phase element of GBs, resistance of *Gs* and capacitance of *Gs* respectively. The presence of constant phase element (CPE or *Q*) in the equivalent circuit represents the deviation of relaxation dynamics from ideal Debye type [73]. The impedance of CPE is defined as $Z_{CPE} = \frac{1}{A}(jw)^{-m}$, where A is a constant and m represents the distribution of relaxation time ($0 \leq m \leq 1$). Above 275 K, the magnitude of arc is found to decrease noticeably with increasing temperature and it indicates a strong negative temperature coefficient of resistance. The value of R_{GB} is found to be larger as compared to the R_G at all temperatures, which may be due to the presence larger amount of structural defect at grain boundaries and makes it difficult for the charge carriers to response to the external electric field. A single hump in the Nyquist plots further confirms that the grain boundaries are the major contributors of impedance in these systems. The charge carriers accumulated at grain boundaries results in interfacial polarization in the system.

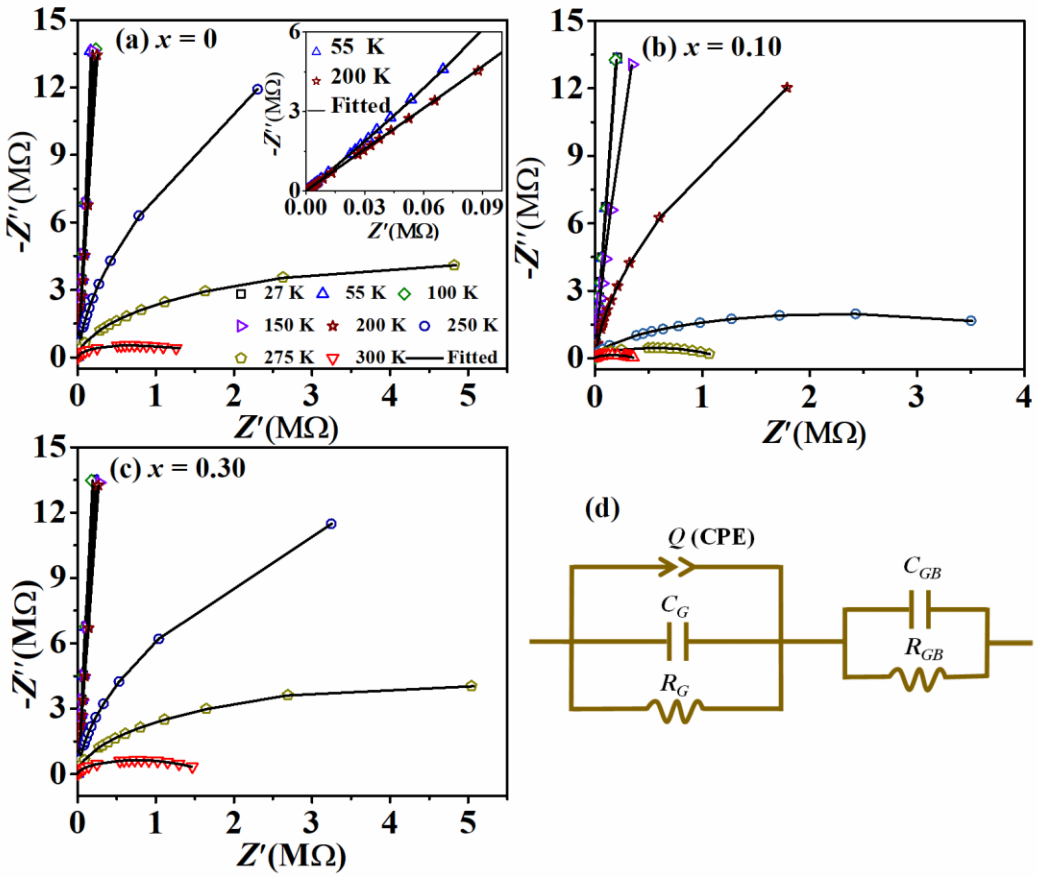

Fig. 4.31: Nyquist plot of (a) x = 0, (b) x = 0.10 & (c) x = 0.30 samples along with equivalent circuit (d).

Fig. 4.32 shows the variations of ac electrical conductivity of x = 0, 0.10, 0.30 samples as a function of frequency in the temperature range 27 K - 300 K. At low frequency the conductivity is almost independent of frequency due to long range translation motion of charge carriers to neighborhood vacant sites. The characteristic behavior of σ_{ac} with frequency at different temperature can be explained in terms of Jonscher power law (JPL) [76].

$$\sigma_{ac}(\omega) = \sigma_{dc} + A\omega^{\kappa} \qquad (4.11)$$

Where, σ_{dc} is dc conductivity (frequency independent) and $A\omega^{\kappa}$ is the frequency dependent ac conductivity term which characterizes dispersion phenomenon. The exponent κ defines the nature of motion of charge carriers. The experimental data of σ_{ac} were fitted to JPL by considering σ_{dc}, A and κ as free parameters.

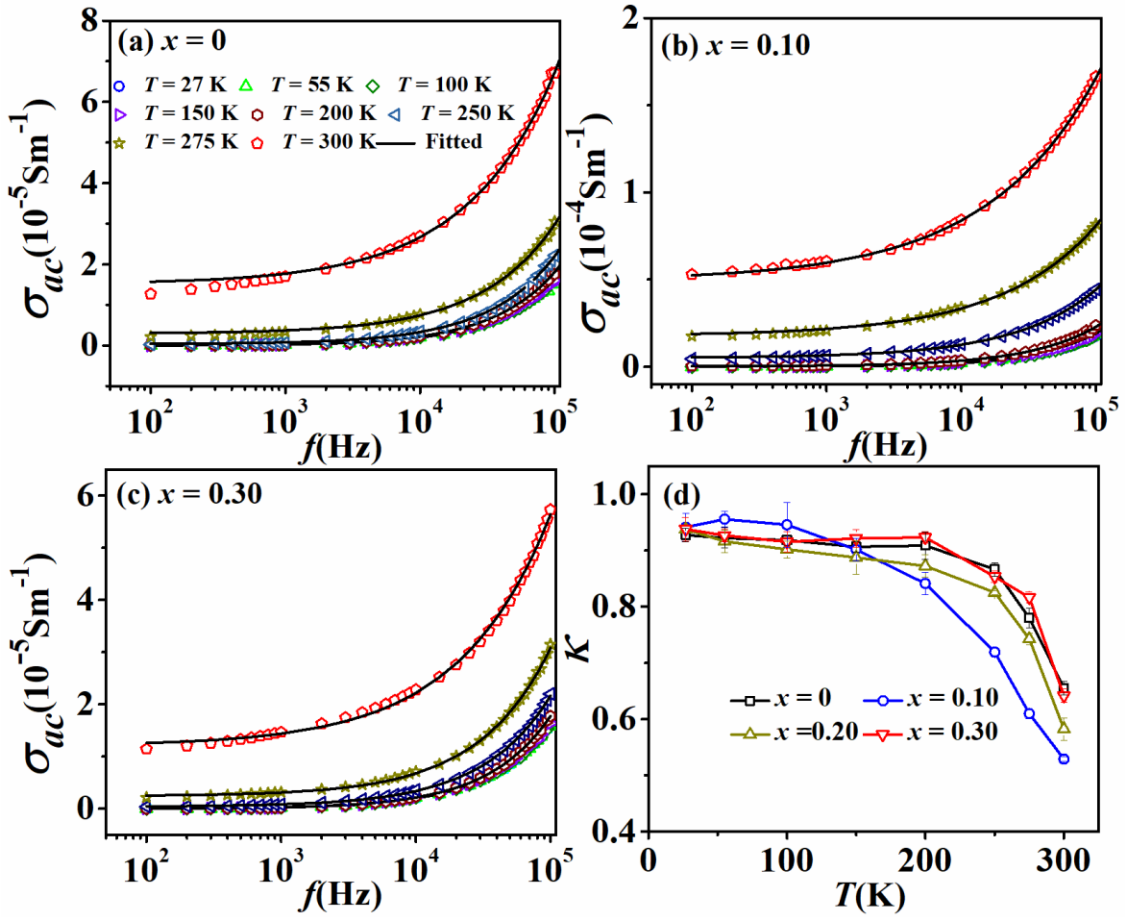

Fig.4.32: Frequency variation of ac conductivity in logarithmic scale along with fitted data (solid lines) using JPL model for (a) $x = 0$, (b) $x = 0.10$ and (c) $x = 0.30$ at different temperatures ranging from 27 K to 300 K. (d) temperature variation of frequency exponent κ.

The parameter κ defines the nature of charge carriers movement as either translational or localized [72]. If the value of $\kappa < 1$, the motion is translational and if $\kappa > 1$, the motion is localized. The variation of the exponent κ with temperature indicates the origin of conduction mechanism in the system. It is well known that if κ increases with rise in temperature then the conduction mechanism is attributed to the small polaron tunneling (SPT) [197]. On the other hand, if κ decreases continuously with temperature the conduction mechanism is correspond to correlated barrier hopping (CBH) [198]. In the present case, it is observed that κ decreases continuously with temperature for all the samples. This suggest that CBH is the predominant conduction mechanism in our system.

4.3 Conclusion

To summarize, we have investigated the structural, magnetic, magnetocaloric properties and critical behavior of $Ni_{1-x}Mn_xCr_2O_4$ (x = 0, 0.10 & 0.50) chromite. Room temperature XRD pattern confirms that synthesized compounds are in single phase form with a structural transformation from tetragonal ($I4_1/amd$) to cubic ($Fd\bar{3}m$) structure with Mn substitution. The lattice constant is found to increase with increase in Mn concentration. All the samples show ferrimagnetic behavior and the transition temperature, T_C is found to decrease with increase in Mn concentration due to the weakening of superexchange interaction. With increase in Mn substitution enhancement in magnetic entropy change is observed in the present series. The maximum magnetic entropy changes of $-\Delta S_M = 2.9$ J·kg^{-1}·K^{-1} is found for x = 0.50 sample for an applied field of H = 9 T at its Currie temperature (38 K). The RCP exhibits a maximum value of 58.2 J·kg^{-1}for x = 0.50 sample, which is significantly higher than RCP value of $NiCr_2O_4$. Scaling analysis shows a second-order transition and the critical exponents deviate from the mean-field model in these compounds.

Similar to Mn substituted series, $Ni_{1-x}Cd_xCr_2O_4$ (x = 0-0.30) samples also exhibits a structural transformation from tetragonal ($I4_1/amd$) for x = 0 to cubic ($Fd\bar{3}m$) phase with Cd substitution. From temperature dependent magnetization measurements, significant modification in magnetic structure has been observed with Cd substitution. The magnetic behaviour in x = 0.20 & 0.30 samples are mostly governed by short range magnetic interactions and shows peculiar magnetic transitions. Observed memory effect and relaxation of thermoremanent magnetization support the metastability of glassy magnetic phase in x = 0.30 sample. Reversible magnetocaloric behavior has been reported for x = 0.20 sample with a maximum negative entropy change of $-\Delta S_M = -0.4$ J·kg^{-1}·K^{-1}. Dielectric, impedance and ac conductivity data have been investigated in the temperature range of T = 27 K – 300 K and frequency range of 100 Hz -10^5 Hz. Study of impedance spectroscopy and ac conductivity indicates the non-Debye type of dielectric relaxation and correlated barrier hopping (CBH) of charge carriers is controlling the conduction mechanism in these samples.

Chapter 5

Co Substituted $NiFe_2O_4$ series

In Chapters 3 and 4, we have discussed the interesting structural, magnetic and electrical properties of Mg, Mn and Cd substituted $NiCr_2O_4$. In contrast to the normal spinel structure of $NiCr_2O_4$, $NiFe_2O_4$ falls under inverse spinel structure [23] and exhibits ferrimagnetism (FIM), as a result of the anti-parallel alignment of magnetic moments of Fe^{3+} ions at tetrahedral sites and those of Ni^{2+} and Fe^{3+} ions at octahedral sites. Similar to nickel ferrite, cobalt ferrite is also a well-known spinel ferrite due to its high coercivity, high magnetostriction coefficient and moderate saturation magnetization. The significant magnetostriction property of $CoFe_2O_4$ is due to the highly positive magnetocrystalline anisotropy and spin-orbital coupling of Co^{2+} ions distributed at the octahedral sites [199]. As discussed in Chapter 1, the Co substituted $NiFe_2O_4$ has attracted much attention due to its interesting magnetic properties such as high coercivity, moderate saturation magnetization, superparamagnetism (SPM), Verwey transition and good dielectric properties etc. [121-126]. Moreover, cobalt substituted nickel ferrites are highly resistive and magnetostrictive. Even though Co substitution is known to play a major role in the optimization of magnetic properties in $NiFe_2O_4$, the detailed analysis of site occupation of different ions and their influence on the structural and magnetic properties are yet to be explained.

In this chapter, the preparation of $Ni_{1-x}Co_xFe_2O_4$ (x = 0-0.50) compounds by sol-gel technique and investigation of structural and magnetic properties have been discussed. In inverse spinel like $NiFe_2O_4$, theoretically the overall magnetic moment is mainly influenced by the Ni^{2+} ions due to the mutual cancellation of magnetic moment of Fe^{3+} ions in both octahedral and tetrahedral sites due to the antiferromagnetic interaction across A-B sublattices. Co^{2+} ion has a noticeably higher magnetic moment as compared to Ni^{2+} ion and can be used to enhance the magnetic moment of the system. Substitution of cobalt in $NiFe_2O_4$ is expected to enhance the magnetocrystalline anisotropy and hence the coercivity (H_C) of the samples. We have used the quantum-mechanical method [137] to estimate the cation distributions at

tetrahedral and octahedral sublattices and their effect on lattice parameters and magnetic properties.

Single phase polycrystalline samples of $Ni_{1-x}Co_xFe_2O_4$ (x = 0-0.50) were synthesized by sol-gel method. Stoichiometric ratio of $Ni(NO_3{\cdot}6H_2O$, $Co(NO_3)_2{\cdot}6H_2O$ and $Fe(NO_3)_3{\cdot}9H_2O$ of 99% purity were used as starting composition for the synthesis. The as-synthesized samples were grinded and pre-sintered at 600 ^{0}C followed by a sintering at 800 ^{0}C. Final sintering was performed at 1000 ^{0}C for 12h. For the structural study, XRD and Raman spectroscopy were performed at room temperature. The particle sizes and morphology were investigated by FESEM and EDX facility as discussed in chapter 2. XPS spectrum was carried out at room temperature to investigate the possible cationic states of the ions in these samples. The magnetization data were recorded by using VSM and PPMS setup.

5.1 Structural Study

The room temperature X-ray diffraction patterns and typical Rietveld refinements are shown in Fig. 5.1 & Fig. 5.2 and they indicate that all the samples are crystallized in cubic crystal structure with space group $Fd\bar{3}m$. With Co substitution, the lattice constant increases from a = 8.3379 (6) Å for x = 0 to a = 8.3584 (6) Å for x = 0.50 compound. The lattice constant for $NiFe_2O_4$ is found to be comparable to earlier reports [200, 201]. The increase in lattice constant with Co substitution is also clearly visible from the shifting of (311) peak towards smaller 2θ angles (Fig. 5.1b). The structural parameters obtained from Rietveld refinement are presented in Table 5.1. The increase in $d_{A\text{-}O}$ and decrease in $d_{B\text{-}O}$ bond length with Co substitution may be due to the partial migration of Co^{2+}/Ni^{2+} cations from octahedral sites to tetrahedral sites in the inverse spinel ferrite.

Table 5.1: Parameters obtained from Rietveld refinement for $Ni_{1-x}Co_xFe_2O_4$ (x = 0-0.50) samples.

x/ Parameters	0	0.10	0.20	0.30	0.40	0.50
a (Å)	8.3378(6)	8.3404(2)	8.3463(2)	8.3504(8)	8.3543(6)	8.3584(6)
d_{A-O}(Å)	1.766	1.907	1.931	1.932	1.935	1.945
d_{B-O}(Å)	2.107	2.028	2.017	2.018	2.018	2.016
d_{A-B}(Å)	3.456	3.458	3.460	3.462	3.464	3.467
χ^2 (%)	2.5	2.4	2.6	3.1	2.3	2.7
R_F (%)	2.7	3.6	5.3	4.6	2.6	5.4
R_{Brag} (%)	3.6	3.9	6.5	6.3	2.7	5.3
R_P (%)	10.2	9.8	11.2	10.9	9.7	11.2
Occupany Ni/Co/Fe(A)/ Fe(B)	0.998/0.000/1.021/0.998	0.859/0.108/0.953/0.944	0.853/0.120/0.882/0.863	0.802/0.325/0.935/0.926	0.580/0.399/0.928/0.916	0.436/0.497/0.966/0.961

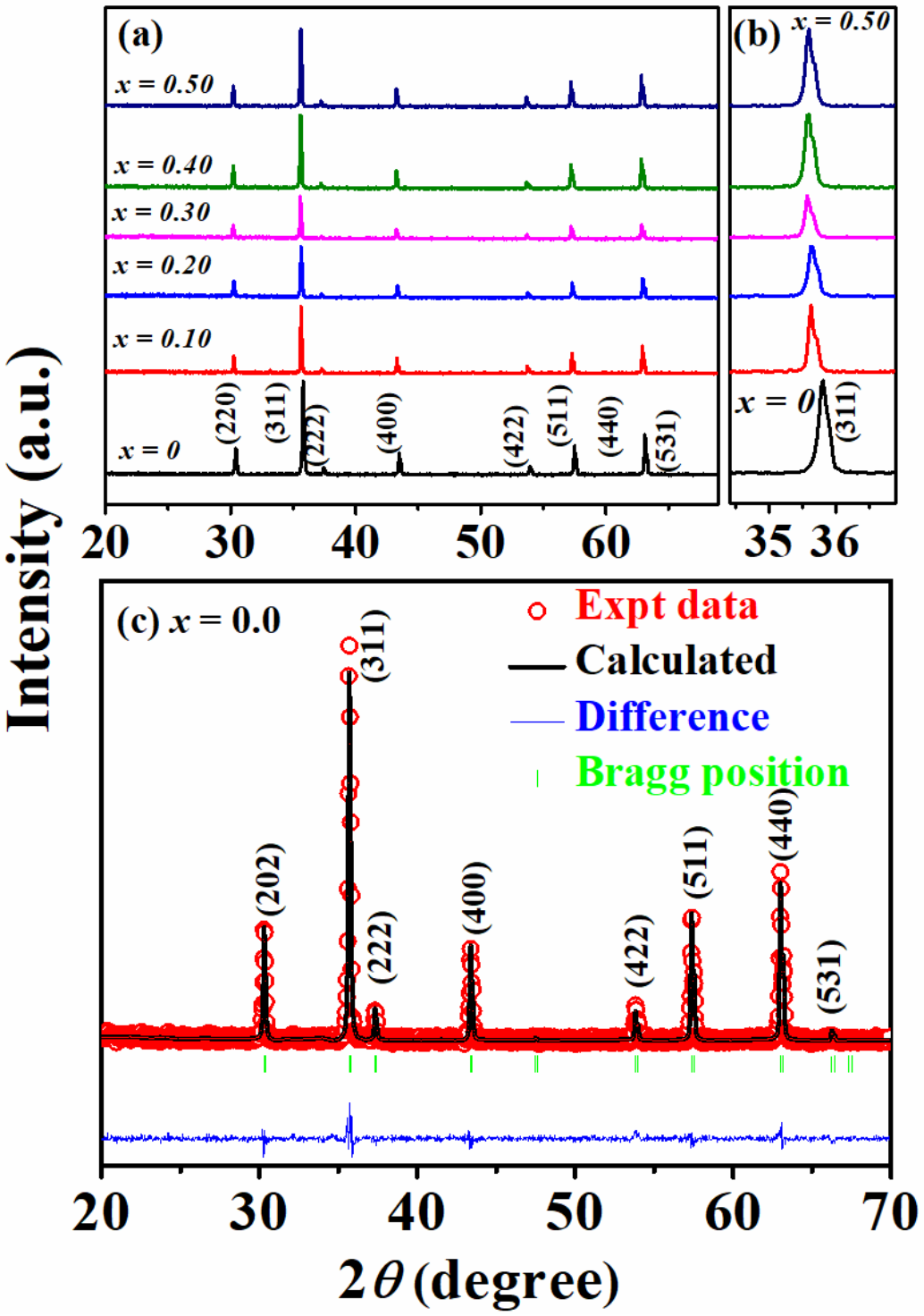

Fig. 5.1: (a) Room temperature X - ray diffraction patterns of $Ni_{1-x}Co_xFe_2O_4$ (x = 0 – 0.50) along with (b) magnified view of (311) peaks and (c) typical Rietveld refinement for x = 0.0 sample. The red open circles are the experimental data and the black solid lines are the fitted data. The bottom line shows the difference between experimental and refined data.

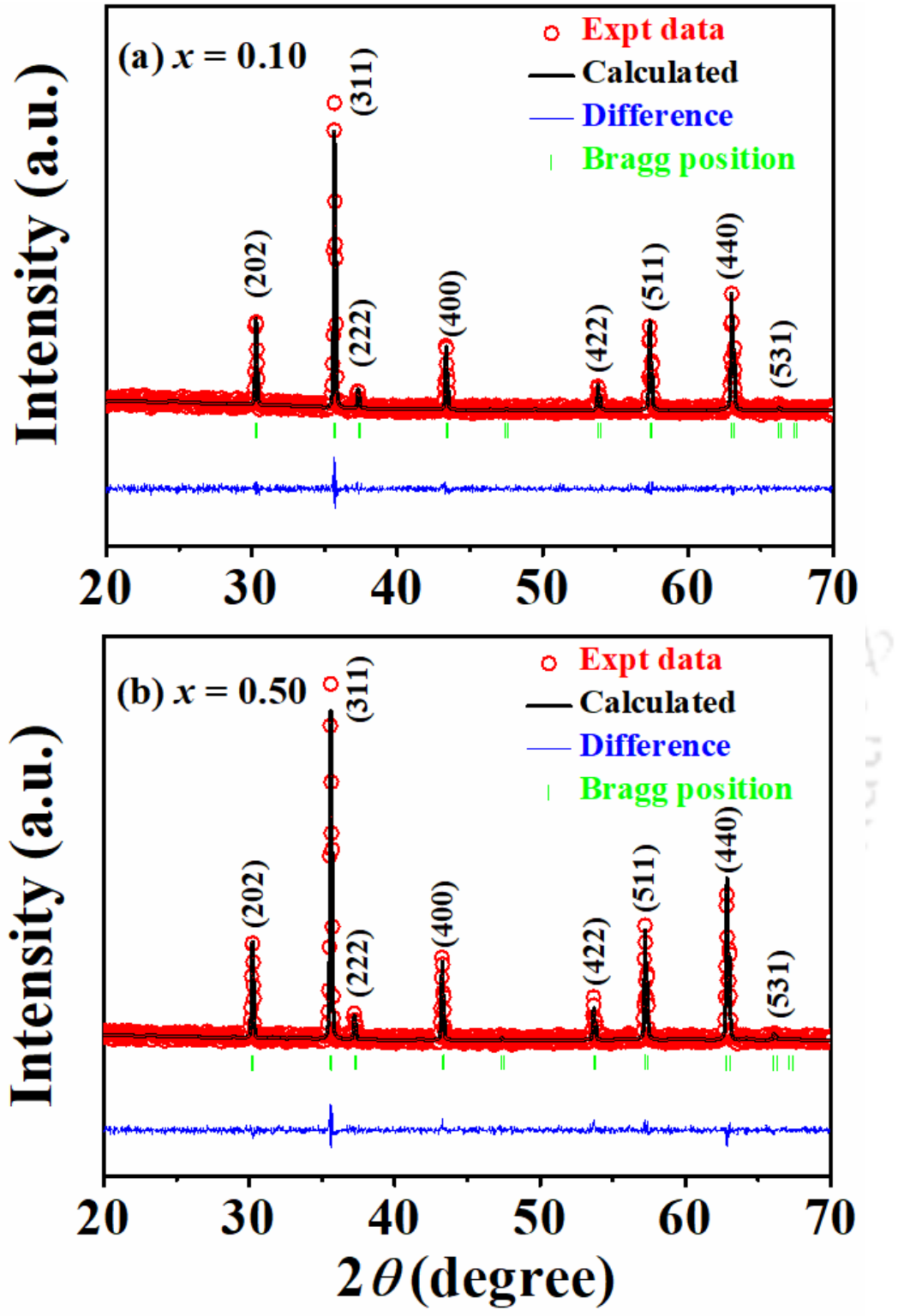

Fig. 5.2: Rietveld refinement of the XRD patterns of (a) $x = 0.10$ and (b) $x = 0.50$ samples. The red open circles are the experimental data and the black solid lines are the fitted data. The bottom line shows the difference between experimental and refined data.

The FESEM micrographs of $Ni_{1-x}Co_xFe_2O_4$ (x = 0 - 0.50) samples are shown in Fig. 5.3. The particle size distribution histograms determined from the FESEM images show significant variation in particle size with Co substitution. For the parent x = 0 compound, the average particle size is found to be around 180 nm and agglomerated. The particle size of x = 0.50 sample is found to be quite large with an average size of 665 nm. The analysis of EDX spectra (Fig. 5.4(a)) reveals that the cationic ratio of Ni: Co: Fe for x = 0.50 sample is found to be 0.52: 0.55: 2.0 and is comparable with the normal starting compositions. The elemental mapping (Fig. 5.4(b)) confirms the uniform distribution of the elements in the sample.

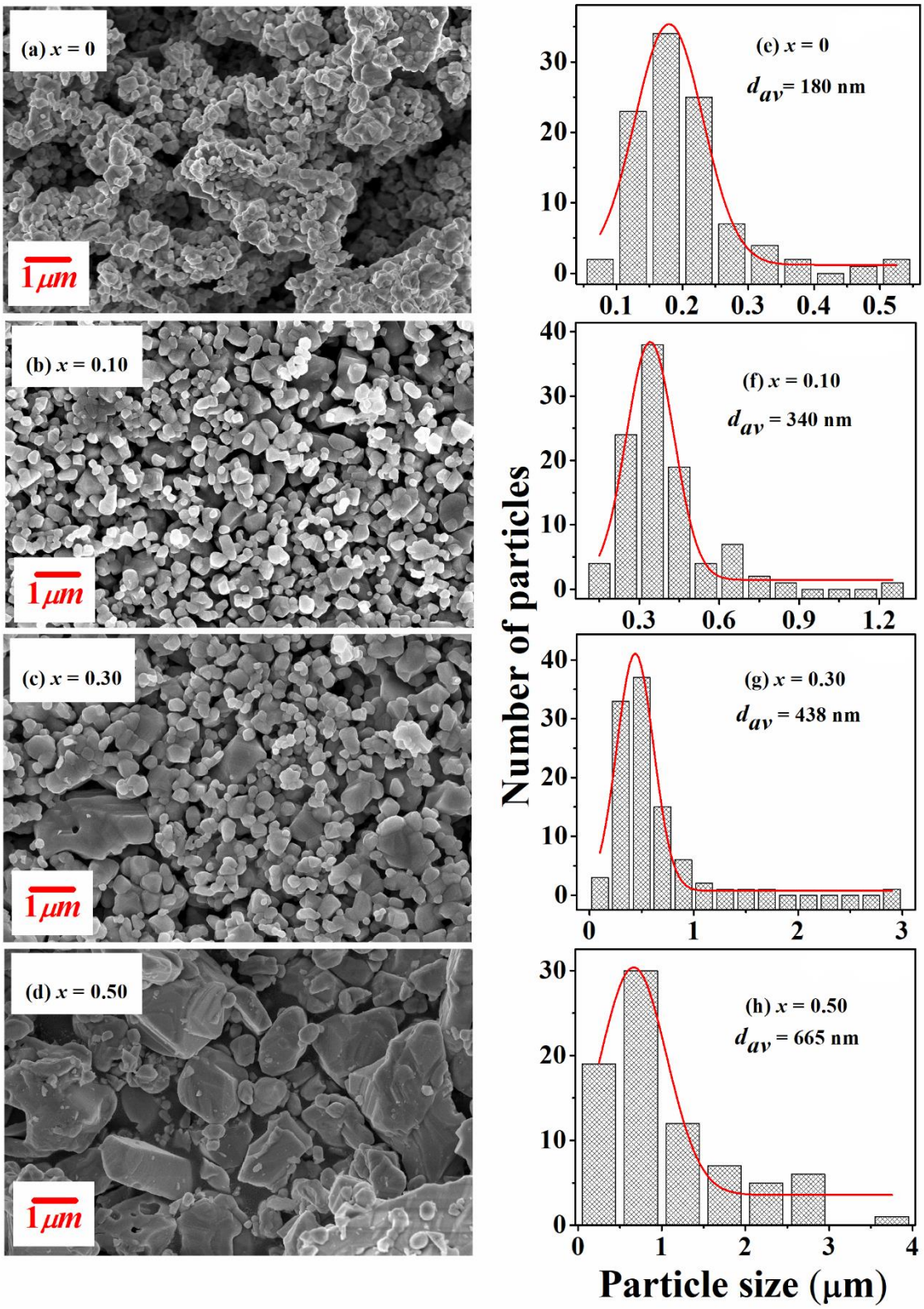

Fig 5.3: FESEM images of $Ni_{1-x}Co_xFe_2O_4$ (x = 0, 0.10, 0.30 & 0.50) samples (a - d) and their particle size distributions (e - h).

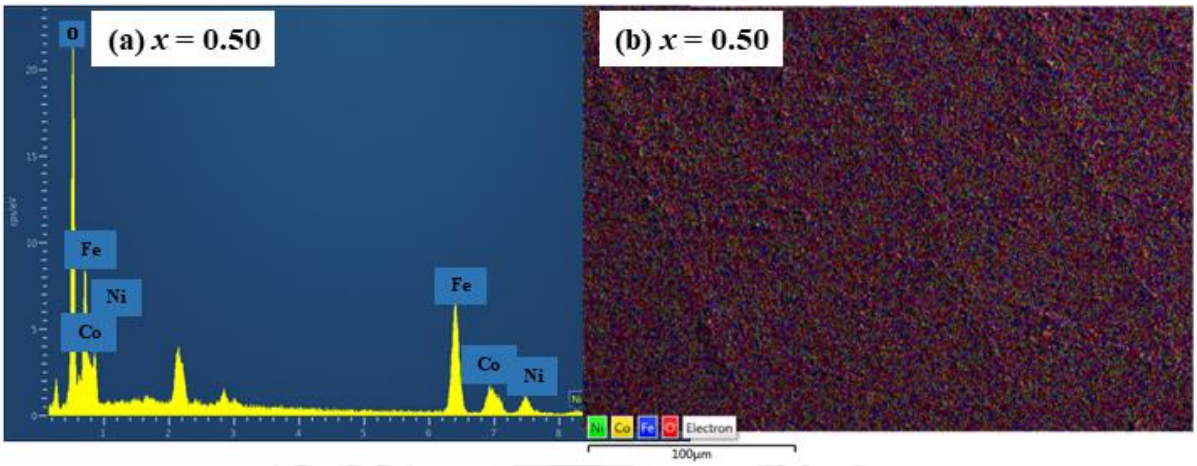

Fig. 5.4: (a) EDX spectra and (b) elemental mapping for x = 0.50 sample.

XPS experiments were carried out for x = 0.10 and 0.50 samples in order to investigate the oxidation state of the ions. The survey spectrum (Fig. 5.5) exhibits the characteristic peaks for Ni, Co, Fe and O elements without other impurity peaks. The fitted core level spectrum of Ni 2*p*, Co 2*p*, and Fe 2*p* are shown in Fig. 5.6 (a & b). The fitted core level spectrum of Fe 2*p*, consists of two spin-orbit doublets. Two satellite peaks at around 718.6 eV and 733.3 eV are generally considered as representative shake-up-type of iron [202]. The two prominent peaks at 710.4 eV and 724.1 eV can be attributed to the spin-orbit coupling peaks of Fe $2p_{3/2}$ and Fe $2p_{1/2}$ respectively [203]. Each of these peaks can be further divided into two peaks, indicating the existence of Fe^{2+} and Fe^{3+} ionic states. Similarly, Fig. 5.6 (c-f) display the spin-orbit peaks and their corresponding cationic states of Co and Ni ions respectively. The spin-orbit peaks of Co $2p_{3/2}$ and Co $2p_{1/2}$ are observed at 780.1 eV and 795.6 eV respectively and can be further decomposed into Co^{2+} and Co^{3+} ionic states [204]. Similarly, Ni XPS spectrum reveals two distinct peaks at 854.6 eV and 872.2 eV for Ni $2p_{3/2}$ and Ni $2p_{1/2}$ respectively [205]. From the above analysis, it is confirmed that all three cations possess both 2^+ and 3^+ ionic states in these samples.

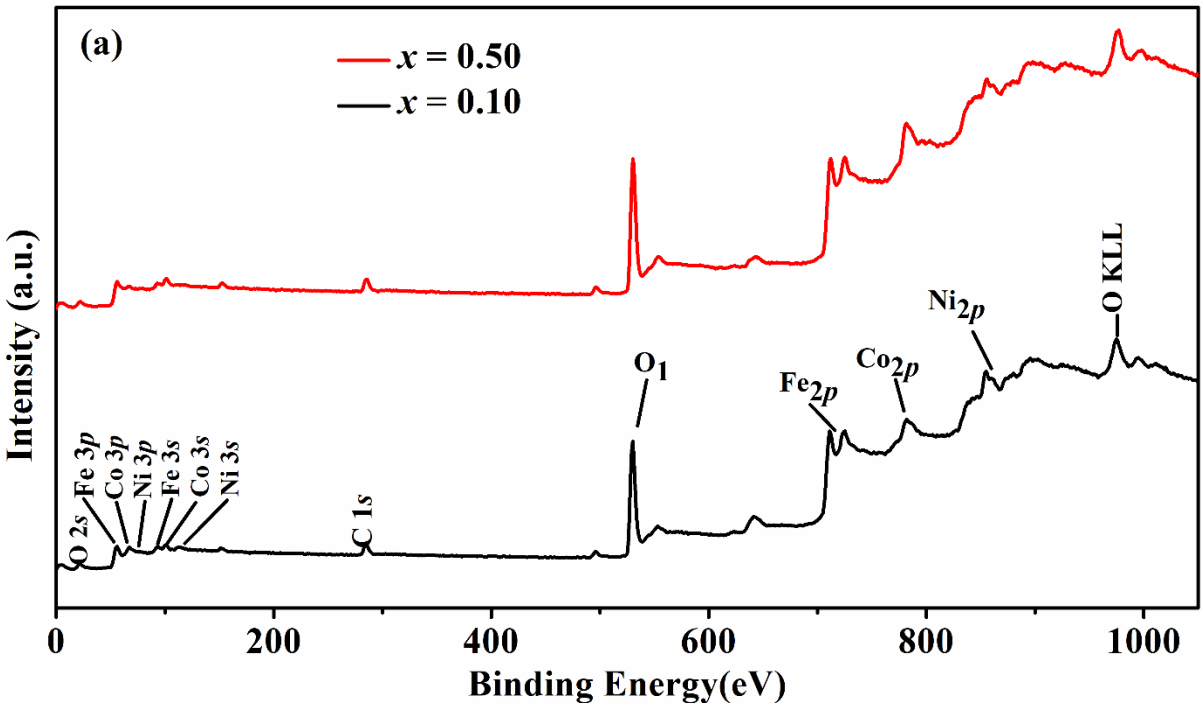

Fig. 5.5: XPS full spectra for x = 0.10 (black) & 0.50 (red).

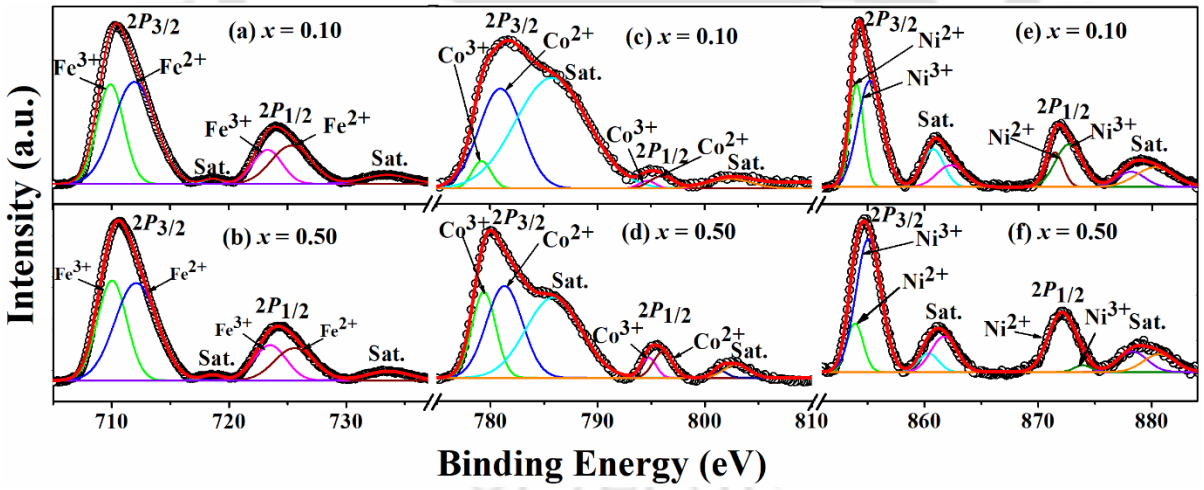

Fig. 5.6: XPS spectrum of $Ni_{1-x}Co_xFe_2O_4$ (x = 0.10 & 0.50) compounds with peaks corresponding to (a, b) Fe 2*p* (c, d) Co 2*p* and (e, f) Ni 2*p*.

5.2 Magnetic Properties and Estimation of Cation Distribution

The temperature variation of magnetization $M(T)$ (normalized by magnetization at 300 K) was measured from 5 K to 300 K in zero field cooled (ZFC) and field cooled (FC) modes for an applied field of 500 Oe as shown in Fig. 5.7. We have observed an increase in magnetization (M_{ZFC} & M_{FC}) with lowering temperature for $x = 0$ sample. However, all the Co substituted samples are showing a gradual decrease in magnetization with lowering the temperature. This may be due to the stiffening of magnetic moment due to its highly anisotropic nature at low temperature. The thermomagnetic irreversibility between ZFC and FC data is estimated by using the relation $\Delta M/M_{ZFC} = (M_{FC} - M_{ZFC})/M_{ZFC}$ and they are shown in Fig. 5.8 for various samples. They are found to increase with Co concentration. The thermomagnetic irreversibility occurs due to the difference between the protocols in which the polycrystalline sample is cooled either in a magnetic field (FC) or in the absence of a field (ZFC). In an external magnetic field, the response of the magnetic spins depends on the competition between internal magnetocrystalline energy and the strength of the external applied magnetic field. At low measuring field compared to the anisotropy field, all the spins will not align along the field direction. Therefore, during the ZFC measurement process, the magnitude of magnetic moment depends on the anisotropy of the compound, which results in larger thermomagnetic irreversibility for highly anisotropic compounds. So, in the present series, magnetic anisotropy increases with increase in Co concentration. We have observed a clear hump in ZFC/FC magnetization data for $x = 0.50$ sample and is in consistent with a sharp rise in thermomagnetic irreversibility below 165 K (Fig. 5.8), which may be due to a possible metal-insulator transition which is also known as Verwey transition (T_V) as a result of sharp change in magnetic anisotropy [124].

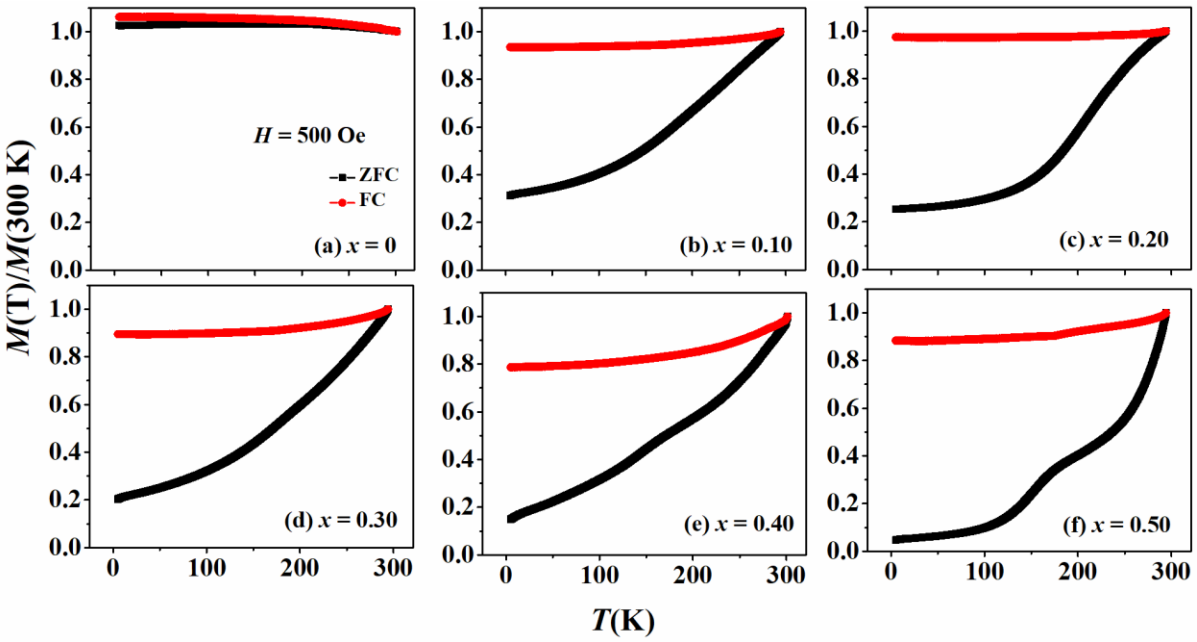

Fig. 5.7: Temperature dependence of normalized magnetization (M) under zero field cooled (ZFC) and field cooled (FC) condition for $Ni_{1-x}Co_xFe_2O_4$ (x = 0 – 0.50) for H = 500 Oe.

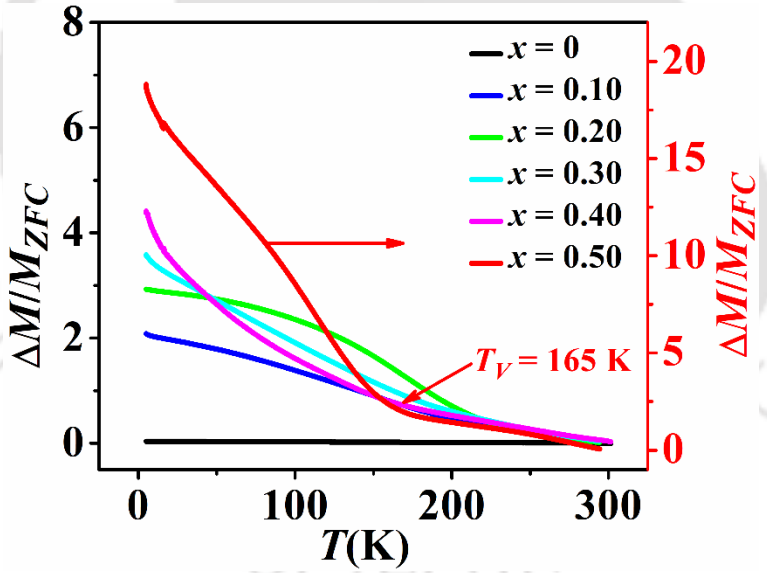

Fig. 5.8: Variation of thermomagnetic irreversibility ($\Delta M/M_{ZFC}$) with temperature (T) for different Co substitution level (x).

In order to further investigate the magnetic properties, we have performed the ZFC magnetization measurement above room temperature and they are shown in Fig. 5.9 (a). The value of FIM to PM transition temperature (T_C) is estimated from dM/dT vs T plot (Fig. 5.9 (b)) and are found to decrease from 835 K for x = 0 to 797 K for x = 0.50 compound as given

in Table 5.2. The drop in T_C is attributed to the weakening of overall A - B super-exchange interaction upon Co substitution. The value of A - B super-exchange interaction J can be calculated by using the following formula [206],

$$J = \frac{3k_B T_C}{[2z \times s(s+1)]} \tag{5.1}$$

where, z = 8, s =1/2 and $k_B = 1.38 \times 10^{-16}$erg K^{-1}. The estimated J values are given in Table 5.2 and is found to decrease with Co concentration. With increase in Co concentration, it is possible that a small quantity of Co^{2+} ions start migrating from octahedral to tetrahedral sites and thus weakening the Fe(A) – O – Fe(B) superexchange interaction.

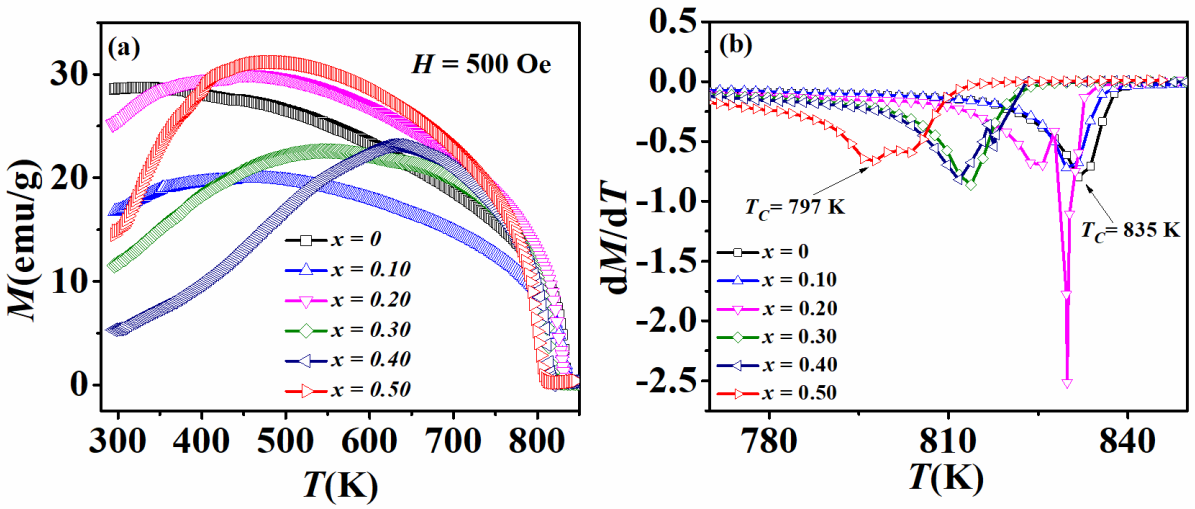

Fig. 5.9: (a) ZFC magnetization measurement as a function of temperature and (b) dM/dT vs T plot for $Ni_{1-x}Co_xFe_2O_4$ (x = 0 – 0.50).

Fig. 5.10 shows the M - H loops recorded for all the samples at T = 5 K and 300 K. The values of saturation magnetization (M_S) and coercivity (H_C) for all the samples are presented in Table 5.2. The increase in M_S with Co substitution can be attributed to the higher magnetic moment associated with Co ions as compared to Ni ions. The remanent ratio ($R = M_r/M_s$) at T = 5 K is found to increase from 0.2 for x = 0 to 0.9 for x = 0.50 sample. A lower remanent ratio generally implies the isotropic nature of a material. In order to evaluate the anisotropy constant of the materials, we have used the law of approach to saturation as discussed in Chapter 3 (Eq. 3.4) and the corresponding fitted parameters are presented in Table 5.2. The value K_1 at T = 5 K is found to increase with Co substitution. In spinel ferrite, the temperature

dependence of zero-field cooled magnetization (M_{ZFC}) is inversely related to the magnitude of coercivity (H_C) at that particular temperature and can be expressed by the following equation [207],

$$M_{ZFC} \approx M_{FC} \frac{H_{app}}{H_{app} + H_C} \tag{5.2}$$

For Co substituted samples we have observed a significant variation in M_{ZFC}, which increases as temperature rises from 5 K to 300 K. Aa a result of which a decrease in H_C at 300 K in comparison to 5 K is expected. Moreover, Stoner Wohlfarth theory also suggest that coercivity is proportional to anisotropy constant K_1 of the material [208]. From Table 5.2, we have observed a relatively higher magneto crystalline anisotropy value of x = 0.40 & 0.50 compounds as a result of which the increase in H_C is prominent for these materials. The origin of this large magnetic anisotropy can be attributed to the presence of Co^{2+} ions at octahedral site as suggested by one-ion anisotropy model [209]. A previous study on Co substituted $NiFe_2O_4$ also suggests that $Ni_{0.50}Co_{0.50}Fe_2O_4$ undergoes a Verwey transition at low temperature and below which a sudden increase in coercivity is observed [124]. Therefore, a high value of coercivity at low temperature is reasonable.

Table 5.2: Magnetic parameters obtained from *M-H* loops recorded at T = 5 and 300 K for $Ni_{1-x}Co_xFe_2O_4$ (x = 0 – 0.50).

x	T_C (K)	J (10^{-21}J)	M_S (5 K) μ_B/f. u.	H_C (5K) Oe	K_1 (5K) 10^6erg/cc	M_S (300K) μ_B/f. u.	H_C (300K)Oe
0	831	2.88	2.16	125	3.7	1.97	110
0.10	829	2.86	2.28	630	9.4	2.16	150
0.20	827	2.85	2.43	980	10.5	2.30	210
0.30	813	2.80	2.53	1100	10.7	2.39	270
0.40	811	2.79	2.65	5750	16.4	2.52	450
0.50	797	2.74	2.76	6050	16.5	2.60	325

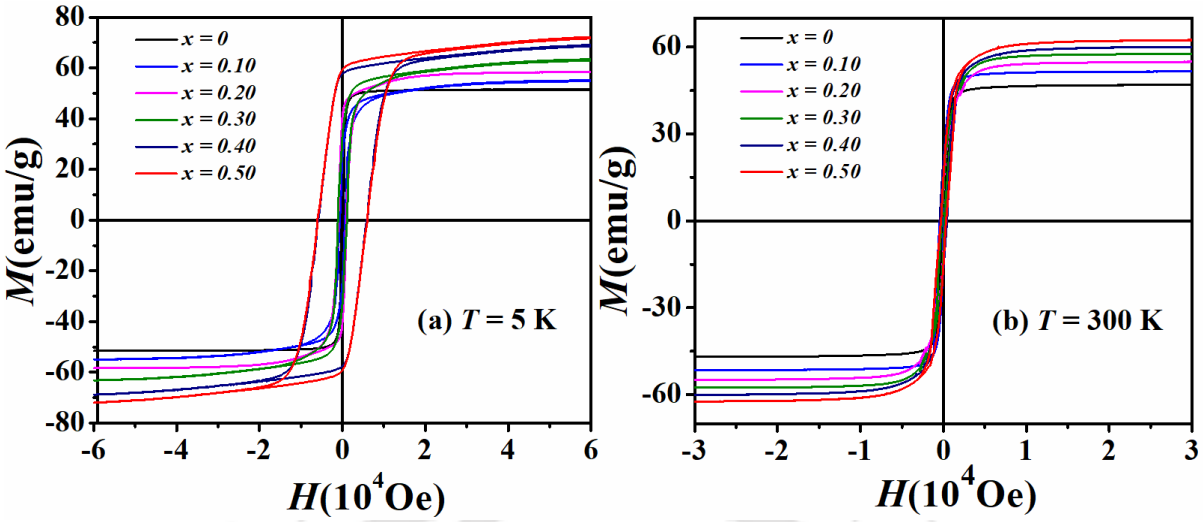

Fig. 5.10: *M*- *H* loops recorded at (a) *T* = 5 K and (b) *T* = 300 K for $Ni_{1-x}Co_xFe_2O_4$ (*x* = 0 – 0.50).

Estimation of cation distribution in a magnetic system is an important tool to understand the magnetic and structural properties of the system. According to the assumption made by Tang et al. [137], there are four important factors that decide the cation distribution in a spinel ferrite compound.

The first factor is a potential barrier that exists between a cation-anion pair and its height is determined by the ionization energy of the last ionized electron of the cation. However, the width of the potential barrier is related to the distance between the neighboring cations and anions. Therefore, the concentration ratio (*R*) of different cations (say C to D) at a particular sublattice is related to the probability of their last ionized electrons penetrating the barrier, and takes the form [210],

$$R = \frac{P(\mathrm{C})}{P(\mathrm{D})} = \frac{V_D}{V_C} exp\left[10.24\left(r_D V_D^{1/2} - c r_C V_C^{1/2}\right)\right] \quad (5.3)$$

where, $P(C)$ and $P(D)$ represents the probability of the last ionized electron of the C and D cations, jumping to the anions through the potential barrier with a height of V_C and V_D and width r_D and r_C respectively. The parameter *c* is a barrier shape correction constant related to the different extents to which the shape of the potential barriers deviates from the square potential barrier. Therefore, when $V_C = V_D$ and $r_C = r_D$ the parameter *c* will be 1. Here,

nanometers (nm) and electron-volts (eV) are used as the units of length and energy. Secondly, the Pauli repulsion energy of the electron cloud between neighboring cations and anions is an important factor to consider. So, depending on the effective ionic radii, distribution of cations take place among tetrahedral and octahedral sublattices. Generally, smaller cations occupy the tetrahedral sites due to their smaller available space as compared to octahedral sites. Thirdly, in order to balance the charge density, some of the M^{2+} cations (larger ionic radii) enter tetrahedral sites from octahedral sites by jumping an equivalent potential barrier V_{BA}. The V_{BA} arises from the Pauli repulsion energy of the electron cloud as well as from the magnetically ordered energy. Finally, in the absence of magnetic ion in one of the sublattices or the substitution of non-magnetic ion would decrease the sublattice moment as well as V_{BA}. So, the smaller V_{BA} would facilitate easy jumping of ions into tetrahedral sites. However, in our case, we have substituted magnetic ion Co and hence more Co^{2+} ions are expected in the octahedral sites with increasing doping level. We have also considered the existence of trivalent (M^{3+}) ionic state for Co and Ni ions in our system as observed from XPS study. As a result of which equal amount of Fe^{3+} to Fe^{2+} conversion was considered for charge neutrality.

Considering all the above factors, the cation distribution in the samples $Ni_{1-x}Co_xFe_2O_4$ (x = 0 - 0.50) can be represented by the following chemical formula,

$$\left(\mathrm{Fe}^{3+}_{1-y_1-y_2}\mathrm{Ni}^{2+}_{y_1}\mathrm{Co}^{2+}_{y_2}\right)\left[\mathrm{Fe}^{3+}_{1+y_1+y_2-z_1-z_2}\mathrm{Fe}^{2+}_{z_1+z_2}\mathrm{Ni}^{2+}_{1-x-y_1-z_1}\mathrm{Ni}^{3+}_{z_1}\mathrm{Co}^{2+}_{x-y_2-z_2}\mathrm{Co}^{3+}_{z_2}\right]\mathrm{O}_4 \quad (5.4)$$

Using Eq. (5.3) the concentration ratios R_{A1} and R_{A2} of Ni^{2+} and Co^{2+} ions with respect to Fe^{3+} ions at the tetrahedral (A) site and ratios R_{B1} and R_{B2} of Ni^{3+} and Co^{3+} ions to Fe^{3+} ions at the octahedral site (B) can be expressed as follows,

$$R_{A1} = \frac{T(\mathrm{Ni}^{2+})}{T(\mathrm{Fe}^{3+})} = \frac{V(\mathrm{Fe}^{3+})}{V(\mathrm{Ni}^{2+})}\exp\left\{10.24\left[\frac{\sqrt{3}}{8}aV(\mathrm{Fe}^{3+})^{1/2} - \frac{\sqrt{3}}{8}aV(\mathrm{Ni}^{2+})^{1/2} - \frac{\sqrt{11}}{8}aV_{BA}(\mathrm{Ni}^{2+})^{1/2}\right]\right\} \quad (5.5)$$

$$R_{A2} = \frac{T(Co^{2+})}{T(Fe^{3+})}$$

$$= \frac{V(Fe^{3+})}{V(Co^{2+})} \exp\left\{10.24\left[\frac{\sqrt{3}}{8} aV(Fe^{3+})^{1/2} - \frac{\sqrt{3}}{8} aV(Co^{2+})^{1/2} - \frac{\sqrt{11}}{8} aV_{BA}(Co^{2+})^{1/2}\right]\right\} \quad (5.6)$$

$$R_{B1} = \frac{T(Ni^{3+})}{T(Fe^{3+})}$$

$$= \frac{V(Fe^{3+})}{V(Ni^{3+})} \exp\left\{10.24\left[\frac{1}{4} aV(Fe^{3+})^{1/2} - \frac{1}{4} aV(Ni^{3+})^{1/2}\right]\right\} \quad (5.7)$$

$$R_{B2} = \frac{T(Co^{3+})}{T(Fe^{3+})}$$

$$= \frac{V(Fe^{3+})}{V(Co^{3+})} \exp\left\{10.24\left[\frac{1}{4} aV(Fe^{3+})^{1/2} - \frac{1}{4} aV(Co^{3+})^{1/2}\right]\right\} \quad (5.8)$$

where the third ionization energies of Ni^{3+}, Co^{3+} and Fe^{3+} ions are $V(Ni^{3+})$ = 35.17 eV, $V(Co^{3+})$ = 33.50 eV and $V(Fe^{3+})$ = 30.65 respectively. For second ionization, these energy values are $V(Ni^{2+})$ = 18.17 eV, $V(Co^{2+})$ = 17.06 and $V(Fe^{2+})$ = 16.18 eV [211]. $V_{BA}(Ni^{2+})$ and $V_{BA}(Co^{2+})$ are the potential barriers which must be jumped by Ni^{2+} and Co^{2+} ions in order to enter (A) sites from [B] sites.

Using the above set of equations, the elemental concentrations y_1, y_2, z_1 and z_2 can be written as follows,

$$y_1 = \frac{R_{A1}(1-x)}{R_{A1}(1-x) + R_{A2}x + 1} \quad (5.9)$$

$$y_2 = \frac{xR_{A2}}{R_{A1}(1-x) + R_{A2}x + 1} \quad (5.10)$$

$$z_1 = \frac{R_{B1}(1 + y_1 + y_2)(1 - x - y_1)}{R_{B1}(1 - x - y_1) + R_{B2}(x - y_2) + 1} \tag{5.11}$$

$$z_2 = \frac{R_{B2}(1 + y_1 + y_2)(x - y_2)}{R_{B1}(1 - x - y_1) + R_{B2}(x - y_2) + 1} \tag{5.12}$$

At low temperature, the magnetic moment per formula unit for the inverse spinel $Ni_{1-x}Co_xFe_2O_4$ can be expressed as,

$$M = M_B - M_A \tag{5.13}$$

where, M_A and M_B are the magnetic moment of (A) and [B] sublattice respectively. Now considering the magnetic moments of Ni^{2+}, Co^{2+} and Fe^{2+} ions as 2 μ_B, 3 μ_B and 4 μ_B and for Ni^{3+}, Co^{3+} and Fe^{3+} ions as 3 μ_B, 4 μ_B and 5 μ_B, we can express M_A and M_B as follows [211],

$$M_A = 5(1 - y_1 - y_2) + 2y_1 + 3y_2 \tag{5.14}$$

$$M_B = 5(1 + y_1 + y_2 - z_1 - z_2) + 4(z_1 + z_2) + 2(1 - x - y_1 - z_1) + 3z_1 + 3(x - y_2 - z_2) + 4z_2 \tag{5.15}$$

So, the net magnetization value is

$$M = 2 + x + 6y_1 + 4y_2 \tag{5.16}$$

In order to estimate the values of y_1, y_2, z_1 and z_2 we have chosen the saturated magnetic moment of $Ni_{1-x}Co_xFe_2O_4$ at T = 5 K from Table 5.2. All the cation distributions for each Co doping level x are estimated by solving the above set of Eqs. (5.4 – 5.16) are given in Table 5.3. According to Ref. [137], the Ni^{2+} potential barrier height $V_{BA}(Ni^{2+}) = 2.71eV$ is required to reproduce the observed magnetic moment 2.3 μ_B/f.u. in $NiFe_2O_4$ at T = 10 K. However, depending on the synthesis process M_S can be different for different samples [212].

In our case the magnetic moment of $NiFe_2O_4$ at T = 5 K is found to be 2.16 μ_B/f.u., for which the required potential barrier height is fixed at 3.34 eV by using the Eqs. (5.5 – 5.12).

The cation distribution results are given in Table 5.3 and they clearly indicate that Ni^{2+} and Co^{2+} have a strong preference for octahedral sites, whereas Fe^{3+} ions have nearly uniform distributions over both A and B sublattices. As Co concentration increases, the Co^{2+} concentration at octahedral sites also increases and it results in large saturation magnetization and magnetic anisotropy. From Table 5.3, we have observed that in A sublattice the total number of divalent cations (sum of Ni^{2+} & Co^{2+} content) per formula unit increases from 0.027 for x = 0 to 0.057 for x = 0.50 and the trivalent cations (Fe^{3+}) per formula decreases from 0.973 for x = 0 to 0.943 for x = 0.50. Since the effective ionic radii of divalent cations Ni^{2+} (0.55 Å) and Co^{2+} (0.58 Å) ions with coordination number four are larger than that of trivalent cation Fe^{3+} (0.49 Å) ions with coordination number four, therefore, we have observed an increase in $d_{A\text{-}O}$ bond length and lattice constant with increase in Co substitution. In spinel ferrites, the strength of the A-O-B superexchange interaction is responsible for magnetic ordering. The drop in T_C with Co substitution can be understood by the weakening of Fe^{3+}-O-Fe^{3+} superexchange interaction due to the decrease in Fe^{3+} and increase in Co^{2+} ions in the tetrahedral sites. The increase in partial conversion of Fe^{3+} to Fe^{2+} ions in the octahedral sublattices (Table 5.3) also influences the reduction of T_C in the Co substituted samples.

Table 5.3: Potential barrier height V_{BA} (Co^{2+}) for Co^{2+} ions jumping from [B] to (A) sites and cations distributions of various ions at the (A) sites and [B] sites per formula unit of $Ni_{1-x}Co_xFe_2O_4$ for different Co-concentration *x*.

x	V_{BA}(Co^{2+})	A site occupation			B site occupation					
	eV.	Ni^{2+}	Co^{2+}	Fe^{3+}	Ni^{2+}	Co^{2+}	Fe^{2+}	Ni^{3+}	Co^{3+}	Fe^{3+}
0	-	0.027	-	0.973	0.698	-	0.275	0.275	-	0.752
0.10	2.02	0.024	0.011	0.966	0.629	0.054	0.283	0.247	0.036	0.752
0.20	2.13	0.021	0.026	0.953	0.559	0.104	0.290	0.220	0.070	0.757
0.30	2.28	0.018	0.032	0.949	0.490	0.160	0.299	0.192	0.107	0.751
0.40	2.36	0.016	0.039	0.945	0.421	0.217	0.308	0.164	0.144	0.747
0.50	2.44	0.013	0.045	0.943	0.352	0.262	0.328	0.135	0.193	0.729

5.3 Raman Spectroscopy and Electron spin resonance Spectra

Raman scattering is an important tool to study the vibrational and lattice dynamics of polycrystalline $Ni_{1-x}Co_xFe_2O_4$ compounds. We have performed the Raman scattering measurement at room temperature for all the samples in the frequency range of 100 – 1000 cm^{-1} by using 488 nm laser excitation as shown in Fig. 5.11. For the inverse spinel ferrite with a space group $Fd\bar{3}m$, group theory predicts five Raman active modes (A_{1g}+ E_g+ $3F_{2g}$) [213]. We have observed all the five Raman active modes at 212, 331, 486, 571 and 701 cm^{-1} for x = 0 system. We have observed a small shifting in the peaks towards the lower wave number side with Co substitution, this red shift is attributed to the higher atomic mass of Co (58.9 amu) as compared to Ni (58.69 amu) ions. Usually the higher frequency mode A_{1g} corresponds to the vibration of metal-oxygen bond in tetrahedral sites (AO_4) and the lower frequency modes are

associated with octahedral sites (BO_6) [122, 123, 214]. A shifting in the A_{1g} mode from 701 cm^{-1} for x = 0 to 695 cm^{-1} for x = 0.50 also confirms the change in the ratio of Co^{2+} to Ni^{2+} concentration at A sites with Co substitution. The variation in intensity and area of the A_{1g} modes (A_{1g}(1) & A_{1g}(2)) confirms the cation migration between the octahedral and tetrahedral sites of these compounds with Co substitution (Fig.5.11 (b)).

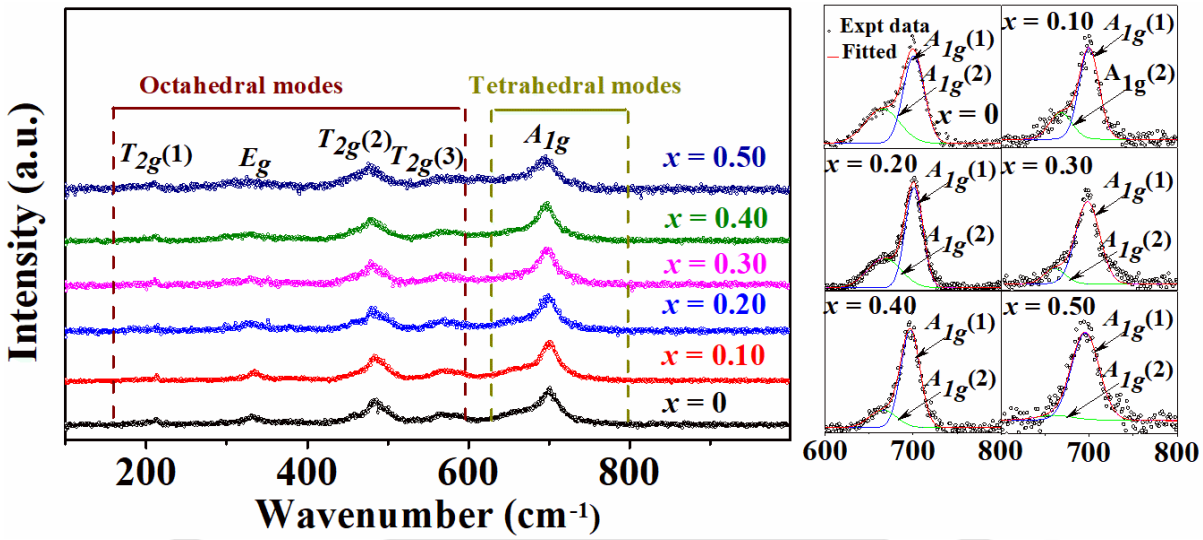

Fig. 5.11: Micro – Raman spectrum of $Ni_{1-x}Co_xFe_2O_4$ (x = 0 – 0.50) compound.

Electron spin resonance (ESR) spectra of $Ni_{1-x}Co_xFe_2O_4$ (x = 0, 0.20 & 0.50) were recorded at room temperature to understand the magnetic properties at high frequency in the system (Fig. 5.12). ESR spectra for the present systems were carried out at a constant *X* band frequency of 9.4 GHz and by scanning the magnetic field up to 1T.

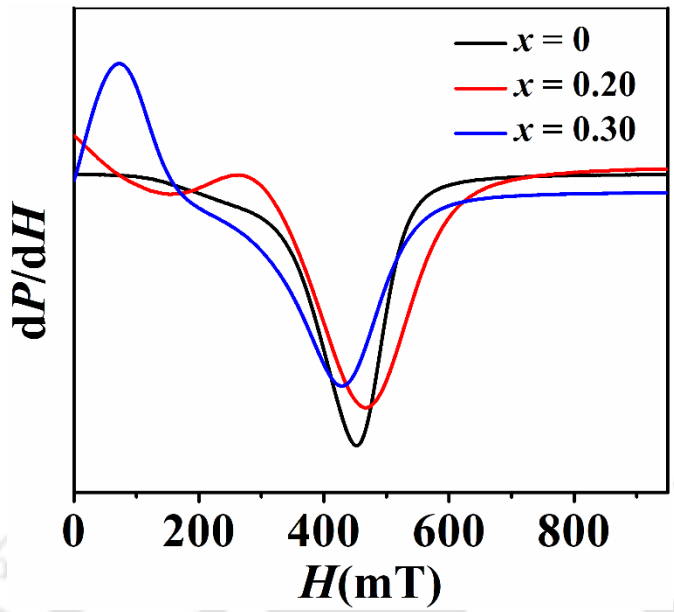

Fig. 5.12: ESR spectra for $Ni_{1-x}Co_xFe_2O_4$ (x = 0, 0.20 & 0.50).

The values of Lande's g factor and peak to peak line width (ΔH_{pp}) are the two most important parameters to understand the strength of superexchange interaction and anisotropy in the systems. The value of Lande's g factor can be estimated by following equation [215],

$$g = \frac{h\upsilon}{\mu_B H_r} \tag{5.17}$$

Here υ is frequency of electromagnetic radiation, h is Plank constant, μ_B is Bohr magneton and H_r is resonance field. The parameters obtained from ESR spectra are given in Table 5.4.

Table 5.4: ESR parameters of $Ni_{1-x}Co_xFe_2O_4$ (x = 0 – 0.50) at room temperature.

Sample	H_r (mT)	ΔH_{pp} (mT)	g
x = 0	332	198	2.02
x = 0.20	293	330	2.29
x = 0.50	222	357	3.03

The obtained value of g is found to increase with Co^{2+} substitution, indicating the weakening of superexchange interaction through Fe^{3+} - O - Fe^{3+} networks. The increase in ESR broadening (ΔH_{pp}) with Co substitution reveals the enhancement in magneto crystalline anisotropy, which is in accordance with magnetization results [216].

5.4 Conclusion

Using the sol gel method, a series of Co substituted $Ni_{1-x}Co_xFe_2O_4$ (x = 0 – 0.50) bulk spinel ferrites are successfully synthesized. Room temperature X-ray diffraction patterns confirm that all samples are crystallized in cubic crystal structure with space group $Fd\bar{3}m$. The increase in lattice parameter with Co substitution can be understood by the influence of divalent cations migrated from octahedral to tetrahedral sublattices. Morphology of the samples is investigated using FESEM micrographs and the mean particle sizes are in the range of 180 – 665 nm. The high temperature magnetization measurements of these samples indicate ferrimagnetic behavior with Curie temperature far above room temperature. The Curie temperature of the samples decreases with increase in Co content due to the reduction of Fe^{3+}-O - Fe^{3+} superexchange interaction. The values of saturation magnetization and magnetic anisotropy are found to increase with Co substitution which would be useful for device application. We have estimated the cation distribution for all the samples with the help of quantum mechanical potential barrier method by using the magnetic moment at 5 K. The cation distribution analysis revealed the preferential occupation of Co^{2+} and Ni^{2+} in octahedral sites and partial occupation in tetrahedral sites, whereas the Fe^{3+} ions has almost equal preference for both the sublattices. Observed red shifting of Raman active mode A_{1g} and ESR results also confirm the presence of Co^{2+}/Ni^{2+} ions at tetrahedral sublattices. The variation of structural and magnetic properties with Co substitution are successfully described based on cation distribution, magnetic anisotropy and superexchange interaction.

Chapter 6

Conclusions

This chapter summarizes the overall results obtained in Chapters 3, 4 and 5. The detailed study of structural and physical properties in $Ni_{1-x}M_xCr_2O_4$ (M = Mg, Mn and Cd) and $Ni_{1-x}Co_xFe_2O_4$ series provides the following conclusions.

Single-phase polycrystalline $Ni_{1-x}Mg_xCr_2O_4$ (x = 0-0.50) samples have been successfully synthesized by the sol-gel method. Rietveld refinement of room temperature XRD patterns confirms the tetragonal ($I4_1/amd$) crystal structure for $NiCr_2O_4$ and cubic ($Fd\bar{3}m$) for Mg substituted samples. The structural transformation can be understood in terms of suppression of Jahn-Teller distortion by Mg ions. Temperature variation of magnetization measurements reveals ferrimagnetic nature for x = 0, 0.05 and 0.10 samples and dominant antiferromagnetic behavior for x = 0.20, 0.30, 0.40 & 0.50. With Mg substitution, the ferrimagnetic transition temperature (T_C) is found to decrease from 70 K for x = 0 to 42 K for x = 0.10. The decrease in T_C is explained by the reduction in strength of overall superexchange interaction between the two sublattices of magnetic structure. Field dependent magnetization measurement indicates competing antiferromagnetic interaction along with long range ferrimagnetic ordering for the parent compound. We have observed short-range cluster glass like magnetic phase for the intermediate compositions x = 0.10, 0.20 & 0.30. The observed glassy magnetic phase is attributed to the competition between antiferromagnetic and ferromagnetic components of the magnetic moment. The observed glassy magnetic phase is confirmed by stretched type relaxation of thermoremanent magnetization (TRM) and significant frustration in the systems. Based on all temperature, time and field-dependent magnetic measurements, we have constructed the complete magnetic phase diagram for the present series. The observed exchange bias (EB) behavior arises due to the anisotropic exchange interaction between ferromagnetic and antiferromagnetic components of the magnetic moment. With Mg substitution, the magnitude of EB field (H_{EB}) at T = 5 K is found to increase from 91 Oe for x = 0 to 747 Oe for x = 0.10. Temperature variation of H_{EB} and

effective coercivity H_C^{eff} have been analyzed based on exponential and modified Kneller's law respectively. The effect of cooling field (H_{FC}) and maximum measuring field (H_{max}) on H_{EB} are also studied and explained in terms of competition between Zeeman energy and anisotropy exchange energy. Training effect is established by recording several consecutive *M-H* loops and it follows the typical power law behavior. At the end of infinite number of hysteresis loops a considerable value of H_{EB} of 448 Oe is obtained for x = 0.05 sample from the fitted data.

In order to study the importance of particle size on magnetic properties, an intermediate composition i.e. 15 atm % Mg substituted $NiCr_2O_4$ is prepared by hydrothermal route. The room temperature XRD pattern and the Rietveld refinement confirms cubic crystal structure with space group $Fd\bar{3}m$. The lattice constant is found to be a = 8.3560(6) Å. FESEM and FETEM micrographs reveal strongly agglomerated nanoparticles with an average particle size of 46 nm. From temperature variation of magnetization (*M-T*) measurement at 200 Oe, we have observed an irreversibility between ZFC and FC magnetization below 125 K due to the blocking nature of nanoparticles magnetization. We have observed a broad ferrimagnetic transition around 76 K followed by a sharp cluster glass like transition around 9.5 K. The occurrence of cluster glass phase is attributed to the interaction between disordered surface spin and ordered FIM core structure. Unlike in bulk nickel chromite system, where substitution of nonmagnetic and non-JT active ions at Ni site leads to enhancement in geometric spin frustration, present nanosystem shows tendency towards collinear ferrimagnetism. The reduction in frustration can be attributed to the domination of Ni-O-Cr superexchange interaction over Cr-O-Cr superexchange and Cr-Cr direct exchange interaction. Field dependent M-T measurement, relaxation and memory effect support the metastability of our cluster glass system. We have studied the dynamics of the nanoparticles in terms of the time and temperature dependence of the thermoremanent magnetization. Below T_f, wait time-dependent aging phenomena have been observed. The observed asymmetric response in magnetic relaxation with respect to change in temperature is may be mediated by ferrimagnetic particle size distribution or exchange coupling between ferrimagnetic core and glassy surface spin.

Similar to Mg substituted series, $Ni_{1-x}Mn_xCr_2O_4$ (x = 0-0.50) samples have been successfully prepared by sol-gel route and their structural, magnetic, magnetocaloric, and

critical behaviors have been examined. Room temperature XRD pattern confirms that synthesized compounds are in single phase form with a structural transformation from tetragonal ($I4_1/amd$) to cubic ($Fd\bar{3}m$) structure with Mn substitution. The increase in lattice constant with increase in Mn concentration for $x \geq 0.05$ confirms the occupation of Mn in the Ni site. All the samples show ferrimagnetic behavior and the transition temperature, T_C is found to decrease with increase in Mn concentration due to the weakening of superexchange interaction. The low temperature hysteresis (*M-H*) loop shows the presence of competing antiferromagnetic interaction in the samples. The presence of positive slope in Arrott plots (M^2 *vs H/M*) confirms the second order ferrimagnetic to paramagnetic (FIM-PM) transition in the series. In order to estimate the magnetic entropy change ($-\Delta S_M$) and critical exponents γ, β and δ, a series of isothermal magnetization curves have been recorded for x = 0, 0.10 and 0.50 about their respective FIM-PM transition temperature. With increase in Mn substitution enhancement in the value of magnetic entropy change is observed in the present series. The maximum magnetic entropy changes of $-\Delta S_M = 2.9\ \mathrm{J\cdot kg^{-1}\cdot K^{-1}}$ is found for x = 0.50 sample for an applied field of H = 9 T at its Currie temperature (38 K). The RCP exhibits a maximum value of $58.2\ \mathrm{J\cdot kg^{-1}}$ for x = 0.50 sample, which is significantly higher than RCP value of $NiCr_2O_4$. Scaling analysis of $-\Delta S_M$ further confirms the second-order transition near T_C. The critical behaviors have been analyzed for x = 0, 0.10 & 0.50 samples. The estimated values of critical exponents are found to deviate from mean-field and other universal models in these compounds. The static scaling plots confirm the reliability of estimated critical exponents in these samples.

$Ni_{1-x}Cd_xCr_2O_4$ with x = 0-0.30 samples are prepared by using sol-gel route. Similar to the previous two series, $Ni_{1-x}Cd_xCr_2O_4$ samples also exhibit a structural transformation from tetragonal ($I4_1/amd$) for x = 0 to cubic ($Fd\bar{3}m$) phase with Cd substitution. The lattice constant is found to increase almost linearly with Cd substitution for $x \geq 0.05$. With Cd substitution, considerable changes in magnetic properties have been observed in temperature dependent magnetization measurements. With Cd substitution the ferrimagnetic transition temperature is found to decrease from 70 K for x = 0 to 45 K for x = 20. The magnetic behaviour in x = 0.20 & 0.30 samples are mostly governed by short range magnetic interactions and shows peculiar magnetic transitions. *M-H* loops recorded at low temperature shows the presence of competing antiferromagnetic interaction in these samples. Exchange bias behavior has been

studied for x = 0.05 and 0.15 samples under field cooling conditions at T = 5 K. The value of exchange bias field (H_{EB}) for x = 0.05 and 0.15 are found to be 1653 Oe and 7477 Oe respectively. Observed memory effect and relaxation of thermoremanent magnetization support the metastability of glassy magnetic phase in x = 0.30 sample. Interestingly, reversible magnetocaloric behavior has been observed for x = 0.20 sample with a maximum negative entropy change of $-\Delta S_M = -0.4\ \mathrm{J{\cdot}kg^{-1}{\cdot}K^{-1}}$. Dielectric, impedance and ac conductivity data have been investigated in the temperature range of T = 27 K – 300 K and frequency range of 100 Hz -10^5 Hz. Study of impedance spectroscopy and ac conductivity indicates non-Debye type of dielectric relaxation and correlated barrier hopping (CBH) of charge carriers is controlling the conduction mechanism in these samples.

$Ni_{1-x}Co_xFe_2O_4$ (x = 0 – 0.50) bulk spinel ferrites are also successfully synthesized by sol-gel method. Unlike the above $NiCr_2O_4$ series, $Ni_{1-x}Co_xFe_2O_4$ do not show any structural transformation and crystallize in cubic crystal structure with space group $Fd\bar{3}m$. The increase in lattice parameter with Co substitution can be understood in terms of the replacement of smaller Ni^{2+} ions by relatively larger Co^{2+} ions in the octahedral environment. Morphology of the samples is investigated using FESEM micrographs and the mean particle sizes are found to be in the range of 180 – 665 nm. The high temperature magnetization measurements of these samples indicate ferrimagnetic behavior with Curie temperature far above room temperature. The Curie temperature of the samples decreases with increase in Co content due to the reduction in strength of Fe^{3+}- O - Fe^{3+} superexchange interaction. The values of saturation magnetization and magnetic anisotropy are found to increase with Co substitution. We have estimated the cation distribution for all the samples with the help of quantum mechanical potential barrier method by using the magnetic moment at 5 K. The cation distribution analysis revealed the preferential occupation of Co^{2+} and Ni^{2+} in octahedral sites and partial occupation in tetrahedral sites, whereas the Fe^{3+} ions have almost equal preference for both the sublattices. We have performed Raman spectroscopy and electron spin resonance spectra (ESR) of $Ni_{1-x}Co_xFe_2O_4$ at room temperature to further support the observed magnetic properties. Observed red shifting of A_{1g} Raman active mode and ESR results also confirm the presence of Co^{2+}/Ni^{2+} ions at tetrahedral sublattices and enhancement in magnetocrystalline anisotropy with Co substitution respectively. The variation of basic structural and magnetic properties with Co

substitution are successfully described based on cation distribution, magnetic anisotropy and superexchange interaction.

Future Scope of Studies:

The above series can be taken up for further studies and the future scope of studies is listed below.

1. A significant magnetoelastic effect in the frustrated lattice can break the symmetry of the crystal via cooperative spin-lattice coupling, therefore studying magnetoelastic coupling in these frustrated magnetic systems would be fascinating.
2. Possible multiferroic properties can be investigated in the doped $NiCr_2O_4$ samples.
3. The dynamics of the glassy magnetic systems can be further studied by ac susceptibility measurements.
4. To better understand the glassy systems, the growth of correlation length as a function of waiting time can be estimated.
5. An interplay between chemical disorder and magnetic frustration or glassy behavior can be investigated in Mg and Cd substituted $NiCr_2O_4$ series.
6. Neutron powder diffraction studies of $Ni_{1-x}Mg_xCr_2O_4$ and $Ni_{1-x}Cd_xCr_2O_4$ compounds at low temperatures would reveal the information about the exact magnetic structure of these compounds near their respective transition temperatures.
7. Preparation of the samples in thin-film form would help to understand the various effects such as film thickness, lattice strain, annealing conditions on basic magnetic properties, exchange bias, anisotropy and magnetic frustration in these samples.

References

1. K. Tomiyasu, J. Fukunage and H. Suzuki, Phys. Rev. B 70, (2004), 214434.
2. L. Balents, Nature 464, (2010), 199.
3. Klemme J. L. van Hemmen, Phys. Rev. A 34, (1986), 3435.
4. T. Roy, J. Math. Phys. 42, (2001), 4283.
5. A. M. Samarakoon, K. Barros, Y. W. Li, M. Eisenbach, Q. Zhang, F. Ye, V. Sharma, Z. L. Dun, H. Zhou, S. A. Grigera, C. D. Batista, D. A. Tennant, Nat Commun. 11, (2020), 892.
6. J. Inoue, Phys. Rev. E. 63, (2001), 046114.
7. J. Maskawa, Empirical Science of Financial Fluctuations, (2002), 153.
8. N. Mufti, G. R. Blake, T Palstra, J. Magn. Magn. Mater. 321, (2009), 11.
9. K. Singh, A. Maignan, C. Simon, C. Martin, Appl. Phys. Lett. 99, (2011), 172903.
10. A. Maignan, C. Martin, K. Singh, C. Simon, O.I. Lebedev, S. Turner, J. Solid State Chem. 195, (2012) 41.
11. V. Kocsis, S. Bordacs, D. Varjas, K. Penc, A. Abouelsayed, C.A. Kuntscher, K. Ohgushi, Y. Tokura, I. Kezsmarki, Phys. Rev. B 87, (2013) 064416.
12. R. Padam, S. Pandya, S. Ravi, A. K. Nigam, S. Ramakrishnan, A. K. Grover, D. Pal, Appl. Phys. Lett 102 (2013), 112412.
13. H. G. Zhang, Z. Wang, E. K. Liu, W. H. Wang, M. Yue, G. H. Wu, J. Appl. Phys 117 (2015), 17B735.
14. L. G. Wang, C. M. Zhu, Z. M. Tian, H. Luo, D. L. G. C. Bao, S. L. Yuan, Appl. Phys. Lett. 107 (2015), 152406.
15. S. Ji, S. H. Lee, C. Broholm, T. Y. Koo, W. Ratcliff, S. W. Cheong and P. Zschack, Phys. Rev. Lett. 103, 037201, (2009).
16. N. A. Spaldin, Magnetic Material: Fundamentals and Application, 2nd ed., Cambridge University Press, Cambridge, (2010).
17. K. K. Kefeni, T. A. M. Msagati, T. TI. Nkambule, B. B. Mamba, Mater. Sci. Eng. C 107, (2020), 110314.
18. Y. Yasukawa, K. Nozawa, T. Tiittanen, M. Karppinen, J. Lindén, S. E. Shirsath, S. Yabukami, Sci. Rep. 11, (2021), 614.

19. A Rabbani, R. Haghniaz, T Khan, R Khan, A Khalid, S. S. Naz, M. Ul-Islam, F. Vajhadin, F. Wahid, RSC. Adv. 11, (2021), 1773.
20. K. E. Sickafus, J. M. Wills, N. W. Grimes, J. Am. Ceram. Soc. 82, (1999), 3279.
21. R. W. Grimes, A. B. Anderson, A. H. Heuer, J. Am. Ceram. Soc. 111, (1989), 1.
22. C. M. Brent, E. D. Jennifer, S. Ram, E. M. Stoudenmire, P. R. Arthur, J. Phys.: Condens. Matter 21, (2009), 216007.
23. G. A. Sawatzky, F. Van Der Wounde, A. H. Morrish, Phys. Rev. 187 (1969) 747.
24. O. Crottaz, F. Kubel, H. Schmid, J. Mater. Chem. 7 (1997), 143.
25. V. Blanco-Gutierrez, J. A. Gallastegui, P. Bonville, M. J. Torralvo-Fernandez, R. Saez-Puche, J. Phys. Chem. C 116, (2012), 24331.
26. F. K. Lotgering, Philips Res. Repts. 11, (1956), 190.
27. K. Siratori, J. Phys. Soc. Jpn. 23, (1967), 948.
28. M. Tanaka, T. Tokoro, Y. Aiyama, J. Phys. Soc. Jpn. 21, (1966), 262.
29. S. Blundell, Magnetism in Condensed Matter, Oxford University Press (2001).
30. B. J. Kennedy, Q. Zhou, J. Solid State Chem. 181, (2008), 2227.
31. K. Ohgushi, Y. Okimoto, T. Ogasawara, S. Miyasaka, Y. Tokura, J. Phys. Soc. Jpn. 77, (2008), 034713.
32. M. Tovar, R. Torabi, C. Welker, F. Fleischer, Physica B 385, (2006),196.
33. B. D. Cullity, C. D. Graham, Introduction to Magnetic Materials, IEEE Press (2009).
34. H. A. Kramers, Physica 1, (1934), 182.
35. J. C. Slater, Quart. Progr. Rep. M. I. T. July 15, 1: Oct. 15 1 (1953).
36. J. B. Goodenough, A. L. Loeb, Phys. Rev. 98, (1955), 391.
37. C. Zener, Phys. Rev. 81, (1951), 440.
38. C. Zener, Phys. Rev. 82, (1951), 403.
39. M. A. Ruderman, C. Kittel, Phys. Rev. 96, (1954), 99.
40. I. Dzyaloshinsky, J. Phys. Chem. Soilds 4, (1958), 241.
41. T. Moriya, Phys. Rev. 120, (1960), 91.
42. A. H. Morrish, The Physical principle of Magnetism, IEEE Press (2001).
43. D. L. Stein, C. M. Newman, Spin Glass and Complexity, Princeton University Press (2013).
44. C. Kittel, Introduction to Solid State Physics, Wiley Press, Singapore (2004).

45. L. Néel, Ann. Phys. 12 (1948) 137.
46. E. Winkler, S.B. Canosa, F. Rivadulla, M.A. López-Quintela, J. Rivas, A. Caneiro, M.T. Causa, M. Tovar, Phys. Rev. B 80, (2009), 104418.
47. J. Kondo, Prog. Theor. Phys. 32, (1964), 37.
48. V. Cannella, J. A. Mydosh, J. I. Budnick, J. Appl. Phys. 42, (1971),1689.
49. W. Kinzel, Phys. Rev. B 19, (1979), 4595.
50. R. V. Chamberlin, G. Mozurkewich, and R. Orbach, Phys. Rev. Lett. *52*, (1984), 867.
51. D. H. Lyons, T. A. Kaplan, K. Dwight, N. Menyuk, Phys. Rev. 126, (1962), 540.
52. E. Schlomann, J. Appl. Phys. 33, (1962), 2825.
53. W. H. Meiklejohn, C. P. Bean, Phys. Rev. 102, (1956) 1413.
54. G. W. Fernando, Handbook of Metal Physics, 4, (2008), 1.
55. J. C. S. Kools, IEEE Trans. Magn. 32 (1996), 3165.
56. J. Nogues, I. K. Schuller, J. Magn. Magn. Mater. 192, (1999), 203.
57. J. Nogues, J. Sort, V. Langlais, V. Skumryev, S. Surinach, J. S. Munoz, M. D. Baro, Phys. Rep. 422, (2005), 65.
58. S. Giri, M. Patra, S. Majumdar, J. Phys.: Condens. Matter 23, (2011), 073201.
59. J. Barman, T. Borah, S. Ravi, J. Magn. Magn. Mater. 385, (2015), 93.
60. H. Singh, T. Chakraborty, K. Srikanth, R. Chandra, C. Mitra, U. Kumar, J. Magn. Magn. Mater. 448, (2014), 77.
61. C. Rath, P. Mohanty, A. Banerjee, J. Magn. Magn. Mater. 323, (2011), 1698.
62. C. Zhu, Z. Tian, L. Wang, S. Yuan, J. Magn. Magn. Mater. 393, (2015), 116.
63. Z. M. Tian, S. L. Yuan, L. Liu, S. Y. Yin, L. C. Jia, P. Li, S. X. Huo, J. Q. Li, J. Phys. D: Appl. Phys. 42, (2009), 035008.
64. J. Yang, Y. P. Lee, Y. Li, J. Appl. Phys. 102, (2007), 033913.
65. V. Franco, J. S. Blazquez, B. Ingale, A. Conde, Annu. Rev. Mater. Res. 42, (2012), 305.
66. N. H. Van Dijk, J. Magn. Magn. Mater. 529, (2021), 167871.
67. H. E. Stanley, Introduction to Phase Transitions and Critical Phenomenon, Oxford University Press, New York, NY, 1997.
68. A. Arrott, J. E. Noakes, Phys. Rev. Lett. 19, (1967), 786.
69. X. Hao, J. Adv. Dielectr. 3, (2013), 1330001.

70. A. Aquino, C. G. Juan, B. Potelon, C. Quendo, IEEE Sensors Letters 5, (2021), 1.
71. A. O′Halloran, F. O′Malley, P. McHugh, J. Appl. Phys. 104, (2008), 071101.
72. K.C. Kao, Dielectric phenomena in solids, Elsevier, 2004.
73. E. Barsoukov, J.R. Macdonald, Impedance spectroscopy: theory, experiment, and applications, John Wiley & Sons, 2018.
74. G.G. Raju, Dielectrics in electric fields, CRC press, Florida, USA, 2017.
75. K. Funke, Jump relaxation in solid electrolytes, Prog. Solid State Chem. 22 (1993) 111–195.
76. A.K. Jonscher, The 'universal'dielectric response, Nature. 267 (1977) 673.
77. E. Prince, J. Appl. Phys. 32, (1961), S68.
78. S. Klemme, J. C. van Milteburg, Phys. Chem. Minerals 29, (2002), 663.
79. K. Tomiyasu, I. Kagomiya, J. Phys. Soc. Jpn. 73, (2004), 2539.
80. H. Ishibashi, T. Yasumi, J. Magn. Magn. Mater. 310, (2007), e610.
81. M. R. Suchomel, D. P. Shoemaker, L. Ribaud, M. C. Kemei, R. Seshadri, Phys. Rev. B 86, (2012), 054406.
82. X. Xu, J. Gao, W. Hong, RSC. Adv. 6, (2016), 29646.
83. P. Zhao, M. Ehara, A. Satsuma, S. Sakaki, J. Catal. 393, (2021), 30.
84. M. Bayhan, N. Kavasoğlu, Sensor and Actuators B 117, (2006), 261.
85. Y. Tokura, J. Magn. Magn. Mater. 310, (2007), 1145.
86. T. Hu, L. Dai, Q. Guo, B. Liu, Q Gui, R. Gang, H. Ji, L. Zhang, ACS Omega 5, (2020), 12672.
87. El –Bassuony, A. A. H, J. Inorg Organomet Polym 30, (2020), 1821.
88. N. Mufti, A. A. Nugroho, G. R. Blake, T. T. M. Palstra, J. Phys.: Condens. Mattre 22, (2010), 075902.
89. G. C. Pandey, K. Nemkovski, Y. Su, C. Rath, Dalton Trans. 49, (2020), 4502.
90. J. Barman, P. D. Babu, S. Ravi, J. Magn. Magn. Mater. 418, (2016), 300.
91. J. Barman, S. Ravi, J. Mater. Sci. 53, (2018), 7187.
92. L. Xie, H. L. Huang, H. G. Zhang, J. Q. Yu, J. Z. Zhang, Y. L. Lu, Scr. Mater. 205, (2021), 114210.
93. P. R. Mandal, R. Singh, A. Das, T. Sarkar, T. K. Nath, J. Magn. Magn. Mater. 432, (2017), 49.

94. S -l Park, C. S. Kim, J. Appl. Phys. 101, (2007), 09N511.
95. C. M. Zhu, L. G. Wang, L. Chen, D. L. G. C. Bao, M. C. Wang, S. L. Yuan, J. Mater. Sci. 51, (2016), 9415.
96. C. Li, T. Yan, G. Zerihun, Q. Fu, R. Zhang, X. Chen, S. Huang, S. Yuan, J. Am. Ceram. Soc. 101, (2018), 5571.
97. M. Kamran, W. Shoukat, K Nadeem, S. S. Hussain, F. Zeb, S. Hussain, Mater. Res. Express. 6, (2019), 076106.
98. C. Ragupathi, S. Narayanan, P. Tamizhdurai, M. Govindasamy, Z. A. ALOthman, M. M. AL-Anazy, J. Saudi Chem. Soc. 47, (2021), 10643.
99. N. A. Noshahi, K. Nadeem, M. Kamran, Ceram. Int. 47, (2021), 10643.
100. K. Devi Chandrasekhar, J. Krishna Murthy, J.-Y. Lin, H. C. Wu, W. J. Tseng, A. Venimadhav, H. D. Yang, Phys. Rev. B, 94 (2016), 205143.
101. M. Kataoka, J. Kanamori, J. Phys. Soc. Jpn. 32 (1972), 113.
102. A. A. Bush, V. Ya. Shkuratov, K. E. Kamentsev, A. S. Prokhorov, E. S. Zhukova, B. P. Gorshunov, V. I. Torgashev, Phys. Rev. B 85, (2012), 214112.
103. M. Reehuis, M. Tovar, D. M. Tobbens, P. Pattison, A. Hoser, B. Lake, Phys. Rev. B 91 (2015), 024407.
104. J. M. Hastings, L.M. Corliss, Rev. Modern Phys. 25, (1953), 114.
105. D.S. Jung, Y.C. Kang, J. Magn. Magn. Mater. 321, (2009), 619.
106. S.T. Hussain, S.R. Gilani, S.D. Ali, H.S. Bhatti, J. Alloy. Compd. 544, (2012), 99.
107. A.D. Mani, I. Soibam, Physica B 507, (2017), 21.
108. M. H. Dhaou, S. Hcini, A. Mallah, M.L. Bouazizi, A. Jemni, Appl. Phys. A 123, (2017), 8.
109. P. Chavan, L.R. Naik, P.B. Belavi, G. Chavan, C.K. Ramesha, R.K. Kotnala, J. Electron Mater. 46, (2017), 188.
110. D. Vladikova, L. Ilkov, S. Karbanov, Phys. Status Solidi A 121, (1990), 249.
111. M. N. Ashiq, M.J. Iqbal, I.H. Gul, J. Alloys Compd. 487, (2009), 341.
112. C.G. Ramankutty, S. Sugunan, Appl. Catal. A General 218, (2001), 39.
113. J. Rawat, S. Rana, R.S. Srivastava, R.D.K. Misra, Mater. Sci. Eng. C 27, (2007), 540.
114. Z. Jia, R.D.K. Misra, Mater. Technol. 26, (2011), 191.
115. X. Wu, W. Chen, W. Wu, H. Li, C. Lin, J. Electron. Mater. 46, (2017), 199.

116. M. Rahimia, M. Eshraghi, P. Kameli, Ceram. Int. 40, (2014), 15569.
117. S. I. Youseef, M.G. Natera, R.J. Begum, B.S. Srinivasan, N.S.S. Murthy, J. Phys. Chem. Solids 30, (1969), 1941.
118. Y. Shi, J. Ding, Z.X. Shen, W.X. Sun, L. Wang, Solid State Commun. 115, (2000), 237.
119. V. Šepelak, D. Baabe, K.D. Becker, J. Mater. Syn. Process. 8, (2000), 333.
120. R. D. K. Misra, A. Kale, R. S. Srivastava, O. N. Senkov, Mater. Sci. Technol. 19, (2003), 826.
121. U. B. Sontu, Narsinga Rao G, F.C. Chou, V. R. Reddy M, J. Magn. Magn. Mater. 452, (2018) 398.
122. A. Kumar, P. Sharma and D. Varshney, Ceram. Int. 40, (2014), 12855.
123. N. B. Velhal, N. D. Patil, A. R. Shelke, N. G. Deshpande and V. R. Puri, AIP Adv. 5, (2015), 097166.
124. G. Datt, M. S. Bishwas, M. M. Raja and A. C. Abhyankar, Nanoscale 8, (2016), 5200.
125. A. A. Ati, J. Mater. Sci. Mater. Electron. 29, (2018), 12010.
126. V. K. Chakradhary, A. Ansari, M. J. Akhtar, J. Magn. Magn Mater. 469 (2019), 674.
127. C.S. Zhang, L. Yang, J. Magn. Magn. Mater. 324, (2012), 1469.
128. R. C. Kamble, P. A. Shaikh, S. S. Kamble, Y.D. Kolekar, J. Alloy Compd. 478, (2009), 599.
129. K. Khan, A. Maqsood, M. Anis-ur-Rehman, M. A. Malik, M. Akram, J. Supercond. Nov. Magn. 25, (2012), 2707.
130. K. Khan, J. Super Cond. Nov. Magn. 27, (2014), 453.
131. A. A. Ati, Z. Othaman, A. Samavati, J. Mol. Struct. 1052, (2013), 177.
132. E. P. Wohlfarth, Ferromagnetic Materials, 3, (1982), 248.
133. A. Maqsood, K. Khan, J. Alloys Compd. 509, (2011), 3393.
134. R. B. Kamble, V.L. Mathe, Sens. Actuat. B Chem. 131, (2008), 205.
135. K. Maaz, W. Khalid, A. Mumtaz, S. K. Hasanain, J. Liu, J. L. Duan, Physica E 41, (2009), 593.
136. H. Sozeri, F. Genç, B. Ünal, A. Baykal, B. Aktaş, J. Alloys Compd. 660, (2016), 324.
137. G. D. Tang, D. H. Ji, Y. X. Yao, S. P. Liu, Z. Z. Li, W. H. Qi, Q. J. Han, X. Hou, D. L. Hou, Appl. Phys. Lett. 98, (2011), 072511.

138. C Kittle, Introduction to Solid State Physics, Wiley Press, Singapore (2004).
139. R. A. Young, The Rietveld method "International Union of Crystallography" New York, Oxford University, (1996).
140. R. Kumar, Atomic and molecular physics, Campus Book International, (2009).
141. S. Hűfner, Photoelectron Spectroscopy: Principles and Applications, Springer, Berlin (2003).
142. M.C. Kemei, S.L. Moffitt, L.E. Darago, R. Seshadri, M. R. Suchomel, D. P. Shoemaker, K. Page, J. Siewenie, Phys. Rev. B 89, (2014), 174410.
143. R. D. Shannon, Acta Cryst. A 32, (1976), 751.
144. E. A. Odo, Nanosci Nanotechnol. 5, (2015), 57.
145. H. C. Gupta, M. M. Sinha, Balram, B. B. Tripathi, Physica B: Condens. Matter 192, (1993), 343.
146. X. Liu, N. Yin, T. Thomas, M. Yang, J. Wang, Q. Shi, RSC Adv. 6, (2016), 112140.
147. L.T. Coutrim, E.M. Bittar, F. Garcia, L. Bufaiçal, Phys. Rev. B 98, (2018), 064426.
148. D. Karmakar, S. K. Mandal, R. M. Kadam, P. L. Paulose, A. K. Rajarajan, T. K. Nath, A. K. Das, I. Dasgupta, G. P. Das, Phys. Rev. B 75, (2007), 144404.
149. K. Dey, S. Majumdar, S. Giri, Phys. Rev. B 90, (2014), 184424.
150. R. N. Bhowmik, R. Ranganathan, R. Nagarajan, Phys. Rev. B 73, (2006), 144413.
151. D. S. Williams, P. M. Shand, T. M. Pekarek, R. Skomski, V. Petkov, D. L. LesliePelecky, Phys. Rev. B 68, (2003), 214404.
152. J. S. Smart, Phys. Rev. 94, (1954), 847.
153. Y. Melikhov, J. E. Snyder, D.C. Jiles, A.P. Ring, J. A. Paulsen, C. C. H. Lo, K. W. Dennis, J. Appl. Phys. 99, (2006), 08R102.
154. Ch. Binek, J. Appl. Phys. 97, (2005), 10C514.
155. Xi Chen, A. Hochstrat, P. Borisov, W. Kleemann, Appl. Phys. Lett. 89, (2006), 202508.
156. D. A. Balaev, A. A. Krasikov, A. A. Dubrovskii, S. V. Semenov, O. A. Bayukov, S. V. Stolyar, R. S. Iskhakov, V. P. Ladygina, L. A. Ishchenko, J. Exp. Theor. Phys. **119**, (2014), 479.
157. N. S. E. Osman, T. Moyo, J. Supercond. Nov. Magn. 29, (2016), 361.

158. D. Paccard, C. Schlenker, O. Massenet, R. Montmory, A. Yelon, Phys. Status Solidi (a), 16, (1966), 301.
159. S. Karmakar, S. Taran, E. Bose, B. K. Chaudhuri, C. P. Sun, C. L. Huang, H. D. Yang, Phys. Rev.B 77, (2008), 144409.
160. B. Issa, I. M. Obaidat, B. A. Albiss, Y. Haik, Int. J. Mol. Sci. 14 (2013), 21266.
161. R. Yanes, O. C. –Fesenko, H. Kachkachi, D. A. Garanin, R. Evans, R. W. Chantrell, Phys. Rev. B 76, (2007), 064416.
162. E. De. Biasi, R. D. Zysler, C. A. Ramos, H. Romero, D. Fiorani, Phys. Rev. B 71, (2005), 104408.
163. E. Winkler, R. D. Zysler, M. V. Mansilla, D. Fiorani, Phys. Rev. B 72, (2005), 132409.
164. D. G. Wickham, J. B. Goodenough, Phys. Rev. 115, (1959), 1156.
165. R. H. Kodama, A. E. Berkowitz, Phys. Rev. Lett. 77, (1996), 394.
166. J. A. De Toro, S. S. Lee, D. Salazar, J. L. Cheong, P. S. Normile, P. Muniz, J. M. Riveiro, M. Hillenkamp, F. Tournus, A. Tamion, P. Nordblad, Appl. Phys. Lett. 102, (2013), 183104.
167. L. Zu, S. Lin, Y. Liu, J. C. Lin, B. Yuan, X. C. Kan, P. Tong, W. H. Song, Y. P. Sun, Appl. Phys. Lett. 108, (2016), 031906.
168. B. C. Melot, J. E. Drewes, R. Seshadri, E. M. Stoudenmire, A. P. Ramirez, J. Phys. Condens. Matter. 21, (2009), 216007.
169. S. H. Lee, C. Broholm, W. Ratcliff, G. Gasparovic, Q. Huang, T. H. Kim, S. W. Cheong, Nature 418, (2002), 856.
170. A. C. Gandhi, T. S. Chan, J. Pant, S. Y. Wu, Nanoscale Res. Lett. 12, (2017), 207.
171. H. Khurshid, P. L. -Kelley, Ò. Iglesias, J. Alonso, M. H. Phan, C. J. Sun, M. L. Saboungi, H. Srikanth, Sci. Rep. 5 (2015), 15054.
172. A. C. Gandhi, S. Y. Wu, RSC. Adv. 7, (2017), 25512.
173. J. M. D. Coey, Phys. Rev. Lett. 27, (1971), 1140.
174. A. Zelenakova, V. Zelenak, I. Matko, M. Streckova, P. Hrubovcak, J. Kovac, J. Appl. Phys. 116, (2014), 033907.
175. R. N. Bhowmik, K. S. Aneeshkumar, J. Magn. Magn. Mater. 460, (2018), 177.
176. E. De Biasi, C. A. Ramos, R. D. Zysler, H. Romero, Phys. Rev. B 65 (2002), 144416.
177. Z. Tian, L. Xu, Y. Gao, S. Yuan, Z. Xia, Appl. Phys. Lett. 111, (2017), 182406.
178. L. Xu, Y. Gao, A. Malik, Y. Liu, G. Gong, Y. Wang, Z. Tian, S. Yuan, J. Magn. Magn. Mater. 469, (2019), 504.

179. V. Markovich, I. Fita, A. Wisniewski, G. Jung, D. Mogilyansky, R. Puzniak, L. Titelman, G. Gorodetsky, Phys. Rev. B 81, (2010), 134440.
180. K. Dey, A. Indra, S. Majumdar, S Giri, J. Magn. Magn. Mater. 435, (2017), 15.
181. A. Ali, Y. Singh, J. Magn. Magn. Mater. 499, 166253 (2020).
182. M. Matsuda, M. Takeda, M. Nakamura, K. Kakurai, A. Oosawa, E. Lelièvre – Berna, J. – H. Chung, H. Ueda, H. Takagi, and S. – H. Lee, Phys. Rev. B **75**, (2007), 104415.
183. J. Garcia-Otero, M. Porto, J. Rivas, A. Bunde, J. Appl. Phys. **85**, (1999), 2287.
184. B. K. Banerjee, Phys. Lett. 12, (1964), 16.
185. A. J. Berlinsky and A. B. Harris, Statistical Mechanics, Graduate Texts in Physics, Springer (2019).
186. F. Fang, B. Hong, L. Ling, J. Xu, H. Jin, D. Jin, X. Peng, J. Li, Y. Yang and X. Wang, RSC. Adv. 6, (2016), 22411.
187. D. Mazumdar, K. Das, I. Das, J Appl. Phys., 127, 127 (2020), 093902.
188. N. Tateiwa, Y. Haga, T. D. Matsuda, E. Yamamoto, Z. Fisk, Phys. Rev. B 89, (2014), 064420.
189. J. Lin, P. Tong, D. Cui, C. Yang, J. Yang, S. Lin, B. Wang, W. Tong, L. Zhang, Y. Zou, Y. Sun, Sci. Rep. 5, (2015), 7933.
190. H. N Bez, H. Yibole, A. Pathak, Y. Mudryk, V. K. Pecharsky, J. Magn. Magn. Mater. 458, (2018), 301.
191. H. Oesterreicher, F. T. Parker, J. Appl. Phys. 55, (1984), 4334.
192. R. C. Sahoo, S. Das, and T. K. Nath, J. Appl. Phys. 123, (2018), 013902.
193. M. Pekala, J. Appl. Phys. 108, (2010), 113913.
194. I.W. Chen, J. Phys. Chem. Solids 61, (2000),197.
195. X.H. Zheng, Z.H. Ma, P.J. Chen, D.P. Tang, N. Ma, J. Mater. Sci. Mater. Electron. 23, (2012), 1533.
196. S. Pattanayak, B.N. Parida, P.R. Das, R.N.P. Choudhary, Appl. Phys. A. 112, (2013), 387.
197. S. Nasri, M. Megdiche, M. Gargouri, Ceram. Int. 42, (2016), 943.
198. M. K. Fayek, M. F. Mostafa, F. Sayedahmed, S. S. Ata-Allah, M. Kaiser, J. Magn. Magn. Mater. 210 (2000), 189.
199. J. C. Slonczewski, J. Appl. Phys., 1961, 32, S253.

200. M. M. Naik, H. S. B. Naik, G. Nagaraju, M. Vinuth, K. Vinu, S. K. Rashmi, J. Mater. Sci.: Mater. Electron. 29, (2018), 20395.
201. M. P. Ghosh, S. Mukherjee, J. Magn. Magn. Mater 489, (2019), 165320.
202. M. Hua, L. Xu, F. Cui, J. Lian, Y. Huang, J. Bao, J. Qiu, Y. Xu, H. Xu, Y. Zhao, H. Li, J. Mater. Sci. 53, (2018), 7621.
203. G. Liu, X. Gao, K. Wang, D. He, J. Li, Int. J. Hydrog. Energy 41, (2016), 17976.
204. S. Hara, J. Aisu, M. Kato, T. Aono, K. Sugawa, K. Sugawa, K. Takase, J. Otsuki, S. Shimizu, H. Ikake, Nanoscale Res. Lett. 13, (2018), 176.
205. X. Liu, C. Hao, H. Jiang, M. Zeng, R. Yu, J. Mater. Chem. C 5, (2017), 3770.
206. J. Massoudi, M. Smari, K. Nouri, E. Dhahri, K. Khirouni, S. Bertaina, L. Bessais and E. K. Hlil, RSC. Adv. 10, (2020), 34556.
207. P. A. Joy, P. S. A. Kumar, S. K. Date, J. Phys. Condens Matter 10, (1998), 11049.
208. S. E. Shirsath, S. S. Jadhav, B. G. Toksha, S. M. Patange, K. M. Jadhav, J. Appl. Phys. 110 (2011), 013914.
209. J. C. Slonczewski, Phys. Rev. 110, (1958), 1341.
210. G. D. Tang, D. L. Hou, W. Chen, X. Zhao, and W. H. Qi, Appl. Phys. Lett., 90 (2007), 144101.
211. H. Zhang, Y. Zhang, Y. Li, Practical Handbook of Chemistry, Science Press, Beijing, 2001, 645.
212. Q. J. Han, D. H. Ji, G. D. Tang, Z. Z. Li, X. Hou, W. H. Qi, S. R. Liu, R. R. Bian, J. Magn. Magn Mater. 324 (2012), 1975.
213. P. Chandramohan, M. P. Srinivasan, S. Velmurugan and S. V. Narasimha, J. Solid State Chem. 184, (2011), 89.
214. D. Varshney, K. Verma and A. Kumar, J. Mol. Struct. 1006, (2011), 447.
215. S. A. V. Prasad, M. Deepty, P. N. Ramesh, G. Prasad, K. Srinivasarao, Ch. Srinivas, K. V. Babu, E. R. Kumar, N. K. Mohan, D. L. Sastry, Ceram. Int. 44, (2018), 10517.
216. K Jalaiah, K. V. Babu, J. Magn. Magn. Mater 423, (2017), 275.

Paper Published in International Journals

1. **Ritupan Borah and S Ravi,** *Spin glass and exchange bias behavior in magnetically frustrated $Ni_{1-x}Mg_xCr_2O_4$ (x = 0 – 0.50)*, **Journal of Magnetism and Magnetic Materials 502, (2020), 166550.**
2. **Ritupan Borah and S Ravi,** *Magnetocaloric effect and critical behavior of $Ni_{1-x}Mn_xCr_2O_4$ (x = 0, 0.10 and 0.50) compounds*, **Journal of Applied Physics 128, (2020), 233901.**
3. **Ritupan Borah and S Ravi,** *Effect of cation distributions on structural and magnetic properties of $Ni_{1-x}Co_xFe_2O_4$ spinel ferrite,* **Journal of Magnetism and Magnetic Materials 538, (2021), 168276.**
4. **Ritupan Borah and S Ravi,** *Investigation of static and dynamic magnetic properties of $Ni_{0.85}Mg_{0.15}Cr_2O_4$ nanoparticles,* **Journal of Magnetism and Magnetic Materials 560, (2022), 169666.**
5. **Ritupan Borah, Debabrata Mazi and S Ravi,** *Evidence of cluster glass phase, reversible magnetocaloric effect and study of electrical properties in $Ni_{1-x}Cd_xCr_2O_4$ (x = 0 - 0.30) spinel.* **(Under Review).**

Paper published in other related work (outside thesis)

1. VM Gaikwad, M Brahma, **Ritupan Borah**, S Ravi, *Structural, optical and magnetic properties of Pr2FeCrO6 nanoparticles*, **Journal of Solid State Chemistry 278, (2019), 120903.**
2. Sikha Sarmah, **Ritupan Borah**, P. K. Maji, S. Ravi and Tribedi Bora, Effect of Al^{3+} substituted on structural, magnetic and dielectric properties of cobalt ferrite synthesized by sol-gel method and correlation with cation distribution**., Physica B: Condensed Matter, 639, (2022), 414017**.

Paper presented in National/International Conferences/Workshops

1. **International conference on Magnetic Materials and Applications (ICMAGMA-2018)** held on 09-13 December 2018 at School of Physical Sciences, NISER-Bhubaneswar: Structural and Magnetic Properties of Magnesium Substituted Nickel Chromite.

2. **Research conclave 2019** held on 08-11 March, 2018 at IIT Guwahati: Magnetic Properties of Nickel-Cobalt Ferrite nanoparticles synthesized by coprecipitation method.
3. **International webinar on Exploring the World of Matter, Materials and Machines** held on 21 Dec. 2020 at Department of Physics Dhenkanal Autonomous College, Dhenkanal.
4. **6th International Conference on Nanoscience and Nanotechnology (ICONN 2021)** held on 01-03 Feb. 2021 at SRM Institute of Science and Technology: A study of crossover from weak ferrimagnetic to spin glass like behavior in $Ni_{0.85}Mg_{0.15}Cr_2O_4$.
5. **Symposium on Magnetism and Spintronics (SMS2021)** held on 25-27 Nov. 2021 at NISER-Bhubaneswar: Structural and Magnetic Characterization of Mn Doped Ni-Co Spinel Ferrite Nanoparticles with Surface Spin Disorder.
6. **7th International Conference on Advanced Nanomaterials and Nanotechnology (ICANN 2021)** held on 14-17 Dec. 2021 at IIT Guwahati: Exchange bias and dynamic magnetic properties of Mg substituted $NiCr_2O_4$ nanoparticles.